AERODYNAMIC AND STRUCTURAL DESIGN
AND ANALYSIS OF AN ELECTRIC POWERED MINI UAV

A THESIS SUBMITTED TO
THE GRADUATE SCHOOL OF NATURAL AND APPLIED SCIENCES
OF
MIDDLE EAST TECHNICAL UNIVERSITY

BY

ALPAY DEMİRCAN

IN PARTIAL FULFILLMENT OF THE REQUIREMENTS
FOR
THE DEGREE OF MASTER OF SCIENCE
IN
AEROSPACE ENGINEERING

MAY 2016

Approval of the thesis:

AERODYNAMIC AND STRUCTURAL DESIGN

AND ANALYSIS OF AN ELECTRIC POWERED MINI UAV

submitted by **ALPAY DEMİRCAN** in partial fulfillment of the requirements for the degree of **Master of Science in Aerospace Engineering Department, Middle East Technical University** by,

Prof. Dr. Gülbin Dural Ünver
Dean, Graduate School of **Natural and Applied Sciences**   _____

Prof. Dr. Ozan Tekinalp
Head of Department, **Aerospace Engineering**   _____

Prof. Dr. Altan Kayran
Supervisor, **Aerospace Engineering Dept., METU**   _____

Examining Committee Members:

Prof. Dr. Serkan Özgen
Aerospace Engineering Dept., METU   _____

Prof. Dr. Altan Kayran
Aerospace Engineering Dept., METU   _____

Prof. Dr. Nafiz Alemdaroğlu
School of Civil Aviation, Atılım University   _____

Asst. Prof. Dr. Ercan Gürses
Aerospace Engineering Dept., METU   _____

Asst. Prof. Dr. Harika S. Kahveci
Aerospace Engineering Dept., METU   _____

                                        Date: _____

I hereby declare that all information in this document has been obtained and presented in accordance with academic rules and ethical conduct. I also declare that, as required by these rules and conduct, I have fully cited and referenced all material and results that are not original to this work.

Name, Last Name   : **Alpay DEMİRCAN**

Signature   :

ABSTRACT

AERODYNAMIC AND STRUCTURAL DESIGN
AND ANALYSIS OF AN ELECTRIC POWERED MINI UAV

Demircan, Alpay

M. S., Department of Aerospace Engineering

Supervisor: Prof. Dr. Altan Kayran

May 2016, 173 pages

The aim of this study is to describe the aerodynamic and structural design of an electric powered portable Mini UAV. Conceptual design, structural design and analysis of the wing and detail design phases of the UAV are presented in the study.

Fixed wing mini UAV configuration with fixed – pitch propeller has been chosen for the design. In order to provide multi-mission capability, payload of the UAV is designed as a replaceable mission compartment. System requirements and mission profiles of the airplane are adopted from competitor analysis and critical design parameters are defined to perform flight performance calculations in the conceptual design phase. A dynamic thrust estimation model is proposed for the electric motor and fixed – pitch propeller propulsion system. Endurance and range calculations for a battery powered aircraft are also described in the study.

Components of the aircraft structure are designed using composite materials. In order to decide structural layout of the wing, CFD analysis of the wing is performed for limit load condition and aerodynamic loading is determined. Structural analysis of the wing is performed for two different structural layouts by using the aerodynamic load determined in CFD analysis. I spar and tubular spar configurations are

considered for the wing structure and comparison of stress loads on the structural components of the wing for these two different design configurations is presented.

Overall structural layout, portability and ease of transportation requirements are considered in the detailed structural design phase. Manufacturing and assembly issues are also taken into account and at the end of this study, ready to manufacture design is presented.

Keywords: Mini UAV, electric powered UAV, fixed pitch propeller, airplane design, finite element analysis, composite structure, structural design

ÖZ

ELEKTRİKLİ BİR MİNİ İHA'NIN
AERODİNAMİK VE YAPISAL TASARIMI VE ANALİZİ

Demircan, Alpay

Yüksek Lisans, Havacılık ve Uzay Mühendisliği Bölümü

Tez Yöneticisi: Prof. Dr. Altan Kayran

Mayıs 2016, 173 sayfa

Bu çalışmanın amacı elektrikli bir portatif Mini İHA'nın aerodinamik ve yapısal tasarımını belirlemektir. Çalışma kapsamında kavramsal tasarım, kanadın yapısal tasarımı ile analizi ve detay tasarım süreçleri gösterilmiştir.

Tasarımda sabit hatveli pervanenin kullanıldığı sabit kanatlı bir Mini İHA konfigürasyonu seçilmiştir. Çoklu görevlere uygunluğun sağlanması için faydalı yük olarak değiştirilebilir bir görev bölmesi seçilmiştir. Sistem gereksinimleri ve görev profilleri rakip analizleriyle belirlenmiş ve konsept tasarım sürecinde uçuş performansı hesaplamalarında kullanılmıştır. Çalışmada sabit hatveli pervane kullanan elektrikli uçaklar için dinamik itki hesaplama modeli sunulmuş, pilli uçaklar için uçuş süresi ve menzil hesaplamaları gösterilmiştir.

Uçağın yapısal bileşenleri kompozit malzeme kullanarak tasarlanmıştır. Kanadın yapısal tasarımının belirlenmek için limit yük koşulları altındaki aerodinamik yükleme HAD analizi yapılarak belirlenmiştir. Kanadın yapısal analizi iki farklı yapısal tasarım için HAD analiziyle elde edilmiş olan aerodinamik yükler kullanılarak yapılmıştır. Kanadın yapısal konfigürasyonlarında I tipi kanat kirişi ve

boru kiriş kullanılmış ve bu iki farklı kanat yapısalı konfigürasyonu için gerilme yüklerinin kıyaslanması gösterilmiştir.

Detay tasarım sürecinde genel yapısal tasarım, portatiflik ve kolay taşınabilirlik gereksinimleri dikkate alınmıştır. Üretim ve birleştirme hususlarının da dikkate alındığı bu çalışmanın sonunda üretime hazır bir tasarım gerçekleştirilmiştir.

Anahtar Kelimeler: mini İHA, elektrikli mini İHA, sabit hatveli pervane, uçak tasarımı, sonlu elemanlar analizi, kompozit yapı, yapısal tasarım

to my grandfather…

ACKNOWLEDGEMENTS

TABLE OF CONTENTS

LIST OF TABLES

LIST OF FIGURES

FIGURES

LIST OF SYMBOLS

Symbol	Description	Unit
C_L	Wing Lift Coefficient	-
C_l	Airfoil Lift Coefficient	-
c_f	Skin-Friction coefficient	-
c_{fe}	Equivalent Skin-Friction Coefficient	-
$c_{r,m}$	Root Chord of Multi-Tapered Wing	m
c_r	Root Chord	m
$c_{t,m}$	Tip Chord of Multi-Tapered Wing	m
c_t	Tip Chord	m
AR	Aspect Ratio	-
b	Wing Span	m
L/D	Lift to Drag Ratio	-
S	Wing Area	m^2
SR	Span Ratio	-
V_∞	Velocity	m/s – km/h
W	Weight	N
α	Angle of Attack	degree, radians
λ	Taper Ratio	-
AF_η	Altitude Factor for Propeller Efficiency	-
PcF	Power Correction Factor	-
μ	Dynamic Viscosity	kg/ms
ρ	Density	kg/m^3
C_D	Wing Drag Coefficient	-
C_d	Airfoil Drag Coefficient	-
$C_{m,c/4}$	Moment Coefficient wrt. Quarter Chord	-
c_K	Coefficient of Parasite Drag Increase	-

LIST OF ABBREVIATIONS

Abbreviation	Description	Unit
AGL	Above Ground Level	m
AMSL	Above Mean Sea Level	m
BLOS	Beyond Line of sight	-
DFMA	Design for Manufacturing and Assembly	-
DGCA	Directorate General of Civil Aviation	-
EPS	Expanded Polystyrene	-
ISR	Intelligence Surveillance and Reconnaissance	-
LOS	Line of Sight	-
Mini UAV	Miniature UAV	-
MSL	Mean Sea Level	m
MTOM	Maximum Take-off Mass	kg
MTOW	Maximum Take-off Weight	N
MUAV	Mini Unmanned Aerial Vehicle	-
RPV	Remotely Piloted Vehicle	-
SAM	Surface to Air Missile	-
SHT-İHA	İnsansız Hava Aracı Sistemlerinin Ayrılmış Hava Sahalarındaki Operasyonlarının Usul ve Esaslarına İlişkin Talimat	-
UAS	Unmanned Aerial System	-
UAV	Unmanned Aerial Vehicle	-
XPS	Extruded Polystyrene	-
wrt.	with respect to	-
MUAS	Mini Unmanned Aerial System	-
UAS	Unmanned Aerial System	-
RTM	Resin Transfer Molding	-
PHA	Positive High Angle of Attack	-
PLA	Positive Low Angle of Attack	-

CFD	Computational Fluid Dynamics	-
HAD	Hesaplamalı Akışkanlar Dinamiği	-
RPM	Revolution per Minute	-
rps	Revolution per Second	-

CHAPTER 1

INTRODUCTION

1.1. Unmanned Aerial Vehicles

Unmanned aerial vehicles (UAV) are mainly designed and operated to minimize operational costs and eliminate risks of life losses during aerial missions such as surveillance, reconnaissance and military operations. Especially for the military operations called "D-cube" (Dangerous-Dirty-Dull) [1] risks of life loss is the main problem and UAV's are the most appropriate solution at these situations. Furthermore, practical mission time or endurance of a UAV may be much higher than human pilots, which is impossible to sustain mission for a human pilot such a long time.

Types of the UAV's can be categorized in two different terms, functional usage and size i.e. range/altitude. Functionally, mission capability is the criteria, which are target and decoy, reconnaissance-surveillance, combat, logistics, research and development, civil and commercial UAV's [2]. In terms of size categorization, range and altitude parameters lead to determine the size of the aircraft. Classification table in terms of mission radius and altitude is given in **Table 1.1** [3].

Table 1.1. NATO UAS Classification Guide [3]

Categories	Category	Operating Altitude	Mission Radius
CLASS 1 **(<150kg)**	Micro (<2 kg)	<200 ft AGL	5 km (LOS)
	Mini (2-20 kg)	<3000 ft AGL	25 km (LOS)
	Small (>20 kg)	<5000 ft AGL	50 km (LOS)
CLASS 2 **(150 kg-600 kg)**	Tactical	<10000 ft AGL	200 km (LOS)
CLASS 3 **(>600 kg)**	MALE	<45000 ft MSL	>200 km (BLOS)
	HALE	<65000 ft MSL	BLOS
	Strike/Combat	<65000 ft MSL	BLOS

1.2. History of Unmanned Aerial Vehicles

Unmanned aerial vehicle (UAV) is basically a flying vehicle without a human pilot aboard. In order to operate a UAV, autonomous flight system or remote control is needed to control flight attitude. During the early years, mechanical and gyroscopic devices are used to control attitude of the flying vehicle. Hewitt-Sperry Automatic Airplane, shown in **Figure 1.1**, better known as the Sperry "Flying Bomb" is regarded as the grandfather of modern UAV's and cruise missiles. Flight attitude is controlled by a gyro based mechanical autopilot which has a capability to hit predefined targets [5].
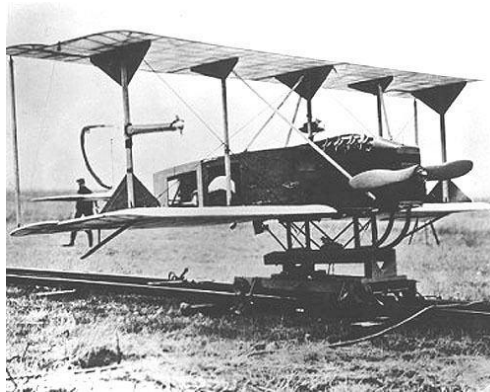
Figure 1.1. Sperry "Flying Bomb" [5]

Another early UAV named Kettering Bug aerial torpedo was a radio controlled aircraft (remotely piloted vehicle, RPV), shown in **Figure 1.2**. It has a capability to fly in a circular path instead of gyro-stabilized straight course. Later on, number of target drones were developed and some of the military planes were transformed into radio controlled UAVs during 1930s [6].

Figure 1.2. Kettering Bug [6]

Development of an applicable UAV for surveillance and reconnaissance missions could not be succeeded until late cold war era since knowledge on electronics was not ready. Therefore UAV applications were limited for a long time. Flying bombs, aerial torpedoes and target drones were the main applications.

During the cold war era, requirement of reconnaissance drones was realized again. In Cuban Missile Crisis in October 1962, a U2 spy plane was shot down by a soviet SAM. This event shows that unmanned reconnaissance was a must. Ryan Model UAV series was developed at the Vietnam War era. They were modern UAVs with all features capability of aerial photography, real time video, electronic intelligence, electronic counter measures, real time communication intelligence and leaflet droppings for psychological warfare [7].

In the late 1970s and 1980s fully autonomous/predefined flight becomes available by the developments in electronics and computer technology. Composite material technology has been improved which leads to decrease weight of the aircraft, increase range and endurance. Israel developed the Scout and the Pioneer, shown in **Figure 1.3**, which represents the modern UAV of today [8].

Figure 1.3. IAI - RQ-2 Pioneer [8]

Starting from the Scout and Pioneer, numerous modern unmanned aerial systems has been developed and categorized in terms of different mission capabilities and sizes mentioned in previous section. However, reciprocating engines and preliminary electronics restrained to make smaller UAV. Small/Mini/Micro UAV concept is improved by the developments in electronics, electric motor, servo and battery technologies. Although small and some mini UAVs are still powered by a small reciprocating engine, efficient electric motor-battery power systems allows to make remarkably smaller aircraft possible. Miniaturization reduces cost and detection risks, increases survivability.

1.3. Mini UAVs

Mini UAVs are the UAV class with 2-20 kg operational weight, which can be carried by a personal to the operation field. Mission radius is the line of sight (LOS) which is about 25 km and 3000 ft operational altitude above the ground (AGL) with 1-2 hour endurance [3], [9]. The most advantageous feature of the mini UAV is the low cost and expandability compared to the Class 2 and Class 3 UAVs mentioned in **Section 1.1**. Mini UAVs are generally used in close range ISR missions, target detection and identification for the military purposes and less amount of crew and less training are needed to operate as shown in **Figure 1.4.**

Figure 1.4. ISR Mission Performed by a Single Operator [10]

Besides military missions, mini UAVs are used for civilian purposes like scientific research, disaster prevention and management, environmental protection, homeland security, communication missions, protection of critical infrastructure. Current situation in European UAS market shows that Small and Mini UAVs (S/MUAS) dominate the civilian market as shown in **Figure 1.5** [11].
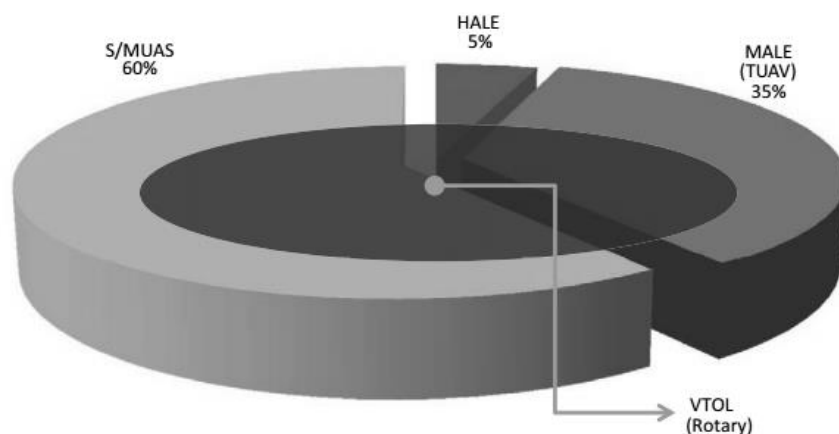
Figure 1.5. Civilian Market for UAS in Europe by Category 2008-2017 [11]

1.4. Demircan Mini UAV

Demircan Mini UAV is a portable mini UAV, designed as a scope of this thesis work. Aircraft is designed to operate in 10 km mission radius, 3000 m service ceiling, 1.5 hour of endurance with 1.5 kg payload. Maximum takeoff weight is 4 kg. As a design requirement, man-portable design and multi-mission capability is also considered. For that reason, main parts of the aircraft can be easily mounted and demounted and placed in a case carried by a personal to the operation field. In order to provide multi-mission capability, two different design features exist.

The first design feature is the body ports under the fuselage which allow mounting different landing gear configurations to adapt different operational environments. If there is a smooth runway on the operation field, tricycle type landing gear can be attached for the conventional takeoff and landing. Hook attachment allows catapult launch and slide-landing on these hooks in order to achieve safe takeoff under harsh environmental conditions if desired. Additionally, if the field is not suitable for the conventional takeoff or catapult launch, hand launch option may be considered since maximum takeoff weight of the aircraft allows achieving 8 to 9 m/s hand launch takeoff speed. In order to achieve safe hand launch and prevent operators hand from injury since the propeller clearance is low, a hand guard may be attached to the aft body.

The other feature to provide multi-mission capability is the "Mission Compartment" which is the top front part of the fuselage. This compartment includes the nose part of the aircraft in order to carry camera gimbal / mechanism or experimental devices etc. Remaining part of the Mission Compartment may include internal power supply of the mission kit, video transmitter, antennas, sensors, data acquisition unit etc. Mission compartment may be designed particularly in line with desired mission requirements.

Stationary components of the aircraft like batteries, mission computer / autopilot card, receiver etc. are attached to the bottom and aft part of the fuselage. This section is structurally strongest part of the aircraft since it includes wing-body joints, mission compartment joints and landing gear ports.

6

Primary design requirements of the Demircan Mini UAV are given in **Table 1.2.** Article (2.3) of SHT-İHA regulations constraints the maximum takeoff weight, maximum velocity and maximum altitude of any UAV, which will be given in **Section 2.1.** These constraints are also taken into consideration as primary requirements.

Table 1.2. Primary Design Requirements of Demircan Mini UAV

Primary Design Requirements	
Mission Radius	10 km
Endurance	90 min
Ceiling	3000 m
Takeoff Speed (Hand Launch)	8 to 9 m/s
Maximum Takeoff Mass	4 kg
Vmax	50 km/h – 13.9 m/s
Maximum Altitude	100m AGL
Take-off from	Runway, Snow
Launched by	Catapult, Hand

1.4.1. Purpose of the Work

Purpose of this thesis work is to make the aerodynamic and structural design and analysis of a mini UAV that meets the design requirements. In order to achieve this aim, conceptual design, numerical analysis and detail design processes have been performed throughout this work. A practical method is described to estimate propulsion system and calculate performance of an electric powered aircraft with fixed pitch propeller.

1.4.2. Scope of the Work

Mission profile for an electric powered mini UAV is defined and design phases are described. One of the most important phases of this thesis work is to come up with different structural designs for the wing and wing structural analyses in order to examine structural design - strength - weight relations of typical wing designs for mini UAVs and model aircraft. In order to perform structural analysis of the wing, computational fluid dynamics (CFD) analysis of the wing at limit load condition is considered. Comprehensive CFD analysis of the design is not within the scope of this thesis. By taking structural behavior into account, one of these candidate configurations is selected as the final structural configuration. However, structural analyses of the fuselage and tail are not covered by this study. At the end of this work, design of the Demircan Mini UAV will be ready to be manufactured from composite materials.

1.4.3. Contributions

Although the design process of a fuel consuming conventional aircraft is well established, determination of propulsion system efficiency and fixed-pitch propeller thrust with respect to flight velocity and altitude is the major challenge for an electric powered aircraft design since the propulsion system of small UAVs account for as much as 60% of the overall weight [12]. As a first contribution, practical power available and dynamic thrust estimation method for a fixed-pitch propeller powered by an electric motor is presented in the conceptual design chapter of the thesis.

In the numerical analysis chapter, common wing structure configurations with composite materials are investigated. Wing configurations with I-Beam and carbon tube spars are structurally analyzed in order to understand structural load distribution due to aerodynamic loads. By this way, structural advantages or disadvantages of these designs can be examined which is the other contribution of the thesis.

1.4.4. Design Methodology

Design methodology of this work includes three main phases. These are the conceptual design phase, numerical analysis and structural design of the wing and detail design of the aircraft. Conceptual design is an iterative phase, where design requirements are checked by performance and constraint analyses. In the numerical analysis phase, CFD analysis of the wing is performed for the limit load defined in the conceptual design phase. Structural configurations for the wings are defined and structural analyses of the wing structure configurations are performed by using referenced material definitions [38]. Finally, structural layout of the wing is decided at the end of the numerical analysis chapter. Overall design and sub-components of the aircraft are specified in the detail design phase. Overall weight of the design is checked, since the MTOW of the aircraft is constrained by Article (2.3) of SHT-İHA regulations [13]. Design for manufacturing and assembly, portability and ease of manufacturing issues are also explained in the detail design phase. Finally design of the aircraft is completed at the end of this study and ready to be manufactured design is presented. **Figure 1.6** shows the design flowchart followed in the study.
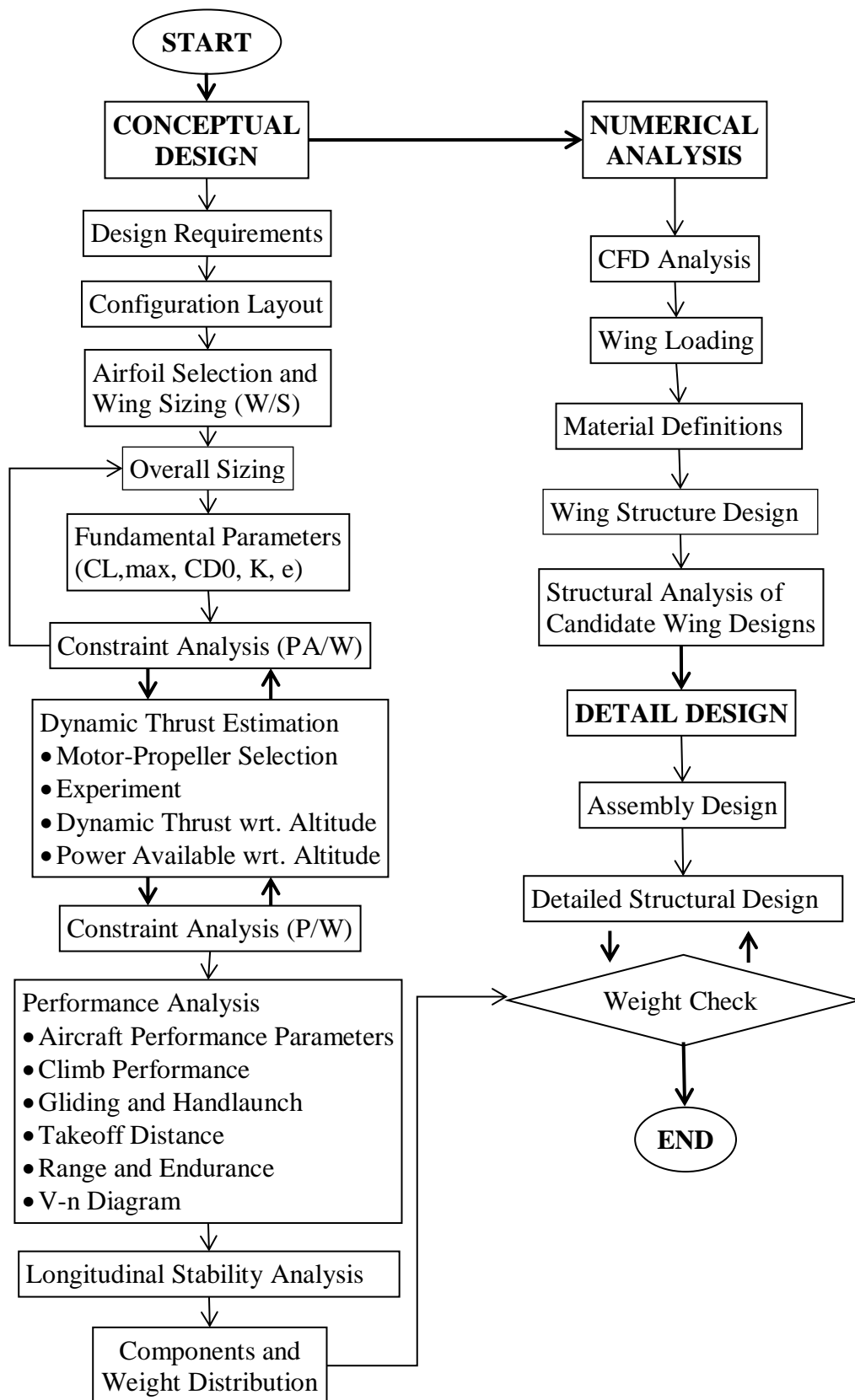
Figure 1.6. Design Flowchart

10

CHAPTER 2

CONCEPTUAL DESIGN

2.1. Introduction

Conceptual design of Demircan Mini UAV is established in this chapter. Design requirements are defined, configuration layout is specified, aircraft performance calculations are accomplished, system components are specified and finally conceptual design is determined. Improved aerodynamic relations and dynamic thrust model specified for electric motor with fixed-pitch propeller are presented. Additionally range and endurance relations for battery powered aircraft are referred to determine required battery capacity for electric powered aircraft. In order to achieve much more reliable design these relations are used in aircraft performance calculations. At the end of this chapter conceptual design is completed.

2.2. Regulations

Regulations of Directorate General of Civil Aviation (DGCA) of Turkey are taken into consideration before deciding the design requirements of the UAV, which is named SHT-İHA. According to Article (4.ş) of SHT-İHA, except from model aircraft used for sport or entertainment, any unmanned flying vehicle capable of autonomous flight or controlled by a ground operator is defined as a UAV. This regulation contains important rules like operational permissions, operator responsibilities, airworthiness requirements, safety rules, air traffic control issues and pilot licensing and proficiency requirements for UAV operations.

In order to design and operate a UAV beyond the scope of this regulation, maximum takeoff mass (MTOM), maximum velocity and maximum altitude (AGL) constraints should be considered as stated in Article (2.3) of SHT-İHA. **Table 2.1** gives the

SHT-İHA constraints. Any UAV, which does not obey these constraints, are subjected to the SHT-İHA regulations and operational permissions should be taken from DGCA of Turkey [13].

Table 2.1. SHT-İHA Constraints

MTOM	4 kg
Vmax	50 km/h – 13.9 m/s
Maximum Altitude	100m AGL

2.3. Design Requirements

Fixed wing Mini UAVs have a wide range of usage and they may be used in almost all environments including high altitude mountains to sea level operations for civil or military purposes. For that reason, ceiling and operational environment will be considered to design the aircraft. Design altitude should be chosen as high as possible and general design layout will be chosen for the desired operational and environmental conditions.

In order to design a mini UAV which can operate in different operational environments, firstly portability issues should be considered for the mobility. In the second place, takeoff and landing configuration of the aircraft should be appropriate for different types of operational fields and in the current study replaceable landing gear configuration is chosen for the design. Conventional landing gear can be attached for runway takeoff and landing and hook attachment can be used for catapult launches, in order to achieve required takeoff speed in safe. Design configuration and MTOW of the aircraft also allows achieving 8-9 m/s hand launch takeoff speed for an average operator.

Payload of the aircraft is a mission compartment up to 1.5 kg which is chosen for the multi-mission capability of the design. Mission radius and endurance are 10 km and 90 min of flight time at 3000 m operational altitude. Additionally, SHT-İHA constraints should be followed.

Table 2.2 gives the general design requirements of Demircan Mini UAV where SHT-İHA constraints are added into the preliminary design requirements given in **Table 1.2**.

Table 2.2. General Design Requirements of Demircan Mini UAV

General Designs Requirements	
Hand Launch Takeoff Velocity	8-9 m/s
Takeoff	Runway, Catapult, Hand
Payload (Mission Compartment)	1.5 kg
Mission Radius	10 km
Endurance	90 min
Ceiling	3000 m
MTOM	4 kg
Vmax	50 km/h
Maximum Flight Altitude	100m AGL – 3000 m AMSL

2.3.1. Mission Profile

Mission profile of the aircraft is performed in 10 km mission radius with 90 minutes of endurance and 100 m AGL operational altitude up to 3000 m AMSL elevation. Takeoff - Cruise – Loiter - Return Cruise and Landing phases are the main phases of the mission profile. Loiter phase is implemented according to the chosen mission kit such as surveillance and reconnaissance, surface mapping or atmospheric data collection etc. Sample mission profile is plotted in **Figure 2.1.**
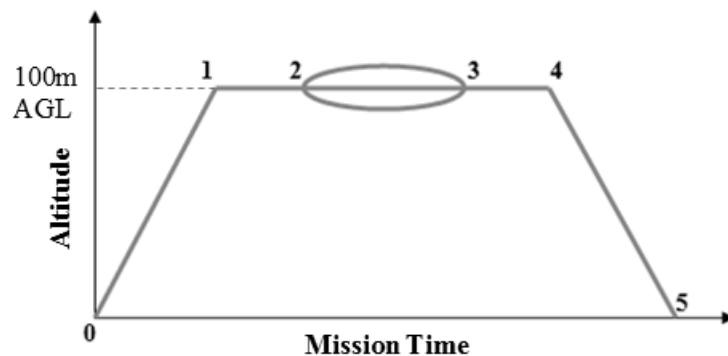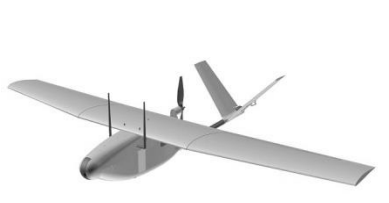
Figure 2.1. Mission Profile

13

At station 0, pre-flight inspections, such as connections, flight control surfaces, ground control units etc. are performed. Climb to 100 m AGL altitude is performed between stations 0-1 at maximum rate of climb condition and cruise is performed between stations 1-2 and 3-4 (return cruise) at $(L/D)_{max}$ value for propeller driven airplanes and maximum propeller efficiency condition in order to maximize range. Since fixed-pitch propeller has the maximum efficiency at a unique advance ratio value, which is the ratio of the design speed and the RPM value of the propeller, selecting a proper propeller that fits the design becomes significant for the cruise flight. Loitering is performed between stations 2-3 at maximum endurance condition $\left(L^{3/2}/D\right)_{max}$ for propeller driven airplane, where flight time is more important than range in this phase. After the return cruise, descending phase to the landing zone is performed between stations 4-5. Flying at cruise and loiter conditions are not only related with proper propeller selection but also related with compatible electric motor selection where current drain is also be needed to minimized at these flight phases in order to achieve longer range and endurance values. Therefore actual cruise and loiter speeds are determined from range and endurance calculations for battery powered aircraft.

2.3.2. Competitor Study

Competitor study is performed in order to obtain initial sizing and performance parameters referring to the present designs that match the desired design requirements. Conventional mini UAV designs are classified according to their fuselage and propulsion types which are Boom-Tractor, Cargo-Pusher and Cargo-Tractor types. Boom type fuselage is the simplest design where wing, tail and payloads are attached to the boom. For the cargo type fuselage, flight system and equipment are placed in a fuselage and wing and tail are attached on the fuselage. Second classification name is the propulsion configuration as tractor and pusher. Layout classifications are shown in **Table 2.3** and some of competitor aircraft are listed with their pictures as examples and all competitors are listed in **Table 2.4**.

Table 2.3. Layout Classification for Mini UAVs

Boom-Tractor	Cargo-Pusher	Cargo-Tractor
Elbit -Skylark 1	Baykar - Bayraktar	METU – Güventürk

(Referenced in Appendix A)

Table 2.4. Layout Classification of Competitor Mini UAVs.

Boom - Tractor	Cargo - Pusher	Cargo - Tractor
Elbit - Skylark 1	AV- Pointer	AV - Puma AE
ST Aero - Skyblade 3	Hydra Tech. - E1 Gavillan	METU - Güventürk
Top I Vision - Casper 250	Nostromo - Cabure 2	
Tasuma - Hawkeye 2	Baykar - Bayraktar	
	MKU - Terp2	
	Tasuma - Hawkeye 3	

Average design parameters are given in the **Table 2.5**. Design specifications and references of competitors are given in **Appendix A**.

Table 2.5. Average Design Parameters of Competitor Mini UAVs

Average Design Parameters of Competitor mini UAVs	
MTOW	4.23 kg
Wing Span	2.12 m
Length	1.46 m
Cruise Velocity	16.1 m/s
Ceiling	2790 m
Mission Radius	9.5 km
Endurance	80 min

ISR missions are the primary objective of mini UAVs for the military applications. Thus, gimbal systems for mini UAVs are also researched and one of them is selected as a candidate for the conceptual design phase. Selected gimbal has object tracking, high definition streaming, real time video stabilization and geo-lock capabilities [14]. Total payload for a gimbal system with power units, transmitter etc. is assumed as 1.5 kg. **Figure 2.2** shows the selected gimbal and specifications of the selected gimbal are given in **Table 2.6**.

Figure 2.2. UAV Vision CM100 Gimbal [14]

Table 2.6. UAV Vision CM100 Specifications [14]

Mass - Weight	0.800 kg – 7.85 N
Dimensions	Diameter : 100 mm
	Length/Height : 129 mm
Power / Voltage	12W / 9-36 V

2.3.3. Initial Design Parameters

Initial design parameters of Demircan mini UAV is specified and given in **Table 2.7** by using competitor averages given in **Table 2.5.**

Table 2.7. Initial Design Parameters of Demircan Mini UAV

Competitor Averages			Demircan Mini UAV	
Wing Span :b	2.12	m	2.2	m/s
Wing Area: S*	0.484	m^2	0.605	m^2
Mean Chord: c*	0.228	m	0.275	m
Aspect Ratio: AR	9.27	-	8	-
Length	1.46	m	1.5	m
MTOW	4.23 / 41.5	kg / N	4 / 39.24	kg / N
Payload	0.95 - 1.5	kg	1.5	kg
V_{max}	26.6	m/s	-	m/s
V_{cruise}	16.1	m/s	13.9	m/s
V_{stall}	11.7	m/s	8 - 9	m/s
Ceiling	2790	m	3000	m
Endurance	80	min	90	min
Mission Radius	9.5	km	10	km

(*Calculated from related parameters)

2.4. Configuration Layout

Layout class of the Demircan mini UAV is Cargo-Pusher as mentioned in **Section 2.3.2.** While choosing the Fuselage-Propulsion class operational advantages and disadvantages, manufacturability issues, performance and stability characteristics are taken into account.

Boom-Tractor type is a simple design but payload/camera pod is generally placed under the fuselage because of the stability issues and mostly propeller blocks the frontal view of the camera. Also, during the landing, camera is the first contact point of the aircraft to the ground. Also there is limited place to locate electronic system in the pod. This configuration allows hand launch but mounting different landing gears on the payload pod is not practical.

Cargo-Tractor type is a conventional design but the most important problem is the location of the camera and payload. Camera should be located under the fuselage and it needs extra precaution mechanisms like retractable camera mechanism or camera door to protect camera system during belly landings. Locating camera system far from the motor in order to enhance monitoring quality due to magnetic interference and vibration of the motor is the other important issue.

Cargo-Pusher type is advantageous for the monitoring since the camera system can be placed at the front of the fuselage. The greatest advantage is airflow over the wing is undisturbed and camera has a clear view. Additionally, undisturbed air flow is preferred for the experimental payload especially for the atmospheric data measurement missions. Protective cautions like nose shield may still be needed for belly landings in order to protect nose camera. Twin boom mounted tail to the wing configuration like in most of the tactical UAVs can be preferred in order to reduce fuselage height and length. By this way, fuselage drag can be reduced and mobility can be increased. Moreover, fuselage can be designed separately for each mission configuration, which allows a flexible design envelope for the fuselage and it is advantageous for the multi-mission concept. For this thesis work, "mission compartment" is considered as the replaceable part of the aircraft. As a result, cargo type fuselage with pusher propeller and twin boom - high tail configuration is chosen for design.

2.4.1. Design Configuration of the Demircan Mini UAV

Fuselage has a rounded box shape with high conic aft in order to keep pusher propeller high as possible and improve propeller clearance. High wing configuration is chosen in order to improve the grip of the body for hand launch and stability of the aircraft.

Tail booms are mounted on the hard points of the wings at the end of the rectangular root section for the structural rigidity of tail and boom ports. Twin vertical tails are placed to the boom end junctions and high tail is placed to the vertical tail tips.

Pusher type propeller configuration is chosen in order to place the camera system at the nose for clear view and undisturbed airflow for the experimental mission compartment. The most important disadvantage of this propeller configuration is low propeller clearance during hand launch and landing. Propeller guard placed to the aft fuselage may be helpful for hand launch and belly landing cases.

Conventional landing gear and hook attachments may be placed to the body ports under the fuselage for safe takeoff and landing as an option. **Figure 2.3** shows the conceptual design of Demircan Mini UAV.
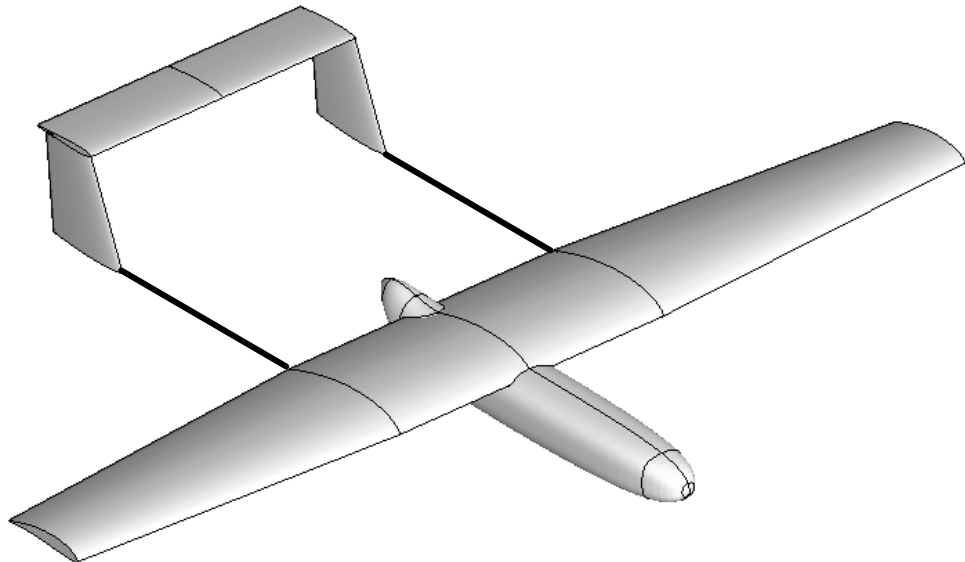
Figure 2.3. Design Configuration of Demircan Mini UAV

2.5. Airfoil Selection and Wing Sizing

Airfoil of the wing is selected by considering design requirement for the maximum lift coefficient and Reynolds number of the wing at the design speed and altitude range. Required maximum lift coefficient of the airfoil is calculated for stall conditions at different operational altitudes. After selecting the airfoil, maximum lift coefficient of the finite wing, which is the fundamental design parameter of the conceptual design phase, is determined. Standard atmosphere parameters, shown in **Table 2.8**, are used for the lift coefficient and Reynolds number calculations.

Table 2.8. Standard Atmosphere Table (AMSL)

Altitude m	Density ρ_∞ kg/m^3	Dynamic Viscosity μ_∞ $kg/(m \cdot s)$
0	1.2250	1.789 x10^{-5}
500	1.1673	1.774 x10^{-5}
1000	1.1117	1.758 x10^{-5}
1500	1.0581	1.742 x10^{-5}
2000	1.0066	1.726 x10^{-5}
2500	0.9570	1.710 x10^{-5}
3000	0.9093	1.694 x10^{-5}

2.5.1. Lift Coefficients

Selected airfoil should satisfy the lift requirement for stall and cruise conditions, which is the MTOW of the aircraft. Stall speed is selected as 8 m/s at 1000 m and 9 m/s at 3000 m. $C_{L,max}$ and $C_{L,cruise}$ requirements for the candidate airfoil are calculated from **Eqn. (2.1)** and **Table 2.9** gives the lift coefficient requirements at different speeds and altitude.

$$L = \frac{1}{2}\rho_\infty V_\infty^2 S C_L \qquad (2.1)$$

$$C_{L,max} = \frac{2W}{\rho_\infty V_{stall}^2 S} \qquad (2.2)$$

$$C_{L,cruise} = \frac{2W}{\rho_\infty V_{cruise}^2 S} \qquad (2.3)$$

Where **W=39.24 N** and **S=0.605 m^2**.

Table 2.9. Lift Coefficient Requirements at Different Speeds and Altitude

V	C_L			
	0m	1000m	2000m	3000m
8 m/s (Stall) (High Aoa)	1.655	**1.823**	2.014	2.229
9 m/s (Stall) (High Aoa)	1.307	1.441	1.591	**1.761**
13.9 m/s (Cruise) (Low Aoa)	0.548	0.604	0.667	0.738
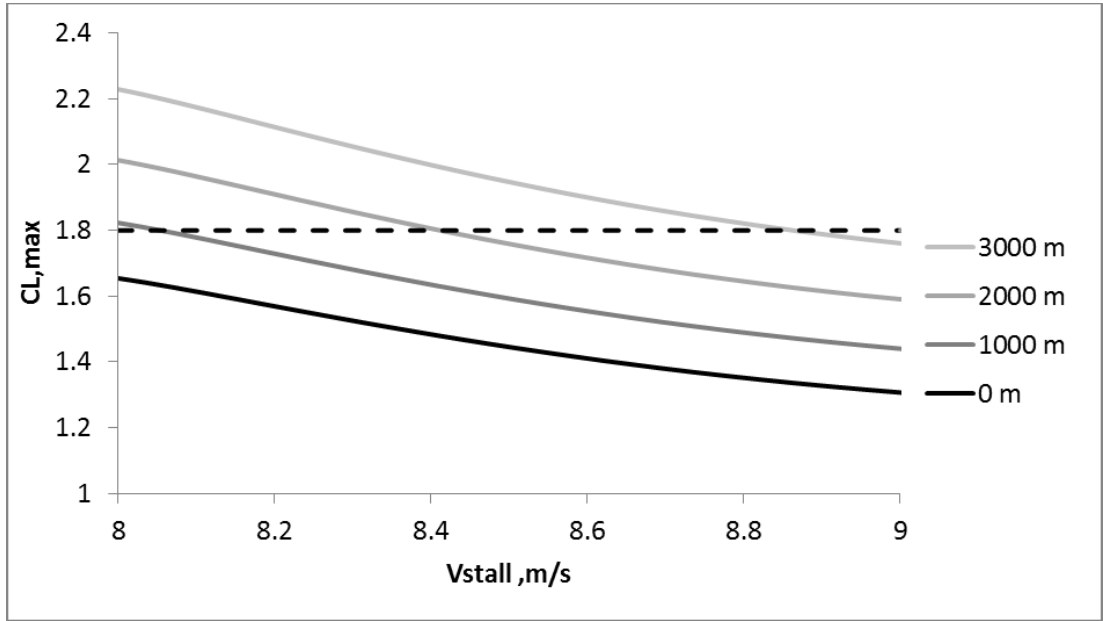
Figure 2.4. Maximum Lift Coefficients for Different Stall Velocities

As can be seen from **Figure 2.4**, although $C_{L,max}$ of the selected airfoil should be at least **1.823** for 1000m operational altitude, required lift coefficient at 8-9 m/s stall speed range for different operational altitudes is selected as **1.8**. Similarly, cruise lift coefficient at low angle of attack should be between **0.55** and **0.74** as given in **Table 2.9** in order to minimize drag at cruise condition.

2.5.2. Reynolds Number

Reynolds number range of the wing is calculated considering the 0 m to 3000 m altitude range, and stall speeds (8-9 m/s) and the design cruise speed. **Table 2.10** gives the Reynolds number ranges at different operational altitudes.

$$Re = \frac{\rho_\infty V_\infty c}{\mu_\infty}$$

(2.4)

$$V_{stall} = 8\,m/s, \qquad V_{cruise} = 13.9\,m/s, \qquad c = 0.275\,m$$

Table 2.10. Reynolds Number Range

Reynolds Number	0m	1000m	2000m	3000m
Vstall = 8 m/s	150642.8	139120.6	-	-
Vstall = 9 m/s	-	-	144341.5	132852.3
Vcruise = 13.9 m/s	261741.9	241722	222927.5	205183

Based on the results given in Table 2.10, Reynolds number range of the design is taken to be 130000 – 260000.Therefore, airfoil search is performed within this range. Nominal Reynolds number is selected for the operational cruise altitudes between 1000 m-2000 m as 230000.

2.5.3. Airfoil Analyses

MH114 airfoil is selected between vast number of low speed / low Reynolds number airfoils. Candidate airfoils are analyzed for the nominal Reynolds number ($Re_{nominal} \approx 230000$) by using XFLR5 – XFOIL Direct Analysis module [16]. XFOIL is a widely used interactive program/module for the design and analysis of subsonic isolated airfoils. Viscous or inviscid analysis capabilities of the tool allows forced or free transition, transitional separation bubbles, trailing edge separation, compressibility correction and lift-drag predictions [17]. Therefore determination of airfoil characteristics is relied on XFLR5 – XFOIL analysis results. Lift coefficient analysis results of four candidate airfoils are shown **Figure 2.5**.
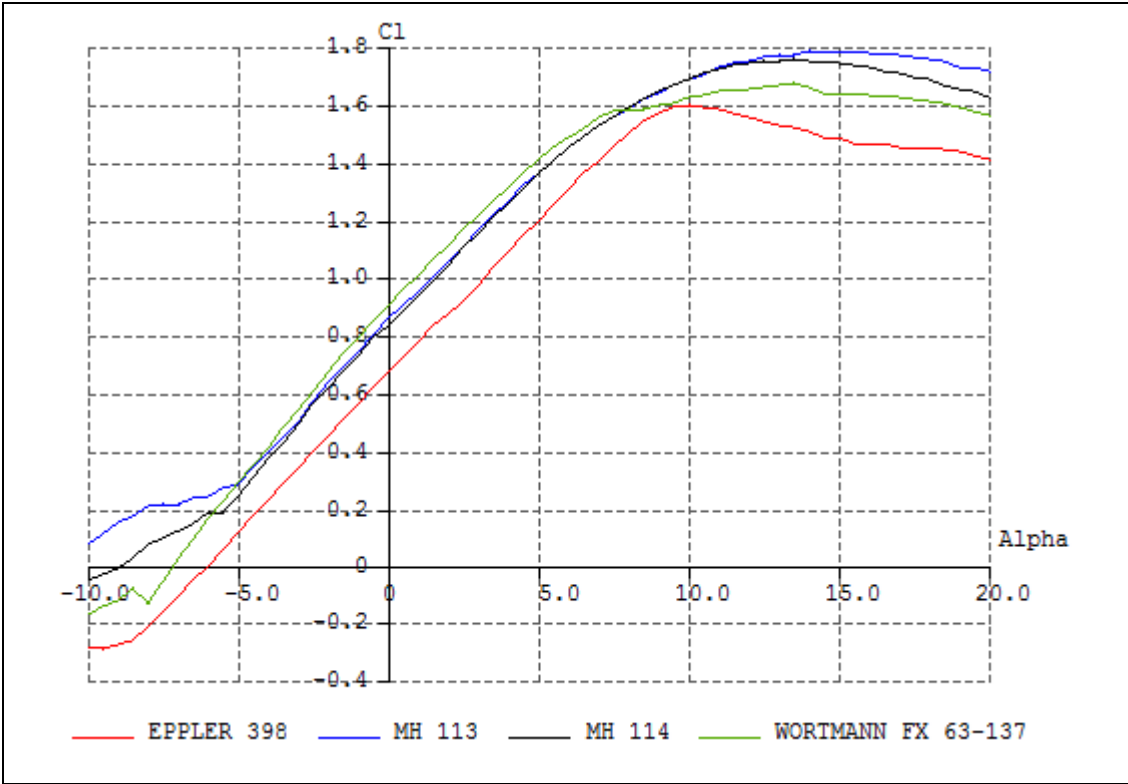
Figure 2.5. C_l vs. Alpha Curves of Candidate Airfoils at Re=230000

22

From **Figure 2.5** (C_l vs. Alpha Curve), MH113 and MH114 airfoils are selected as the final candidates since lift coefficient at zero angle of attacks are satisfactory and maximum lift coefficient of these airfoils are close to $C_{L,max} = 1.8$. Maximum lift coefficient of the finite wing is lower than the 2D airfoil due to finite wing-body losses. It is seemed to be unsatisfactory for the maximum lift coefficient requirement to satisfy lift requirement at 8-9 m/s stall speeds but flapped wing configuration is considered for different operational altitudes in order to minimize wing drag at level flight phases. Lift to drag ratio (C_l/C_d) is the critical parameter on deciding the airfoil. Selected airfoil should have the highest lift and at the same time it should have the lowest drag. Therefore, airfoil with the highest C_l/C_d value is the most appropriate choice for the design. C_l/C_d results are shown in **Figure 2.6.**
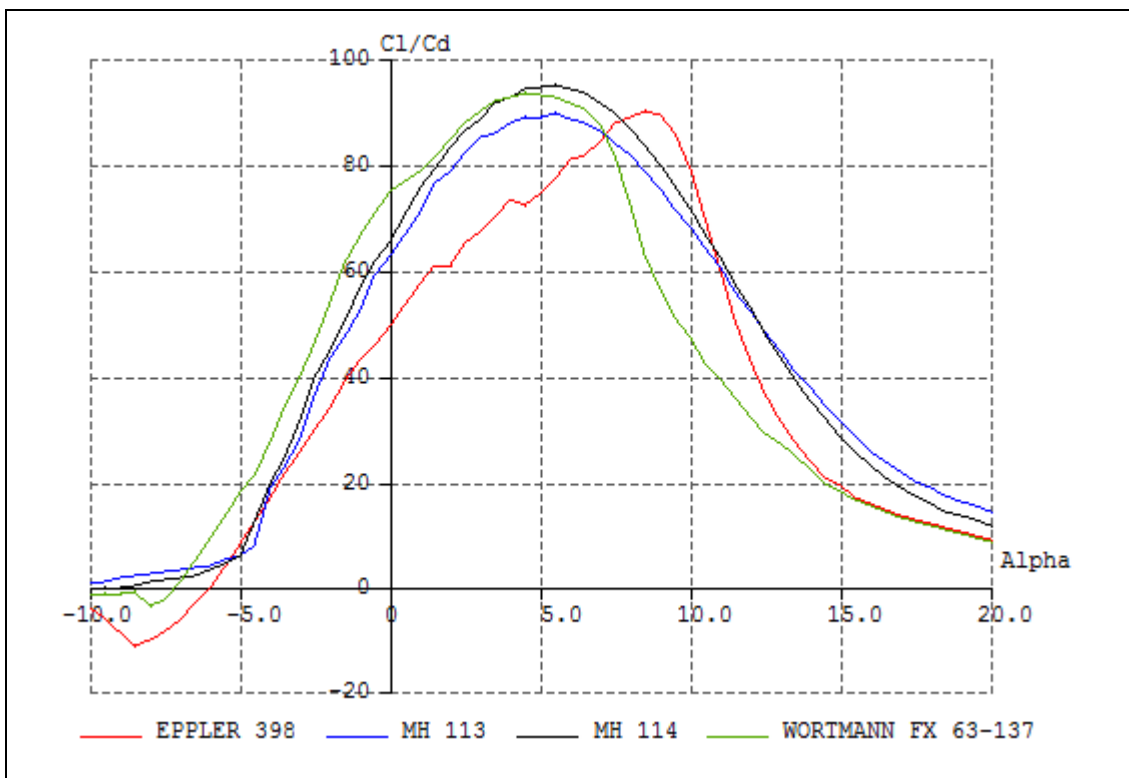
Figure 2.6. C_l/C_d vs. Alpha Curves of Candidate Airfoils at Re=230000

From **Figure 2.6**, C_l/C_d value of MH114 is higher than MH113 since MH114 airfoil is thinner, which is also better for low Reynolds number flight regime. Hence, MH114 airfoil is selected for the design and shown in **Figure 2.7.**

Figure 2.7. MH114 Airfoil

C_l vs. angle of attack curve of the MH114 airfoil at Reynolds number 230000 is shown in **Figure 2.8.**
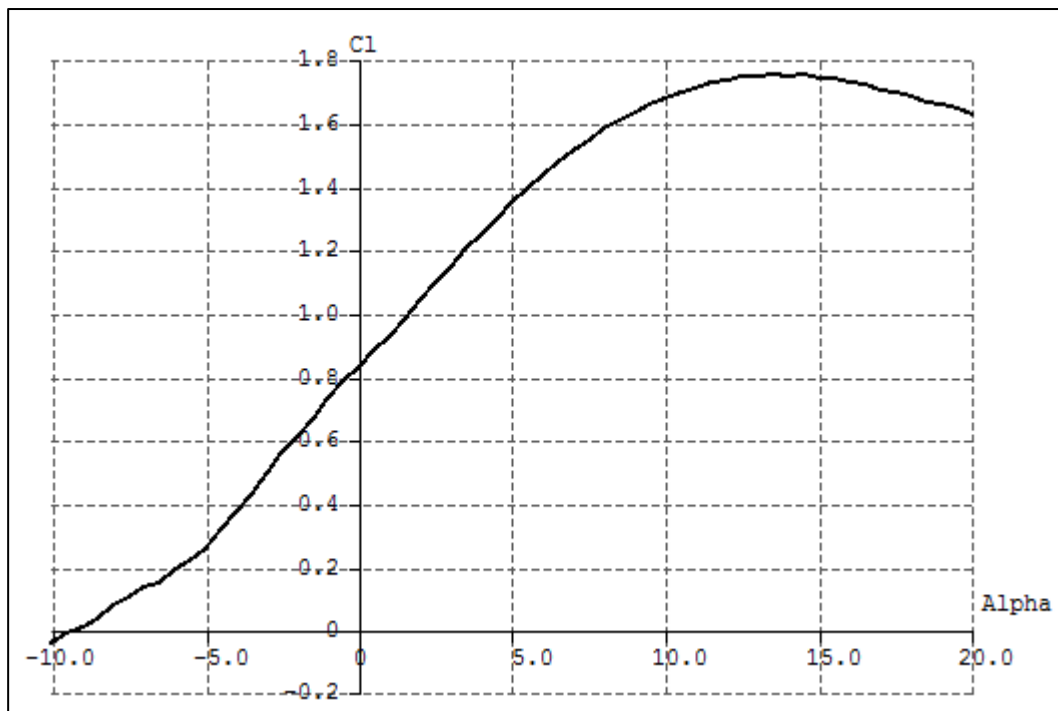
Figure 2.8. Cl vs. Alpha Curve of MH114 at Re=230000

Figure 2.8 shows that maximum lift coefficient $C_{l,max}$ is 1.75 at **13.5** degree angle of attack. C_l/C_d vs. angle of attack and $C_{m,c/4}$ vs. angle of attack curves of MH114 at Re=230000 are given in **Figure 2.9** and **Figure 2.10** respectively. **C_l/C_d** has the maximum value at 5 degree angle of attack as shown in **Figure 2.9** and moment coefficient at quarter chord is about **-0.18** at low angle of attacks as shown in **Figure 2.10**.

24
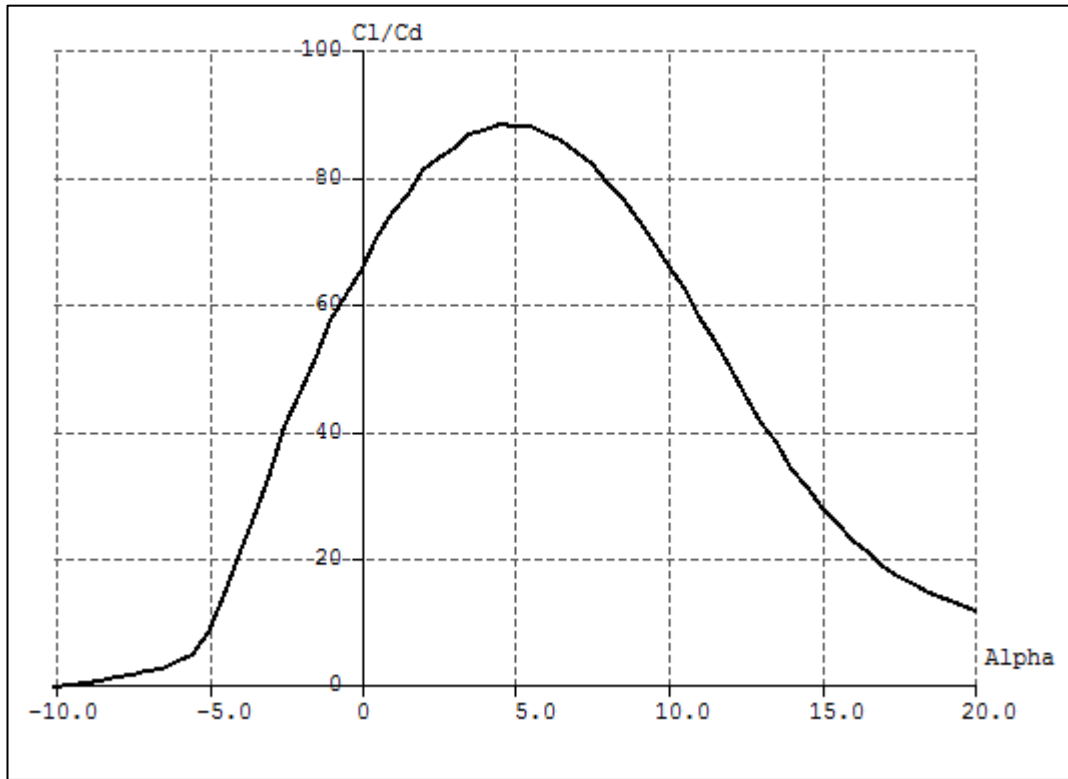
Figure 2.9. C_l/C_d vs. Alpha Curve of MH114 at Re=230000
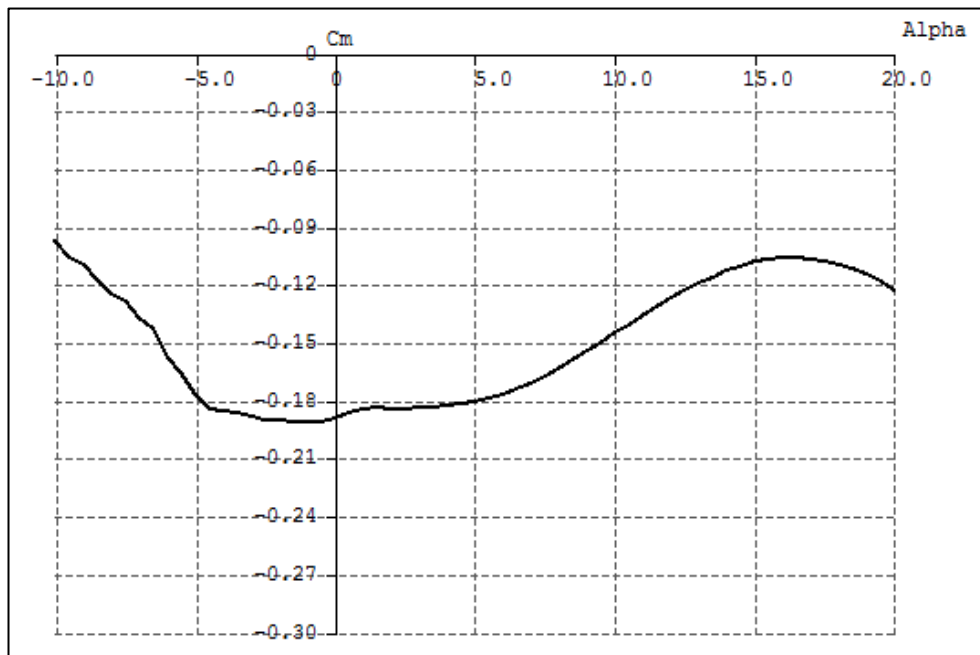
Figure 2.10. $C_{m,c/4}$ vs. Alpha Curve of MH114 at Re=230000

25

Table 2.11 summarizes aerodynamic coefficients of the MH114 Airfoil. Lift coefficient of the finite wing (C_L) and maximum lift coefficient of the flapped wing $(C_{L,max})$ are discussed in the following section.

Table 2.11. Aerodynamic Coefficients of the MH114 Airfoil.

$C_{l,max}$ = 1.75	@ $\alpha = 13.5°$
$C_{l,\alpha=0}$ = 0.83	@ $\alpha = 0°$
$C_{l,L=0}$ = 0	@ $\alpha = -9.5°$
$(C_l/C_d)_{max}$ = 88	@ $\alpha = 5°$
$c_{m,c/4}$ = -0.18	At low AOA.

2.5.4. Stall Constraint and Wing Loading

Stall constraint is the most important requirement for hand launch. $C_{L,max}$ is specified as 1.8 in the previous section. Initial wing sizing is needed to be updated and flap size should be determined to achieve the required lift coefficient. It should be noted that wing loading and wing area are the fundamental constraints for the wing sizing at this point. Stall constraints are minimum wing area required and maximum wing loading for 8m/s stall speed at 1000 m altitude.

$$\left(\frac{W}{S}\right)_{stall} = \frac{1}{2}\rho_\infty V_{stall}^2 C_{L,max} \qquad (2.5)$$

$$\left(\frac{W}{S}\right)_{stall} = 64.034 \ N/m^2$$

$$S_{min} = \frac{W}{(W/S)} = \frac{39.24}{64.034} = 0.613 \ m^2$$

Wing dimensions are re-calculated for the new wing loading parameter, where **AR=8**.

$$AR = b^2/S \qquad (2.6)$$

$$b = \sqrt{AR \cdot S} \approx 2.22 \ m$$

$$S = 2.22^2/8 = 0.616 \ m^2$$

26

2.5.5. Single-Tapered Wing

Flow separation moves to the wing root as the taper ratio approaches to 1at near-stall condition, which is a rectangular wing and desired for stall warning. However, moderate taper ratio is favorable to approach elliptical lift distribution and lighter wing structure due to bending moment approaches to the wing root [15]. Wing with 0.5 taper ratio is a good choice for single-tapered wing in order to keep away the flow separation from ailerons at the wing tip and flaps at the wing root as can be seen from **Figure 2.11**. However, as discussed in the next section, wing configuration is selected as multi-tapered in order to ease manufacturing and transportation of the wing and approach to elliptic lift distribution. For the single tapered wing, taper ratio of the wing is reduced by increasing the tip chord and reducing the root chord. Therefore taper ratio of the wing is selected as **0.65** for moderate wing stall characteristics.
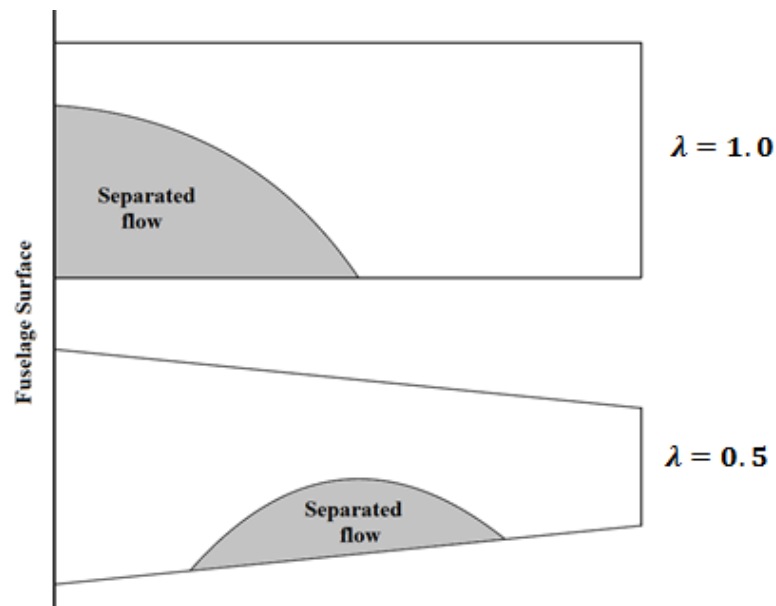
Figure 2.11. Effect of Taper Ratio on Flow Separation at Near-Stall Conditions [15]

Tip chord and root chord of the wing is calculated as,

$$c_r = \frac{2S}{(\lambda + 1)b} = 0.336 \, m \tag{2.7}$$

$$c_t = \lambda \cdot c_r = 0.218 \, m \tag{2.8}$$

27

Wing dimensions of the single-tapered wing are shown in **Figure 2.12**.
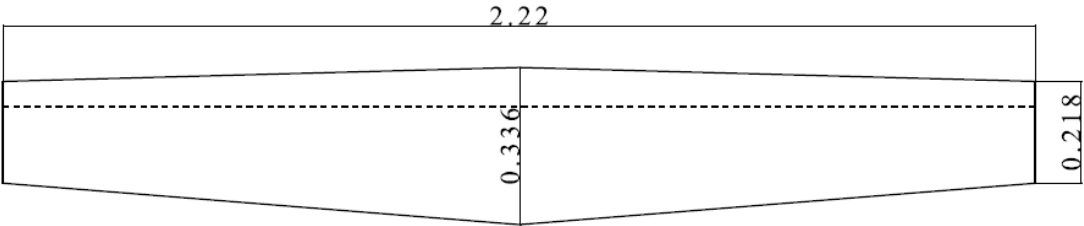
Figure 2.12. Single-Tapered Wing Dimensions

(Dimensions are in m)

2.5.6. Multi-Tapered Wing

Tip chord and root chord dimensions can be reduced by multi-tapering in order to increase the mobility. Additionally, with multi-tapering approach wing shape and lift distribution approaches to an elliptical wing. However, the effect of multi-tapering is minor on lift distribution compared to the single-tapered wing. In the present study, constant chord root section (rectangular) and tapered outer wing section is considered for multi-tapering. Manufacturing of a multi-tapered wing is more complex than a single-tapered wing for general aviation aircraft. On the contrary, multi-tapering is considered to ease manufacturing and increase mobility by manufacturing rectangular root section and tapered outer wings separately. In other words, the wing consists of three separate parts as shown in **Figure 2.13**.

Figure 2.13. Multi-Tapered Wing

In the **Figure 2.14**, single-tapered and multi-tapered wings are shown together. Reference area of single-tapered wing and multi-tapered wing are same, but root and tip chord dimensions are reduced for the multi-tapered wing (gray). In **Figure 2.14**, black areas are excess parts of the single-tapered wing.

28
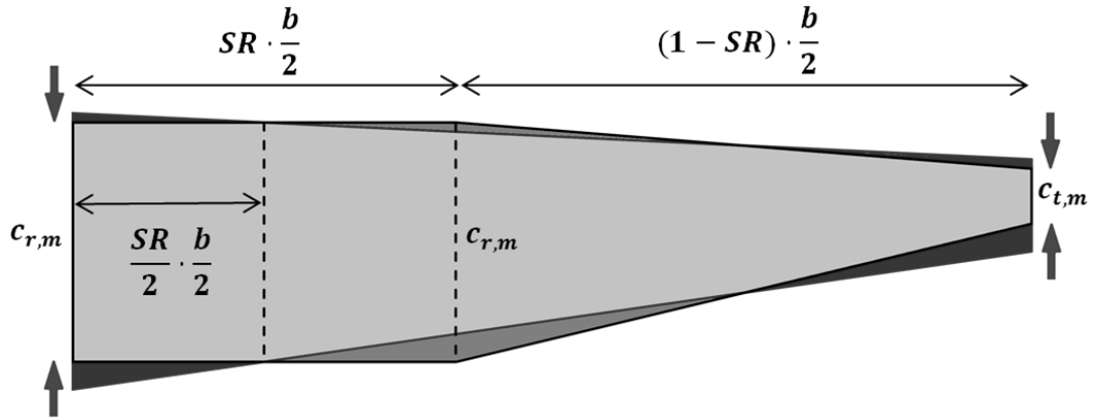
Figure 2.14. Chord Reduction and Dimensions of the Multi-Tapered Wing

Dimensions of the multi-tapered wing are calculated with respect to the span ratio (**SR**) parameter, which is the ratio of the rectangular span to the wing span. Span ratio is zero for a single-tapered wing and one for a rectangular wing. Chord distribution along half span of a single-tapered wing is given by

$$c(y) = c_r - (c_r - c_t)\left(\frac{y}{b/2}\right)$$
(2.9)

Root chord of the multi-tapered wing is the chord length at the wing span at (SR/2)(b/2) as shown in **Figure 2.14** and given by Eqn.(2.10).

$$c_{r,m} = c_r - (c_r - c_t)\left(\frac{SR}{2}\right)$$
(2.10)

Total chord difference is same at the root and at the tip.

$$\Delta c = (c_r - c_t)\left(\frac{SR}{2}\right)$$
(2.11)

$$c_{t,m} = c_t - \Delta c$$
(2.12)

$$c_{t,m} = c_t - (c_r - c_t)\left(\frac{SR}{2}\right)$$
(2.13)

In the present study, span ratio is selected as 0.3.Tip chord, root chord and taper ratio of the multi-tapered wing are calculated as,

$$c_{r,m} = 0.336 - (0.336 - 0.218)\left(\frac{0.3}{2}\right) \approx 0.318\ m$$

$$c_{t,m} = 0.218 - (0.336 - 0.218)\left(\frac{0.3}{2}\right) \approx 0.200\ m$$

$$\lambda = \frac{c_{t,m}}{c_{r,m}} = \frac{0.318}{0.200} = 0.629$$

Final values of reference wing area and wing loading are determines as:

$$S = \left(c_{r,m} \cdot SR \cdot b\right) + \left[\left(c_{r,m} + c_{t,m}\right) \cdot (1 - SR) \cdot b/2\right] = 0.614\ m^2$$

$$\frac{W}{S} = \frac{39.24}{0.614} = 63.88\ N/m^2$$

Mean aerodynamic chord of a wing with variable chord is calculated as,

$$\bar{c} = \frac{2}{S} \int_0^{b/2} c(y)^2 \cdot dy \qquad (2.14)$$

Chord distributions along half span of a multi-tapered wing is divided into rectangular and tapered sections, and they are calculated as,

$$c_1(y) = c_{r,m} \qquad (2.15)$$

$$c_2(y) = c_{r,m} - \left(\frac{c_{r,m} - c_{t,m}}{(1 - SR) \cdot b/2}\right) y \qquad (2.16)$$

Eqn. (2.14) can be solved for rectangular and tapered sections separately yielding the mean aerodynamic chord for the multi-tapered wing.

$$\bar{c} = \frac{2}{S}\left[\int_0^{SR.b/2} c_1(y)^2 \cdot dy + \int_0^{(1-SR).b/2} c_2(y)^2 . dy\right] \qquad (2.17)$$

$$\bar{c} = \frac{b}{S}\left[SR \cdot c_{r,m}{}^2 + \left(c_{r,m}{}^2 + c_{r,m} \cdot c_{t,m} + c_{t,m}{}^2\right)\frac{(1 - SR)}{3}\right] \qquad (2.18)$$

$$\bar{c} = 0.282\ m$$

Final wing dimensions and parameters are given in **Table 2.12** and wing planform is shown in **Figure 2.15.**

Table 2.12. Wing Parameters

Span: b	2.22	m
Aspect Ratio: AR	8	
Span Ratio: SR	0.3	
Taper Ratio: λ	0.629	
Root chord: cr	0.318	m
Tip chord: ct	0.200	m
M.A.C.	0.282	m
S_wing, Sref	0.614	m^2
W/S	63.88	N/m^2
Swet_wing*	1.268	m^2

(*:Wetted surface of the wing is determined from CAD drawing of the wing)
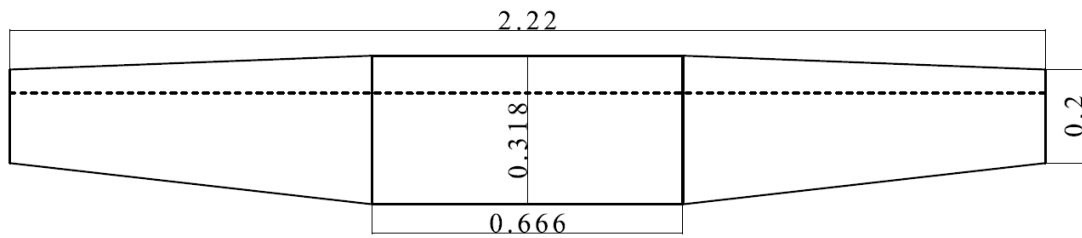
Figure 2.15. Multi-Tapered Wing Dimensions

(Dimensions are in m)

2.6. Preliminary Wing Analysis

In this section, finite wing analysis (FWA) of the multi-tapered wing is performed with XFLR5 software. XFLR5 is an analysis tool for airfoils, wings and planes operating at low Reynolds numbers [16]. It includes XFOIL's [17] direct and inverse airfoil analysis capabilities. Wing design and analysis capabilities of the tool are based on Lifting Line Theory (LLT), Vortex Lattice Method with horseshoe vortex (VLM1) and ring vortex (VLM2) options and 3D Panel Method.

Multi-tapered wing elements generated in XFLR5 are shown in **Figure 2.16.** 2D VLM elements, analyzed in LLT and VLM, are automatically generated on the mean camber line by projecting 3D panel elements generated on wing surfaces.
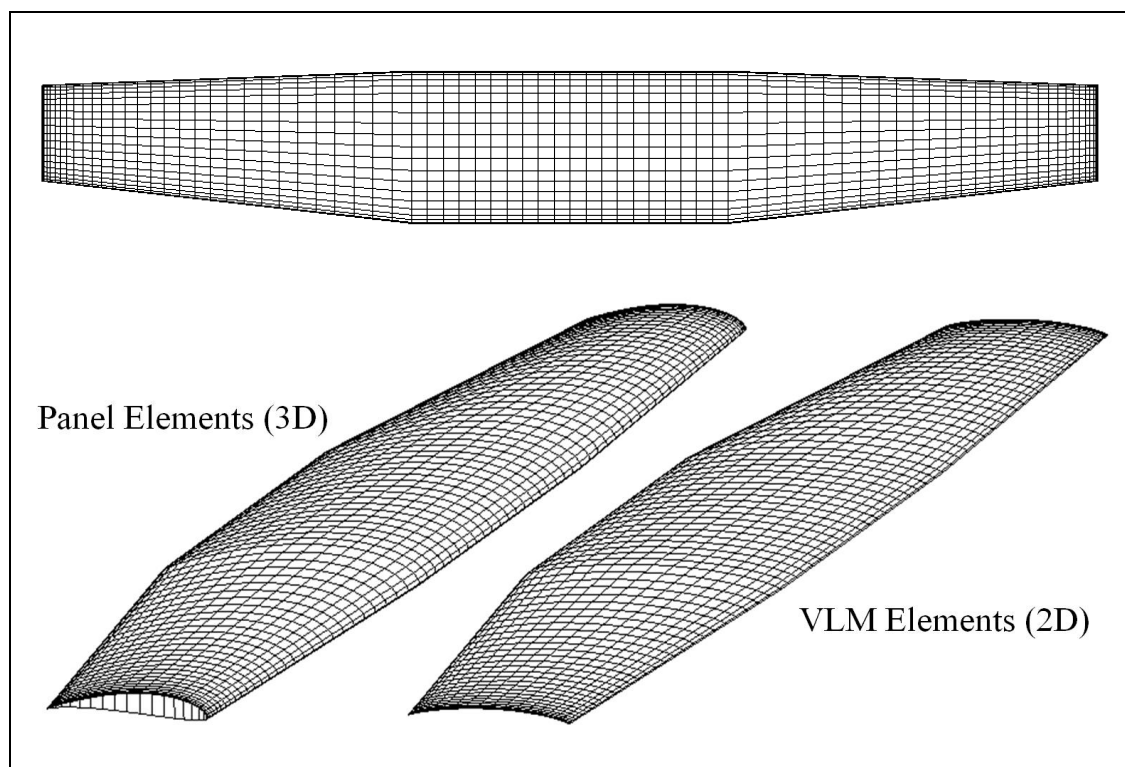
Figure 2.16. Wing Elements (3240 Panel Elements – 1600 VLM Elements)

Finite wing analyses are performed for LLT, VLM and 3D Panel Methods at 1000 m and 13.9 m/s cruise condition. As can be seen from **Figure 2.17**, lift curves at small angle of attacks are almost same but Panel Method gives higher lift coefficients.

VLM and Panel solutions do not converge near stall but stall behavior is detected with LLT analysis and maximum lift coefficient results are almost same for all solutions.
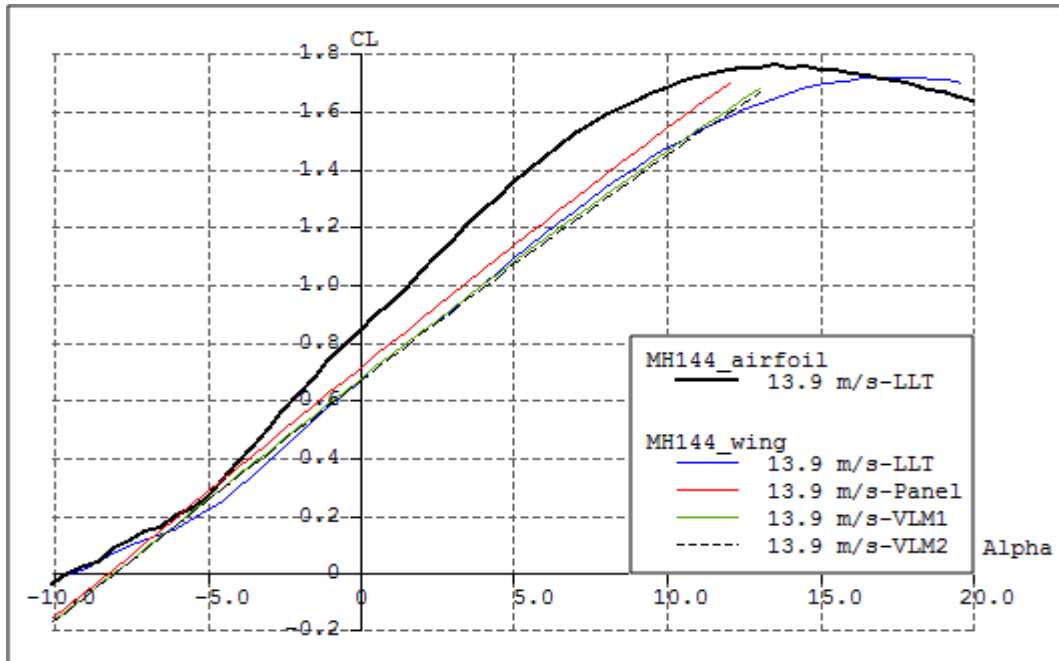
Figure 2.17. C_L vs Alpha Results for 2D airfoil and 3D Wing Analyses.

Lift to drag ratio (C_L/C_D) and moment coefficient at quarter chord $(c_{m,c/4})$ results are also determined and plotted in **Figure 2.18** and **Figure 2.19**, respectively. Moment coefficient is selected from VLM analysis for which $c_{m,c/4}$ is constant and highest. Aerodynamic parameters selected from the results of wing analysis by different solvers available in XFLR5 are summarized in **Table 2.13**.

Table 2.13. Aerodynamic Coefficients of the Multi-Tapered Wing

$C_{L,max}$	$= 1.7$	@ $\alpha \approx 15°$
$C_{L,\alpha=0}$	$= 0.66$	@ $\alpha = 0°$
$C_{L,L=0}$	$= 0$	@ $\alpha = -8°$
$(C_L/C_D)_{max}$	$= 20.6$	@ $\alpha = 0°$
$c_{m,c/4}$	$= -0.21$	

33
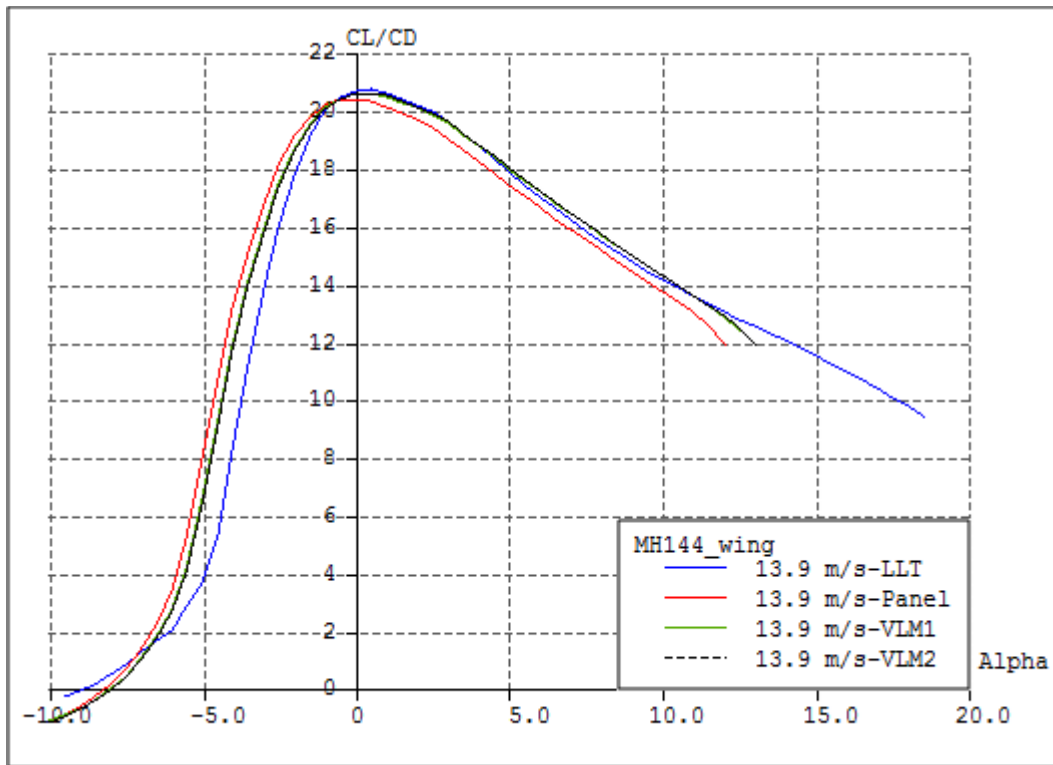
Figure 2.18. C_L/C_D Curves of Finite Wing Analysis Results.
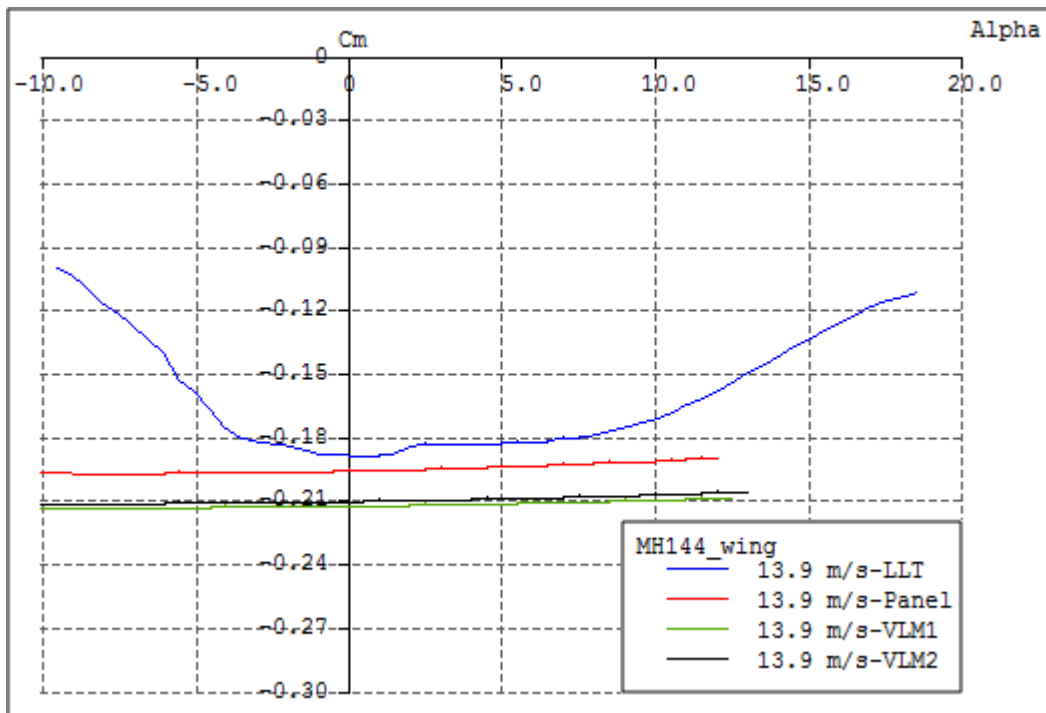
Figure 2.19. $Cm_{c/4}$ vs Alpha Results of Wing Analysis Results

34

Pressure coefficient (Cp) distribution on the wing is determined with the Panel Method solution and results are shown in **Figure 2.20** and **Figure 2.21**. Aerodynamic load on the wing can be calculated by exporting mesh data and Cp data. It may be reasonable to interpolate aerodynamic pressure data on the wing structure in order to perform structural analysis. Reliability of pressure coefficient results is discussed in **Chapter 3**, in which CFD analysis of the wing is performed.
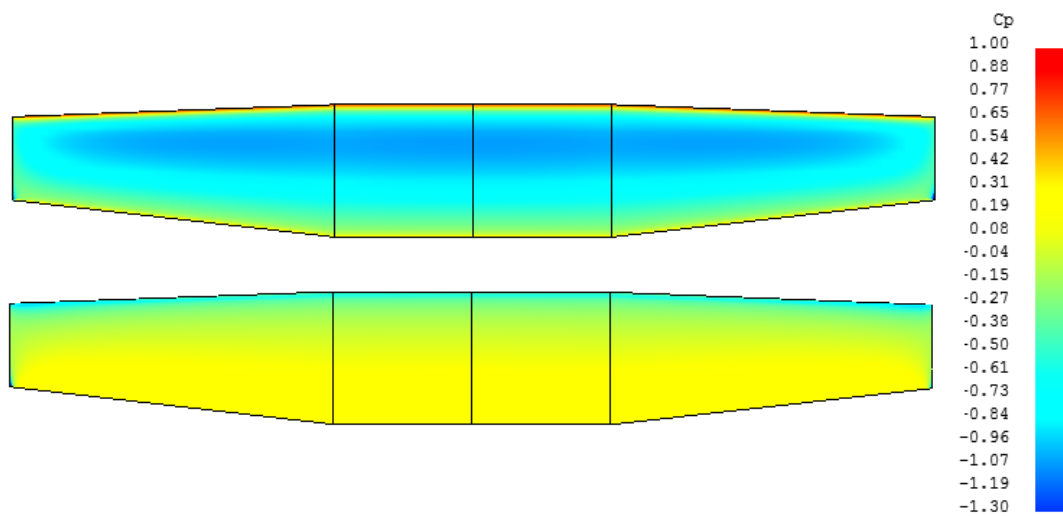
Figure 2.20. Cp Distribution on the Upper and Lower Surfaces at $\alpha = 0°$.
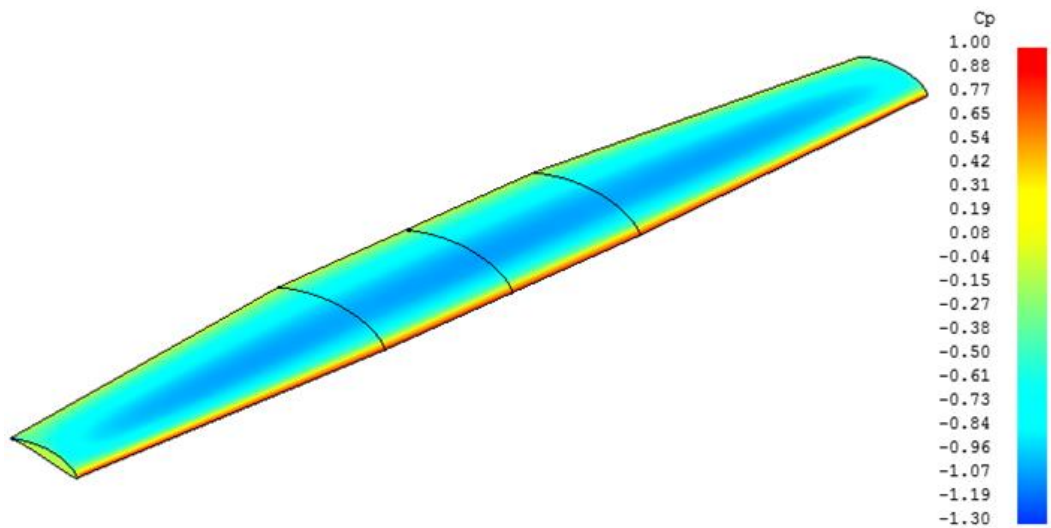
Figure 2.21. Cp Distribution on Wing at $\alpha = 0°$ (Isometric View)

Maximum required lift coefficient of the wing is 1.8 due to stall constraint. However, maximum lift coefficient of the wing is determined as $C_{L,max} = 1.7$ for the unflapped condition. Therefore, high-lift device is needed to achieve stall velocity requirement. Lift coefficient contribution of various high-lift devices are discussed and tabled in the literature but in the present study, literature assumption is not preferred since they are based on empirical relations on large aircraft. Therefore, flapped wing conditions, which are taken as full span flap and 40% span flap conditions with 30° deflection angle at $V_{stall} = 8\,m/s$, are analyzed to determine more acceptable results. Analysis with higher deflection angles results with convergence error due to high turbulence level. Therefore, 30° moderate flap deflection angle is chosen for the takeoff condition. LLT analysis is preferred to observe the lift decrement near stall condition. Wing models of wing without flap, wing with full span plain flap and wing with 40% span plain flap conditions shown in **Figure 2.22** are analyzed for the cruise and the stall velocity conditions at 1000 m altitude.
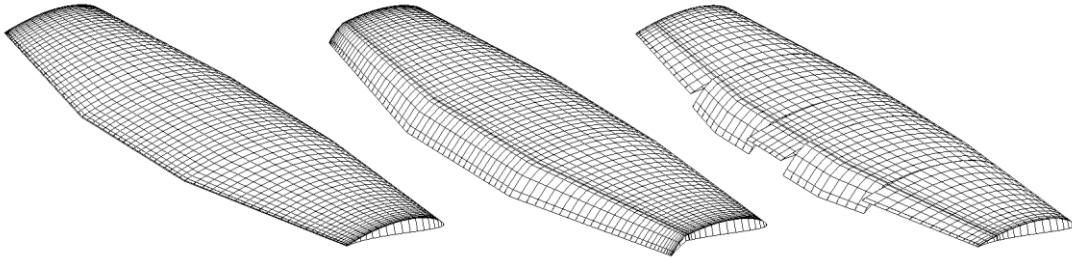
Figure 2.22. Flapped and Unlapped Wing Conditions

Lift coefficients vs. angle of attack curves of the flapped and unflapped conditions are presented in **Figure 2.23**. Lift coefficient of 1.7 is again obtained for the multi-tapered wing without flap as before and maximum lift coefficient of wing with full flap is determined as 1.95. Maximum lift coefficient is determined as 1.8 for the multi-tapered wing with 40% spanwise flap as aimed. Analysis result for $C_{L,max}$ is also consistent with analytical calculation of 40% spanwise flap condition given by **Eqn. 2.19** [18].

$$C_{L,max} = C_L + 0.4 \cdot \Delta C_L = 1.70 + 0.4 \cdot (1.95 - 1.70) = 1.80 \qquad \textbf{(2.19)}$$

36
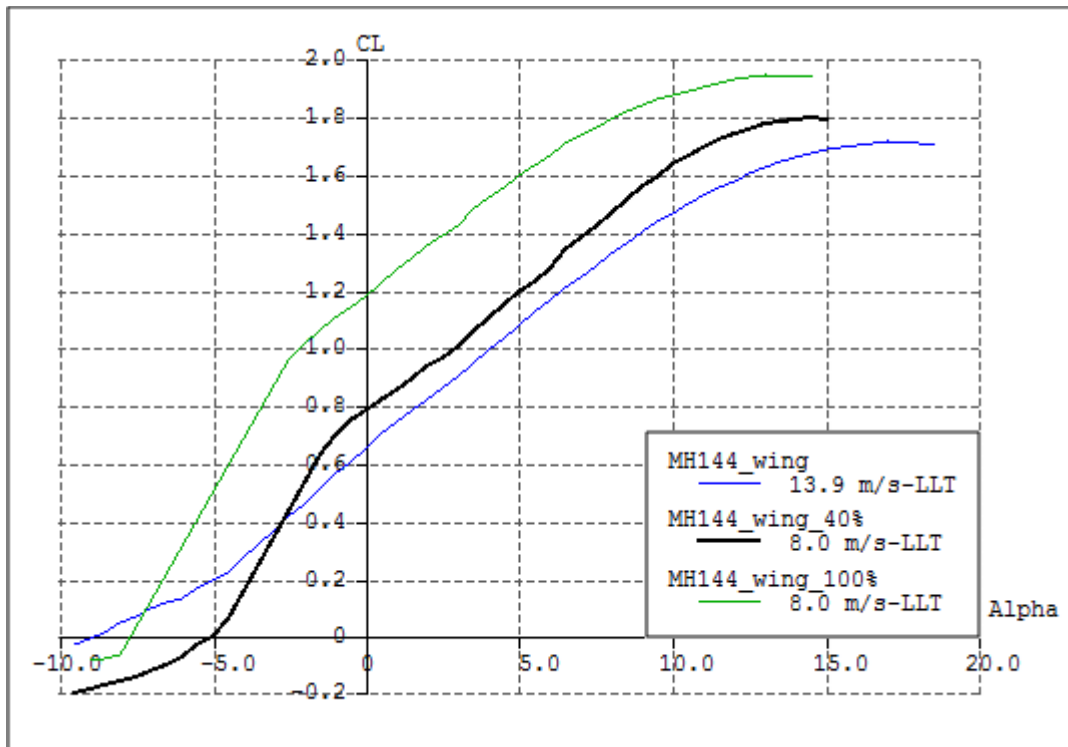
Figure 2.23. C_L vs. Alpha Results for LLT Analysis

Table 2.14 summarizes the maximum lift coefficient results obtained for flapped and unflapped conditions.

Table 2.14. Lift Coefficient Table

Unflapped	$C_{L,\alpha=0°} = 0.66$	$C_{L,max} = 1.70$
100% span flap, $\delta = 30°$	$\left(C_{L,\alpha=0°}\right)_{100\%} = 1.175$	$C_{L,max,100\%} = 1.95$
40% span flap, $\delta = 30°$	$\left(C_{L,\alpha=0°}\right)_{40\%} = 0.827$	$C_{L,max,40\%} = 1.80$

Another important result determined with wing analysis is C_L vs C_D relation of the wing which is the drag polar. Aerodynamic coefficients and parameters at minimum drag are important to determine aircraft performance relations. C_L /C_D vs angle of attack results are shown in **Figure 2.24** and drag polar result of the XFLR5 analysis is shown in **Figure 2.25**.
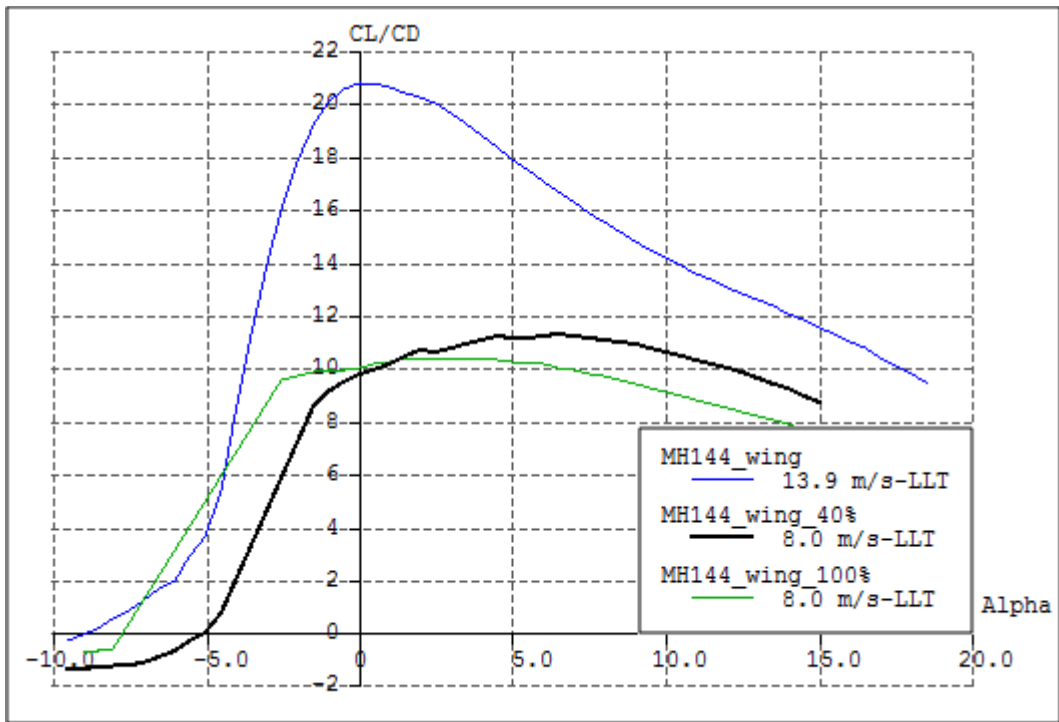
Figure 2.24. C_L/C_D vs. Alpha Results for LLT Analysis
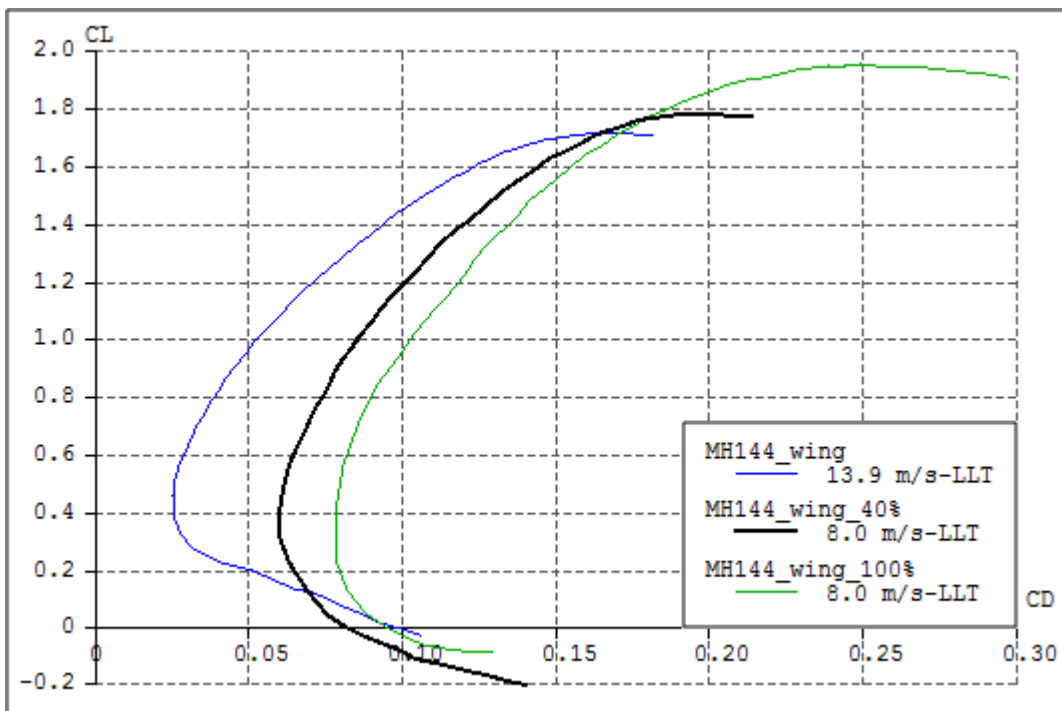
Figure 2.25. Drag Polar of the Wing

38

The following results are obtained from the drag polar and lift coefficient versus angle of attack curves. Firstly, minimum drag value and corresponding lift coefficient value are determined from the drag polar, then corresponding angle of attack is determined from the lift coefficient curves.

- $C_{D,min} = 0.026$ and $(C_L)_{mindrag} = 0.41$ for unflapped wing at $\alpha = -2.5°$
- $C_{D,min} = 0.058$ and $(C_L)_{mindrag} = 0.37$ for 40% flapped wing at $\alpha = -2.5°$.

These parameters are important to determine drag polar given in **Section 2.8.5** and aerodynamic relations associated with lift, drag and flight speeds given in **Section 2.8.6.**

2.7. Sizing

Overall sizing of the aircraft is performed by referencing Aircraft Performance and Design book of Anderson and Aircraft Design book of Raymer [18]. Wing dimensions are determined in **Section 2.5.6** by taking stall constraint into account. Anderson stated that one of the most empirical aspects of the airplane design process is the sizing of the tail [15]. Thus, tail dimensions are determined by using tail volume ratio values based on historical empirical data and tail moment arm is selected for keeping the overall aircraft length at 1.5 m as given in **Table 2.7** which is summarized in **Table 2.15.**

Table 2.15. Initial Sizing Parameters of Demircan Mini UAV

Wing Span :b	2.2	m/s
Wing Area: S	0.605	m^2
Mean Chord: c	0.275	m
Aspect Ratio: AR	8	-
Overall Length	1.5	m

2.7.1. Multi-tapered Wing

Wing dimensions are determined in **Section 2.5.6**.

2.7.2. Horizontal Tail

Horizontal tail volume ratio is the horizontal tail sizing parameter which is calculated by [15],

$$V_{HT} = \frac{l_{HT} \cdot S_{HT}}{\bar{c} \cdot S_{wing}} \tag{2.20}$$

where V_{HT} is the horizontal tail volume ratio, l_{HT} is the horizontal tail moment arm and S_{HT} is the planform area of the horizontal tail. Based on typical horizontal tail volume ratios of homebuilt aircraft from Raymer [18], volume ratio of the horizontal tail is chosen as **0.5.**

Fuselage length and weight are not affected by the tail arm length, since tail is boom mounted. Although tail booms are lighter than conventional aft fuselage, aeroelastic properties are more disadvantageous. Boom deflection due to tail lift is higher for longer tail arms and it tends to twist wing from wing-tail boom joints. Additionally reduction in control surface effectiveness of the horizontal tail or control reversal because of the complete angle of attack change due to boom deflection is a common aeroelastic problem for twin boom tail designs. Due to the fact that, tail moment arm should be short as possible but propeller wash should be also taken into account.

Conceptual sizing of the horizontal tail moment arm is selected to keep overall length at 1.5 m. Therefore, it is selected as 0.84 m than required planform area S_{HT} is calculated. Horizontal tail dimensions are presented in **Table 2.16** and horizontal tail planform is shown in **Figure 2.26.**

Table 2.16. Horizontal Tail Dimensions

HT Volume Ratio	: V_HT	0.5	
HT Moment Arm	:L_HT	0.84	m
HT Area	:S_HT	0.103	m^2
HT Aspect Ratio	: AR_HT	4.3	
HT Taper Ratio	: λ_HT	1	
HT Span	: b_HT	0.666	m
HT Root Chord	: cr_ht	0.155	m
HT Tip Chord	: ct_ht	0.155	m
HT Mean Aero. Chord	: c_ht	0.155	m
Wetted Area	: Swet_HT	0.206	m^2
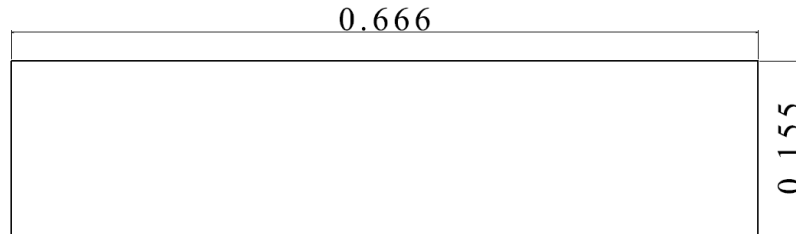
Figure 2.26. Horizontal Tail Dimensions (m)

2.7.3. Vertical Tail

Vertical tail volume ratio is the vertical tail sizing parameter which is calculated by [15],

$$V_{VT} = \frac{l_{VT} \cdot S_{VT}}{b \cdot S_{wing}}$$ (2.21)

where V_{VT} is vertical tail volume ratio, l_{VT} is vertical tail moment arm and S_{VT} is planform area of the vertical tail. Based on typical vertical tail volume ratio value of homebuilt aircraft from Raymer [18], volume ratio of the vertical tail is chosen as **0.04**. Vertical tail arm is iterated by using horizontal tail arm since leading edge of the vertical tail tip and leading edge of the horizontal tail are at the same point. Once tail arm is selected as a first guess, required planform area S_{VT} is calculated and tail dimensions are calculated by using predefined design parameters like aspect ratio and taper ratio. Aerodynamic center of the vertical tail is recalculated and vertical tail moment arm is checked which is the distance between aerodynamic center of the wing and aerodynamic center of the vertical tail.

All calculations are repeated starting from the moment arm selection and final dimensions are determined. Vertical tail dimensions are presented in **Table 2.17** and vertical tail planform is shown in **Figure 2.27**.

Table 2.17. Vertical Tail Dimensions (Double Fin)

VT Volume Ratio	: V_VT	0.04
VT Moment Arm	: L_VT	0.792 m
VT Area	: S_VT	0.035 m^2
VT Aspect Ratio	: AR_VT	1.3
VT Taper Ratio	: λ_VT	0.65
VT Height	: h_VT	0.212 m
VT Root Chord	: cr_vt	0.197 m
VT Tip Chord	: ct_vt	0.128 m
VT Mean Aero. Chord	: c_vt	0.165 m
Wetted Area	: Swet_VT	0.138 m^2
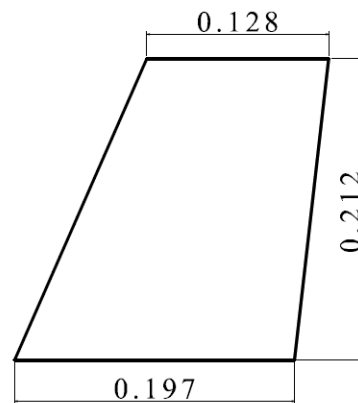
Figure 2.27. Vertical Tail Dimensions (m)

2.7.4. Fuselage

Fuselage is sized for drag estimation at this stage. Raw shape of the fuselage is considered for an ISR mission in order to perform drag calculations. Nose part of the fuselage is half spherical (gimbal), mid-fuselage is cylindrical and aft body is conical. Electric motor is placed above the aft body.

Width of the fuselage is selected as 0.12 m in order to ease grip of the body for hand launch. Height of the body and diameter of the nose are assumed same as the width of the fuselage. Fuselage length is 0.85 m by taking system component sizes and placement into account. Simplified fuselage dimensions are presented in **Table 2.18** and shown in **Figure 2.28**.

Table 2.18. Fuselage Dimensions

Sectional Lengths		Sectional Area
Nose (Half Sphere)	0.06 m	0.023 m^2
Body(Cylinder)	0.6 m	0.226 m^2
Aft Body (Conical)	0.19 m	0.056 m^2
Motor Case (Half Cylinder)	0.22 m	0.014 m^2
Motor Case Height	0.04 m	
Body Height	0.12 m	
Total Length	0.85 m	
Swet_Fuselage		0.319 m^2
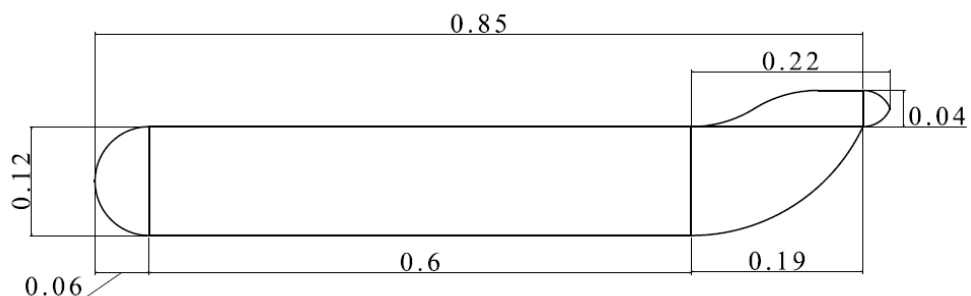
Figure 2.28. Fuselage Dimensions (m)

2.7.5. Boom

Boom length is equal to the distance between leading edge of the wing and trailing edge of the vertical tail root. Boom dimensions are presented in **Table 2.19** and in **Figure 2.29**.

Table 2.19. Boom Dimensions

Length	0.984	m
Radius	0.006	m
Area	0.037	m^2

0.984

0.012
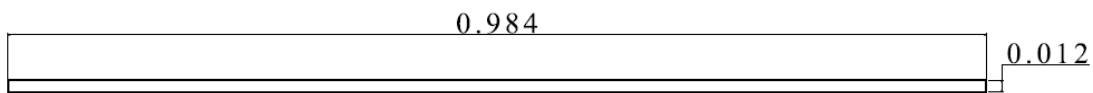
Figure 2.29. Boom Dimensions (m)

2.7.6. Configuration Layout

Conceptual sketch of the configuration layout is shown in **Figure 2.30**. Since tail dimensions are specified by using tail volume ratio and predefined parameters, center of gravity location is adjusted to ensure longitudinal stability by placing system components. System components and weight distribution of the aircraft are given in **Section 2.16**.
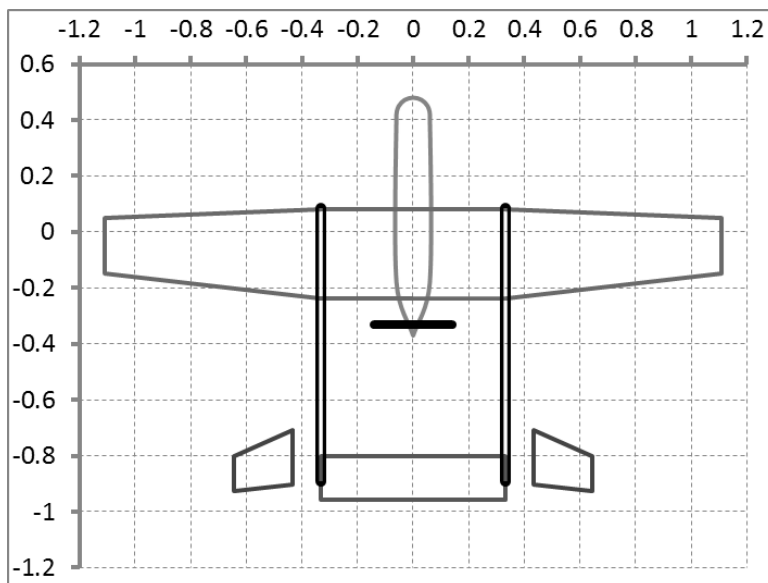
Figure 2.30. Conceptual Configuration Layout

(All dimensions are in m)

44

2.7.7. Total Wetted Area (S_{wet})

Wetted surface areas of the aircraft components are given in **Table 2.20**.S_{wet}/S ratio is a fundamental parameter to determine parasite drag coefficient.

Table 2.20. Wetted Areas

Components	Swet
Wing	1.268 m^2
Horizontal Tail	0.206 m^2
Vertical Tail	0.138 m^2
Fuselage	0.319 m^2
Boom	0.037 m^2
TotalSwet	1.968 m^2
Swet/S	3.205

2.8. Fundamental Design Parameters

Fundamental design parameters are wing loading (W/S), parasite drag coefficient ($C_{D,0}$), Oswald span efficiency factor (e) and induced drag factor (K) used in aircraft performance relations.

2.8.1. Wing Loading (W/S)

Wing loading has been determined in **Section 2.5.6**.

$$\frac{W}{S} = 63.88 \; N/m^2$$

2.8.2. Parasite Drag Coefficient ($C_{D,0}$)

Subsonic parasite drag is estimated by using component buildup method which estimates the drag contribution of each part of the aircraft. Following equations are referenced from Raymer [18].

$$(C_{D0})_{subsonic} = \frac{\sum(C_{fc}FF_cQ_cS_{wet,c})}{S_{ref}} + C_{D,misc} + C_{D,L\&P} \tag{2.22}$$

Flat-Plate skin friction coefficients:

$$C_{f,laminar} = \frac{1.328}{\sqrt{Re}} \tag{2.23}$$

$$C_{f,turbulent} = \frac{0.455}{(\log(Re))^{2.58}(1 + 0.144M^2)^{0.65}} \tag{2.24}$$

Form factor for wing, tail, strut and pylon:

$$FF = \left[1 + \frac{0.6}{(x/c)_m}\left(\frac{t}{c}\right) + 100\left(\frac{t}{c}\right)^4\right]\left[1.34M^{0.18}(\cos \Lambda_m)^{0.28}\right] \tag{2.25}$$

Hinged surface form factor is 10% higher.

$$FF_{wing,tail} = 1.1FF$$

Form factor for fuselage:

$$FF = \left(1 + \frac{60}{f^3} + \frac{f}{100}\right) \tag{2.26}$$

where

$$f = \frac{l}{d} = \frac{l}{\sqrt{(4/\pi)A_{max}}} \tag{2.27}$$

Component interference factors Q are given in **Table 2.21**.

Table 2.21. Interference Factors, Q

High Wing	1
Horizontal Tail	1.08
Vertical Tail	1.08
Fuselage	1
Boom	1.1

Flap contribution:

$$\Delta C_{D0,flap} = 0.0023\frac{flapspan}{wingspan}\delta_{flap} \tag{2.28}$$

Miscellaneous drags due to antenna, landing gear etc. contribution is assumed 10% of the total basic parasite drag.

$$C_{D,misc} = 0.1 \, C_{D0,basic}$$

(2.29)

Leakage and Protuberance Drags (L&P) are 10% of the basic parasite drag for propeller aircraft.

$$C_{D,L\&P} = 0.1(C_{D0})_{Basic}$$

(2.30)

Turbulent flow is assumed behind maximum thickness location (30%) of the wing and the tail surfaces. Component drag buildup method calculations for **13.9 m/s** design velocity and **1000 m** design altitude are given in **Appendix B** in detail. Results are summarized in **Table 2.22** and parasite drag contribution percentages are shown in **Figure 2.31.**

Table 2.22. Parasite Drag Coefficient Components

Components	C_{D0}		
Wing	0.009571	30% Laminar, 70% Turbulent	
Horizontal Tail	0.002096	30% Laminar, 70% Turbulent	
Vertical Tail	0.001378	30% Laminar, 70% Turbulent	
Fuselage	0.002852	Turbulent	
Boom	0.001001	Turbulent	
$(C_{D0})_{basic}$	0.016898		
Miscellaneous	0.001690		
L&P	0.001690	ΔFlap, 30°	0.02760
$(C_{D0})_{total}$	**0.02028**	$(C_{D0})_{total,flapped}$	**0.04788**
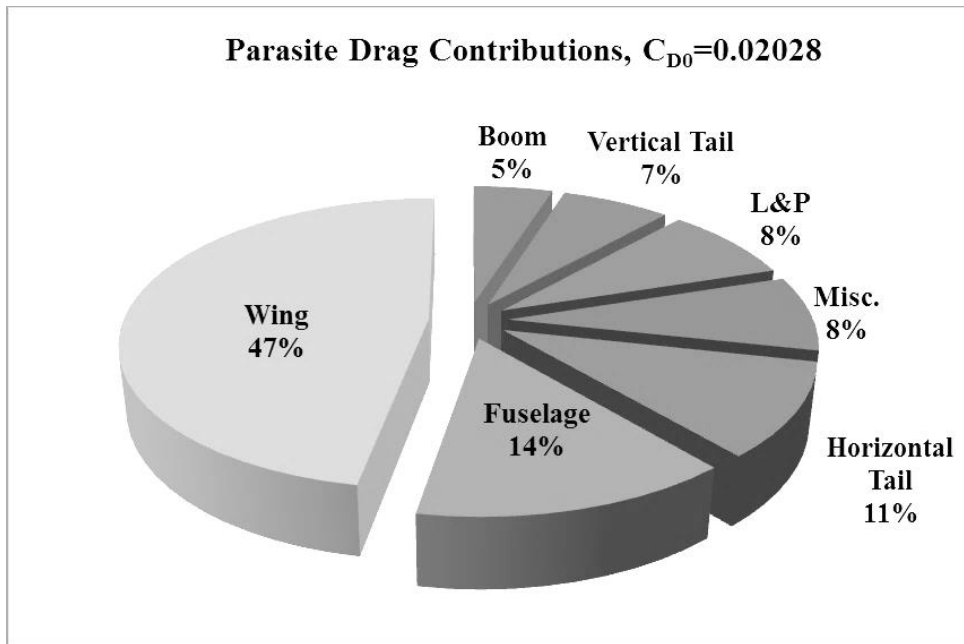
Figure 2.31. Parasite Drag Contributions

2.8.3. Oswald Span Efficiency Factor (e)

Span efficiency factor (e) for wing is calculated as,

$$e = \frac{1}{1 + \delta}$$ (2.31)

where δ is calculated from lifting line theory and plotted in **Figure 2.32**.
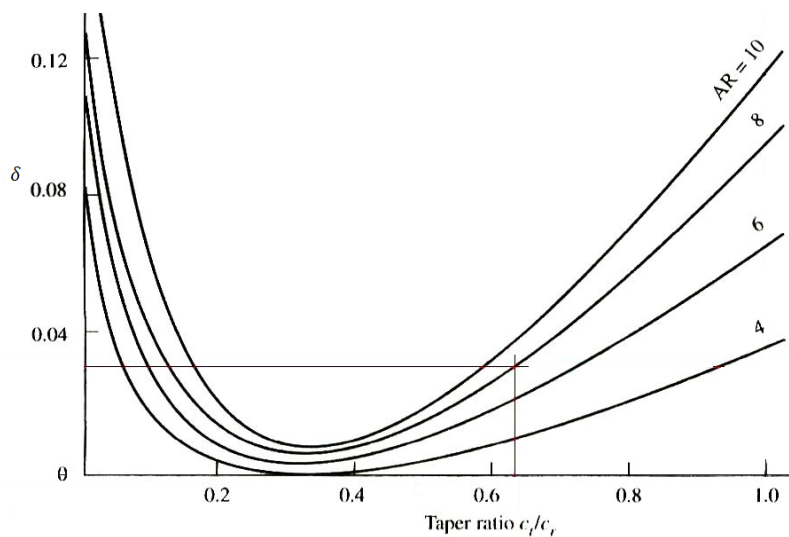
Figure 2.32. Induced Drag Factor, δ for different AR and λ [15]

Taper ratio (λ) is 0.629 and aspect ratio (AR) is 8 then $\delta = 0.03$ as can be seen from **Figure 2.32**. Oswald Span Efficiency Factor (e) for the wing is then calculated as,

$$e = \frac{1}{1 + \delta} = \frac{1}{1 + 0.03} = 0.97$$

which is reasonable since multi-tapered wing lift distribution approaches to elliptical lift distribution. However, efficiency factor of an aircraft is much smaller due to wing separation drag and body interaction. More realistic estimation for a straight wing aircraft is given as [18],

$$e = 1.78(1 - 0.045 \cdot (AR)^{0.68}) - 0.64 \tag{2.32}$$
$$e = 0.81$$

2.8.4. Induced Drag Factor, K

Induced Drag Factor (K) is calculated as,

$$K = \frac{1}{\pi e AR} = \frac{1}{\pi \cdot 0.81 \cdot 8} = 0.04913 \tag{2.33}$$

Induced drag factor relation is determined from Prandtl Lifting Line Theory and **Eqn. (2.33)** is the basic form of induced drag factor relation. It is needed to be expanded for high lift coefficient airfoils [19]. General form of the adjusted value of the induced drag factor can be expressed as;

$$K^* = K + c_K \tag{2.34}$$

"c_K" is the coefficient indicating the parasite drag increase of the airfoil, obtained from its drag polar. Therefore, it has no specific definition since it may be different for each airfoil and can be found by experiment or numerical analysis. Difference between relations given in equations **(2.31)** and **(2.32)** can be represented on induced drag factor result and "c_K" value can be found as a constant.

$$c_K = K^* - K = \frac{1}{\pi \cdot 0.81 \cdot 8} - \frac{1}{\pi \cdot 0.97 \cdot 8} = 8.1 \times 10^{-3}$$

More realistic representation of the "c_K" coefficient can be expressed as a function of lift coefficient. However, experimental validation and comprehensive numerical analysis of the design are not covered in the thesis work. Therefore, "c_K" value is not investigated and determined in terms of lift coefficient variation. Simple result given in **Eqn. (2.33)** is used in further calculations for simplicity in the derivations performed in **Section 2.8.6** where "c_K" is taken as constant.

2.8.5. Drag Polar

General form of the drag polar for symmetrical airfoil is given by;

$$C_D = C_{D0} + KC_L^2 \qquad (2.35)$$

Parasite drag coefficient (C_{D0}) is the minimum drag coefficient $(C_{D,min})$ at zero angle of attack for symmetrical airfoils, where $C_L = 0$. However, drag at zero lift angle of attack $(\alpha_{L=0})$ does not have minimum value for cambered airfoils and drag polar is needed to be translated by the minimum drag lift coefficient. $C_{L,Dmin}$ values are **0.41** for the unflapped wing and **0.37** for the flapped wing configurations as determined in **Section 2.6.** Therefore, one can express drag coefficients for no flap and flap cases by **Eqn. (2.37)** and **(2.38)**.

$$C_D = C_{Dmin} + (K + c_K) \cdot (C_L - C_{L,Dmin})2 \qquad (2.36)$$
$$C_D = 0.02028 + 0.04913(C_L - 0.41)^2 \qquad (2.37)$$
$$C_{D,flapped} = 0.04788 + 0.04913(C_L - 0.37)^2 \qquad (2.38)$$
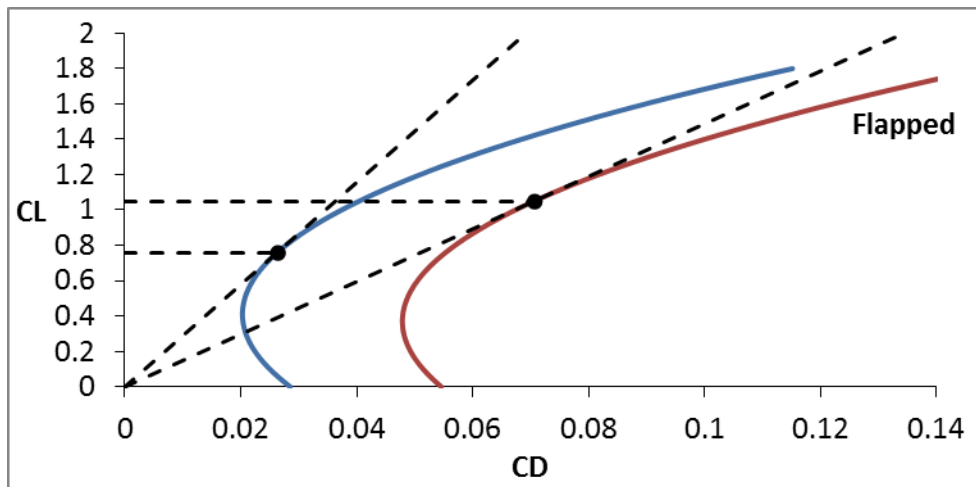
Figure 2.33. Drag Polar

As shown in **Figure 2.33**, tangent lines to the drag polar curve drawn from the origin indicate $(L/D)_{max}$ locations. Corresponding $\boldsymbol{C_L}$ values are **0.76** for the unflapped wing at $\alpha = \boldsymbol{1.2°}$ and **1.05** for the flapped wing at $\alpha = \boldsymbol{4.2°}$.

2.8.6. Aerodynamic Relations Associated with Lift, Drag and Flight Speed

Fundamental parameters (K, C_{D0}) defined in previous section are used to determine aerodynamic relations associated with lift, drag and flight speed.

$(L/D)_{max}$ condition is the $(T_R)_{min}$ condition where drag (thrust required) is minimized in steady level flight, in other words $(L/D)_{max}$ condition is the cruise condition and maximum range is achieved at this speed for propeller driven aircraft. Relations for $(L/D)_{max}$ and $V_{(L/D)_{max}}$ are derived from symmetrical airfoil and they are expressed as;

$$\left(\frac{L}{D}\right)_{max} = \left(\frac{C_L}{C_D}\right)_{max} = \frac{1}{\sqrt{4C_{D,0}K}} \tag{2.39}$$

$$V_{(L/D)_{max}} = \left(\frac{2}{\rho_\infty}\sqrt{\frac{K}{C_{D0}}}\frac{W}{S}\right)^{1/2} \tag{2.40}$$

However, $(L/D)_{max}$ of a cambered wing should be determined again to obtain more reasonable result due to drag polar offset caused by minimum drag condition.

$$\frac{L}{D} = \frac{C_L}{C_D} = \frac{C_L}{C_{D0} + K(C_L - C_{L,Dmin})^2} \tag{2.41}$$

$(L/D)_{max}$ can be found from **Eqn. (2.41)**. Details are given in **Appendix C.**

$$\left(\frac{L}{D}\right)_{max} = \left(\frac{C_L}{C_D}\right)_{max} = \sqrt{\frac{1}{4KC_{D0}} + \left(\frac{C_{L,Dmin}}{2C_{Dmin}}\right)^2} + \frac{C_{L,Dmin}}{2C_{Dmin}} \tag{2.42}$$

$$\boxed{\left(\frac{L}{D}\right)_{max} = 28.90}$$

Derivation of $V_{(L/D)_{max}}$ is given in **Appendix C** and **Table 2.23** gives $(L/D)_{max}$ velocities at different altitudes.

$$V_{(L/D)_{max}} = V_{(T_R)_{min}} = \left(\frac{2}{\rho_\infty}\sqrt{\frac{K}{C_{Dmin} + KC_{L,Dmin}^2}}\frac{W}{S}\right)^{1/2} \tag{2.43}$$

Table 2.23. (L/D)max Velocities with Altitude

Altitude	$V_{(L/D),max} = V_{(TR),min}$
0 m	11.7 m/s
1000 m	12.3 m/s
2000 m	12.9 m/s
3000 m	13.6 m/s
4000 m	14.3 m/s

Theoretically, maximum endurance is achieved at minimum power required and it is proportional to $\left(C_L^{3/2}/C_D\right)_{max}$ for a propeller driven airplane. Standard relation for $\left(C_L^{3/2}/C_D\right)_{max}$ is derived from symmetrical airfoil which is expressed as;

$$\left(\frac{C_L^{3/2}}{C_D}\right)_{max} = \frac{1}{4}\left(\frac{3}{C_{D,0}^{1/3}K}\right)^{3/4} \tag{2.44}$$

$$V_{\left(C_L^{3/2}/C_D\right)_{max}} = \left(\frac{2}{\rho_\infty}\sqrt{\frac{K}{3C_{D0}}}\frac{W}{S}\right)^{1/2} \tag{2.45}$$

Modified expression for cambered airfoil is determined as,

$$\frac{C_L^{3/2}}{C_D} = \frac{C_L^{3/2}}{C_{Dmin} + K\left(C_L - C_{L,Dmin}\right)^2} \tag{2.46}$$

Derivation of $\left(C_L^{3/2}/C_D\right)_{max}$ and $V_{\left(C_L^{3/2}/C_D\right)_{max}}$ are given in **Appendix C.** Lift coefficient at $\left(C_L^{3/2}/C_D\right)_{max}$ is determined as,

$$C_L^* = \sqrt{\frac{3C_{Dmin}}{K} + 4C_{L,Dmin}^2} - C_{L,Dmin} \tag{2.47}$$

$$\left(\frac{C_L^{3/2}}{C_D}\right)_{max} = \frac{1}{4}\frac{\left(C_L^* + 3C_{L,Dmin}\right)(C_L^*)^{1/2}}{C_{Dmin}} \tag{2.48}$$

$$\left(\frac{C_L^{3/2}}{C_D}\right)_{max} = 26.77$$

Flight velocity at $\left(C_L^{3/2}/C_D\right)_{max}$ is determined as.

$$V_{\left(C_L^{3/2}/C_D\right)_{max}} = \left(\frac{2}{\rho_\infty}\frac{W}{S}\left(\sqrt{\frac{3C_{Dmin}}{K} + 4C_{L,Dmin}^2} - C_{L,Dmin}\right)^{-1}\right)^{1/2} \qquad (2.49)$$

Table 2.24. $(C_L^{3/2}/C_D)$max Velocities at Different Altitudes

Altitude	$V_{(CL^{3/2}/CD),max}$
0 m	10.4 m/s
1000 m	10.9 m/s
2000 m	11.4 m/s
3000 m	12.0 m/s
4000 m	12.7 m/s

Modified aerodynamic relations derived in this section are compared with classical relations for symmetrical airfoils in **Appendix C.** Relative differences are calculated with respect to symmetrical airfoil relations, and results are summarized in **Table 2.25** and **Table 2.26**.

$$Difference \% = \frac{(Cambered) - (Symmetrical)}{(Symmetrical)} \times 100 \% \qquad (2.50)$$

Table 2.25. Comparison of $(L/D)_{max}$ and $(C_L^{3/2}/C_D)_{max}$ Results

	$(L/D)_{max}$	$\left(C_L^{3/2}/C_D\right)_{max}$
Symmetrical	15.84	14.47
Cambered	28.90	26.77
Difference %	**82.4 %**	**85.0 %**

Table 2.26. Comparison of $(L/D)_{max}$ and $(C_L^{3/2}/C_D)_{max}$ Velocities at Different Altitudes

Altitude (m)	$V_{(L/D),max}$ (m/s)		$V_{(CL^{3/2}/CD),max}$ (m/s)	
	Symmetrical	**Cambered**	**Symmetrical**	**Cambered**
0	12.7	11.7	9.7	10.4
1000	13.4	12.3	10.2	10.9
2000	14.1	12.9	10.7	11.4
3000	14.8	13.6	11.2	12.0
4000	15.6	14.3	11.8	12.7
Difference%	-	- 8.2 %	-	+7.0 %

As can be seen from comparison tables, relative differences are quite high if classical relations for symmetrical airfoil are used in performance analysis for cambered airfoils. $(L/D)_{max}$ and $\left(C_L^{3/2}/C_D\right)_{max}$ results are **82.4%** and **85%** higher for cambered airfoils compared to the classical approach. These results show that classical approach estimates higher drags at cruise and loitering conditions. Additionally corresponding velocities calculated from modified relations are **8.2%** lower for the cruise condition and **7%** higher for the loitering condition. Since design speed range is too narrow for small scaled aircraft like the design in this thesis work, modified aerodynamic relations for cambered airfoils derived in this section should be preferred in order to avoid misleading cruise and loitering velocity results, which may lead to miscalculated flight time and flight range. It should be noted that determination of the required battery capacity for maximum range and endurance is also related with cruise and loitering conditions. Variations of cruise and loitering velocities with altitude are given in **Figure 2.34.**
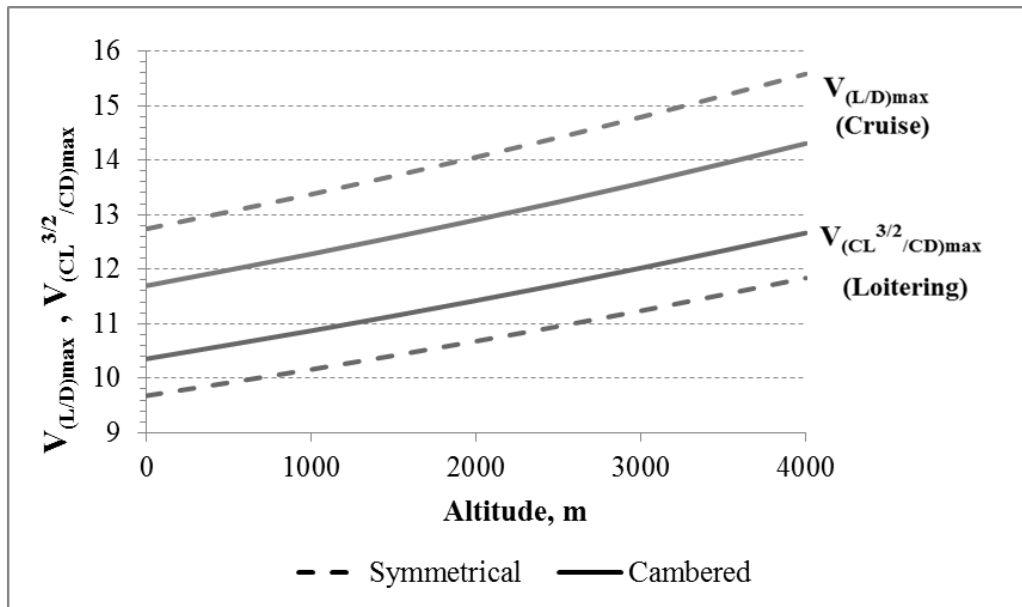
Figure 2.34. Variation of Cruise and Loitering Velocities with Altitude

Variations of C_L/C_D and $C_L^{3/2}/C_D$ relations vs. velocity are plotted for 1000 m altitude and plotted in **Figure 2.35.**
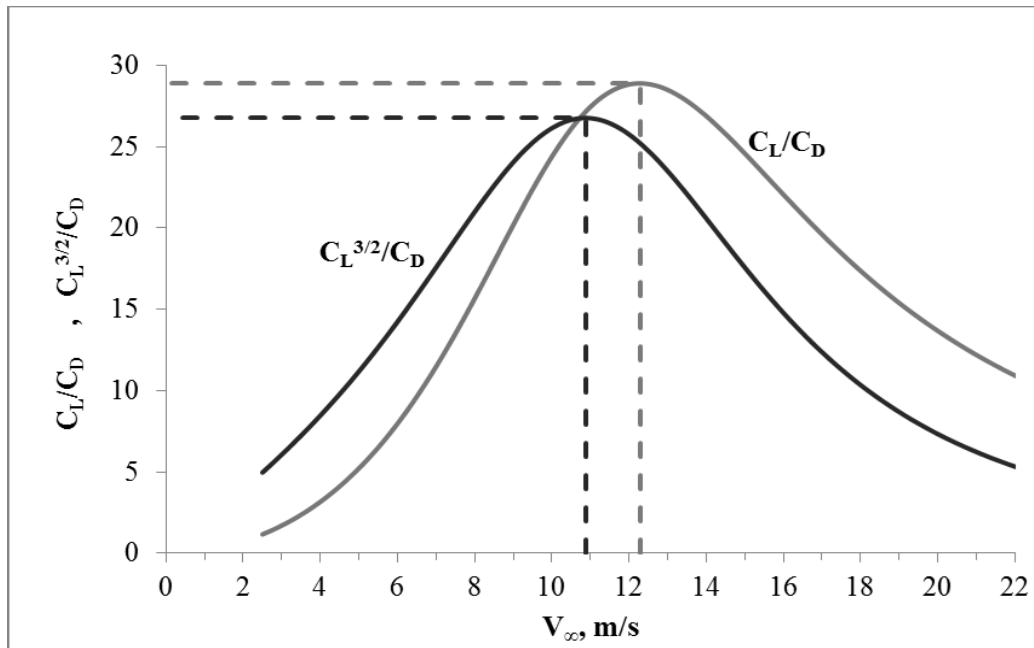
Figure 2.35. Variations of C_L/C_D and $C_L^{3/2}/C_D$ relations vs. Velocity at 1000 m

2.8.7. Summary of Fundamental Design Parameters

Fundamental design parameters determined in previous sections are shown together in **Table 2.27.**

Table 2.27. Summary of Fundamental Design Parameters

Wing Loading	$W/S = 63.88 \, N/m^2$
Parasite Drag	$C_{Dmin} = 0.02028$
	$C_{Dmin,flapped} = 0.04788$
Span Efficiency Factor	$e = 0.81$
Induced Drag Factor	$K = 0.04913$
Drag Polar	$C_D = 0.02028 + 0.04913(C_L - 0.41)^2$
	$C_{D,flapped} = 0.04788 + 0.04913(C_L - 0.37)^2$

2.9. Constraint Analysis (W/S vs. P_A/W)

Constraint analysis allows identifying solution space for the airplane design. Wing loading (W/S), Thrust to Weight ratio (T/W) and Power to Weight ratio (P/W) are important design parameters and most of the aircraft performance equation can be expressed in terms of these parameters. However, for a propeller driven aircraft, P/W and T/W parameters are not meaningful without flight velocity and corresponding propeller efficiency. **Equation (2.51)** gives the power and power available expressions.

$$P = TV_\infty, \qquad P_A = \eta_{pr}P \tag{2.51}$$

where

$$P = \frac{P_A}{\eta_{pr}} = \frac{T_A V_\infty}{\eta_{pr}} \tag{2.52}$$

Propeller efficiency η_{pr} varies with flight velocity and altitude for fixed pitch propeller, thus P_A/W term is more meaningful instead of P/W or T/W parameters used in constraint analysis of a fixed pitch propeller driven aircraft since propeller efficiency is already included in power available term as a variable.

Initial design requirements and additional performance requirements are taken into account and presented in **Table 2.28.** Stall speed and maximum speed constraints are general design requirements. 0.5 m/s (or 100 ft/min) is the maximum rate of climb speed for general aviation aircrafts but it is taken as 0.3 m/s for the study. Maximum turn load is also calculated for 45° of bank angle, which is also specified for this study.

Table 2.28. Constraint Analysis Requirements

Constraints	
Stall Speed	$V_{stall} = 8 \, m/s$ @1000m
Climb Speed at Maximum Climb Angle	$V_{\theta,max} = V_{stall}$ @3000m
Maximum Rate of Climb	0.3 m/s @ 3000m
Maximum Speed	13.9 m/s @ MSL
Sustained Level Turn	$n, \max turn = 1.41$ @ 45° bank angle

Aircraft performance equations are referenced from Anderson [15] and Raymer [18]. Derivations of the constraint equations are given in **Appendix D**.

2.9.1. Stall Speed Constraint

Stall speed constraint is the hand launch requirement. Aircraft should survive at minimum 8 m/s throw speed at 1000 m as a design requirement. Stall speed constraint is given in **Section 2.5.4**.

$$(W/S)_{stall} = 64.034 \, N/m^2$$

2.9.2. Climb Speed Constraint

Climb speed is the other hand launch requirement. Aircraft should climb at stall speed at 3000 m altitude with maximum climb angle which also constraints the throw velocity and throw angle.

$$V_{\theta_{max}} = V_{stall}$$

$$\frac{P_A}{W} = \frac{4K(W/S)}{\rho_\infty V_{stall}} - \frac{(V_{stall})^3 \rho_\infty C_{D,0}}{(W/S)} \tag{2.53}$$

2.9.3. Maximum Rate of Climb Constraint

Maximum rate of climb constraint is the service ceiling requirement which is 0.3 m/s at 3000 m altitude. For simplicity, maximum rate of climb equation for aircraft with symmetrical airfoil is preferred for the constraint analysis.

$$\frac{P_A}{W} = \left(\frac{R}{C}\right)_{max} + \left(\frac{2}{\rho_\infty}\frac{W}{S}\left(\sqrt{\frac{3C_{D0}}{K} + 4C_{L,Dmin}^2} - C_{L,Dmin}\right)^{-1}\right)^{1/2}$$

$$\times \frac{1.155}{\sqrt{\frac{1}{4KC_{D0}} + \left(\frac{C_{L,Dmin}}{2C_{D0}}\right)^2} + \frac{C_{L,Dmin}}{2C_{D0}}} \tag{2.54}$$

2.9.4. Maximum Speed Constraint

Maximum speed constraint is not a fundamental requirement since the maximum velocity of the aircraft is limited. Even so, power required to achieve the cruise speed at sea level should be defined. Sea level is the determinant condition for maximum speed since air density and drag is higher.

$$
\frac{P_A}{W} = \sqrt{\frac{2}{\rho_0}\left(C_{D0} + K\left(\frac{\left(\frac{W}{S}\right)}{\frac{1}{2}\rho_0 V_{max}^2} - C_{L,Dmin} \right)^2 \right)\left(\frac{\left(\frac{1}{2}\rho_0 V_{max}^2\right)^{3/2}}{(W/S)} \right)} \tag{2.55}
$$

2.9.5. Sustained Level Turn Constraint

In the present study, maneuverability of the aircraft is not the preliminary requirement. Sustained turn is constrained to maximum 45 degree bank angle, which corresponds to 1.41 g turn. Sustained level turn constraint becomes dominant at higher bank angles which is not preferred. Sustained level turn is constrained by the thrust available or power available at a specified flight speed, and given as,

$$
\left(\frac{P_A}{W}\right) = \frac{1}{2}\rho_\infty V_\infty^3 \frac{C_{D0}}{(W/S)} + \frac{n^2 K(W/S)}{\frac{1}{2}\rho_\infty V_\infty} \tag{2.56}
$$

2.9.6. Constraint Diagram and P_A/W Requirement

Determined constraint equations are plotted in **Figure 2.36.** Design points for empty weight (W_0) condition to MTOW are indicated with the red dots. Since portability requirement is also considered for constant MTOW constraint, which leads to minimum size design, minimum wing area and highest possible wing loading point is selected as shown in the **Figure 2.36**. Unfortunately power available is not constant due to propeller efficiency variation with speed as mentioned. Therefore, design points indicated in the constraint diagram are not actual design points but give an idea about power requirement at a specific condition. Dominant performance constraint is the maximum rate of climb requirement at 3000 m altitude, where maximum power available is needed to achieve maximum rate of climb. Therefore $P_A/W = 1.7$ is point is selected as an appropriate design value to estimate propulsion requirements.
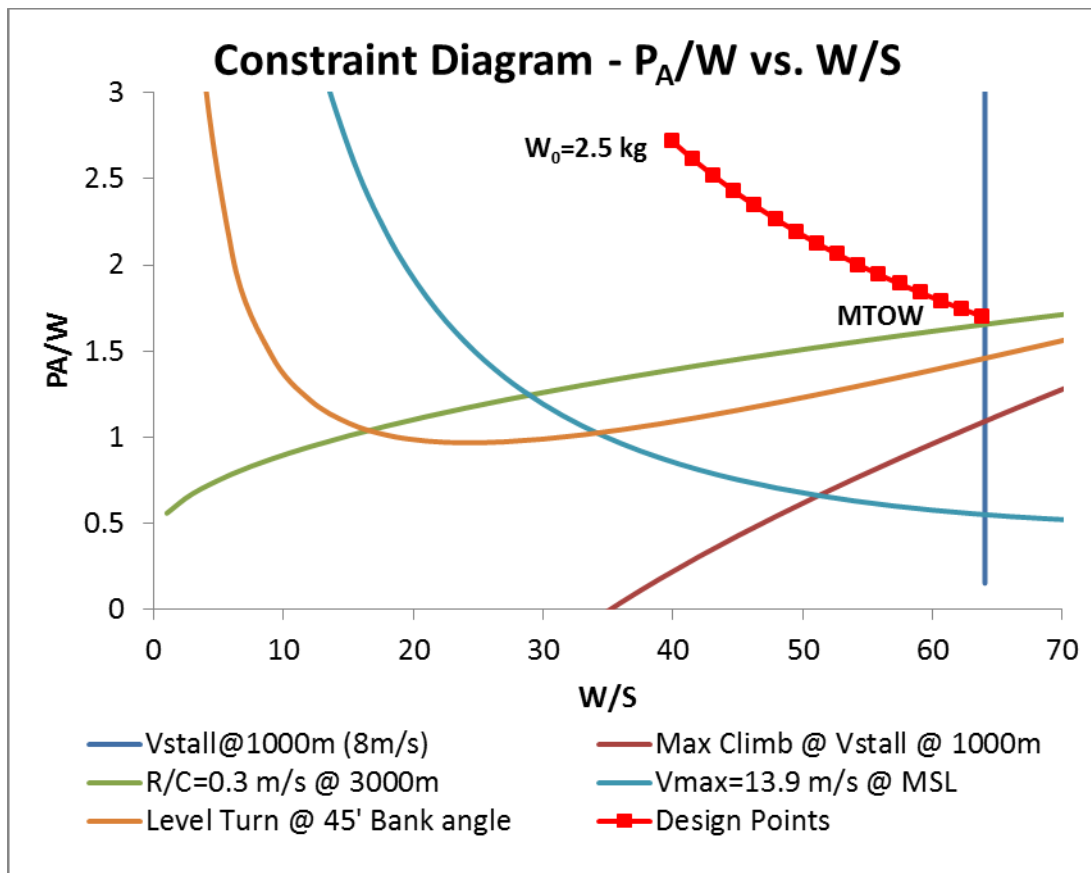
Figure 2.36. Constraint Diagram for P_A/W

2.9.7. Thrust Requirement at the Design Point

Thrust at maximum rate of climb requirement is estimated from power available requirement at maximum rate of climb velocity at 3000 m.

$$\frac{P_A}{W} = \frac{T}{W} \cdot V_{(R/C)max@3000m}$$

$$1.7 = \frac{T}{(39.24\ N)}(12.0\ m/s)$$

Thrust requirement to sustain maximum rate of climb at 3000 m is determined as.

$$T = 5.6\ N = 0.57\ kgf\ (@\ 12\ m/s\ ,@3000m).$$

Selected propulsion system should provide estimated thrust requirement at the design point and thrust estimation should be checked after dynamic thrust calculations.

60

2.10. Dynamic Thrust Estimation

Dynamic thrust estimation of a fixed pitch propeller – electric motor system is very important to determine reliable aircraft performance results. In this section, electric motor and fixed pitch propeller combination is chosen and dynamic thrust results of the propulsion system is determined by wind tunnel experiment. Results are used to determine and validate dynamic thrust estimation model presented in the study in order to estimate high altitude thrust and power available.

Dynamic thrust of a propeller decreases with increasing velocity since relative angle of attack decreases due to increasing forward flight velocity component. Therefore, propeller efficiency η_{pr} varies with velocity, which is maximized at the best design speed - RPM ratio (V/n). In more detail, propeller efficiency η_{pr} is expressed as a function of the advance ratio (J) which includes freestream velocity (V_∞), propeller revolution per second (rps) (N) and propeller diameter (D). Advance ratio is given by **Eqn. (2.57)** and **Figure 2.37** shows the variation of the propeller efficiency with respect to the advance ratio for various pitch angles.

$$J = \frac{V_\infty}{ND} \qquad (2.57)$$
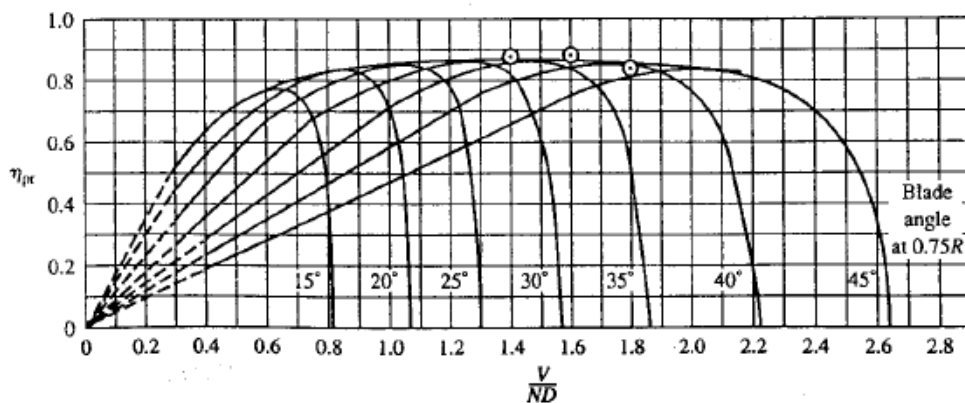
Figure 2.37. Propeller Efficiency vs. Advance Ratio for Various Pitch Angles [20]

As can be seen from **Figure 2.37**, propeller efficiency can be maximized by changing the blade angle for variable-pitch propellers. However, maximum propeller efficiency, corresponding advance ratio and consequently flight velocity varies for

different fixed-pitch propellers. Therefore, propeller efficiency cannot be assumed as a constant for fixed-pitch propellers.

It should be noted that, propeller efficiency is also related with aerodynamic characteristics, i.e. lift and drag coefficients of the airfoil used in the propeller blade which is related with Reynolds number. Lift and drag coefficients decrease with decreasing Reynolds number for increasing altitude due to air density and viscosity change. Therefore, propeller efficiency is also decrease and propeller pitch should be increased with altitude in order to maintain best efficiency. Thus, propellers with different pitch should be used for different operation altitudes. However, only performance variation of the selected propeller is determined for aircraft performance calculations. Since maximum speed requirement is not the primary requirement, low-pitch propeller and proper electric motor is chosen for the design. Propellers with different pitch or diameter are not studied in this work.

2.10.1. Electric Motor and Propeller Selection

Propeller thrust gradually decreases and propeller efficiency changes with forward flight velocity. Additionally, maximum forward velocity achievable which is called as pitch speed is different for each propeller having different pitch. Therefore selecting the propeller-motor combination is performed by trial and error. Selecting the propulsion system requires some experience on drive systems.

Literature research and numerical experiments on propeller and drive system calculators is performed and EMAX – GT 2218/11 motor is chosen for the low energy consumption and sufficient thrust generation with the recommended propeller [22], [23], [24]. **Figure 2.38** shows the selected EMAX – GT2218/11 brushless out-runner motor.

Figure 2.38. EMAX – GT2218/11 Brushless Out-Runner Motor

Performance data of the selected motor with the recommended propellers is given in **Table 2.29** [22].

Table 2.29. EMAX – GT2218/11 Performance with Recommended Propellers [22]

Model	Cell Count	RPM/V	Prop (APC)	RPM	Max Current (<60S)	Thrust
GT2218/11	3S	930	11x4.7	7000	17A	1120 gr
	3S	930	12x6	6700	18A	1150 gr

Based on the data provided in **Table 2.29**, APC – Slow Flyer – 11x4.7 propeller is chosen for low maximum current requirement. Experimental propeller performance data is taken from reference [21] and given in **Appendix E**. Maximum propeller efficiency η_{pr}, max is given as 0.648. Selected propeller and propeller efficiency versus advance ratio plot at different RPMs are shown in **Figure 2.39**.
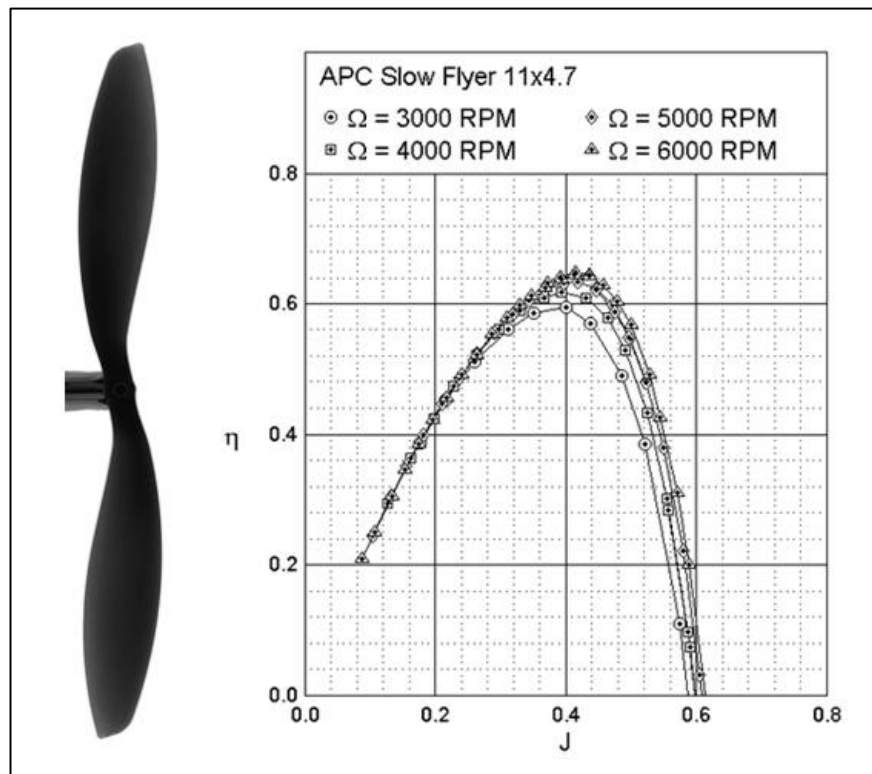
Figure 2.39. APC Slow Flyer 11x4.7 Propeller and η_{pr} vs. J plot

2.10.2. Dynamic Thrust Experiment

In order to determine the performance of the motor-propeller combination and verify dynamic thrust model explained in following section, dynamic thrust experiment is conducted in a low speed, continuous flow blower type wind tunnel located in METU Aerospace Engineering Department Hangar Facilities which is shown in **Figure 2.40**.

Figure 2.40. METU Aerospace Engineering Dept. Low Speed Wind Tunnel

Motor is mounted on a 6-axis load cell (ATI F/T Sensor: Gamma [25]) in order to measure the thrust force and the propeller torque. Load cell power is supplied by DC – Power supply and data is gathered by the National Instruments, NI-USB-6211 data acquisition system and LabVIEW Software specialized by ATI Sensors [26]. Setup components are given and identified by letters in **Table 2.30.**

Table 2.30. Experimental Setup Components

A	APC – Slow Flyer – 11x4.7 Propeller	**F**	40 A - ESC
B	EMAX – GT2218/11 Motor	**G**	DC – Power Supply (11.1 V)
C	ATI F/T Sensor: Gamma Load Cell	**H**	Computer
D	RPM Sensor	**I**	2.4 GHz Transmitter
E	Test Mount	**J**	2.4 GHz Receiver

Experimental setup components are shown in **Figure 2.41** and **Figure 2.42** shows the experimental setup placed in the wind tunnel.

Figure 2.41. Experimental Setup
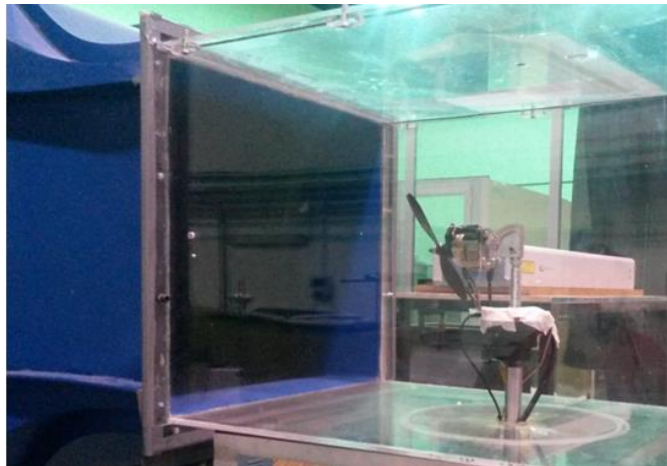
Figure 2.42. Experimental Setup Placed in the Wind Tunnel

Dynamic thrust experiment is performed for flow speeds ranging from 2.2 m/s to 17.6 m/s at the maximum throttle condition and at **930m** (AMSL) altitude. Static thrust (V=0) test is performed before the wind tunnel experiment and results are presented in the dynamic thrust result table given in **Table 2.31.** Thrust and torque data are gathered from load cell measurements. Power, power available and propeller efficiency data are calculated from,

$$P = 2\pi \cdot n \cdot Q, \qquad P_A = T \cdot V, \qquad \eta_{pr} = P_A/P \tag{2.58}$$

65

Table 2.31. Experimental and Calculated Results

	\	\	\	\	\		\	\	\
	Experimental Results						**Calculated Results**		
	V (m/s)	**T (N)**	**Q (N.m)**	**n (RPM)**	**I (Amp)**		**P (Watt)**	**P_A (Watt)**	**η_{pr}**
Static	**0**	**9.891**	**0.164**	**6970**	**15.80**		**120.00**	**0**	**0**
Dynamic Thrust	2.22	9.142	0.158	6972	15.13		115.43	20.30	0.176
	3.09	8.785	0.156	6977	14.80		113.69	27.14	0.239
	5.51	7.729	0.148	7003	14.23		108.75	42.58	0.392
	7.75	6.745	0.143	7055	13.80		105.94	52.27	0.493
	9.94	5.756	0.138	7152	13.30		103.06	57.21	0.555
	11.83	4.798	0.131	7281	12.70		100.11	56.76	0.567
	13.60	3.888	0.125	7419	12.14		96.73	52.88	0.547
	15.00	3.031	0.119	7553	11.64		93.81	45.46	0.485
	16.15	2.288	0.114	7669	11.20		91.63	36.95	0.403
	17.07	1.724	0.111	7755	10.88		89.98	29.42	0.327

Measured dynamic thrust and calculated power available data with respect to velocity are given together in **Figure 2.43**. As mentioned, power available varies with velocity. Propeller efficiency is calculated from dynamic thrust and power available data and shown in **Figure 2.44**. As expected, maximum propeller efficiency is smaller than reference data which is obtained at lower altitude [21]. Measured RPM, shaft power and current plots are given in **Figure 2.45**, **Figure 2.46** and **Figure 2.47** respectively. According to the experimental results, maximum shaft power is **120 W**, maximum static thrust is **9.89 N** and maximum draining current is **15.8 Amp** which approximately matches with the manufacturer data given in **Table 2.29.**
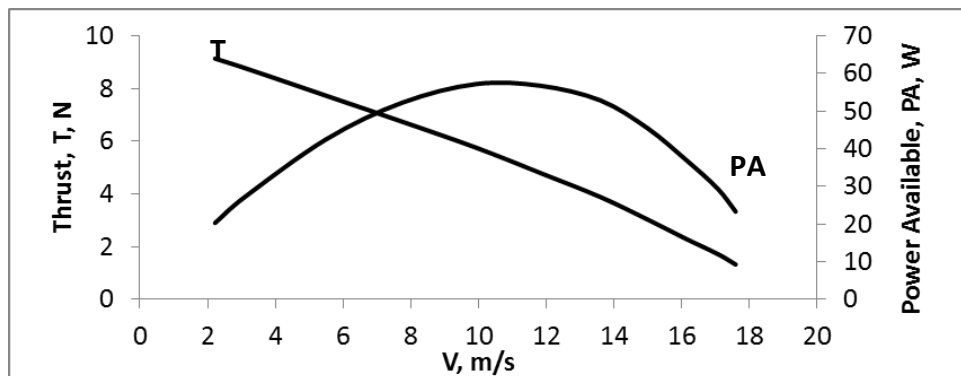
Figure 2.43. Dynamic Thrust and Power Available vs. Velocity
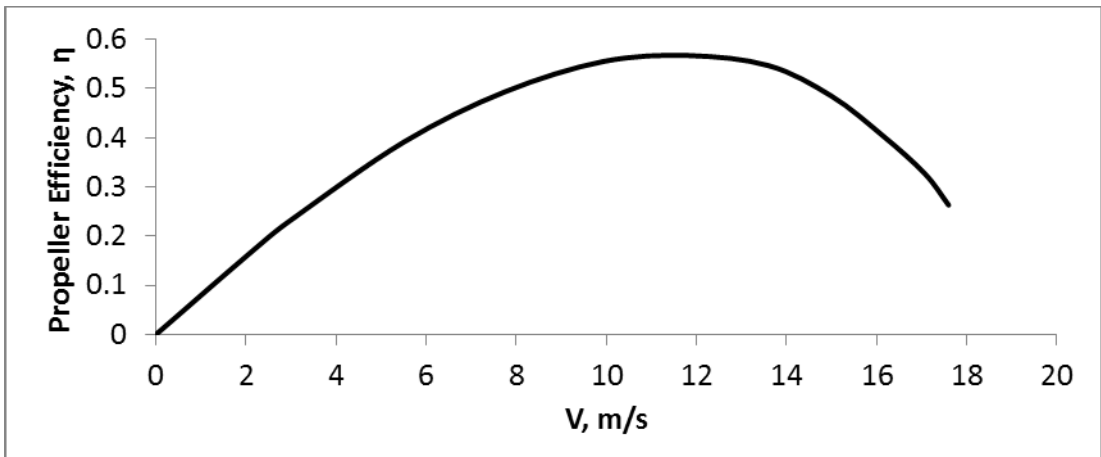
Figure 2.44. Propeller Efficiency vs. Velocity
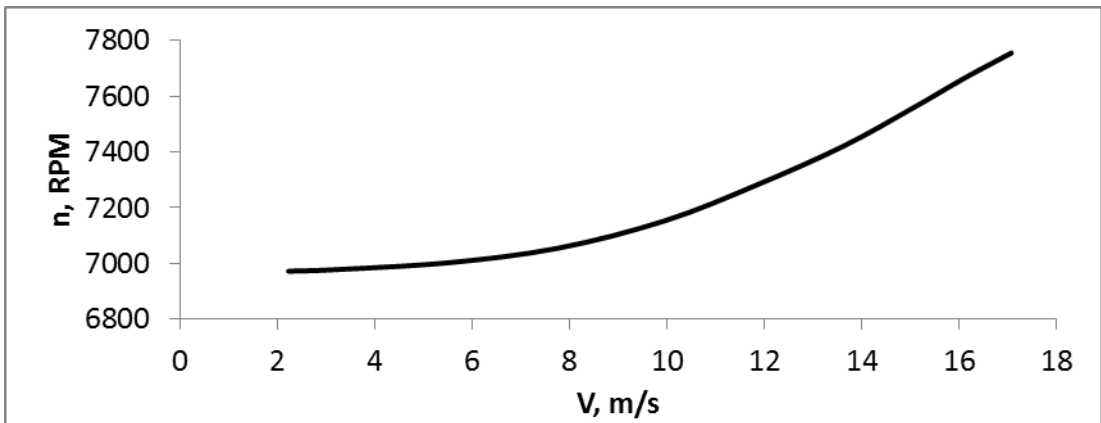
Figure 2.45. Propeller RPM vs. Velocity
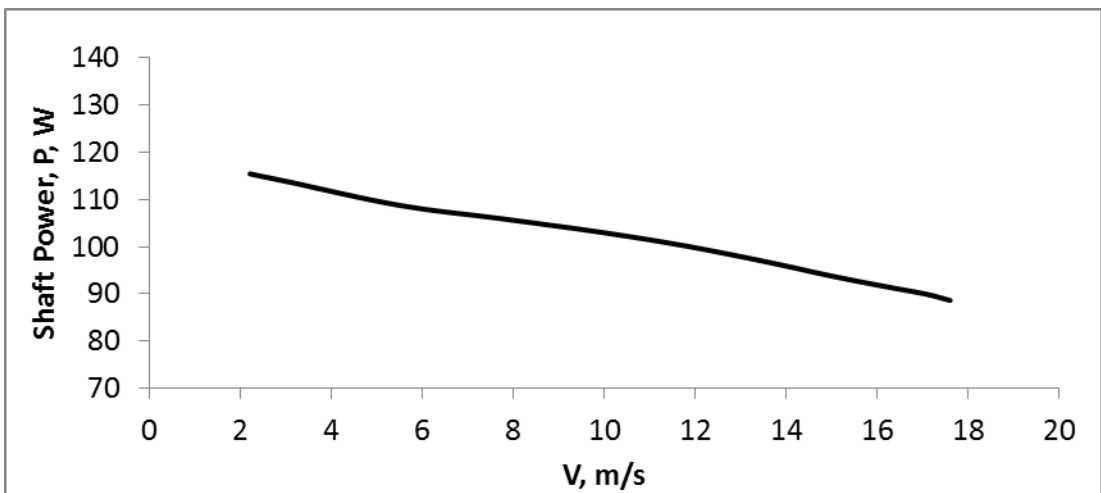
Figure 2.46. Shaft Power vs. Velocity
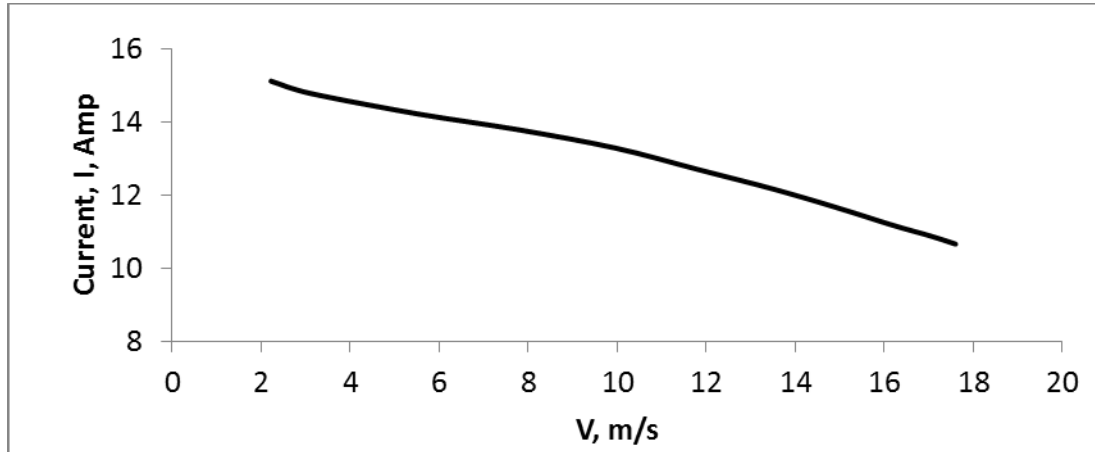
Figure 2.47. Draining Current vs. Velocity

RPM vs. shaft power and RPM vs. draining current relations can also be determined from experimental results. However, dynamic thrust estimation model given in the following section is only focused on the dynamic thrust and power available variation with respect to flight velocity. Therefore it should be noted that actual RPM value is not decisive in the model but increment of the RPM is considered in calculations.

2.10.3. Dynamic Thrust Estimation Model

In this section, dynamic thrust estimation model is presented as a contribution of the study. As mentioned, presented model is focused on the dynamic thrust and power available results calculated from propeller performance data which can be determined from manufacturer or an experimental study. In this study experimental propeller performance data is used [21] and standard definitions of propeller aerodynamic coefficients given in **Eqn. (2.59)** [27] are used to determine dynamic thrust and power available results.

$$J = \frac{V}{nD}, \qquad C_T = \frac{T}{\rho n^2 D^4}, \qquad C_P = \frac{P}{\rho n^3 D^5}, \qquad \eta_{pr} = \frac{TV}{P} = \frac{C_T J}{C_P} \quad \textbf{(2.59)}$$

Main point of the model is utilizing the propeller performance data in order to calculate reference altitude (sea level) results and adding power correction factor (PcF) and altitude correction factors (AF) for high altitude calculations. Since performance data of the propeller obtained from reference [21] is low altitude

68

experimental data, dynamic thrust calculations performed for higher altitudes are needed to be corrected by using these correction factors.

Experimental propeller performance data is taken from [21] and first 5 rows of the data are given in **Table 2.32**. Complete data table is provided in **Appendix E**. Advance ratio vs. propeller efficiency plot of the performance data was given in **Figure 2.39.**

<p align="center">Table 2.32. APC-SF-11x4.7, Experimental Performance Data [21]</p>

J	C_T	C_P	η_{pr}
0.087	0.1151	0.0482	0.209
0.107	0.112	0.0477	0.250
0.133	0.1071	0.0468	0.305
0.155	0.1033	0.0461	0.346
0.175	0.0996	0.0454	0.385
...	...	...	...

Determination of the dynamic thrust with respect to altitude involves multi-variable and coupled relations. Propeller efficiency η_{pr} is determined from the thrust generated and power available at any speed. Thrust and aerodynamic power of the propeller are also related to the propeller revolution and the diameter. Although propeller diameter is constant, propeller RPM varies with the density and with the forward flight velocity due to the variation of the aerodynamic torque. Electric motor efficiency also varies with the number of revolution, draining current, operating temperature, battery voltage and discharge rate. There are many dependent variables to obtain a direct analytical relation of dynamic thrust for various altitudes, and this is not within the scope of the thesis. Detailed experimental studies at various altitudes are suggested to investigate propulsive efficiency of the motor and the fixed-pitch propeller combinations for the maximum throttle condition. In the present study, dynamic thrust calculation for fixed-pitch propeller is performed for the reference altitude and an approximation method is presented to estimate dynamic thrust results for higher altitudes.

Propeller aerodynamic coefficients given in **Eqn. (2.59)** are rewritten as follows,

$$nD = \frac{V}{J}, \qquad C_T = \frac{T}{\rho(nD)^2 D^2}, \qquad C_P = \frac{P}{\rho(nD)^3 D^2} \qquad \textbf{(2.60)}$$

From the power coefficient ($\boldsymbol{C_P}$) expression,

$$P = C_P \rho (nD)^3 D^2$$

$$P = C_P \rho \left(\frac{V}{J}\right)^3 D^2 \qquad \textbf{(2.61)}$$

where P is the maximum mechanical power (shaft power) generated by the electric motor. As can be seen from RPM vs. Velocity plot and Shaft Power vs. Velocity plot given in **Figure 2.45** and **Figure 2.46**, shaft power decreases with RPM. In order to represent the shaft power decrease of the electric motor due to RPM increase, relation between RPM and shaft power is expressed with a power correction factor (PcF).

As a starting point, maximum power is assumed constant as 120 W. Hence, initial estimation for forward flight velocities at the reference altitude can be determined for each $J - C_P$ data given in **Table 2.32**.**Eqn. (2.61)** can be solved for velocity as,

$$V_{init} = \left(\frac{P_0 J^3}{C_P \rho D^2}\right)^{1/3} \qquad \textbf{(2.62)}$$

By substituting **Eqn. (2.62)** into the advance ratio equation, initial estimation of the propeller rps is calculated for each of the initial flight velocity at the reference altitude.

$$n_{init} = \frac{\left(\frac{P_0 J^3}{C_P \rho D^2}\right)^{1/3}}{JD} \qquad \textbf{(2.63)}$$

Corrected dynamic shaft power can be calculated using the initial number of revolution ratio and hypothetical Power correction Factor (**PcF**), which can be taken as a number around 3, since power is related to the third power of the propeller rps. In the present study, **Eqn. (2.64)** is proposed as the corrected dynamic shaft power relation.

Calculation results are given in **Table 2.33** and **Figure 2.48** for **PcF=2.7** value for the selected motor – propeller combination which is determined by trial and error for this study.

$$P_c = P_0 \left(\frac{n_0}{n}\right)^{PcF}$$ **(2.64)**

Table 2.33. Corrected Shaft Power Calculations

Po	V,init	n,init	Pc
120	2.58	106.08 (n_0)	120.00
120	3.18	106.45	118.88
120	3.98	107.12	116.86
120	4.66	107.66	115.28
120	5.29	108.21	113.71
120	5.98	108.70	112.35
...	...	...	...
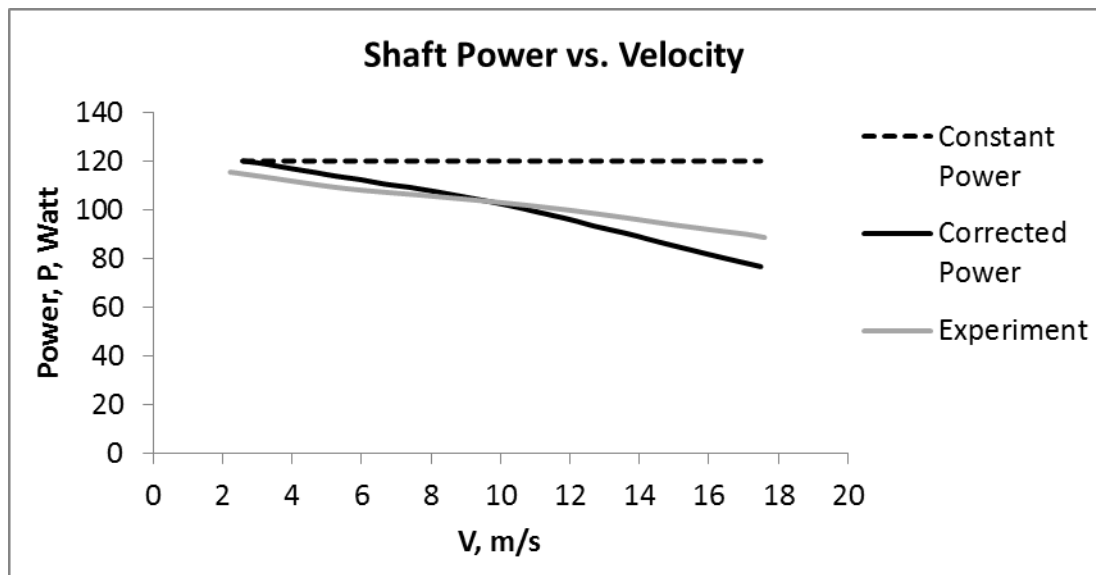
Figure 2.48. Constant and Corrected Shaft Power vs. Velocity

PcF adjusts shaft power at higher flight speeds where rotational speed of the propeller is increased due to propeller torque decrease. By this way, pitch speed of the propeller is decreased. Graphically, PcF has a rotation effect on the dynamic thrust curve in clockwise direction as shown in **Figure 2.49.**
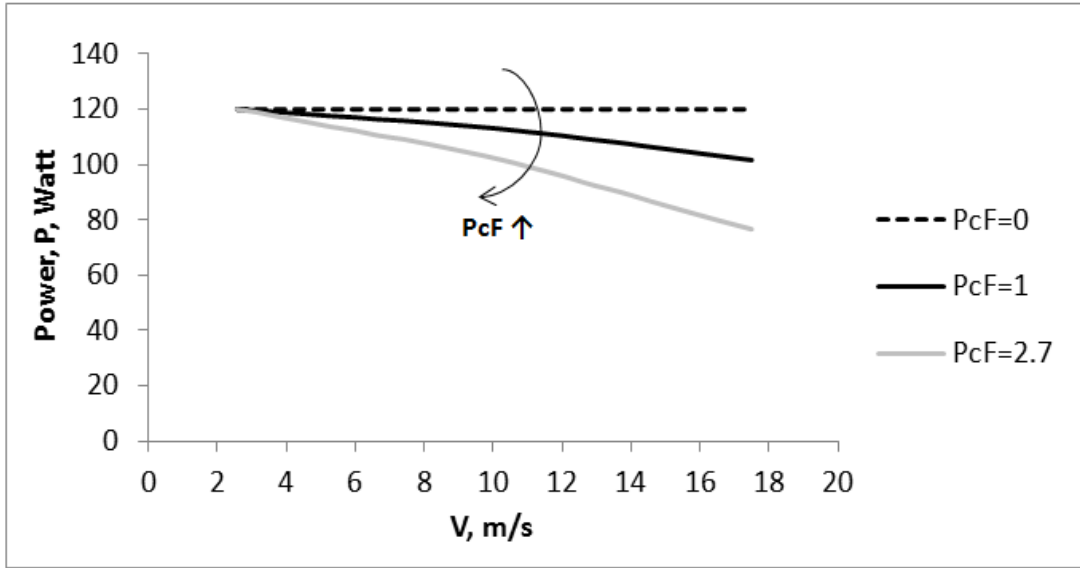
Figure 2.49. Effect of Power Correction Factor on Shaft Power

By using the corrected shaft power, forward flight velocity and propeller rps can be calculated as follows.

$$V = \left(\frac{P_c J^3}{C_P \rho D^2} \right)^{1/3} \tag{2.65}$$

$$n = \frac{\left(\frac{P_c J^3}{C_P \rho D^2} \right)^{1/3}}{JD} \tag{2.66}$$

From the thrust coefficient relation (C_T) given by **Eqn. (2.59)**, dynamic thrust can be calculated for each flight velocity and corresponding rotational speed as,

$$T = C_T \rho n^2 D^4 \tag{2.67}$$

As given in **Eqn.(2.67)**, thrust is directly proportional to the air density for constant rotational speed. However, at higher altitudes, rotational speed of the propeller increases due to the torque decrement of the propeller since Reynolds number and consequently drag coefficient of the propeller decreases with increasing altitude. As a result thrust generated is amplified and propulsive efficiency is also affected due to the change in the rotational speed of the motor, as mentioned before. In order to estimate the dynamic thrust generated at high altitude, density ratio between the

target altitude and the reference altitude should be used by taking the thrust amplification into account.

In the present study, another hypothetical parameter "Altitude Factor for Propulsive Efficiency (AF_η)" is proposed to estimate the thrust ratio between the target altitude and the reference altitude. Altitude Factor for Propulsive Efficiency is defined by Eqns. **(2.68)** and **(2.69)** and it is given by the air density ratio raised to power AF which is less than 1.

$$\frac{T}{T_0} = \frac{P_A}{P_{A,0}} = \left(\frac{\rho}{\rho_0}\right)^{AF} \tag{2.68}$$

$$AF_\eta = \left(\frac{\rho}{\rho_0}\right)^{AF} \tag{2.69}$$

As can be seen from **Eqn. (2.68),** altitude factor AF_η is analogous with the altitude variation approximation for turboprop engines for which propulsive power is mainly generated by the propeller [15]. "**AF**" factor can be related with diameter, pitch angle of the propeller and airfoil characteristics of the propeller blade which are directly related with the propeller performance.

Up to this point, definitions and effects of the correction factors are given. Complete model of the dynamic thrust estimation model proposed in the study is shown in **Figure 2.50.** Firstly corrected dynamic thrust and power available calculations are performed for the reference altitude and then higher altitude results are determined by using the Altitude Factor.
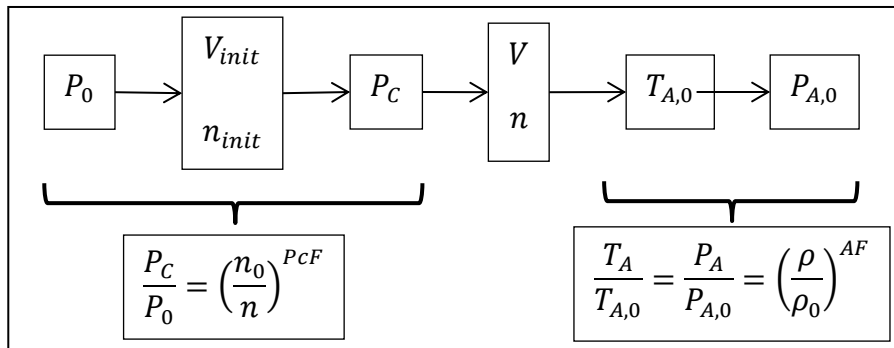
Figure 2.50. Dynamic Thrust Estimation Model

As mentioned before, Power Correction Factor **PcF** and Thrust Amplification Factor (Altitude Factor) **AF** parameters are hypothetical parameters, which are "Motor Performance and Design Unknown" and "Propeller Performance and Design Unknown". Altitude Factor (AF) corrects maximum thrust value for higher altitudes with respect to reference altitude and Power Correction Factor (PcF) corrects maximum pitch speed value by reducing power at higher speeds (**Eqn. (2.65)**). Effect of these correction parameters on thrust curve are shown in **Figure 2.51**.
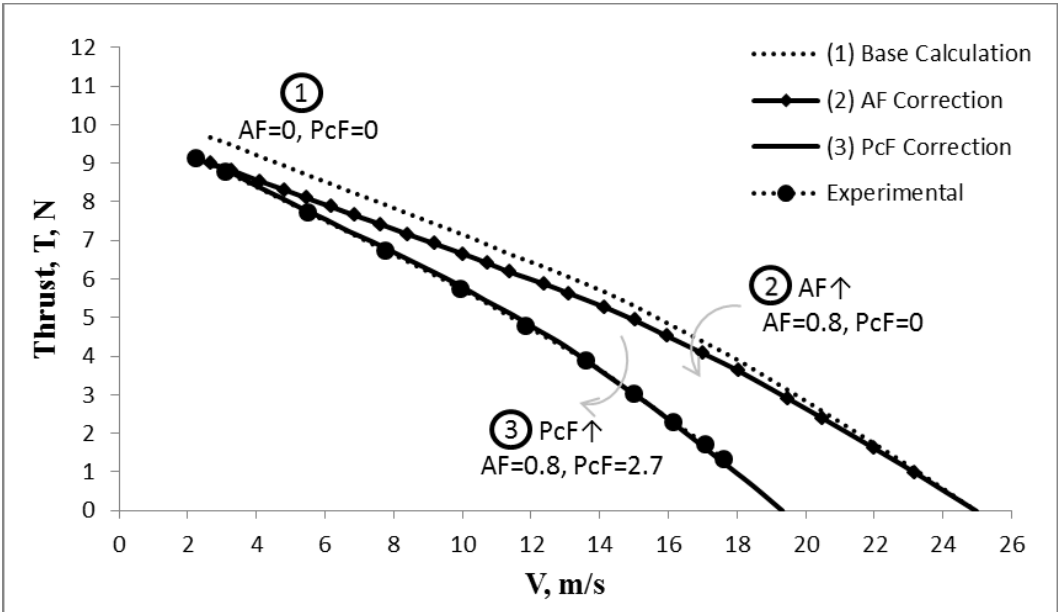
Figure 2.51. Effects of AF and PcF parameters on Dynamic Thrust Curve

As can be seen from the dynamic thrust curves given in **Figure 2.51**, firstly AF and PcF parameters are set to zero as a starting point, then AF parameter is applied for maximum thrust correction and then PcF parameter is applied for maximum pitch speed correction. Correction factor values are found by trial and error for the present design. **AF** parameter is set to **0.8** and **PcF** parameter is set to **2.7** in order to meet the estimated dynamic thrust and power available curves with experimental results performed at 930 m (AMSL) altitude.

Final dynamic thrust and power available versus speed curves are shown in **Figure 2.52** and **Figure 2.53** respectively. Uncorrected results of thrust and power available calculations are also shown for comparison. For uncorrected case PcF is set to **0** for constant maximum power assumption as shown in **Figure 2.49** and AF is set to **1** for direct analytic solution calculated from **Eqn.(2.67)**. As mentioned pitch speed calculation is quite high and shaft power is not decreased with velocity and RPM increase for uncorrected case. As a result, thrust available, power available and pitch speed results are found illusively high for uncorrected calculations. However, corrected results of the dynamic thrust estimation model fit with experimental results almost perfectly.
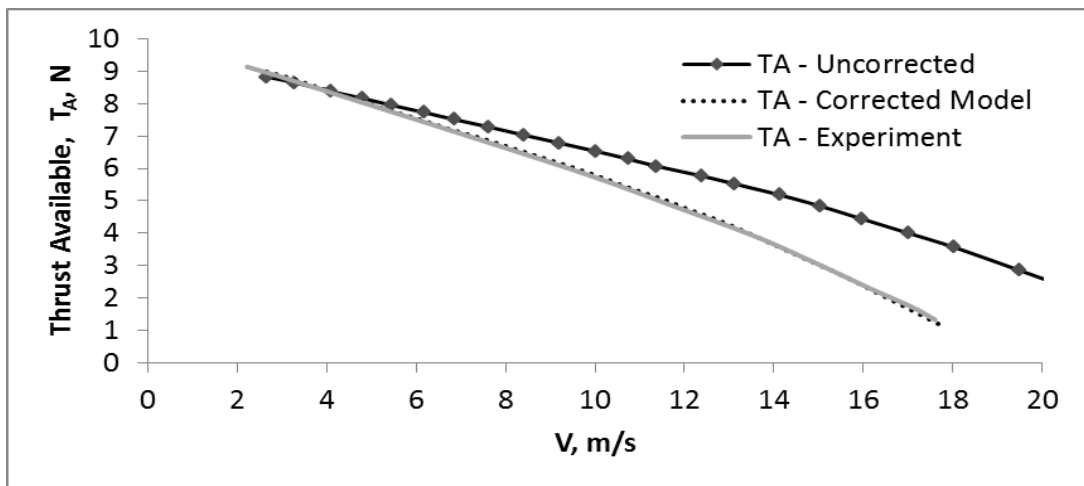
Figure 2.52. Dynamic Thrust Model and Experimental Thrust Results
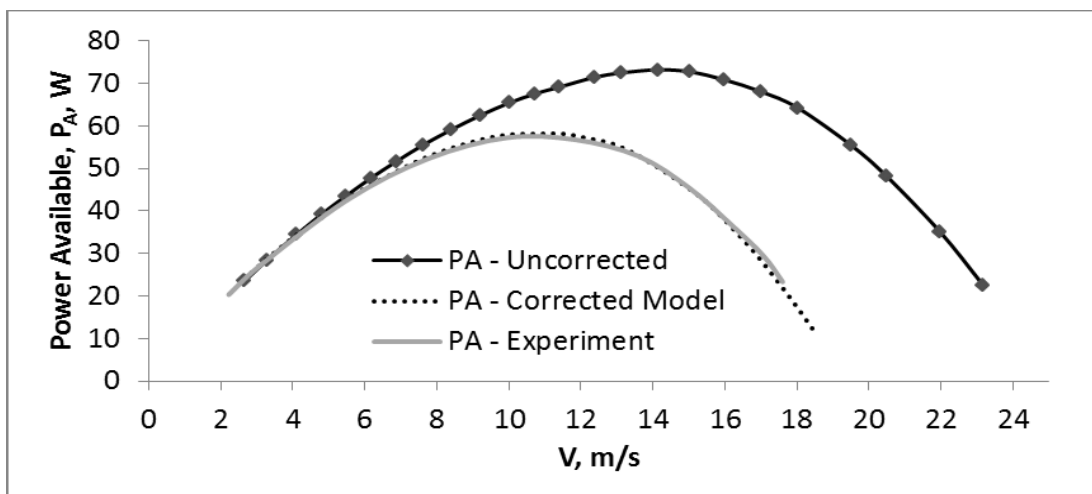
Figure 2.53. Power Available Curves of Experimental and Dynamic Thrust Model

75

2.10.4. Dynamic Thrust Variation with Altitude

Dynamic thrusts at different altitudes are calculated from **Eqn. (2.70)** and results are presented in **Figure 2.54.**

$$T_A = T_{A,0} \cdot AF_\eta = T_{A,0} \cdot \left(\frac{\rho}{\rho_0}\right)^{0.8} \qquad (2.70)$$
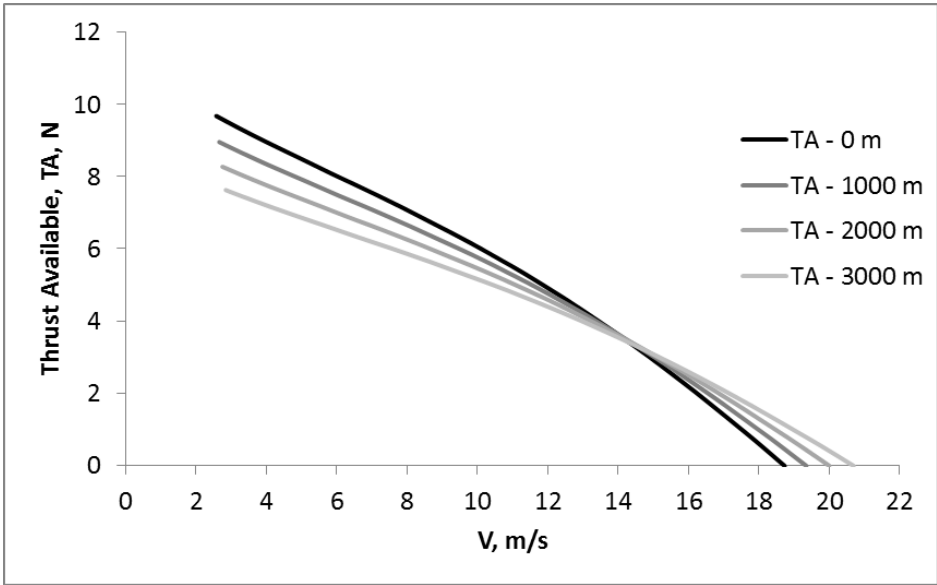
Figure 2.54. Dynamic Thrust at Various Altitudes

Increase behavior in RPM with velocity and altitude drives the dynamic thrust estimation model. As mentioned before, actual RPM values are not interested at this point but the behavior of the increment is. Firstly, RPM of the propeller at the reference altitude is calculated from **Eqn. (2.63)** then rotational speeds at high altitudes are obtained from **Eqn. (2.67)** by using the approximated dynamic thrust values. Results are given in **Figure 2.55.**
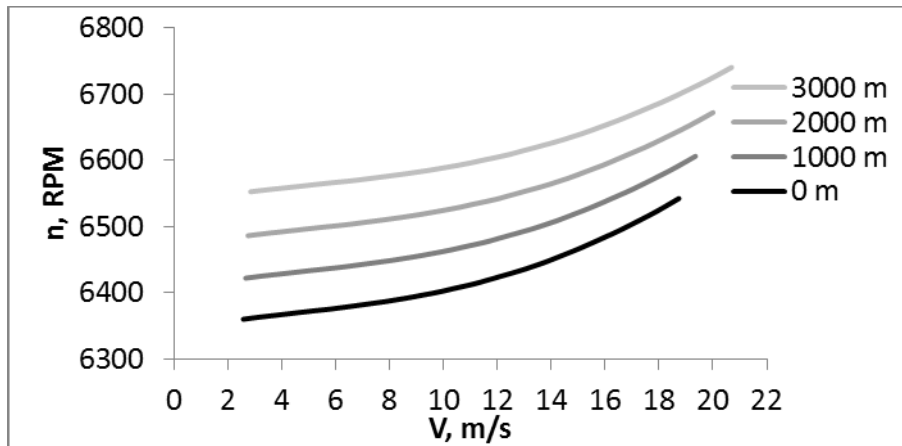
Figure 2.55. Rotational Speed of the Propeller vs. Velocity at Various Altitudes

Power available and corresponding propeller efficiencies are also calculated using the dynamic thrust approximations, as given in **Eqn. (2.71)**. Propeller efficiencies, given by **Eqn. (2.72)**, are then used to determine "P/W" curves in the constraint diagram at velocities specified in constraint analysis.

$$P_A = \eta_{pr}P = T_A V \tag{2.71}$$

$$\eta_{pr} = \frac{P_A}{P} \tag{2.72}$$

$$P = \frac{P_A}{\eta_{pr}} \tag{2.73}$$

Power available and propeller efficiency vs. velocity plots are given in **Figure 2.56** and **Figure 2.57** at various altitudes. These plots allow one to use more realistic available power and propeller efficiency values which in reality change with the altitude as opposed to using single power available and propeller efficiency curves which what is commonly practiced.
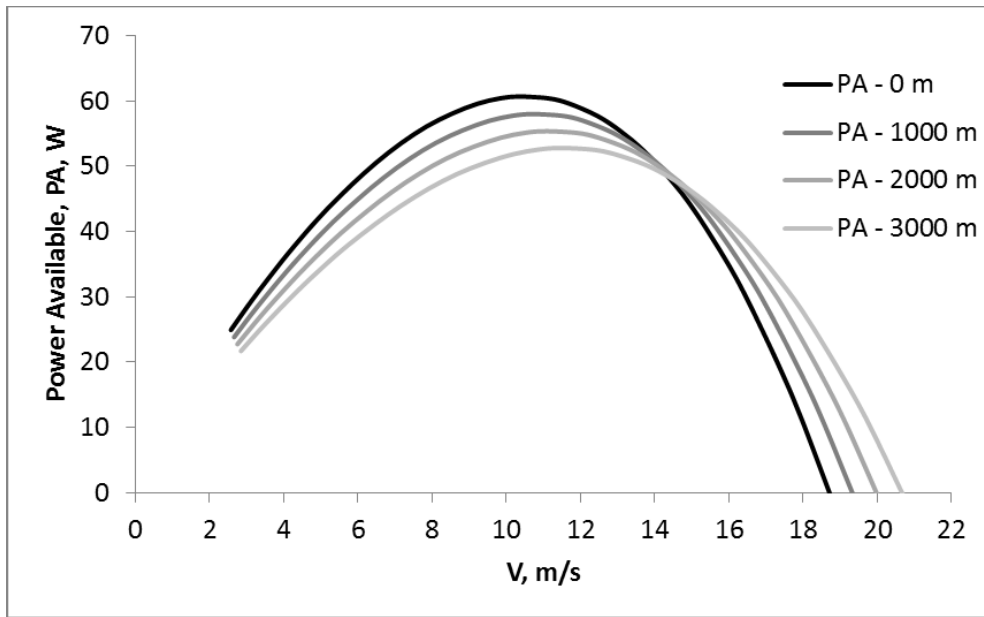
Figure 2.56. Power Available vs. Velocity for Various Altitudes
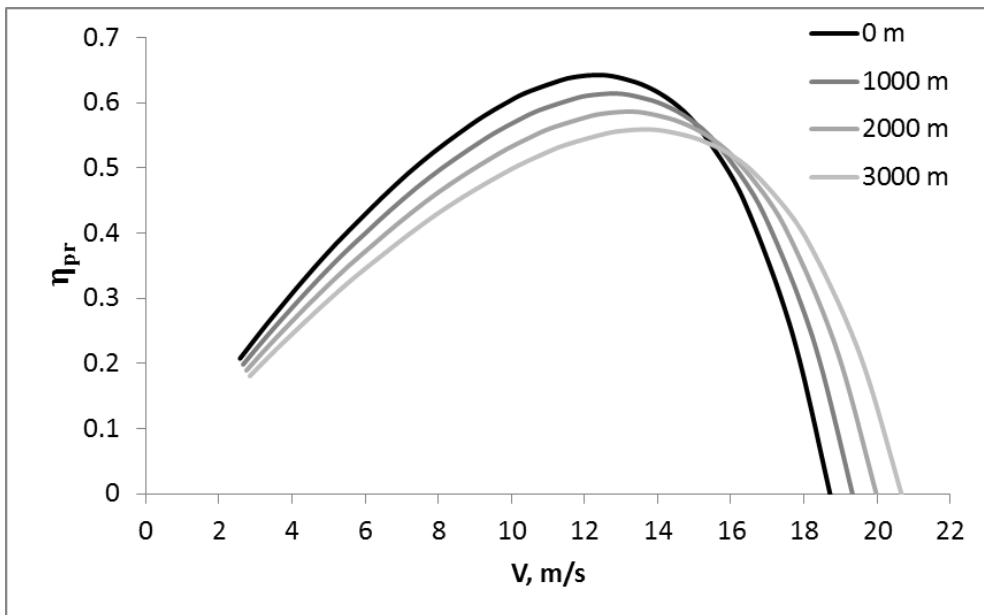
Figure 2.57. Propeller Efficiency vs. Velocity for Various Altitudes

2.11. Constraint Analysis (W/S vs P/W)

Propeller efficiency, thrust available and power available curves are determined for each flight velocity and flight altitude in the previous section. **P$_A$/W** curves given in **Figure 2.36** are converted to **P/W** by dividing with the corresponding propeller efficiencies at specified flight velocities determined from propeller efficiency curves given in **Figure 2.58.**

$$\frac{P}{W} = \frac{1}{\eta_{pr}} \frac{P_A}{W} \quad\quad\quad (2.74)$$
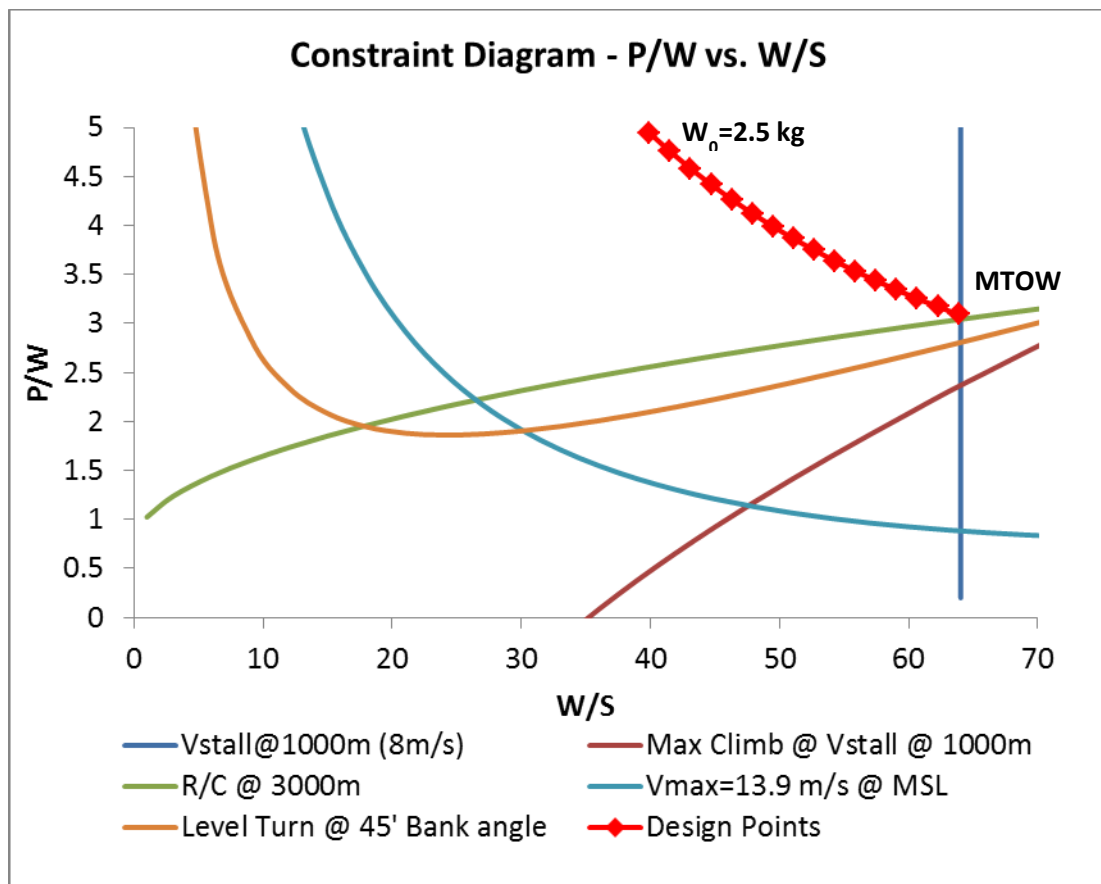
Figure 2.58. Constraint Diagram for P/W

Power to Weight Ratio (**P/W**) with selected motor-propeller combination is **3.06** W/N and Thrust to Weight Ratio (**T/W**) at maximum static thrust is **0.28**.

$$\frac{P}{W} = \frac{120\ W}{39.24\ N} = 3.06\ W/N, \quad\quad \frac{T}{W} = \frac{1.12\ kg}{4\ kg} = 0.28$$

2.12. Aircraft Performance Analysis

Aircraft performance analysis is performed by using the standard performance equations referenced from Anderson [15] and Raymer [18].In classical performance analysis of a propeller-driven aircraft, performance equations are derived for constant power available assumption, where propeller efficiency is constant due to constant speed – variable pitch propeller assumptions. However, for a fixed-pitch propeller driven aircraft, such assumptions are not applicable since propeller efficiency varies with speed and altitude. Thus, direct analytical approaches leads to incorrect results and graphical approach is suggested to determine the performance parameters for a fixed-pitch propeller driven aircraft.

2.12.1. Aircraft Performance Parameters (T_R, P_R, T_A, P_A) and Critical Velocities

Thrust required, which is equal to the drag of the aircraft, is calculated by,

$$T_R = D = \frac{1}{2}\rho_\infty V_\infty^2 S C_D \tag{2.75}$$

where drag coefficient which is given in **Eqn. (2.37)** is recalled.

$$C_D = 0.01457 + 0.04102(C_L - 0.43)^2$$

Thrust available curves are determined in **Section 2.10.3** by using **Eqn. (2.70)**.

$$T_A = T_{A,0} \cdot AF_\eta = T_{A,0} \cdot \left(\frac{\rho}{\rho_0}\right)^{0.8}$$

Power required and power available are calculated by,

$$P_R = T_R V_\infty = D V_\infty \tag{2.76}$$

$$P_A = T_A V_\infty \tag{2.71}$$

Dynamic thrust and power curves for design altitude boundaries are shown in **Figure 2.59** and **Figure 2.60** with critical design velocities. As calculated before and summarized in **Table 2.26** in **Section 2.8.6**, cruise velocities are **11.7 m/s** at sea level and **13.6 m/s** at 3000 m design altitudes where thrust required values are minimum. Similarly, loiter speeds are **10.4 m/s** at sea level and **12 m/s** at 3000 m design altitudes where power required values are minimum. Attainable maximum velocities are **16.2** m/s and **17.6** m/s for sea level and 3000 m design altitudes, respectively.
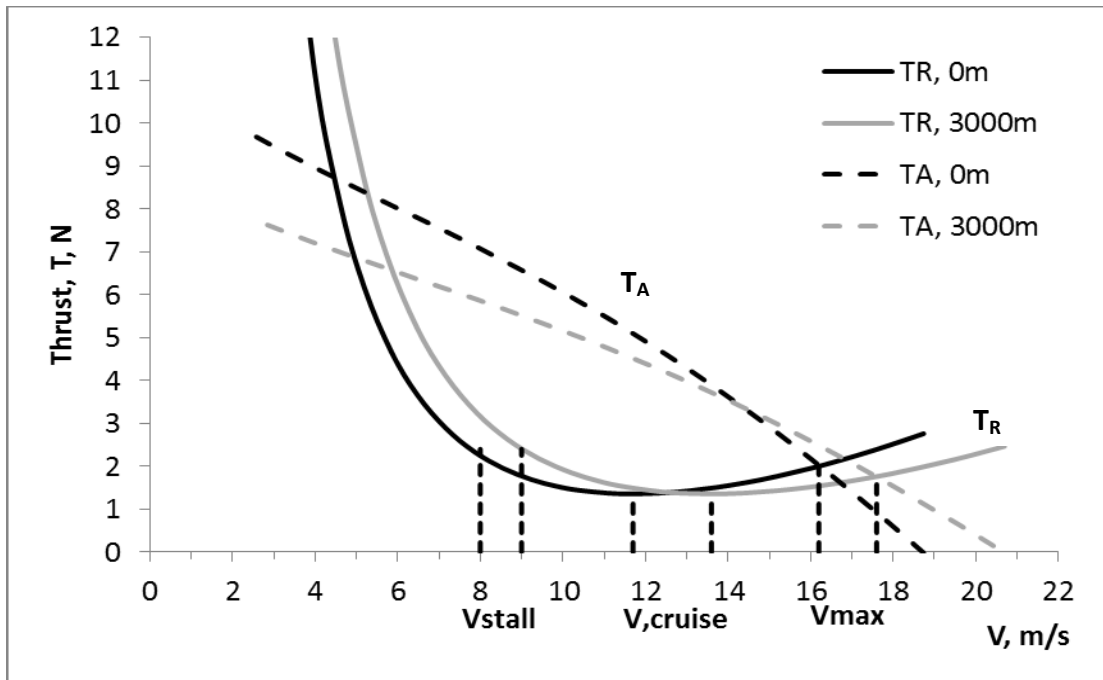
Figure 2.59. Drag (T_R) and Thrust Available Curves
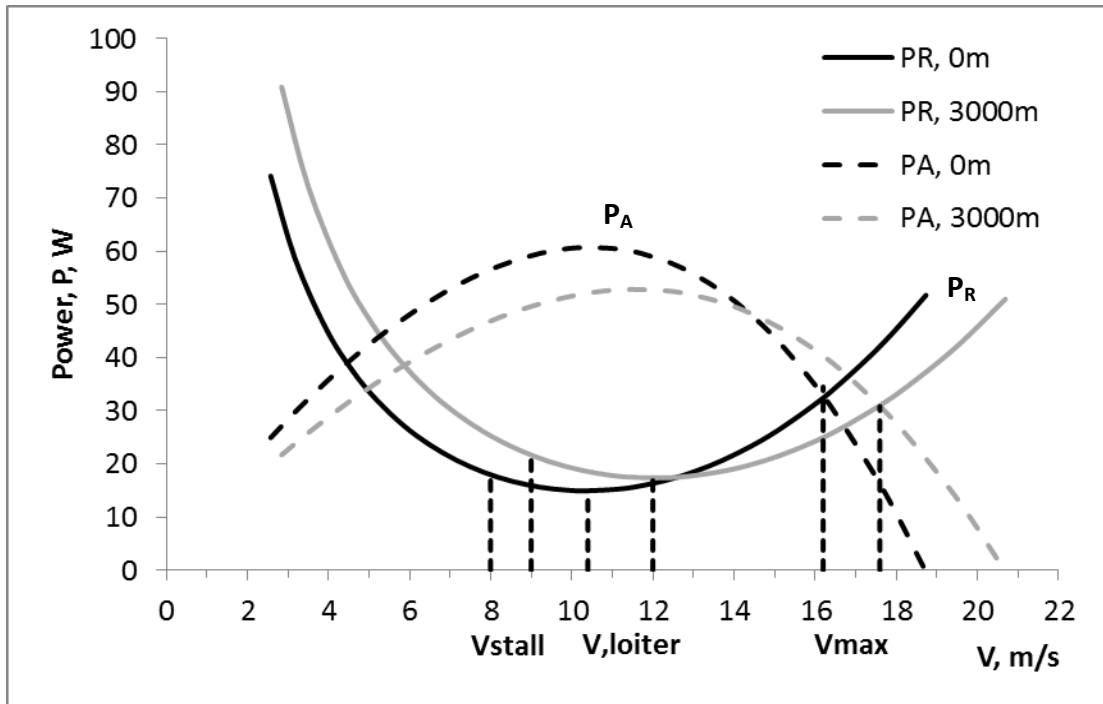
Figure 2.60. Power Required and Power Available Curves

$$\begin{pmatrix} V_{loiter}@\,0m = 10.4\,m/s & , & V_{loiter}@\,3000m = 12.0\,m/s \\ V_{cruise}@\,0m = 11.7\,m/s & , & V_{cruise}@\,3000m = 13.6\,m/s \\ V_{max}@\,0m = 16.2\,m/s & , & V_{max}@\,3000m = 17.6\,m/s \end{pmatrix}$$

2.12.2. Climb Performance

Climb performance parameters are determined in this section. Main climb parameters are maximum rate of climb, maximum rate of climb velocity, climb angle, ceiling and time to climb. Rate of climb is calculated utilizing excess power.

$$R/C = \frac{excess\ power}{W} = \frac{\Delta P}{W} = \frac{P_A - P_R}{W} \tag{2.77}$$

For a propeller-driven aircraft, excess power and rate of climb are maximized at the minimum power required for constant power available assumption and theoretical maximum rate of climb velocity is calculated by **Eqn. (2.78)**.

$$V_{(R/C)max}, theo = \left(\frac{2}{\rho_\infty} \sqrt{\frac{K}{3C_{D0}} \frac{W}{S}} \right)^{1/2} \tag{2.78}$$

However, excess power may not be maximized at minimum power required velocity for constant pitch propeller. As shown in **Figure 2.61**, minimum power required velocity, i.e. theoretical maximum rate of climb velocity and actual maximum rate of climb velocity are slightly different from other. Nevertheless, this result verifies that propulsion system choice is quite sufficient for the design.
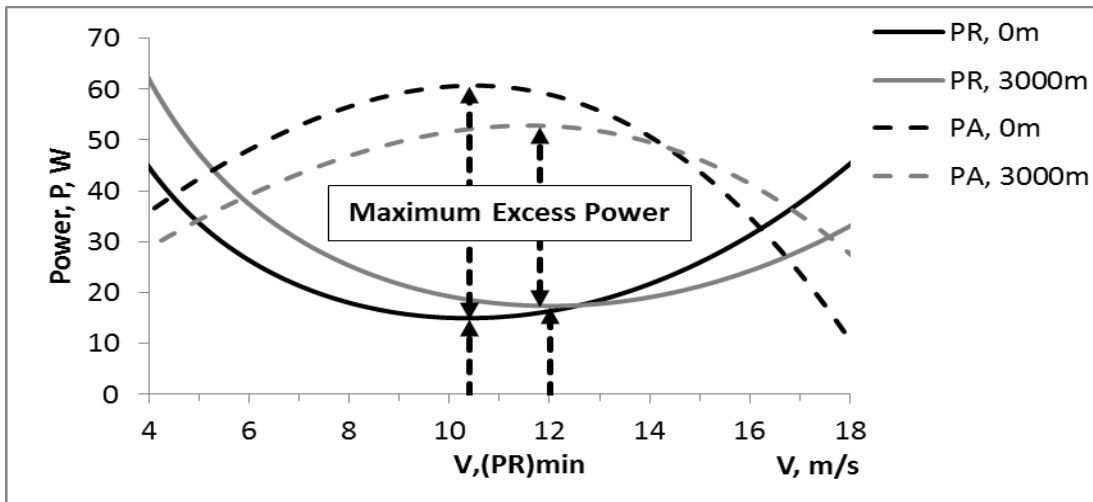
Figure 2.61. $(P_R)_{min}$ and $(R/C)_{max}$ Velocities

$$\begin{pmatrix} V_{(R/C)max}@\ 0m = 10.4\ m/s & , & V_{(R/C)max}@\ 3000m = 11.8\ m/s \\ V_{PR,min}@\ 0m = 10.4\ m/s & , & V_{PR,min}@\ 3000m = 12.0\ m/s \end{pmatrix}$$

Difference between theoretical and actual rate of climb velocities might be much higher if different propeller were chosen. Therefore graphical approach is needed to determine actual maximum rate of climb velocity for aircraft with constant pitch propeller. Rate of climb variation with altitude are also calculated from excess power values shown in **Figure 2.61** and **Eqn. (2.77)**.
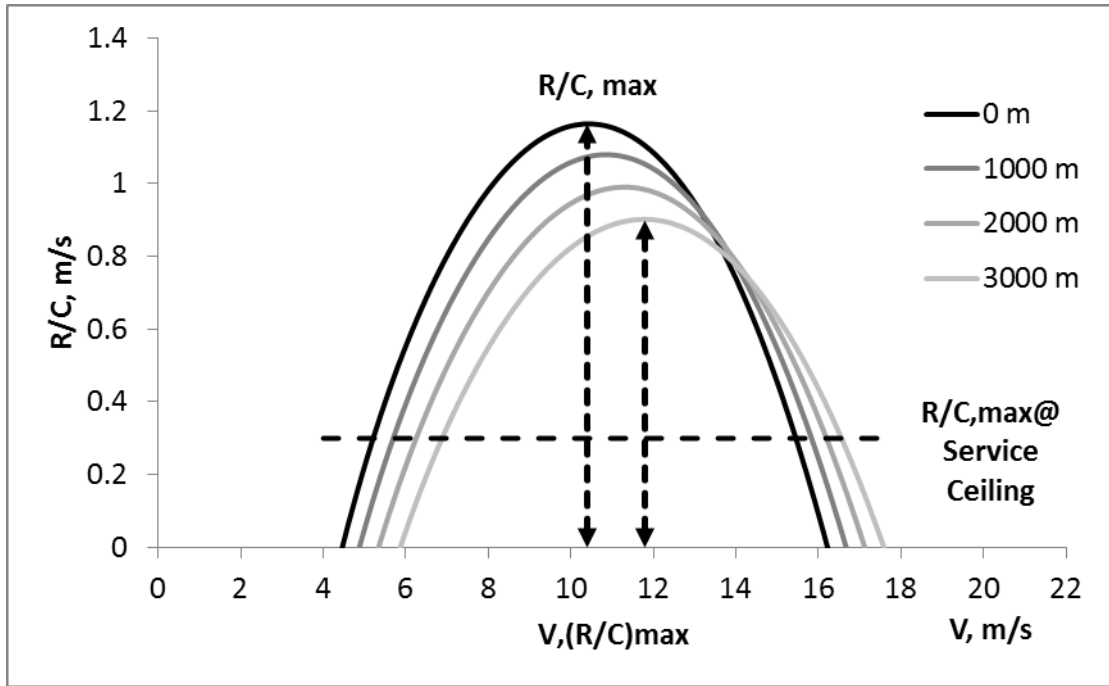
Figure 2.62. Rate of Climb Variation with Altitude

Theoretical maximum rate of climb velocities and actual maximum rate of climb velocities shown in **Figure 2.62** are summarized in **Table 2.34.** As it is mentioned before, closeness between theoretical and actual maximum rate of climb velocities verifies the suitability of the propulsion system choice.

Table 2.34. Theoretical and Actual $V_{(R/C)max}$ Variation with Altitude

Altitude	Theoretical $V_{(R/C)max} = V_{PR,min}$	Actual $V_{(R/C)max}$
0	10.4	10.4
1000	10.9	10.9
2000	11.4	11.3
3000	12.0	11.8

2.12.2.1. Climb Angle

Climb angle for a propeller-driven aircraft can be directly calculated by **Eqn. (2.79)**, where V_∞ is maximum rate of climb velocity and P_A is the power available at maximum rate of climb velocity.

$$\sin\theta = \frac{P_A}{V_\infty W} - \frac{1}{2}\rho_\infty V_\infty^2 \left(\frac{W}{S}\right)^{-1} C_{D0} - \frac{W}{S}\frac{2K}{\rho_\infty V_\infty^2} \qquad (2.79)$$

Table 2.35. Climb Angles with Altitude

Altitude, m	0	1000	2000	3000	4000
θ, deg	5.1	4.3	3.5	2.8	2.1
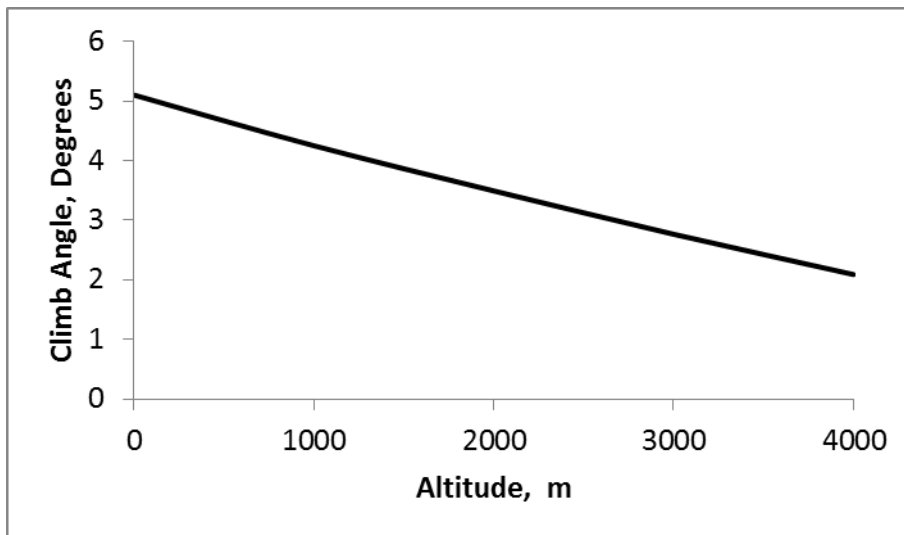
Figure 2.63. Climb Angle with Altitude at Maximum Rate of Climb

2.12.2.2. Service and Absolute Ceiling

Service ceiling is the altitude where maximum rate of climb is **0.5 m/s** (100 ft/min) for general aviation aircraft[18], which is quite high for a Mini UAV. **0.3 m/s** maximum rate of climb is assumed for the design. Maximum rate of climb with altitude has a linear trend which is shown in **Figure 2.64.**

84
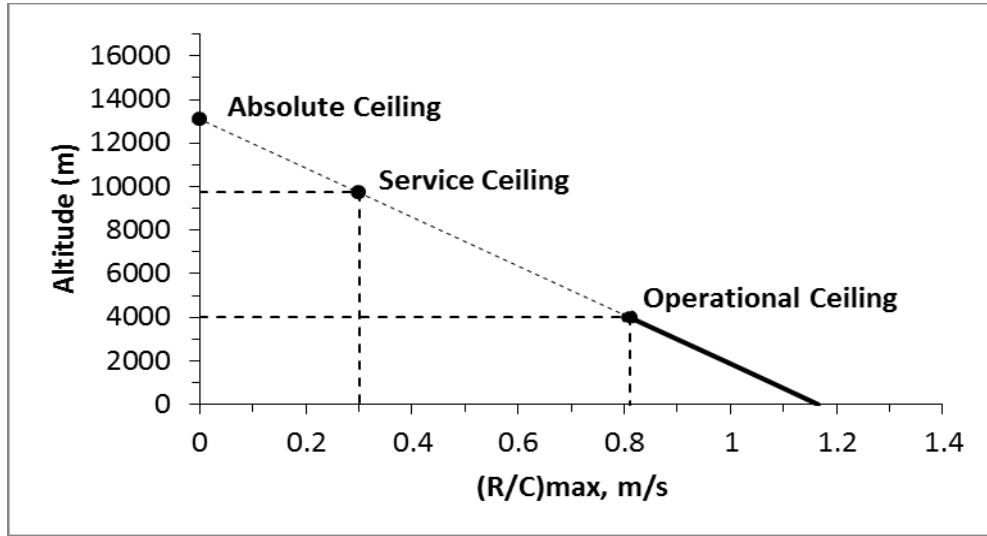
Figure 2.64. Maximum Rate of Climb Trend

It is seen from the trend plot that, service and absolute ceiling values determined as 13000 m and 9750 m are not realistic. Ceiling calculations are performed based on approximations shown in **Section2.10.3** where altitude factor AF_η assumption is assumed for limited altitude values and temperature effects on propulsion system are not included. Nevertheless, rate of climb calculations may be assumed realistic in design altitudes with a large safety margin. Additionally, mini UAV's structures and systems are not designed for very high altitude operations where air temperature and pressure are extremely low. Therefore, operational ceiling is limited up-to **4000 m.**

2.12.2.3. Time to climb

Minimum time to climb is calculated from maximum rate of climb, where $(R/C)_{max}$ equation can be approximated from maximum rate of climb trend shown in **Figure 2.64**.

$$(R/C)_{max} = -0.00009h + 1.16602 \tag{2.80}$$

$$t_{min} = \int_{h1}^{h2} \frac{dh}{(R/C)_{max}} \tag{2.81}$$

$$t_{min} = (11111.1 \cdot \ln(1.16602 - 0.00009 \cdot h1)) \\ - (11111.1 \cdot \ln(1.16602 - 0.00009 \cdot h2)) \tag{2.82}$$

Minimum time to climb results are calculated and presented in **Table 2.36**.

Table 2.36. Time to Climb Table

h_1 (Ground Level)	h_2 (100 m AGL)	t_{min} (min:sec)
0	100	1:26
1000	1100	1:33
2000	2100	1:42
3000	3100	1:52
0	**3100**	**48:47**

Average climb time is **1:40 min (100 sec)** to climb 100 m AGL operation altitude and **50 minutes** is needed to climb 3000 m from sea level.

2.12.3. Gliding and Unpowered Hand Launch

Determination of gliding parameters of the aircraft is important for unpowered flight phase due to the fact that hand launch of the mini UAV may be initialized unpowered for safety considerations. Minimum glide angle is independent from the flight altitude and determined as,

$$\tan \theta_{min} = \frac{1}{(L/D)_{max}} = \frac{1}{\sqrt{\frac{1}{4KC_{D0}} + \left(\frac{C_{L,Dmin}}{2C_{D0}}\right)^2} + \frac{C_{L,Dmin}}{2C_{D0}}} \qquad (2.83)$$

Minimum glide angles for flapped and unflapped aircraft are calculated as given in **Table 2.37**.

Table 2.37. Minimum Glide Angles

	$(L/D)max$	θ_{min} (degrees)
Flapped	28.90	1.98
Unflapped	14.90	3.85

Gliding velocity at minimum glide angle is the $(L/D)max$ velocity at any altitude.

$$V_{glide} = V_{(L/D)max}$$ (2.84)

Rate of descent of the aircraft at equilibrium glide velocity is given by,

$$V_V = V_{(L/D)max} \cdot \sin(\theta_{min})$$ (2.85)

Equilibrium glide velocities and rate of descent of the aircraft for various altitudes are calculated by using $(L/D)max$ velocities and minimum glide angles given in **Table 2.37.** Results are presented in **Table 2.38** and **Figure 2.65.**

Table 2.38. Glide velocities, Minimum Glide Angles and Descent Rates

Altitude, m	Flapped $\theta_{min} = 1.98°$		Unflapped $\theta_{min} = 3.85°$	
	$Vglide, m/s$	$V_V, m/s$	$Vglide, m/s$	$V_V, m/s$
0	9.9	0.34	11.7	0.78
1000	10.4	0.36	12.3	0.82
2000	11.0	0.38	12.9	0.87
3000	11.5	0.40	13.6	0.91
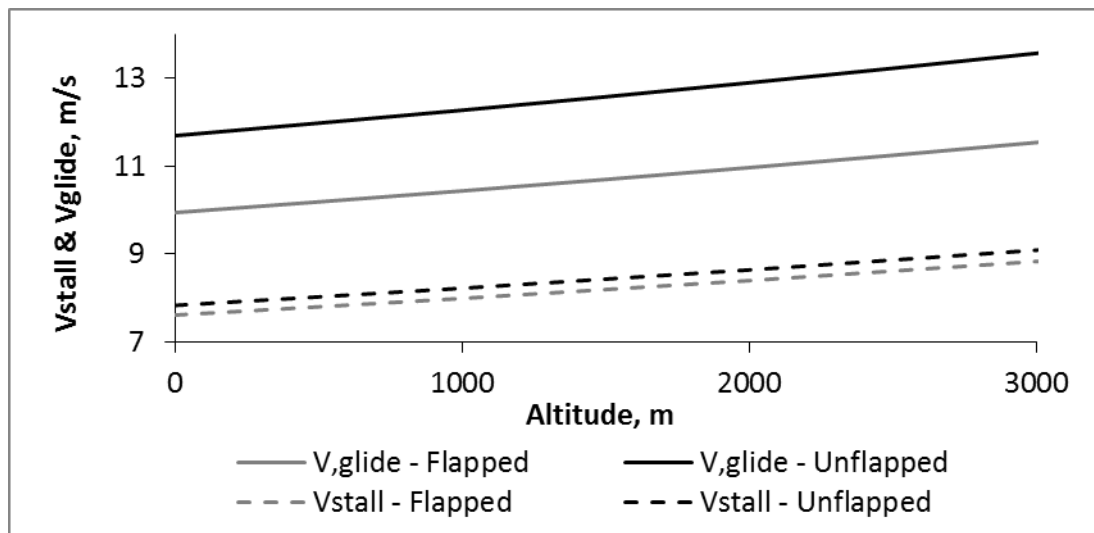
Figure 2.65. Variation of Glide Velocities and Stall Velocities vs Altitude

2.12.4. Takeoff Distance

Takeoff distance is calculated considering simple ground roll approximation since the primary design requirement is takeoff by hand-launch. Takeoff requirement is chosen as 35 m as given in the Constraint Analysis section. By assuming that thrust is much higher than the drag and the rolling friction, ground roll can be approximated as,

$$s_g \approx \frac{1.21 \cdot (W/S)}{g \cdot \rho_\infty \cdot (C_L)_{max} \cdot (T/W)} \tag{2.86}$$

Thrust to Weight ratio is not constant for propeller driven aircraft. Thrust at takeoff is calculated from lift off speed which is given by,

$$V_{LO} = 1.1\, V_{stall} \tag{2.87}$$

Lift off speeds are calculated from stall velocities at design altitudes and corresponding thrust values are taken from the thrust data found in **Section 2.10.3**. By using the calculated T/W values, ground roll is calculated and given in **Table 2.39**.

Table 2.39. Takeoff Distances for Various Altitudes

Altitude (m)	V_{LO}(m/s)	T_A (N)	T/W	s_g (m)
0	8.4	8.11	0.207	17.3
1000	8.8	7.49	0.191	20.6
2000	9.2	6.90	0.176	24.7
3000	9.7	6.33	0.161	29.8

2.12.5. Range and Endurance Calculations for Electric-Powered Aircraft

Range and endurance relations are well established for piston propeller and jet aircraft, which are derived from the specific fuel consumption and the fuel weight fraction. However, specific fuel consumption and fuel weight fraction are not available in electric-powered electric aircraft. Instead of these parameters, battery discharge rate, current draw and battery capacity are used for the range and the endurance estimations of the electric-powered aircraft. High performance battery types that are widely used in small aircraft like R/C airplanes and Mini UAV's are

Nickel-Cadmium (Ni-CD), Nickel-Metal Hydride (Ni-MH) and Lithium-Polymer (Li-Po). Because of high energy rates per battery weight, Li-Po battery type is chosen for the present design.

Li-Po battery cells are packed in serial and parallel connections in order to increase the battery voltage and the overall capacity. However it is not possible to use the 100% of the battery capacity due to design feature of the Li-Po batteries since cells exponentially discharge below critical cell voltages and become unusable. From the typical discharge curves for low discharge rate and high discharge rate batteries given in **Figure 2.66**, it is seen that about 15% of the Li-Po battery capacity should be remained unused to protect the battery life. In other words, 85% of the battery capacity should be taken to into account for range and endurance calculations.
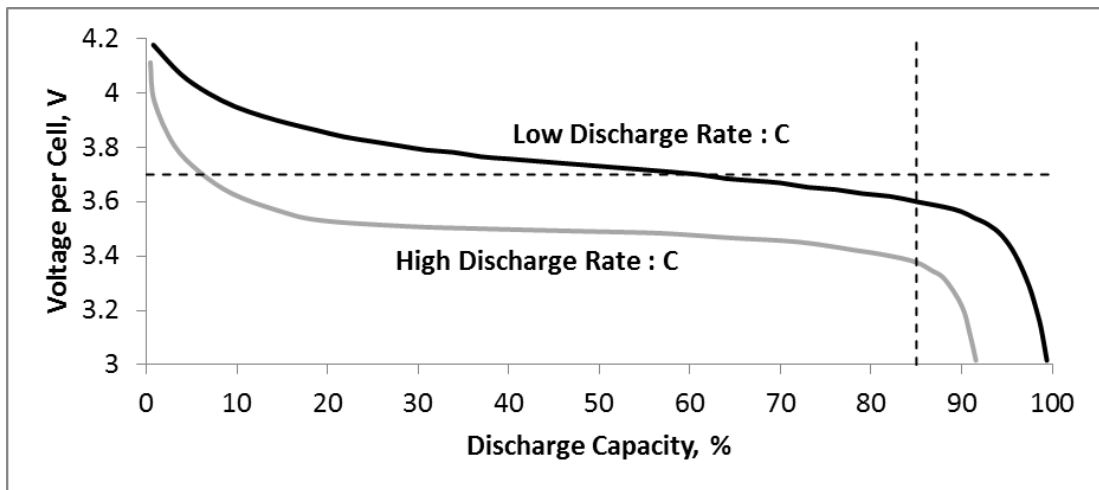
Figure 2.66. Typical Discharge Curves of Li-Po Batteries

Range and endurance calculations for electric-powered aircraft are performed by referencing Traub's work [28] for typical Li-Po battery parameters. In order to determine the endurance for electric-powered aircraft, discharge time of the battery is calculated by using Peukert's Equation in terms of battery capacity, current draw and discharge rate.

$$t = \frac{Rt}{i^n}\left(\frac{C}{Rt}\right)^n \tag{2.88}$$

Power required of the aircraft is provided by the battery pack,

$$P_R = P_B = Vi \qquad (2.89)$$

Substitution of the discharge current "**i**" in **Eqn. (2.88)** into **Eqn. (2.89)** yields,

$$P_R = V \frac{C}{Rt} \left(\frac{Rt}{t}\right)^{1/n} \qquad (2.90)$$

where,

t   : Discharge time in hours (h)

i   : Discharge current in amperes (A)

V   : Battery voltage in volts (V)   →V=11.1 V (3S Li-Po Battery)

C   : Battery capacity in amp. hours (Ah)

Rt   : Battery hour rating in hours (h)   →Rt=1   (Based on 1 hour discharge

                                                    for portable batteries)

n   : Battery discharge rate   →n=1.3 for typical Li-Po Battery [28]

Power output of the battery is reduced by the useable capacity factor, thermal losses, mechanical losses and aerodynamic losses due to propeller efficiency. Total efficiency can be expressed as,

$$\eta_{tot} = \eta_{capacity} \cdot \eta_{thermal} \cdot \eta_{mechanical} \cdot \eta_{pr} \qquad (2.91)$$

Where useable capacity factor is 0.85, thermal and mechanical losses are assumed as 0.75 and propeller efficiencies are taken from the corresponding data given in **Figure 2.57**.

$$\eta_{tot} = 0.85 \cdot 0.75^2 \cdot \eta_{pr} = 0.478 \cdot \eta_{pr}$$

Total efficiency is added into **Eqn. (2.90)**and time results in endurance equation for electric-powered aircraft are calculated.

$$E = t = Rt^{1-n} \left(\frac{\eta_{tot} V \cdot C}{P_R}\right)^n \qquad (2.92)$$

where endurance is in hours for any flight velocity and altitude. Note that power required is in terms of flight velocity and air density. Endurance plot calculated for

various flight speeds and battery capacities is given in **Figure 2.67** for 1000 m flight altitude.
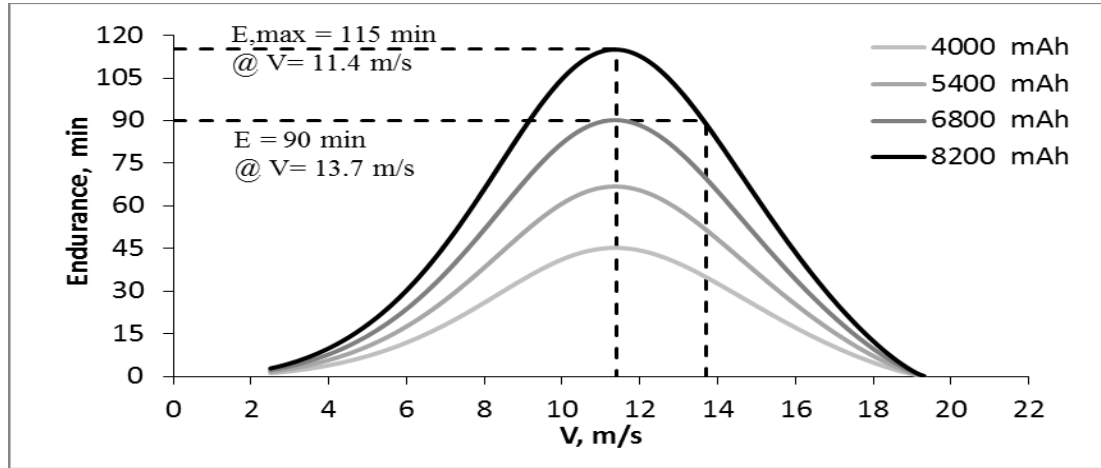
Figure 2.67. Effect of Battery Capacity on Endurance at 1000 m Altitude

6800 mAh battery capacity is sufficient for 90 minutes of endurance requirement with 11.4 m/s flight velocity at 1000 m flight altitude. However, 8200 mAh battery capacity is required to achieve endurance requirement at the maximum cruise velocity and 3000 m flight altitude as shown in **Figure 2.68**. 8200 mAh battery provides 129 minutes of maximum endurance at sea level and 90 minutes of endurance at 3000 m flight altitude for fixed loitering speed.**Table 2.40** summarizes maximum endurances and corresponding velocities at various altitudes.
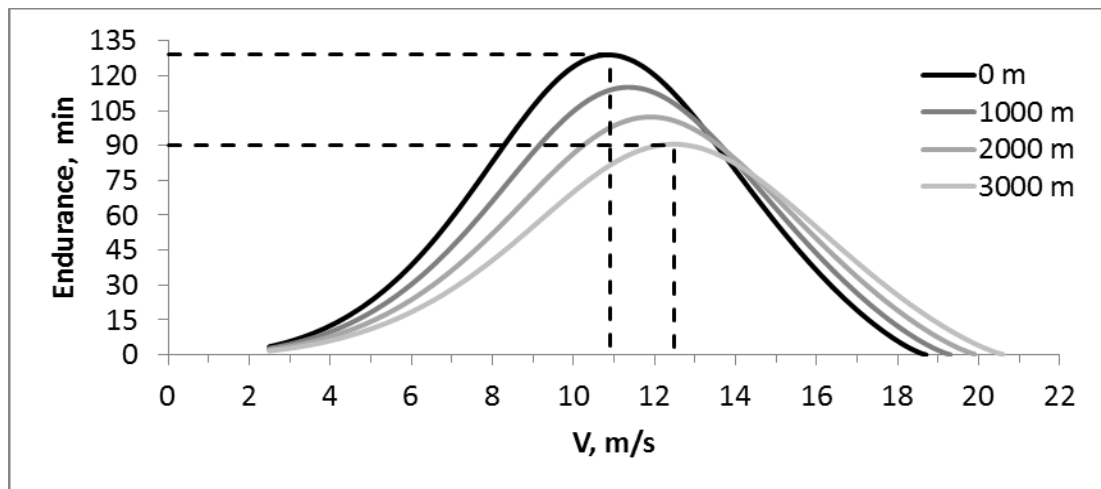
Figure 2.68. Endurance vs Flight Velocity at Various Altitudes

Table 2.40. Maximum Endurance and Corresponding Velocities at Various Altitudes

Altitude (m)	V_{Loiter} (m/s)	$V_{E,max}$ (m/s)	E,max (min)
0	10.4	11.3	129.0
1000	10.9	11.5	115.0
2000	11.4	12.7	102.3
3000	12.0	12.9	90.6

From **Table 2.40**, it is seen that maximum endurance of the aircraft is 129 minutes at level and 90 minutes at 3000 m with the determined maximum endurance velocities. Since theoretical loiter velocities and maximum endurance velocities are not identical because of fixed pitch propeller efficiency change, calculated maximum endurance velocities are determined as the actual loiter velocities. This results shows that theoretical loiter speed is not reliable for fixed-pitch propeller aircrafts.

Range of the aircraft is simply calculated by multiplying flight time and flight velocity shown in **Figure 2.68** and **Figure 2.69**. **Table 2.41** summarizes maximum ranges and corresponding velocities at various design altitudes.

$$R = E \cdot V_\infty \tag{2.93}$$
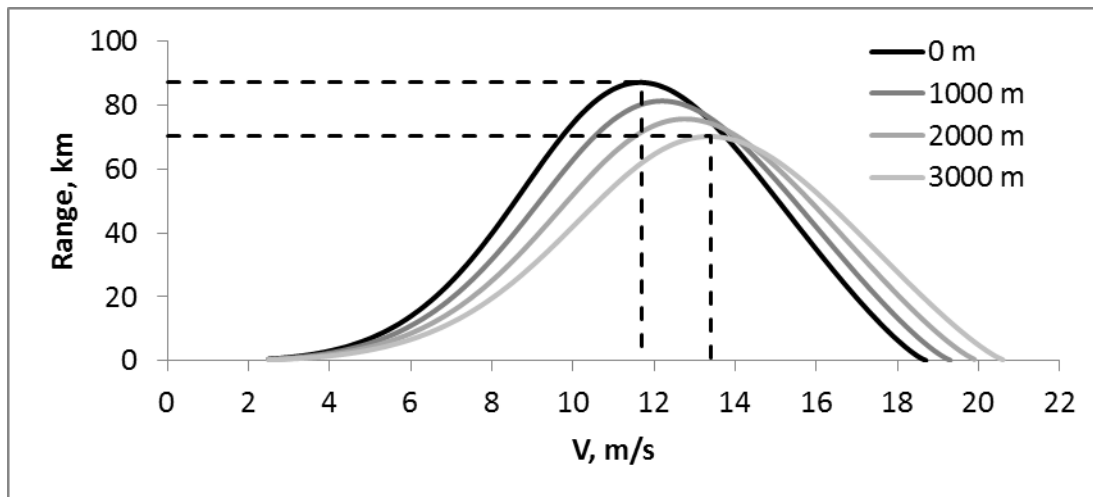
Figure 2.69. Range vs Flight Velocity for Various Altitudes

Table 2.41. Maximum Ranges and Corresponding Velocities at Different Altitudes

Altitude (m)	V_{Cruise} (m/s)	$V_{R,max}$ (m/s)	R,max (km)
0	11.7	11.7	87.1
1000	12.3	12.2	81.3
2000	12.9	12.8	75.7
3000	13.6	13.4	70.2

From **Table 2.41**, it is seen that maximum range of the aircraft is 87 km at sea level and 70 km at 3000 m with the determined maximum range velocities and cruise velocities determined by the graphical approach are quite close to calculated maximum range velocities. Hence, cruise speeds and maximum range speed are practically identical as expected. Calculated ranges are total distances covered through mission time for fixed cruise speed at design altitudes. Actual battery capacity requirement is determined by taking mission profile into account by utilizing the calculated takeoff speed, climb speed, loitering and cruise speed determined in the previous sections.

Mission profile of the aircraft was introduced in **Section 2.3.1** and simple mission profile was given in **Figure 2.1** is referenced for the calculations. Design velocities at each mission phase are determined as given in **Table 2.42.**

Table 2.42. Critical Design Speeds

Phase	Phase Velocity	0 m	1000 m	2000 m	3000 m
Takeoff	$V_{takeoff} = 1.1 \cdot V_{stall}$	8.4 m/s	8.8 m/s	9.2 m/s	9.7 m/s
Climb	$V_{climb} = V_{(R/C)max}$	10.4 m/s	10.9 m/s	11.3 m/s	11.8 m/s
Loiter	$V_{loiter} = V_{E,max}$	11.3 m/s	11.5 m/s	12.7 m/s	12.9 m/s
Cruise	$V_{cruise} = V_{R,max}$	11.7 m/s	12.2 m/s	12.8 m/s	13.4 m/s
Descend	$V_{descend} = V_{glide}$	11.7 m/s	12.3 m/s	12.9 m/s	13.6 m/s

Actual battery capacity requirement is determined by using **Eqn. (2.92).** Required battery capacity at each mission phase is calculated as,

$$C_{phase} = \frac{P_R}{\eta_{tot}V}(Rt)^{\frac{n-1}{n}}(t)^{1/n} \tag{2.94}$$

Power requirement at the take off and climb phases is $P_{A,max}$ and for the rest of the mission phases at the corresponding flight velocities and flight altitudes, calculated power required values are used. Note that, power available varies with velocity and altitude for fixed pitch propeller as mentioned before. Elapsed time and distances covered during the mission time are calculated and given in **Table 2.43** for 1000 m operational altitude.

Table 2.43. Mission Profile and Required Battery Capacity

Stations	Phase	Flight Velocity (m/s)	Elapsed Time (min:sec)	Distance Covered (km)	Required Battery Capacity (mAh)
0	Take-off	8.8	00:05	0.021	130
0 – 1	Climb	10.9	01:33	1.01	1190
1 – 2	Cruise (10 km)	12.2	13:40	10.0	1745
2 – 3	Loitering	11.5	59:40	41.2	5290
3 – 4	Return Cruise (10 km)	12.2	13:40	10.0	1745
4 – 5	Descend	12.3	01:22	1.01	300
5	Landing	8.8	-	-	-
			Mission Time	**Total Distance**	**Total Capacity**
			90 min	**63.2 km**	**10400 mAh**

Similarly, mission time, total distance covered and total battery capacity requirement are calculated for each design altitude and given in **Table 2.44**.

Table 2.44. Total Battery Capacity Requirement at Design Altitudes

Altitude	Mission Time	Total Distance	Total Capacity
0 m	90 min	61.6 km	9600 mAh
1000 m	90 min	63.2 km	10400 mAh
2000 m	90 min	68.4 km	11500 mAh
3000 m	90 min	70.1 km	12400 mAh

According to **Table 2.44**, required battery capacity is **12400 mAh** for the main battery at 3000 m design altitude. Auxiliary battery is also needed to supply the power requirement of the mission compartment and avionics of the aircraft. Therefore **3 packs** of parallel connected **5100 mAh 3S1P Li-Po** battery (**3S3P**) is used for the design [29].

Figure 2.70. Iris+ 5100 mAh 3S1P Li-Po Battery [29]

Total battery capacity is **15300 mAh** and output voltage is **11.1V** for selected 3S3P battery pack. If needed, main battery capacity, in other words weight of the main battery, may be decreased to ensure MTOW is not exceeded, which also reduces mission time.

2.13. V-n Diagram

Structural limitations of the aircraft are defined in this section. Since Demircan Mini UAV is not an aerobatic aircraft, limit loads are kept as small as possible. In order to determine limit flight loads, firstly loads at sustained level turn are determined and bending moment load for wing tip test is determined since wing tip test is necessary and practical way to ensure the structural reliability of the wing structure. Finally, limit load is defined considering the higher load factor.

2.13.1. Load at Sustained Level Turn

Sustained level turn is constrained by the maximum thrust available at any flight speed where thrust available varies with the velocity for the propeller driven airplane. Load factor at sustained level turn is calculated as,

$$n = 1/\cos\phi \qquad (2.95)$$

where maximum load factor "n_{max}" was chosen as **1.41** for **45°** bank angle in constraint analysis as a requirement. In this section, maximum load factor and sustained level turn performance of the aircraft is calculated for the selected propulsion system. Load factor in terms of (T/W) and flight performance parameters is defined as,

$$n = \left\{ \frac{\frac{1}{2}\rho_\infty V_\infty^2}{K(W/S)} \left[\frac{T}{W} - \frac{1}{2}\rho_\infty V_\infty^2 \frac{C_{D0}}{W/S} \right] \right\}^{1/2} \qquad (2.96)$$

where (T/W) varies with the velocity. Maximum thrust available of a propeller is the static thrust at zero velocity. Therefore, we cannot simply assume that load factor is maximized at (T/W)max. Graphical solution methodology is needed to determine maximum load factor at the sustained level turn for a propeller driven airplane.

Load factors are calculated for different altitudes by using the flight velocities and the corresponding thrust available values determined in **Section2.10.3**. Load factor results calculated from **Eqn. (2.96)** are plotted for design altitudes in **Figure 2.71.**
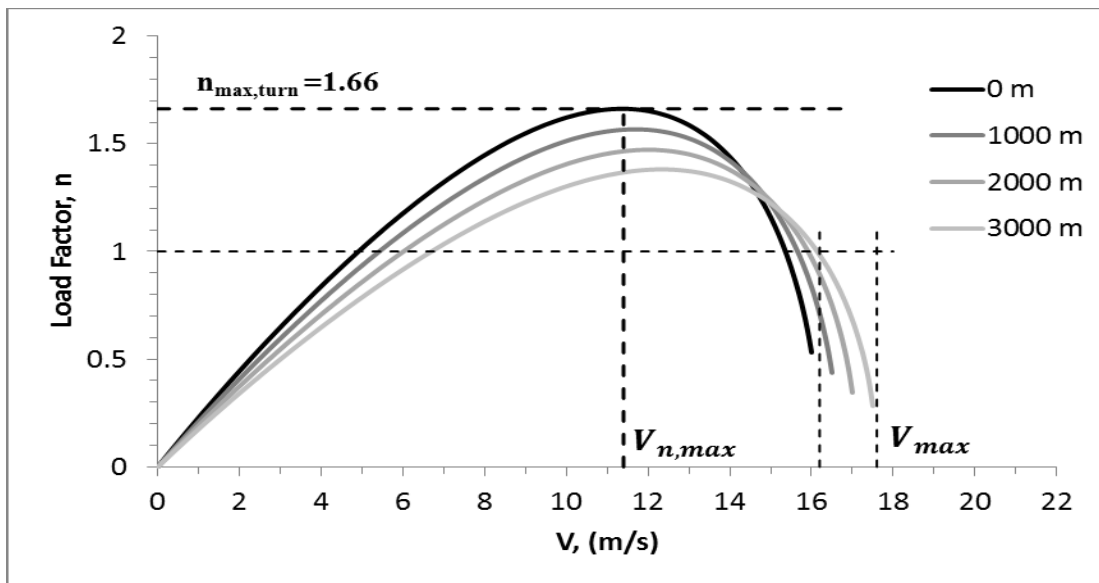
Figure 2.71. Thrust Constraint on Load Factor for Various Altitudes

Maximum turn load is obtained at sea level, where $n_{max,turn} = 1.66$ at **11.4 m/s**. Maximum achievable level flight (**n=1**) velocity is **16.2 m/s** at **3000 m** altitude and maximum flight velocity is **17.6 m/s** at **3000 m** altitude with **n=0.28** which shows that aircraft cannot sustain level flight and should dive with **73.4°** dive angle. This dive velocity is also determined from intersection of drag and thrust available curves and above this dive speed, aircraft drag overcomes the available thrust as shown in **Figure 2.59.**
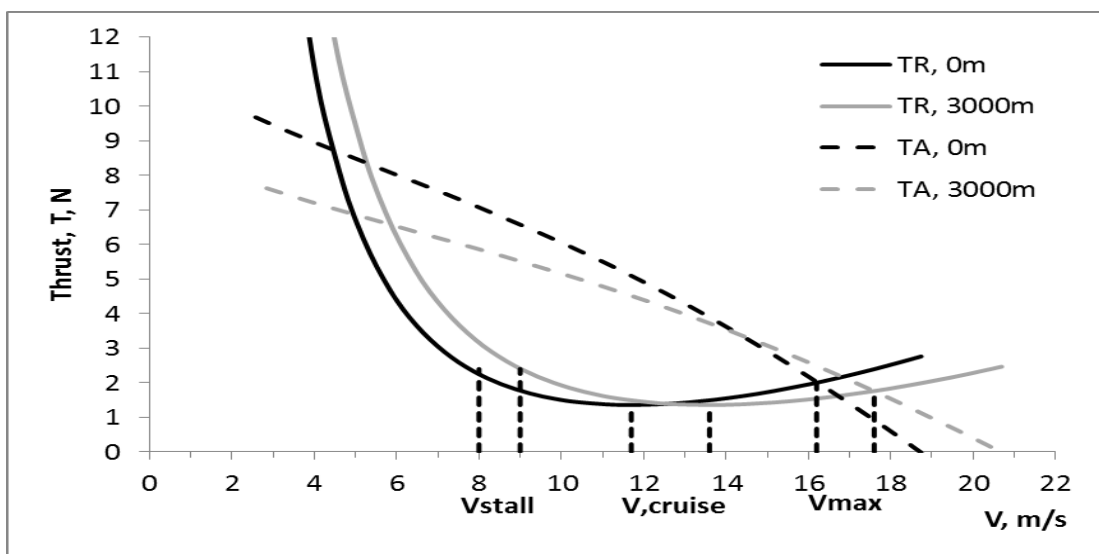
Figure 2.59. Drag (TR) and Thrust Available Curves vs Velocity

Turn radius for any flight velocity and load factor is calculated as;

$$R = \frac{V_\infty^2}{g\sqrt{n^2 - 1}} \qquad (2.97)$$

Maximum load factors, bank angles and turn radii at corresponding flight velocities for various altitudes are given in **Table 2.45**.

Table 2.45. n_{max}, Bank Angles, Turn Radii for Various Altitudes

Altitude (m)	V_∞(m/s)	n,max	ϕ (deg)	R (m)
0	11.4	1.66	53.0	10.0
1000	11.7	1.57	50.4	11.6
2000	12.0	1.47	47.2	13.6
3000	12.3	1.38	43.6	16.2

Maximum lift coefficient also constraints maximum load factor which is practically the stall constraint with the load factor, where $C_{L,max}$ is 1.8. Lift equation and stall velocity with the load factor is given in **Eqn. (2.98)** and **Eqn. (2.99)**.

$$L = nW = \frac{1}{2}\rho_\infty V_\infty^2 S C_L \qquad (2.98)$$

$$V_{stall} = \sqrt{\frac{2}{\rho_\infty}\frac{W}{S}\frac{n}{C_{L,max}}} \qquad (2.99)$$

Hence, load factor for $C_{L,max}$ constraint can be expressed as,

$$n_{CL,max} = \frac{1}{2}\frac{\rho_\infty V_\infty^2 C_{L,max}}{W/S} \qquad (2.100)$$

Note that maximum load factor at instantaneous maneuver is also limited by $C_{L,max}$ at the design velocity constraint which is 13.9 m/s at the sea level.

$$n_{max,inst.} = \frac{1}{2}\frac{\rho_\infty V_{max}^2 C_{L,max}}{W/S} = 3.33$$

Instantaneous load factor is defined at sea level and 13.9 m/s as $\boldsymbol{n_{max,inst.} = 3.33.}$ This load factor is not considered for the limit load due to positive high angle of attack (PHA)($\alpha \approx 8.5°$) requirement at maximum velocity. which is not applicable to determine dive speed of the aircraft.

Positive load factors at $C_{L,max}$ and $T_{A,max}$ constraints are shown in **Figure 2.72.**
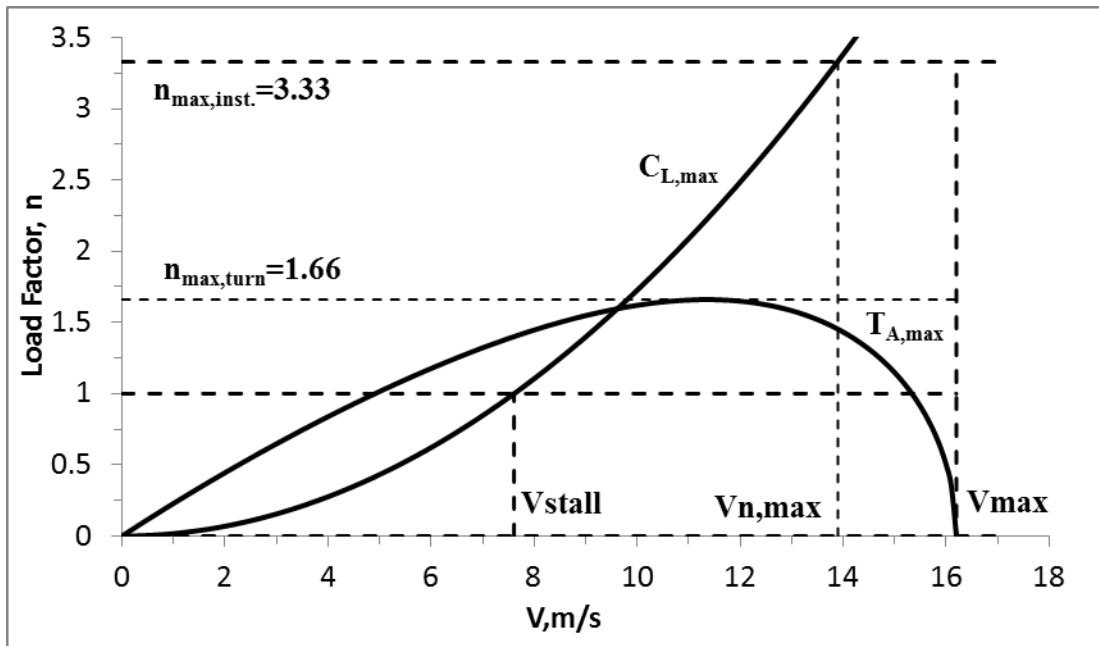
Figure 2.72. Positive Load Factor Constraints at Sustained Level Turn

2.13.2. Bending Moment Load at the Wing Tip Test

Lift at each half wing generates bending moment with respect to the root of the wing such that moment arm of the lift is the spanwise lift center for each half span. At level flight, wing root is exposed to 1g bending moment load. In order to determine the lift center of the half span, centroid of the lift distribution is needed to be determined by **Eqn. (2.101)**.

$$C_y = \frac{\int y L'(y)\, dy}{\int L'(y)\, dy} \tag{2.101}$$

Lift distribution is obtained from XFLR5 – 3D Panel analysis and lift center of the half wing is determined at **0.442%** of the half span, as shown in **Figure 2.73**.
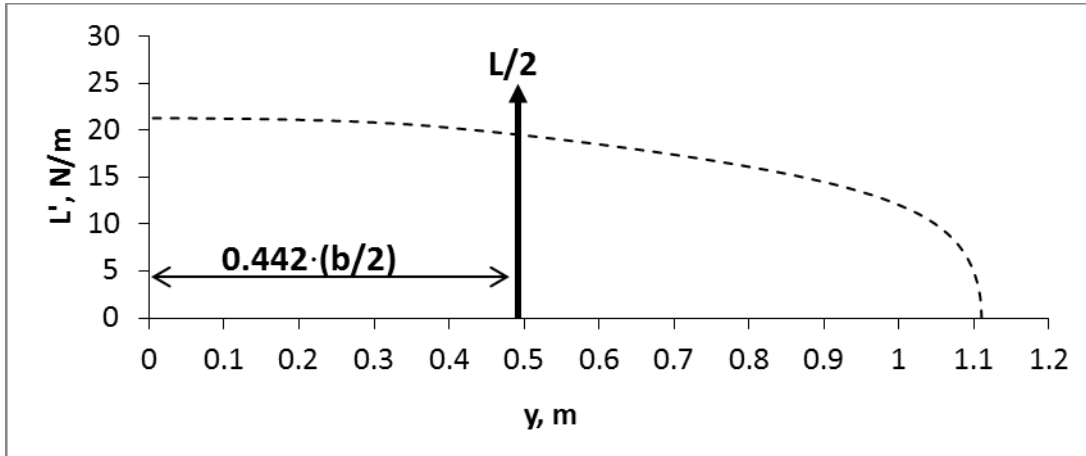
Figure 2.73. Half Span Lift Distribution and Lift Center

As it is mentioned before, total lift generated by the half wing generates 1g moment load with respect to **0.442%** of the half span. If wing tip test is performed, 100% of the half span is the moment arm of the balancing force which is equal to the half weight of the aircraft for the ground test. Bending moments for the level flight case and the tip test case are determined as,

$$(Mx), Lift = (Mx), 1g = (L/2) \cdot 0.442 \cdot (b/2)$$
$$(M_x), tiptest = (L/2) \cdot (b/2) \tag{2.102}$$

Ratio of the bending moment loads gives the equivalent tip test load.

$$n_{tip\ test} = \frac{(M_x), tiptest}{(Mx), 1g} = \frac{(L/2) \cdot (b/2)}{0.442 \cdot (L/2) \cdot (b/2)} = 2.26\ g$$

Tip test load factor is selected as $\boldsymbol{n_{tip\ test} = 2.3}$ with a small safety margin.

2.13.3. V-n Diagram

Positive limit load factor determined from the tip load test is selected as **2.3**. Although, the thrust available constraints maximum load factor at level flight, aircraft may be exposed to limit loads during pull-up, pull-down or dive maneuvers. However, stall constraint is still fundamental constraint for the flight envelope. Thus, stall constraint and determined limit load factor constraints the positive boundaries of the flight envelope. Maximum load factor for instantaneous maneuver is also taken into account for the upper boundary which is assumed as the ultimate load factor.

Instant maneuvers should be avoided during flight in order to avoid structural failure risk. Negative load factors are determined for minimum lift coefficient $C_{L,min} = -0.28$ at $\alpha = -14°$ angle of attack and **n= -1** is the negative limit load factor. According to determined positive and negative limit load factors, flight envelope, "V-n Diagram" is defined and given in **Figure 2.74.**
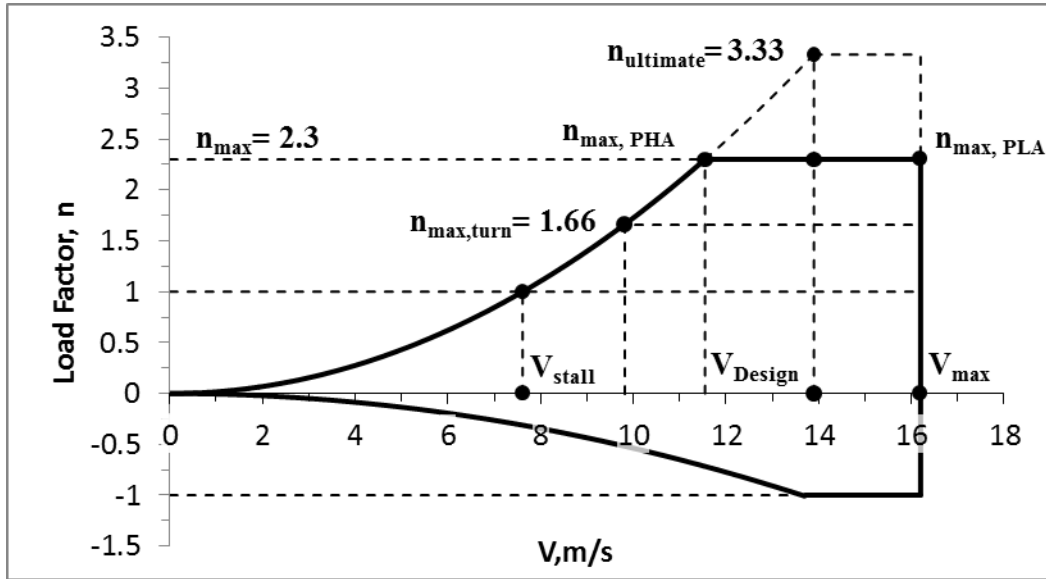
Figure 2.74. V-n Diagram

Load factor and corresponding velocities are given in **Table 2.46.**

Table 2.46. Load Factor and Corresponding Velocities at Sea Level

Ultimate Load Factor	n=3.33 @ V=13.9 m/s (∗)
Limit Load Factor @ Positive High Aoa (PHA)	n=2.3@ V=11.55 m/s
Limit Load Factor @ Positive Low Aoa (PLA)	n=2.3@ V=16.2 m/s
Maximum Load Factor at Sustained Level Turn	n=1.66 @ V=11.4 m/s
Minimum Limit Load Factor	n= -1

(∗) Maximum flight velocity is limited by the design requirement as **13.9 m/s**. Thus, ultimate load factor is assumed for the instantaneous load at the maximum design speed. However, instantaneous load analysis is not within the scope of this study. Limit load factor **2.3** at the maximum velocity is constrained by the thrust (**V=16.2 m/s**), and load factor of **2.3** is considered for the structural analysis of the wing due to positive low angle of attack (PLA).

Required lift coefficient for the limit load factor is calculated as,

$$L = nW = \frac{1}{2}\rho V^2 S C_L$$

$$C_L = \frac{2nW}{\rho V^2 S} = \frac{2 \cdot (2.3) \cdot (39.24)}{(1.225) \cdot (16.2)^2 \cdot (0.614)} = 0.914$$

Based on XFLR5 – 3D Panel and LLT analyses, required lift coefficient is expected to be determined between 3-4 degrees angle of attack, as shown in **Figure 2.75**. CFD analysis and determination of the aerodynamic loads at limit load will be given in **Chapter 3**.
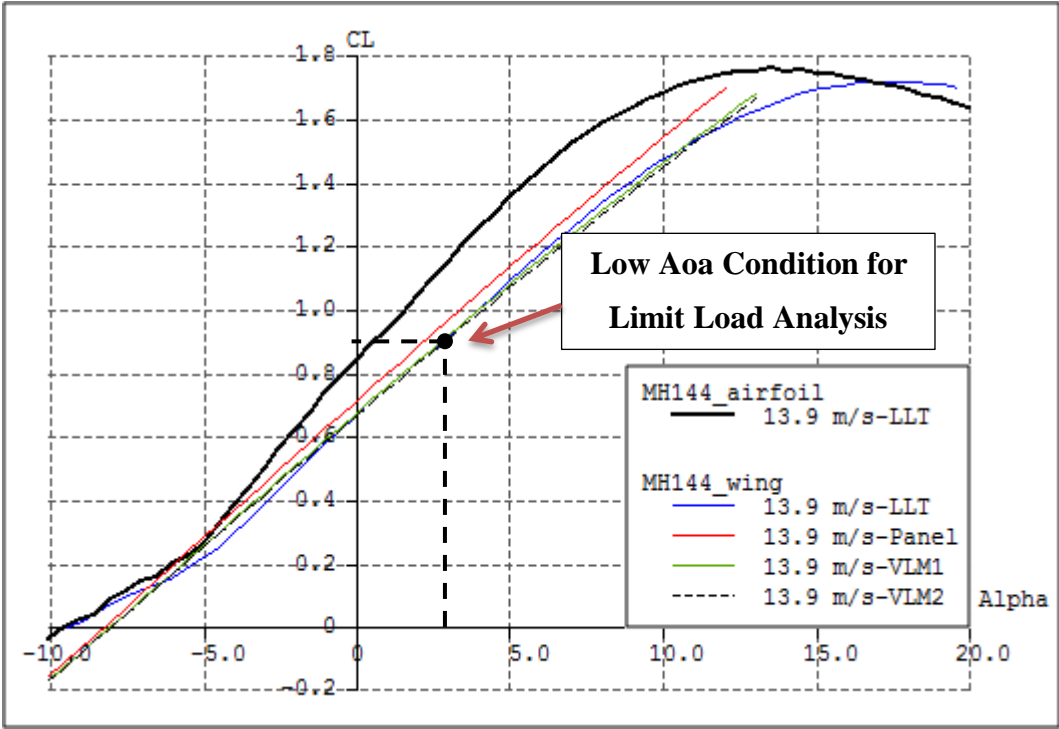
Figure 2.75. Positive Low Aoa Condition for Limit Load Analysis

2.14. Preliminary Performance Analysis

Airfoil and wing analysis of the design was performed in XFLR5 [16] analysis tool in **Section 2.5.3** and **Section 2.6** at the beginning of the conceptual design. Aircraft performance analysis capability of the XFLR5 is used at this stage.

Fixed lift analysis option is chosen for the aircraft performance analysis for fixed weigh aircraft where flight condition is determined to sustain level flight. Complete aircraft is modeled and VLM analysis utilizing horseshoe vortex method is performed at **1000 m** altitude. XFLR5 models of flapped and unflapped aircraft are shown in **Figure 2.76** and pressure coefficient distribution over unflapped condition with wing tip vortices is shown **Figure 2.77**.
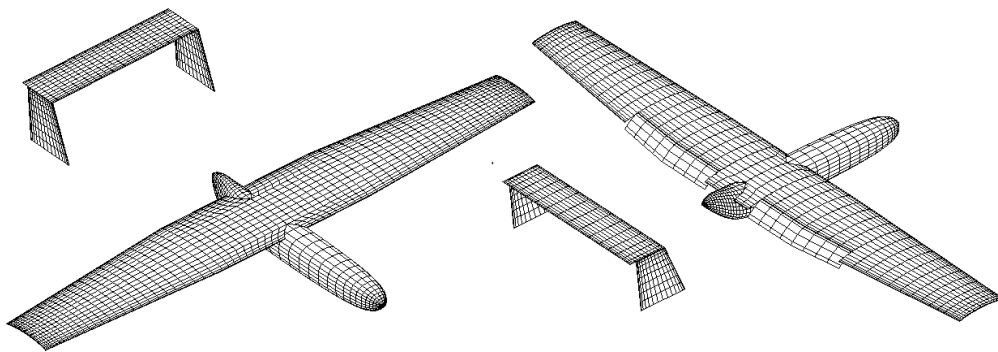
Figure 2.76. XFLR5 Models of Demircan Mini UAV
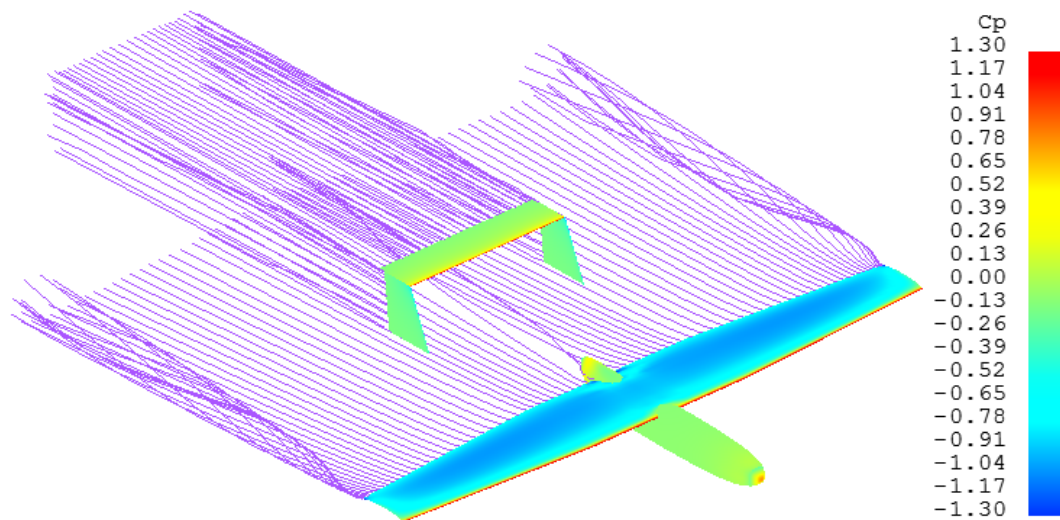
Figure 2.77. Cp Distribution and Wing Tip Vortices at the Cruise Condition

Fixed lift analysis for the flapped condition is performed and stall speed is determined as **8.03 m/s** at **13.5** degrees maximum angle of attack. Note that stall speed was defined as **8 m/s** at 1000 m altitude. Cruise velocity is determined as **13.41 m/s**at level flight which is quite close to the design cruise speed. XFLR5-VLM Analysis results for stall and cruise conditions are given in **Table 2.47.**

Table 2.47. XFLR5 – VLM Analysis Results for Stall and Cruise Conditions

V,stall	8.03 m/s	**V,cruise**	13.41 m/s
Alpha	13.5 deg	**Alpha**	0.5 deg
CL	1.782	**CL**	0.640
CD	0.190	**CD**	0.037
CL/CD	9.401	**CL/CD**	17.326
Cm	-0.322	**Cm**	-0.181

It should be noted that cruise speed was calculated as **12.3 m/s** in **section 2.8.6** for the $(L/D)_{max}$ condition, while cruise speed is determined as **13.41 m/s**with XFLR5 analysis. This disagreement is considered to be due to the differences in the drag calculation. It should be noted that XFLR5 analyzes full aircraft geometry for different angle of attack values and calculates flight velocities in order to sustain the level flight at the given angle of attack. Drag contributions of the body and the tail is included in the total drag at higher angle of attacks, i.e. lower velocities, while the required lift coefficient calculations are exactly the same. Since body and tail contributions at higher angle of attack values are not included in the analytical approach, XFLR5 calculates higher drag coefficients at corresponding flight velocities. In order to reduce the difference between the analytical approach and XFLR5, parasite drag coefficient should be determined for each angle of attack and corresponding flight velocities. Fuselage and tail contributions should also be included for varying angle of attack and flight speeds. Comparison of drag coefficient and drag polar of analytical approach and XFLR5 analysis are shown in **Figure 2.78** and **Figure 2.79.**
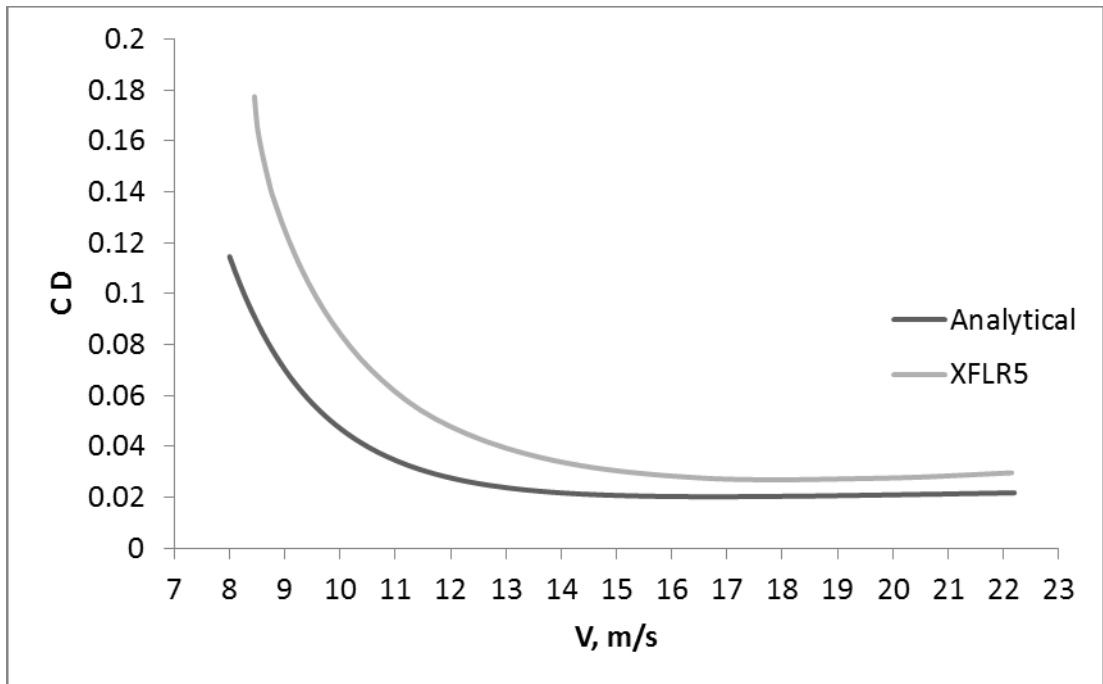
Figure 2.78. Drag Coefficient Variation of Analytical and XFLR5 Results
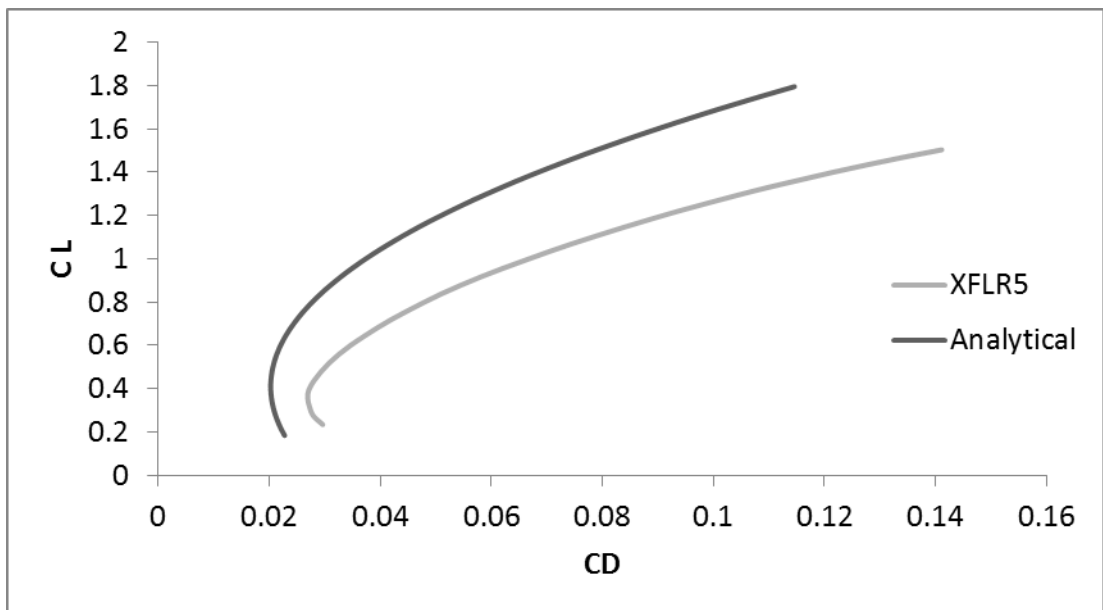
Figure 2.79. Drag Polars for Analytical Approach and XFLR5 Analysis

Lift and moment coefficient curves for the flapped and the unflapped conditions obtained by XFLR5 are given in **Figure 2.80** and **Figure 2.81** respectively.
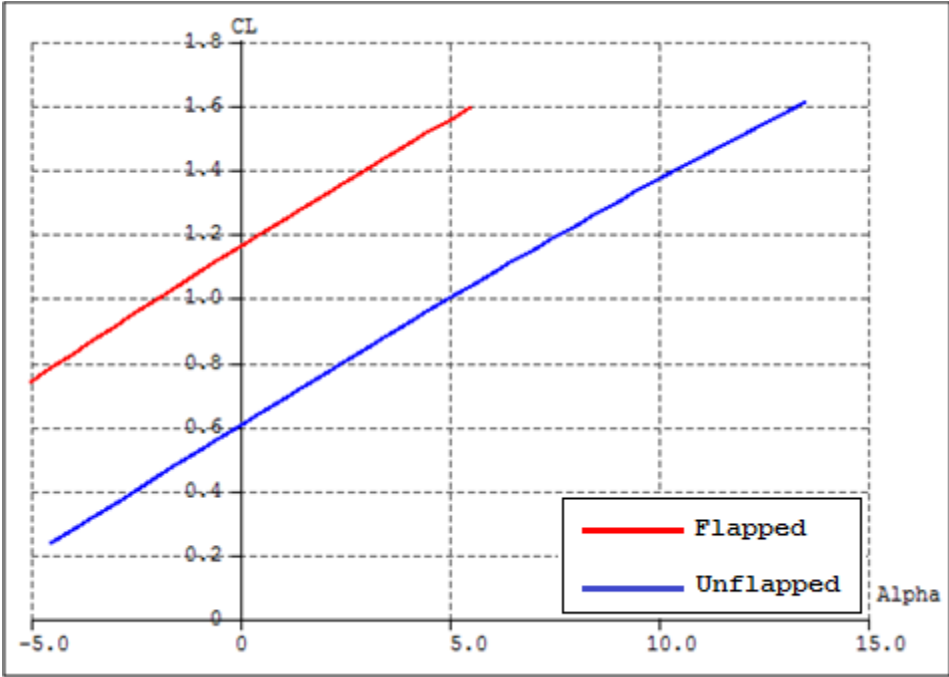
Figure 2.80. C_L vs Angle of Attack
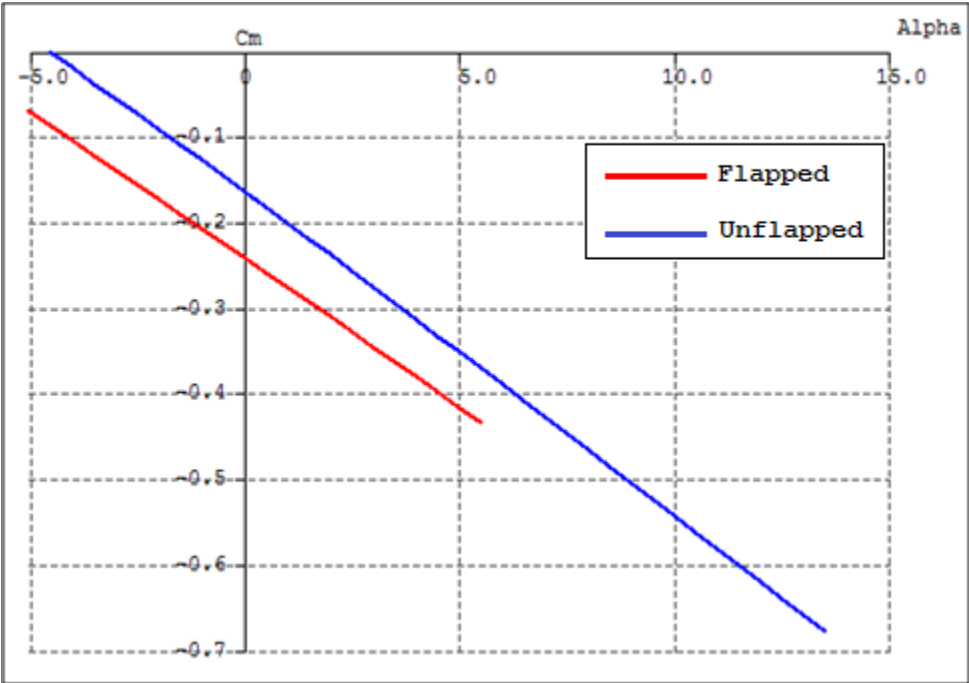
Figure 2.81. $Cm_{c/4}$ vs Angle of Attack

106

Cm,c/4 vs. angle of attack curve gives information about aerodynamic center and stability characteristics of the aircraft. Since Cm,c/4 is negative at zero angle of attack, aircraft has a downward pitching moment about quarter chord of the wing and absolute value of the moment coefficient increases with angle of attack. This indicates that downward pitching moment increases as angle of attack increases and longitudinal stability of the aircraft is ensured. The other result determined from the analysis is that the center of gravity location should be moved backwards with respect to quarter chord in order to balance the aerodynamic moment with the weight of the aircraft. In the present study, as a result of XFLR5 analysis, center of pressure location is determined as **7.309cm** and **5.405 cm** with respect to the quarter chord for the flapped and the unflapped conditions. CG location with respect to the quarter chord should be located in this range. **Table 2.48** summarizes the XFLR5 results obtained at 1000 m.

Table 2.48. Table of XFLR5 – VLM Analysis Results at 1000 m

	Flapped Condition		**Unflapped Condition**
C_L,max	1.78	C_L,max	1.7
Vstall @ $\alpha = 13.5°$	8.03 m/s	Vstall @ $\alpha = 13.5°$	8.47 m/s
V_∞ @ $\alpha = 0°$	9.97 m/s	V_∞ @ $\alpha = 0°$	13.85 m/s
(C_L/C_D)max	9.401	(C_L/C_D)max	17.317
C_L @ $\alpha = 0°$	1.156	C_L @ $\alpha = 0°$	0.599
C_D @ $\alpha = 0°$	0.131	C_D @ $\alpha = 0°$	0.035
Cm,c/4 @ $\alpha = 0°$	-0.24	Cm,c/4 @ $\alpha = 0°$	-0.163
X,Cp (wrt. c/4)	7.309 cm	X,Cp (wrt. c/4)	5.405 cm

Angle of attack variation with the flight velocity is shown in **Figure 2.82**. Negative angle of attacks are needed to fly faster than the cruise speed for the unflapped steady level flight case. Reverse flap or elevator trim is needed to fly faster at zero angle of attack flight condition. Therefore, cruise velocity is a natural boundary for steady level flight with zero degree angle of attack and zero trim conditions. Zero-trim velocities are **9.97 m/s** for the flapped wing and **13.85 m/s** for the unflapped condition.
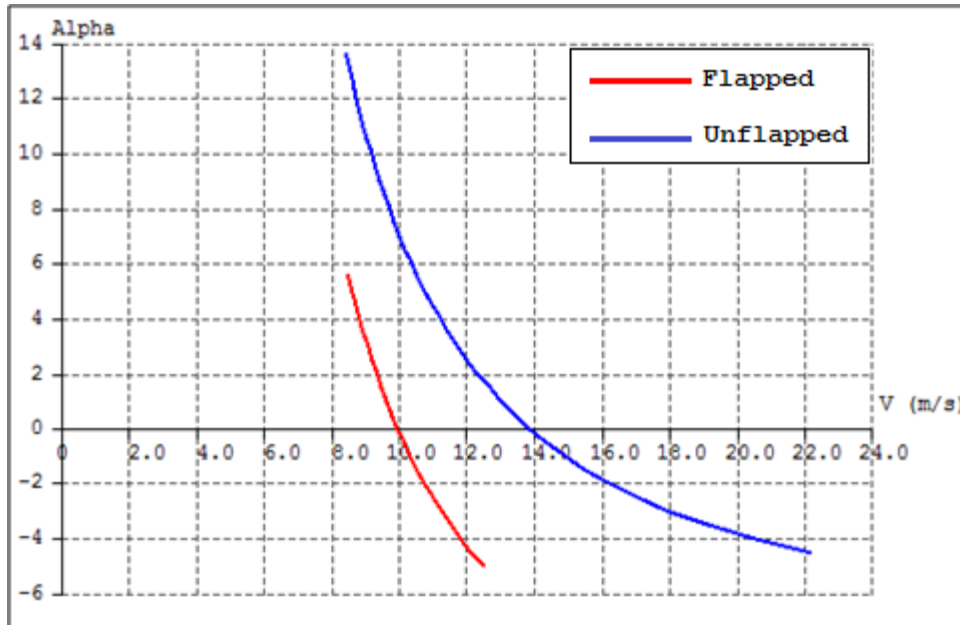
Figure 2.82. Angle of Attack vs Velocity

(Red – Flapped, Blue – Unflapped)

2.15. Longitudinal Stability and CG Location

Longitudinal stability of the aircraft is related to the distance between aerodynamic center of the aircraft, which is the neutral point, and the center of gravity (CG) of the aircraft. Static margin of the aircraft is defined as,

$$Static\ Margin = SM = \frac{X_n - \bar{x}}{\bar{c}} \qquad (2.103)$$

where X_n is the neutral point of the aircraft, $\bar{x}$ is the CG location and $\bar{c}$ is the mean aerodynamic chord of the wing. Neutral point of the aircraft is determined for zero degree angle of attack flight condition when the horizontal tail angle of attack is zero and the lift contribution of the horizontal tail is eliminated. At this condition, lift and weight of the aircraft are at the same location which is the neutral stability.

Lift center is defined by the moment coefficient with respect to quarter chord. By calculating aerodynamic moment, moment arm can be determined for balancing the weight. Here moment arm is the neutral point distance and balancing weight is the weight of aircraft. Influence of the propeller thrust, downwash of the propeller hitting to the horizontal tail is neglected. Moment of the wing and CG location $\bar{x}$ with respect to quarter chord are calculated as,

$$M_{c/4} = W \cdot X_n \tag{2.104}$$

$$M_{c/4} = \frac{1}{2}\rho_\infty V^2 S\bar{c}C_{m,c/4} \tag{2.105}$$

where corresponding velocity is,

$$V = \sqrt{\frac{2W}{\rho_\infty SC_L}}$$

By substituting, moment and corresponding velocity into **Eqn. (2.104)**, neutral point with respect to quarter chord can be determined as,

$$X_n = \frac{\frac{1}{2}\rho_\infty \left(\frac{2W}{\rho_\infty SC_L}\right)S\bar{c}C_{m,c/4}}{W}$$

$$\frac{X_n}{\bar{c}} = \frac{C_{m,c/4}}{C_L} \tag{2.106}$$

Calculated neutral point location with respect to quarter chord is,

$$\frac{X_n}{\bar{c}} = \frac{0.21}{0.6} = 0.35 = 35\%, wrt.\,0.25\bar{c}$$

$$X_n = 0.35\bar{c} = 0.0987m, wrt.\,0.25\bar{c}$$

Neutral point location with respect to leading edge can be determined as,

$$\left(\frac{X_n}{\bar{c}}\right)_{LE} = 0.25 + \frac{X_n}{\bar{c}} \tag{2.107}$$

$$\left(\frac{X_n}{\bar{c}}\right)_{LE} = 0.25 + 0.35 = 0.6 = 60\%, wrt.\,LE\ of\ M.A.C.$$

$$X_{n,LE} = 0.6\bar{c} = 0.1692m, wrt.\,LE\ of\ M.A.C.$$

Determination of the neutral point location with respect to root chord of the wing is more practical. Neutral point location for unswept wing with respect to leading edge of the wing root is calculated as,

$$X_{n,LE} = 0.25c_r + 0.35\bar{c} = 0.1782\ m, wrt.\ LE\ of\ c_{root}$$

$$\left(\frac{X_n}{c_r}\right)_{LE} = \frac{0.1782}{0.318} = 0.5603 = 56.0\%, wrt.\ LE\ of\ c_{root}$$

Static margin is selected as **5%-10%** of the mean aerodynamic chord of the wing. CG locations for each static margin values with respect to leading edge of the mean aerodynamic chord are calculated as,

$$\frac{\bar{x}}{\bar{c}} = \frac{X_n}{\bar{c}} - SM$$

$$\frac{\bar{x}}{\bar{c}} = 0.35 - \begin{Bmatrix}0.05\\0.10\end{Bmatrix} = \begin{Bmatrix}0.30\\0.25\end{Bmatrix} = \begin{Bmatrix}30\%\\25\%\end{Bmatrix}, wrt.\ 0.25\bar{c}$$

$$\left(\frac{\bar{x}}{\bar{c}}\right)_{LE} = 0.6 - \begin{Bmatrix}0.05\\0.10\end{Bmatrix} = \begin{Bmatrix}0.55\\0.50\end{Bmatrix} = \begin{Bmatrix}55\%\\50\%\end{Bmatrix}, wrt.\ LE\ of\ M.A.C.$$

Center of gravity location with respect to the root chord of the wing is calculated as,

$$\bar{x}_{LE} = 0.25c_r + \begin{Bmatrix}0.30\\0.25\end{Bmatrix}\bar{c} = \begin{Bmatrix}0.1641\\0.1500\end{Bmatrix}m, wrt.\ LE\ of\ c_r$$

$$\left(\frac{\bar{x}}{c_r}\right)_{LE} = \frac{\begin{Bmatrix}0.1641\\0.1500\end{Bmatrix}}{0.318} = \begin{Bmatrix}0.561\\0.472\end{Bmatrix} = \begin{Bmatrix}56.1\%\\47.2\%\end{Bmatrix}, wrt.\ LE\ of\ c_r$$
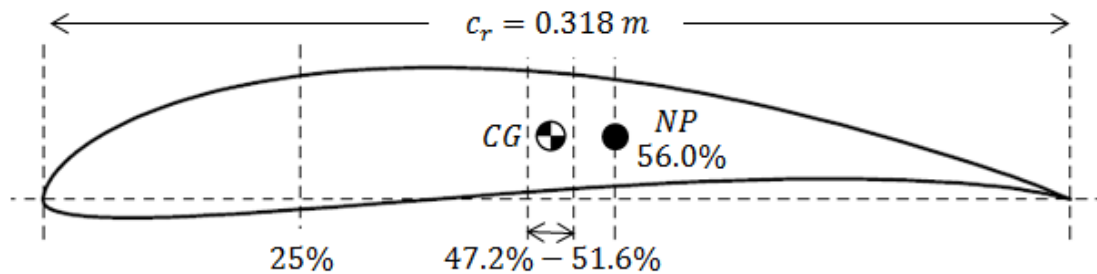
Figure 2.83. Neutral Point and CG Margin on the Root Chord

2.16. System Components and Weight Distribution

Aircraft component weight build-up and center of gravity estimation is an essential phase of classical aircraft analysis methodology. Size of the aircraft components affect component weights, component weights affect the center of gravity location, center of gravity location affects stability characteristics and stability characteristics affect aircraft component sizes. This is why aircraft design is an iterative process. Simple diagram of these interactions are shown in **Figure 2.84.**
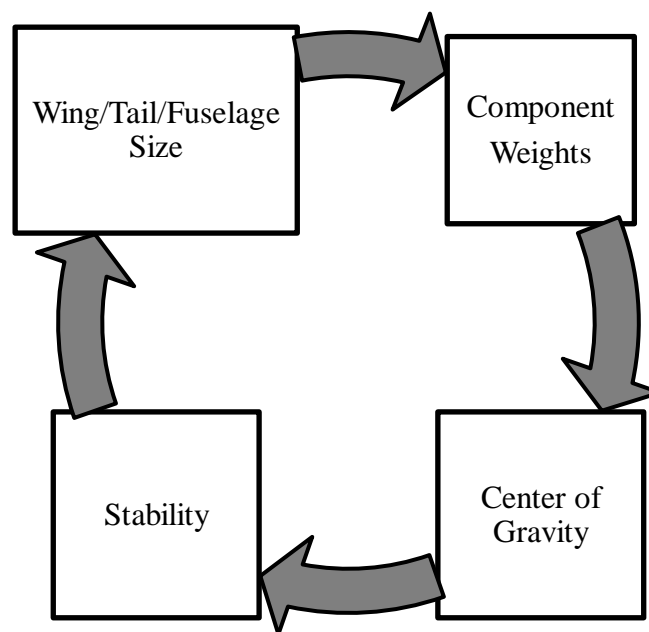
Figure 2.84. Aircraft Design Interactions

However, maximum takeoff weight is constrained by the design requirement and conceptual design phase is performed for the maximum design weight allowed. Additionally, aircraft weight does not change during the flight since there is no fuel consumption. Therefore, component weights and system weights need not to be specified until now. In this section, system weights are specified, aircraft component weights are estimated and center of gravity location is determined in order to perform a detailed stability analysis. Structural weights of wing, tail and fuselage are estimated by using weight per unit wetted area values determined the in previous composite mini UAV design and manufacturing study [41], [42]. Aircraft components are given in **Table 2.49**.

111

Table 2.49. Aircraft Components

Component	Mass
Wing	860 gr
Horizontal Tail	170 gr
Vertical Tail	140 gr
Fuselage	396 gr
Prop System	129 gr
Battery	934 gr
Camera System	1140 gr
Avionics	231 gr
Total Mass	**4000 gr**

Detailed components, corresponding masses and locations relative to the quarter chord are given in **Table 2.50**. Mass points given in **Table 2.50** are shown in the **Figure 2.85**. Center of gravity location is **47.3%** with respect to the LE of the root chord, which satisfies **47.2%** to **56.1%** CG margin calculated in the previous section.
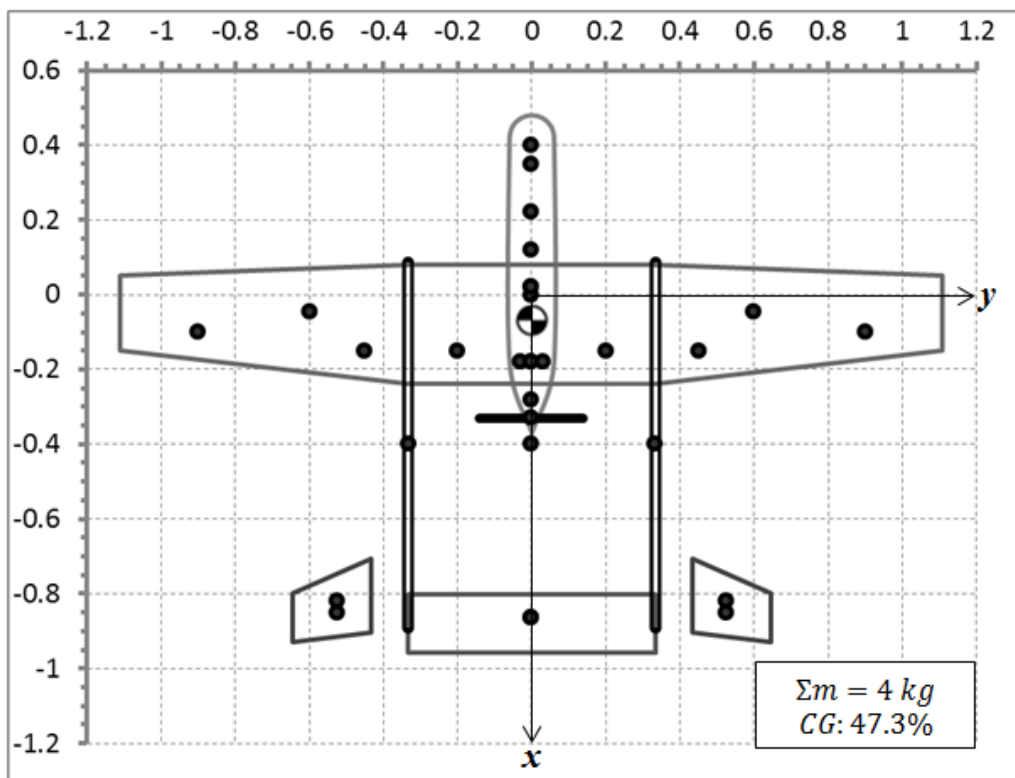
Figure 2.85. Aircraft System Components and the CG Location

Table 2.50. Aircraft System Components and CG Locations

Component	Mass (m)	x,arm (m)	y,arm (m)	z,arm (m)	Mx (gr.m)	My (gr.m)	Mz (gr.m)
Left Wing	250	-0.045	-0.6	0	-11.25	-150	0
Center Wing	270	-0.045	0	0	-12.15	0	0
Right Wing	250	-0.045	0.6	0	-11.25	150	0
Servo - LA	15	-0.1	-0.9	0	-1.5	-13.5	0
Servo - LF1	15	-0.15	-0.45	0	-2.25	-6.75	0
Servo - LF2	15	-0.15	-0.2	0	-2.25	-3	0
Servo - RF1	15	-0.15	0.2	0	-2.25	3	0
Servo - RF2	15	-0.15	0.45	0	-2.25	6.75	0
Servo - RA	15	-0.1	0.9	0	-1.5	13.5	0
Horizontal Tail	155	-0.865	0	0.212	-134.075	0	32.86
Servo HT	15	-0.865	0	0.212	-12.975	0	3.18
Vertical Tail 1	55	-0.818	-0.525	0.1	-44.99	-28.875	5.5
Vertical Tail 2	55	-0.818	0.525	0.1	-44.99	28.875	5.5
Servo VT 1	15	-0.85	-0.525	0.1	-12.75	-7.875	1.5
Servo VT 2	15	-0.85	0.525	0.1	-12.75	7.875	1.5
Boom 1	53	-0.4	-0.333	0	-21.2	-17.649	0
Boom 2	53	-0.4	0.333	0	-21.2	17.649	0
Wiring	120	-0.4	0	-0.4	-48	0	-48
Main / Aux. Battery	172	-0.18	0	-0.06	-30.96	0	-10.32
Main Battery	381	-0.18	0.03	-0.06	-68.58	11.43	-22.86
Main Battery	381	-0.18	-0.03	-0.06	-68.58	-11.43	-22.86
Fuselage	290	0.02	0	-0.06	5.8	0	-17.4
Autopilot Module	50	0.22	0	-0.06	11	0	-3
GPS 2	15	0	0	0	0	0	0
Gimbal	800	0.4	0	-0.06	320	0	-48
Telemetry	340	-0.08	0	-0.06	-27.2	0	-20.4
Receiver	11	0.02	0	0	0.22	0	0
Motor	86	-0.28	0	0.02	-24.08	0	1.72
ESC	30	-0.18	0	0	-5.4	0	0
Propeller	13	-0.33	0	0.02	-4.29	0	0.26

Σm (gr)	4000

ΣM (gr.m)	-284	0	-142.02
X_{CG} (m) (wrt. c/4)	-0.071	0	-0.036
X_{CG}(%c_{root})	**47.33%**	-	-

2.17. Final Conceptual Design

Up to the present, airfoil selection, conceptual sizing, propulsion system calculations, performance analysis, weight distribution and longitudinal stability analysis of the aircraft has been performed. Thus, conceptual design of Demircan Mini UAV is completed. Chord distance of %20 of the mean aero chord is selected for typical control surface size for the conceptual design. Dimensions of the conceptual design are shown in **Figure 2.86.**
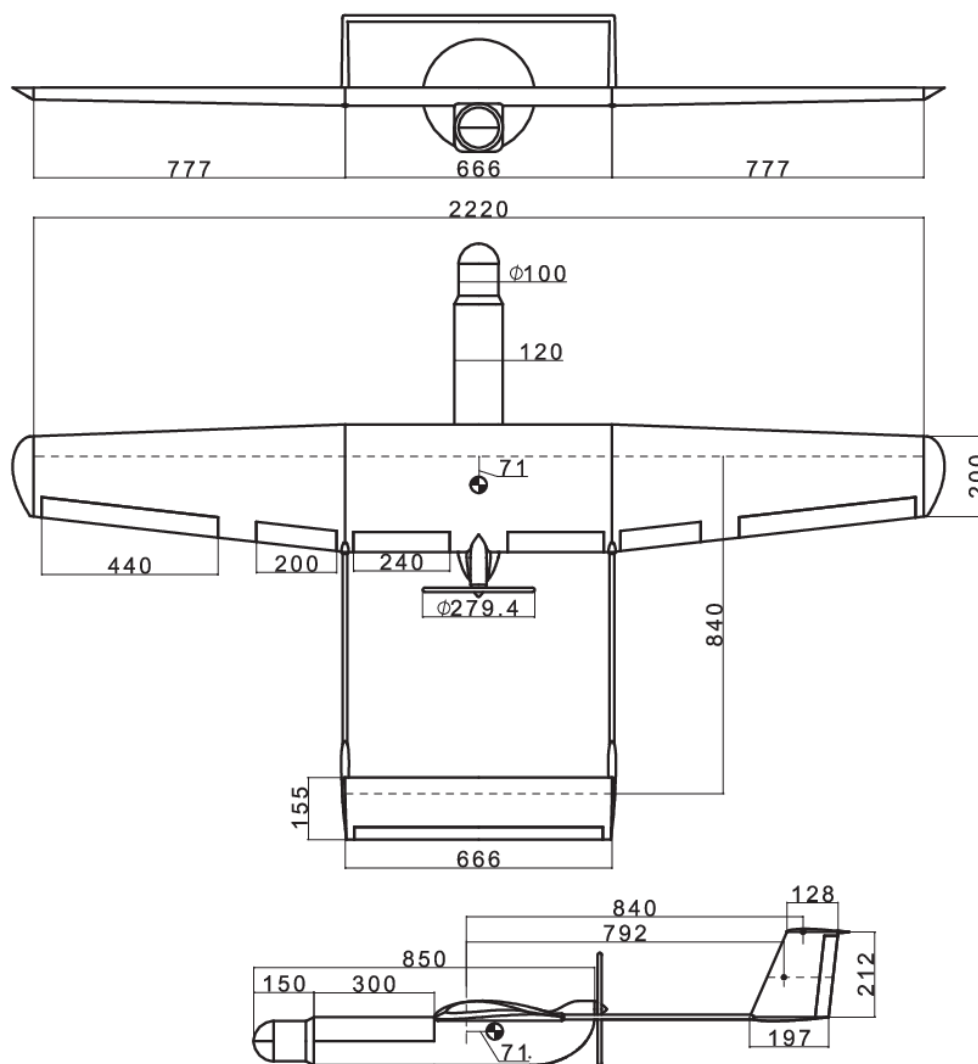
Figure 2.86. Conceptual Design Dimensions of Demircan Mini UAV

(All dimensions are in millimeters)

CAD model of Demircan Mini UAV is drawn as a solid model for CFD analysis. Hand-Launch configuration (**Figure 2.87**) and configurations with tricycle landing gear (**Figure 2.88**) and hook attachments (**Figure 2.89**) are given as a conceptual sketch. It should be noted that internal structures are not included and details are neglected in conceptual design phase.
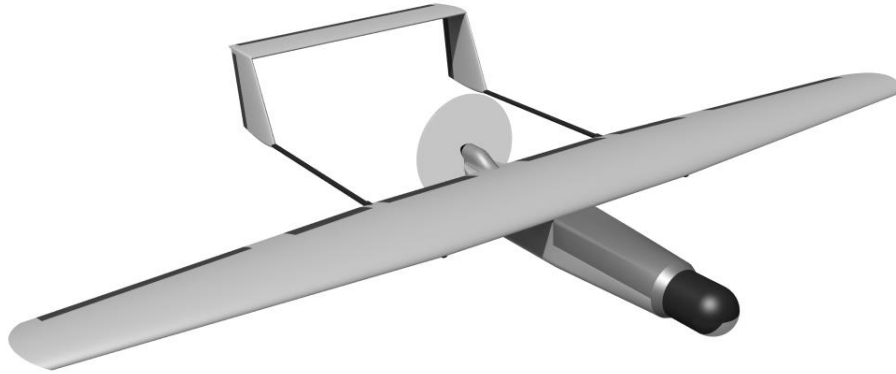
Figure 2.87. Final Conceptual Design of Demircan Mini UAV
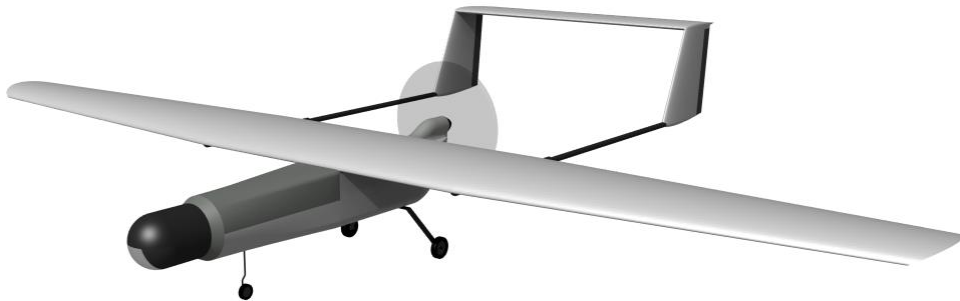
Figure 2.88. Conceptual Design with Landing Gear
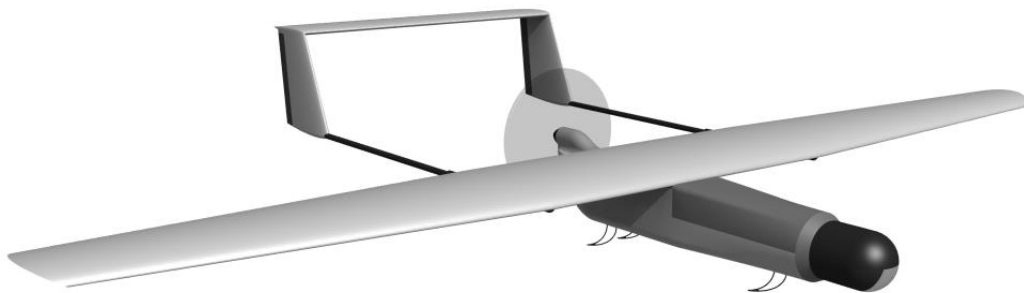
Figure 2.89. Conceptual Design with Hook Attachment

Summary of aircraft sizing parameters and general design features are given in **Table 2.51.**

<p style="text-align:center;">**Table 2.51.** Summary of General Design Features</p>

Maximum Takeoff Weight		MTOM	4 kg
Wing Span		b	2.22 m
Total Length		L	1.484 m
Payload	ISR System	Camera System	1.2 kg (∗)
Propulsion System	Motor Propeller Battery	EMAX APC SF 3S Li-Po	GT2218/11 11x4.7 11.1 V - 12400 mAh 934 gr (∗)
Design Velocities	@ 1000 m	V,stall V,climb V,loiter V,cruise	=8 m/s =10.9 m/s =11.5 m/s =12.2 m/s
Endurance		E	=90 min
Mission Radius		R	=10 km
Maximum Range	@ 1000 m	R,max	=63.2 km
Flight Altitude		AGL	=100 m
Operational Ceiling (Limited)		AMSL	=4000 m

(∗ : Payload weight may be different based on mission and battery weight may be decreased to ensure that MTOW is not exceeded)

CHAPTER 3

NUMERICAL ANALYSIS OF THE WING

3.1. Introduction

In this section, computational fluid dynamics (CFD) analysis of the wing at positive low angle of attack limit load condition is performed and aerodynamic load acting on the wing is determined. Structural analysis of the wing is performed by using the limit load determined from CFD analysis. ANSYS – Fluent CFD software [32] is used to determine aerodynamic load acting on the wing and finite element model of the wing structure is analyzed in MSC Nastran/Patran Software [34], [35]. Two different wing structure concepts, which are structures with I-spar and Tubular Spar, are considered and structural analyses of these wings are performed by using the pressure data determined from the CFD result of the wing. At the end of this section, structural loading differences between wing structures with I-spar configuration and tubular spar configuration are examined and structural layout of the wing is decided.

3.2. CFD Analysis of the Wing at Limit Load

ANSYS – Fluent CFD software is used to determine aerodynamic wing loading at positive low angle of attack (PLA) limit load condition defined in the **Section 2.13.3**. Limit load condition parameters are given in **Table 3.1**.

Table 3.1. Limit Load Condition Parameters

Limit load Factor	$n = 2.3$
Angle of attack (PLA)	$\alpha = 3 - 4\ degrees$
Velocity	$V = 16.2\ m/s$
Altitude	$h = 0\ m$
Required lift coefficient	$C_L = 0.914$

At the end of CFD analyses, pressure load acting on the wing is determined as a structural load for the wing structure analyses. Limit load at positive low angle of attack condition is chosen for the analysis case since aim of this phase is to determine distributed pressure load at limit load condition. Comprehensive CFD study of the design is not considered for this work.

3.2.1. CFD Model

CAD model of the wing and flow domain are created by using CATIA and shown in **Figure 3.1** and **Figure 3.2** respectively.
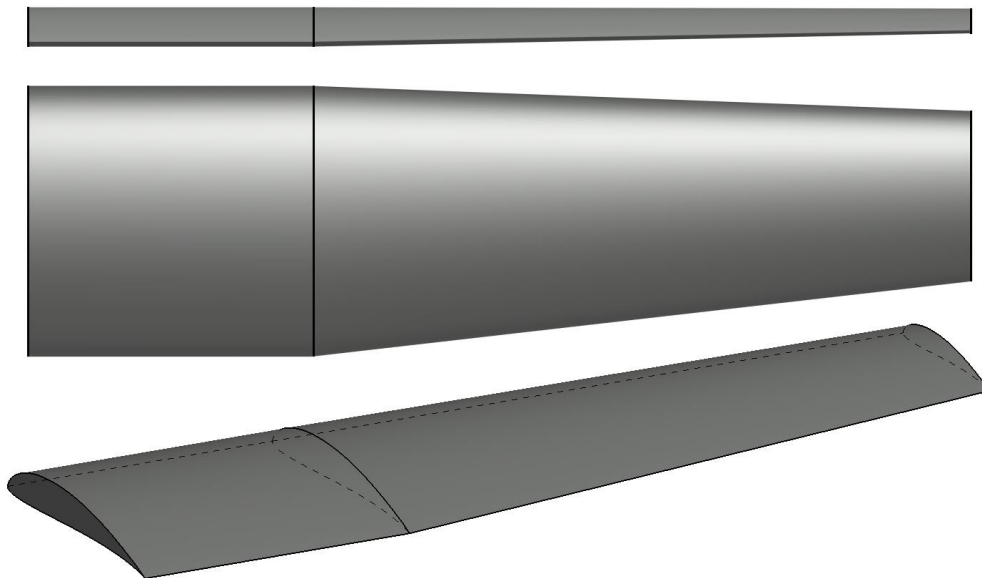
Figure 3.1. CAD Model of the Half Wing

Based on XFLR5 – 3D Panel and LLT analyses performed in **Chapter 2**, required lift coefficient is expected to be determined between 3-4 degrees angle of attack. Since flow domain is the subtraction of solid wing from the rectangular enclosure volume, each flow domain with different angle of attack is needed to be re-meshed and all solver settings are needed to be set from the beginning. Thus, instead of changing the geometric angle of attack of the half wing with respect to the flow domain, velocity vector at the inlet boundary is changed.

Flow domain dimensions are determined according to wing span and chord sizes. However dimensions are not strictly defined. All boundaries should be far enough where variation of the pressure gradients is insignificant. After trial analyses it is seen that domain dimensions and boundary spacing is satisfying for the current work. Dimensions of the flow domain defined in terms of wing dimensions and flow domain around the half wing are shown in **Figure 3.2**.
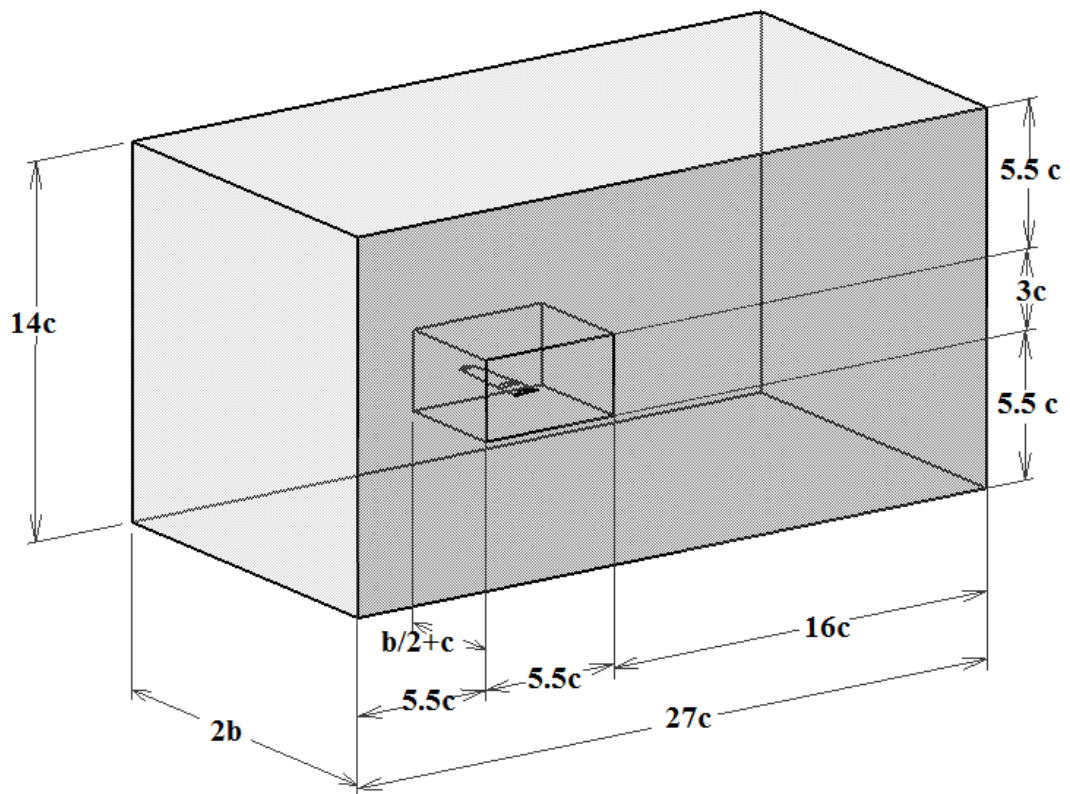
Figure 3.2. Flow Domain Around the Half Wing
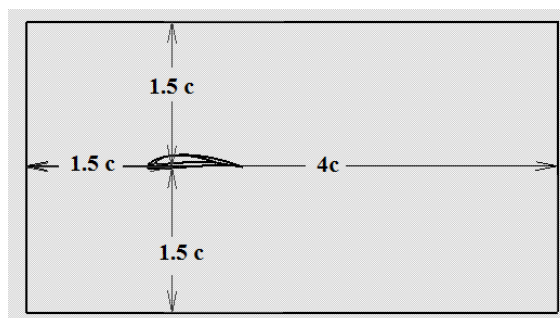
Figure 3.3. Dimensions of the Fine Mesh Domain

Investigation of enclosure volume size effects on results are studied by Gölcük [36]. Result of this investigation shows that modification or increasing of enclosure volume has insignificant effect on C_L values. MH114 airfoil is analyzed in the study and domain size effect results are shown in **Figure 3.4.** Therefore flow domain is decided and continued with the current domain sizes.
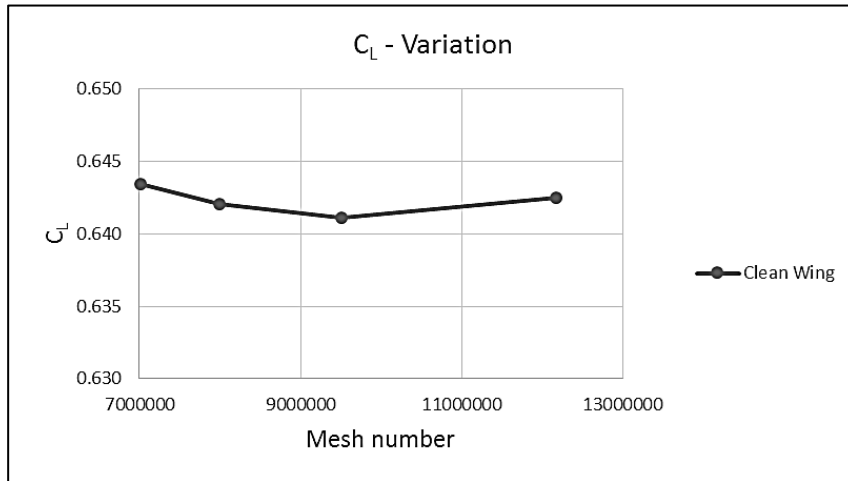
Figure 3.4. C_L Variations According to Flow Domain Adjustment for Different Mesh Numbers [36]

3.2.1.1. Mesh Generation

Boundary layer mesh (inflation) generation around the wing is one of the most important steps of the meshing process. Before meshing the enclosure volume, first layer thickness is needed to be determined. Boundary layer wall distance is calculated by using relations given in reference [30] for parameters given in **Table 3.2.**

Table 3.2. Wall Distance Estimation Parameters for Wing Analysis

Dynamic Viscosity	μ	$1.789 \times 10^{-5} \ kg/ms$
Density	ρ	$1.225 \ kg/m^3$
Freestream Velocity	U_∞	$16.2 \ m/s$
Reference Length	$\bar{c}$	$0.282 \ m$
Dimensionless Wall Distance	y^+	1

Reynolds Number is calculated from,

$$Re = \frac{\rho U_\infty \bar{c}}{\mu}$$

(3.1)

Skin friction coefficient is calculated by using Schlichting correlation,

$$C_f = [2\log_{10}(Re) - 0.65]^{-2.3} \; for \; Re < 10^9$$

(3.2)

Wall shear stress is calculated as,

$$\tau_w = C_f \cdot \frac{1}{2}\rho U_\infty^2$$

(3.3)

Friction velocity is calculated from,

$$u_* = \sqrt{\tau_w/\rho}$$

(3.4)

Wall distance is calculated as ,

$$y = y^+\mu/\rho u_*$$

(3.5)

And finally, by using equations above, estimated wall distance is calculated as,

$$y = 1.9 \times 10^{-5} \; m$$

By taking calculated first layer thickness into account, inflation and global mesh sizing settings are set. Mesh around the wing is refined by using the inner enclosure volume shown as a small rectangular volume in **Figure 3.2**.Generated mesh domain and boundary layer mesh around the half wing is shown in **Figure 3.5**. Mesh statistics are given in **Table 3.3.**
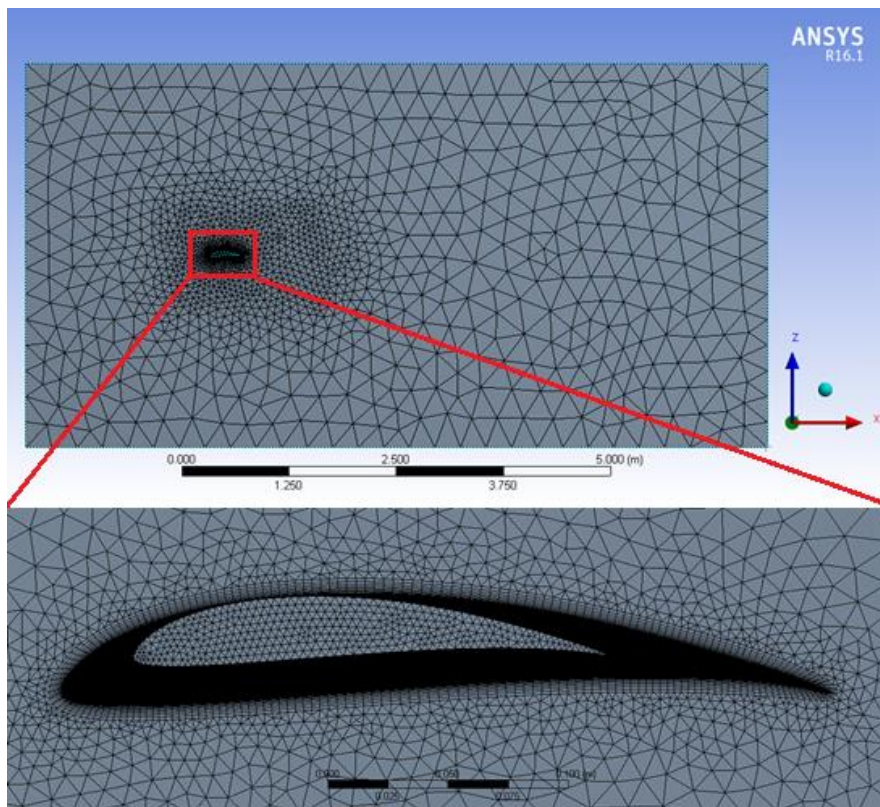
Figure 3.5. Global Mesh and Boundary Layer Mesh

Table 3.3. Mesh Statistics

Nodes	1225387
Elements	3946868
Minimum Skewness	7.9452e-005
Maximum Skewness	0.96134
Average Skewness	0.22288

Skewness is the measure of mesh quality. Mesh quality with respect to skewness parameter is given in **Table 3.4.** According to these parameters, average mesh quality of the generated mesh is excellent.

Table 3.4. Mesh Quality wrt. Skewness Value [31]

Value of Skewness	0-0.25	0.25-0.50	0.50-0.80	0.80-0.95	0.95-0.99	0.99-1.00
Cell Quality	excellent	good	acceptable	poor	sliver	degenerate

122

Since mesh quality is satisfying, boundary conditions are applied to the domain. As mentioned before, inlet velocity vector is changed instead of changing the geometric angle of attack in order to use generated mesh in varying positive angle of attack analyses. Therefore, "velocity inlet" boundary condition is set to the lower surface of the enclosure volume and "pressure outlet" boundary condition is set to the upper surface of the enclosure volume as can be seen in **Figure 3.6**. Wing surface boundaries are set to "wall" boundary condition and symmetry plane of the wing and far side of the enclosure volume are set to "symmetry" boundary conditions which are shown in **Figure 3.7**.
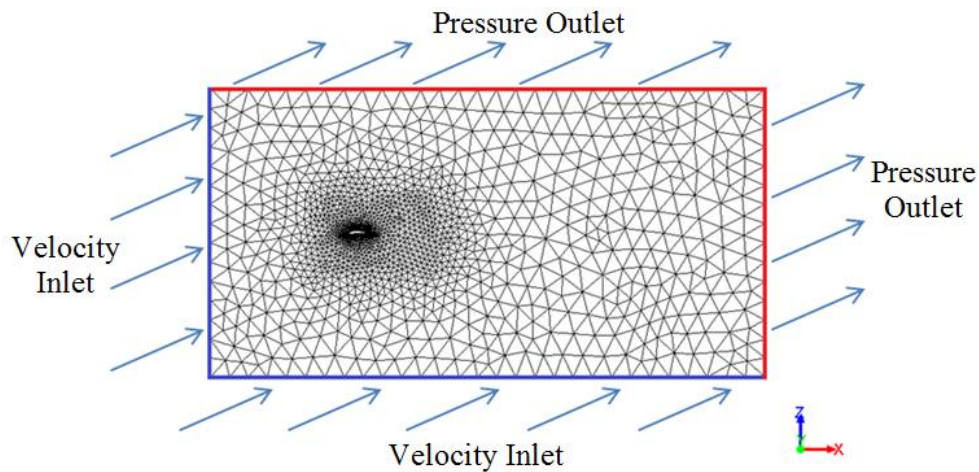
Figure 3.6. Boundary Conditions for Velocity Vector with Positive aoa
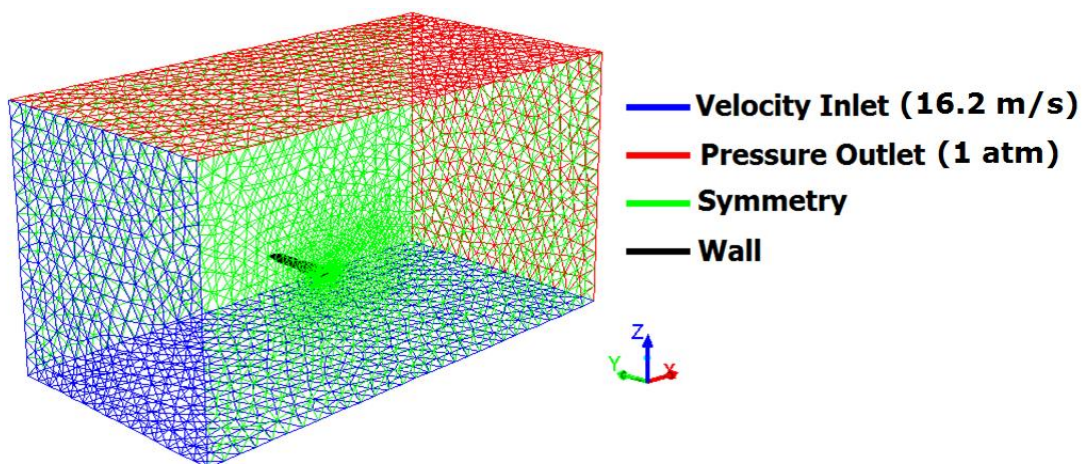
Figure 3.7. Boundary Conditions of the Global Mesh

Mesh convergence study is performed for whether solution converges or not by decreasing mesh sizes and increasing number of elements. However, determining the aerodynamic load acting on the wing at limit load is the main objective of CFD study. Therefore finding a proper pressure data which gives the target loading value and importing the pressure distribution to the structural mesh is sufficient for the study. During the structural analysis phase, resultant force calculated from the imported data is checked and it is seen that target load is achieved. Thus, mesh convergence study is not covered in the study.

3.2.1.2. Solver and Turbulence Model

Pressure based steady solver is set for solver options and Spalart-Allmaras one-equation model is chosen as turbulence model. Spalart-Allmaras turbulence model is developed for aerospace industry and it is low memory and accurate model for low Reynolds number attached wall-bounded flows [33]. It is reliable for wing analysis and mesh independency is verified with experimental studies [37].

3.2.1.3. Wing Analysis Results at Limit Load Condition

Wing analysis is performed for various angle of attack values between 3 and 4 degrees. Required loading is determined at **3.8** degree angle of attack. Total lift, drag and moment values of the half wing, corresponding aerodynamic coefficients and limit load factor are given in **Table 3.5.**

<div align="center">

Table 3.5. Limit Load Analysis Results for $\alpha = 3.8°$

</div>

L	45.2533	N	C_L	0.917	n	2.31
D	2.69477	N	C_D	0.05458		
M,c/4	-2.39923	N.m	Cm,c/4	-0.17232		

Pressure distribution on the wing is also determined, shown in **Figure 3.8.** Result is exported as Nastran input format and applied to the wing structure.
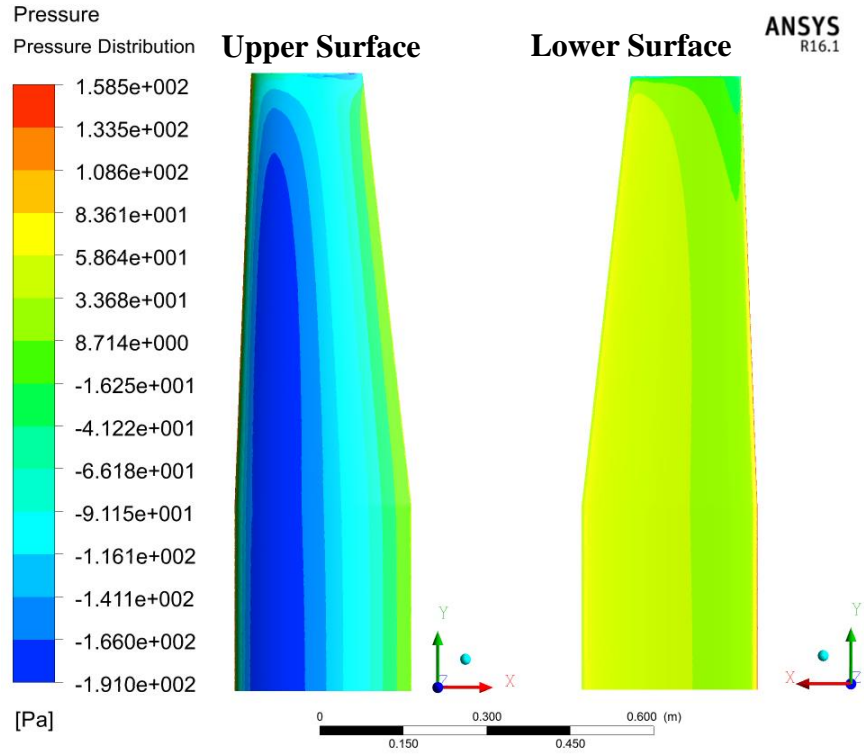
Figure 3.8. Pressure Distribution on the Wing

3.3. Wing Structure Design

Wing structure is designed for two different spar configurations. First configuration is the classical I Spar configuration, where spar carries shear, axial and bending loads and distribute and transfer shear loads on the upper and lower surfaces. Closed section behind the front spar is acting like torque box for this configuration. Second configuration is the tubular spar configuration which is already a closed section torque carrying structure. However, in small aircrafts like R/C models, it works as a bending load carrier due to small cross section. It is preferred to ease manufacturing which are simply aligned on the tubular spar from rib holes. Aim of choosing to compare these two spar configuration is to decide which one is safer. Design models for two different configurations are given in **Figure 3.9.**
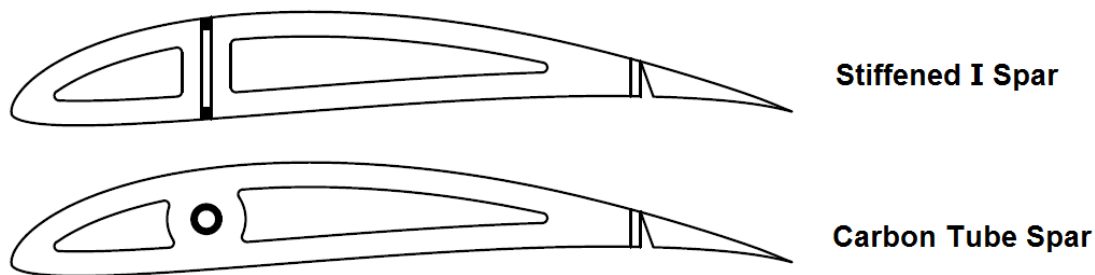
Figure 3.9. Structural Design Models for Different Spar Types

Lightening openings on the ribs shown in **Figure 3.9** are not taken into account in the structural analysis models. By this way stress concentration difference on ribs due to configuration difference can be examined better since opening sizes are different. Analysis of the ribs with openings can be studied in a future work.

E-Glass/Balsa composite material is chosen for the thin shell surfaces of the structures. Stiffeners with rectangular box cross-section and tube spar components are chosen as extruded carbon/epoxy profiles, which are unidirectional composite materials with orthotropic material properties. Structural models of the wing configurations are shown in **Figure 3.10** and **Figure 3.11.** Upper and lower surfaces are hidden in order to show inner structure.

126
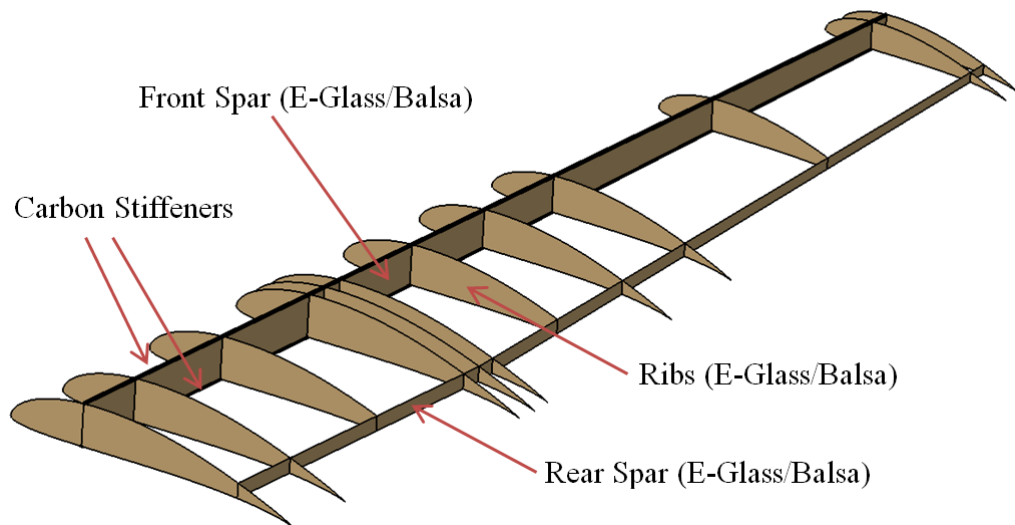
Figure 3.10. Stiffened I Spar Configuration
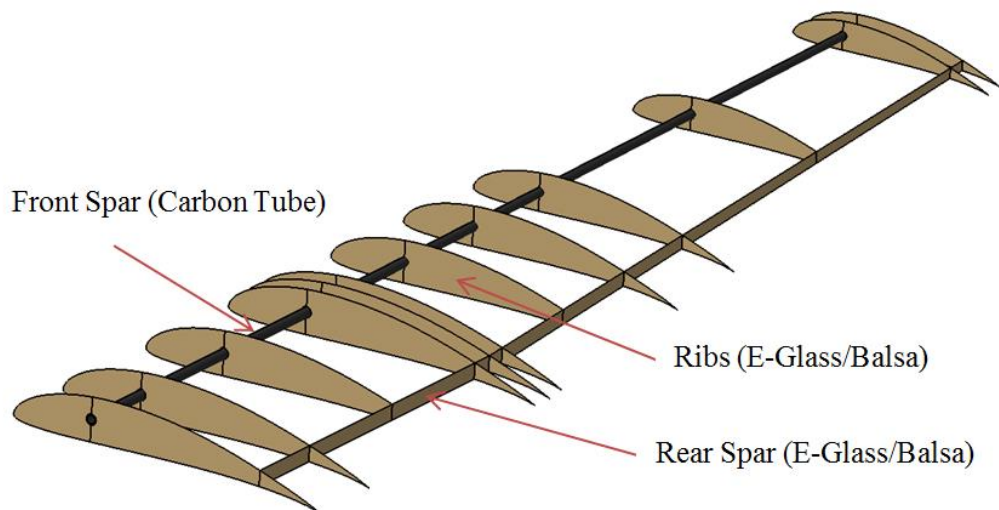
Figure 3.11. Carbon Tube Spar Configuration

3.4. Material Definitions

Weights of the wings with different spar configurations are kept same by selecting proper dimensions for carbon structures. E-Glass/Balsa composite component thicknesses are specified for commercially available 1-2 mm balsa wood. Upper and lower skin material is 1 mm E-Glass/Balsa and rib-spar materials are 2 mm E-Glass/Balsa. Material definitions of the wing structure components are given in **Table 3.6.**

Table 3.6. Material Definitions

I Spar Configuration	
Upper Skin	1 mm E-Glass/Balsa
Lower Skin	1 mm E-Glass/Balsa
Ribs	2 mm E-Glass/Balsa
Front Spar	2 mm E-Glass/Balsa
Rear Spar	2 mm E-Glass/Balsa
Stiffeners	2x2 mm Carbon Profile

Carbon Tube Spar Configuration	
Upper Skin	1 mm E-Glass/Balsa
Lower Skin	1 mm E-Glass/Balsa
Ribs	2 mm E-Glass/Balsa
Front Spar	10 mm (Dia.) Carbon Tube
Rear Spar	2 mm E-Glass/Balsa

Material properties are referenced from Master's Thesis work of Turgut, T .[38].

Table 3.7. Material Properties to be used in Finite Element Analysis [38]

E-glass/Epoxy (E-Glass Fabric) (Test Result)	$E_{11} = 22.29\,\text{GPa}$, $E_{22} = 22.29\,\text{GPa}$, $\nu_{12} = 0.08$ $G_{12} = 3\,\text{GPa}$, $G_{23} = 2.4\,\text{GPa}$, $G_{13} = 2.4\,\text{GPa}$ $\rho = 1450\,\text{kg/m}^3$
Carbon / Epoxy (Unidirectional)	$E_{11} = 115.14\,\text{GPa}$, $E_{22} = 6.71\,\text{GPa}$, $\nu_{12} = 0.28$ $G_{12} = 2.2\,\text{GPa}$, $G_{23} = 2.7\,\text{GPa}$, $G_{13} = 2.7\,\text{GPa}$ $\rho = 1190\,\text{kg/m}^3$
Balsa Wood (Unidirectional)	$E_{11} = 3378\,\text{MPa}$, $E_{22} = 50.67\,\text{MPa}$, $\nu_{12} = 0.229$ $G_{12} = 125\,\text{MPa}$, $G_{23} = 17\,\text{MPa}$, $G_{13} = 182\,\text{MPa}$ $\rho = 160\,\text{kg/m}^3$

3.5. Structural Analysis of Wing

Structural analyses of the wing configurations are performed to decide which configuration will be used in the final configuration. Therefore actual stress and deflection of the wing are not critical for the study and mesh dependency and convergence of the result studies are skipped. Nevertheless, maximum stress locations and magnitudes are interested to compare two different configurations.

Finite element models of the wing structures are created on MSC Patran. Structural components and finite elements representation of the wing configurations are shown in **Figure 3.12.**Wing skin, ribs and spar elements are 2D shell elements, stiffener (**Figure 3.13.a**) and tubular front spar (**Figure 3.13.b**) elements are 1D Beam elements with corresponding cross-sections shown in **Figure 3.13.**
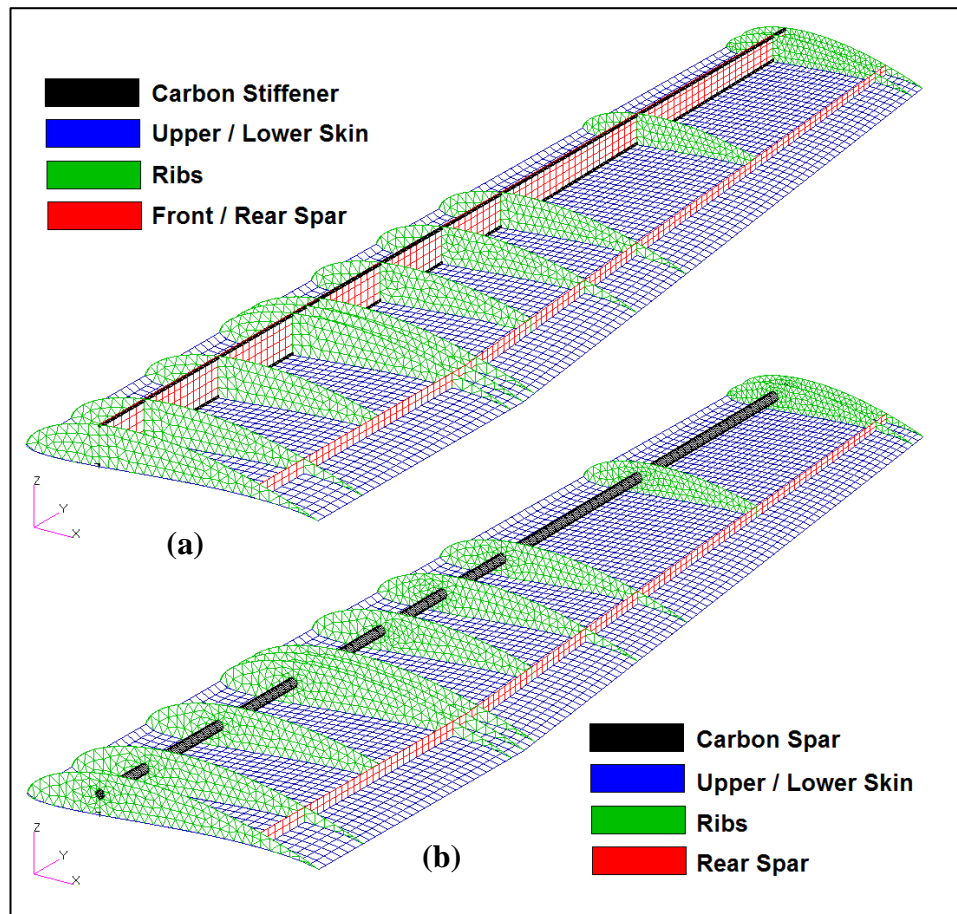
Figure 3.12. Finite element models of I Spar (a) and Tube Spar (b) Structures

129

Elements types and number of elements used in the finite element models are given in **Table 3.8**. Note that, two 1D stiffeners are used in the I-spar configuration and one 1D front spar is used in the tube spar configuration. Additional 2D elements in CQUAD are come from the front spar elements of I-spar configuration.

Table 3.8. Element Types and Number of Elements of Structural Models

Structural Element	Element Type	I Spar Configuration Number of Elements	Tube Spar Configuration Number of Elements
Stiffener & Tube Spar (1D)	CBAR	220	110
Skin & I-Spar (2D)	CQUAD4	7700	7260
Ribs (2D)	CTRIA3	2256	2691

Total		10176	10061

The CBAR element is a six degree of freedom general purpose beam that supports tension and compression, torsion, bending in two perpendicular planes, and shear in two perpendicular planes. Its formulation is derived from classical beam theory. The neutral axis may be offset from the grid points which are useful for modeling stiffened plates [39]. Stiffener element section is shown in **Figure 3.13.a** and tube spar section is shown in **Figure 3.13.b**.
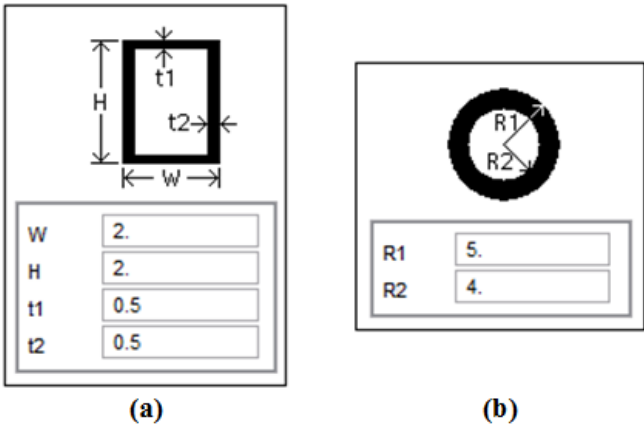
Figure 3.13. CBAR Element Sections (Dimensions are in mm)

3.5.1. Boundary Conditions

Defining boundary conditions properly is very important in finite element analysis. Patran uses to **<T1, T2, T3>, <R1, R2, R3>** notation to define boundary conditions and degree of freedoms. Where "T" represents translation, "R" represents rotation axes in "123" (x, y, z) directions respectively.

Since half wing model is used in the analysis, boundaries of the root rib are constrained as a symmetry plane (T2=0) As the first boundary condition, root rib is not allowed to bend in X (chordwise) axis (R1=0) but it is allowed to rotate in Y (spanwise) axis (R2=1) or move in XZ (symmetry) plane (T1=T3=1) because of the wing twist. Therefore, first boundary condition is defined as;

BC1: <T1 T2 T3> , <R1 R2 R3> = <101>, <010> = 246

Wing is mounted to the aircraft by clamping the first spar section. Therefore, second boundary condition is applied to the first spar sections between root rib and second rib. First sections of the spars are constrained in six degree of freedom which means they are not allowed to move freely or rotate in any direction.

BC2: <T1 T2 T3> , <R1 R2 R3> = <000> , <000> = 123456

Boundary conditions applied on the root rib and first spar sections are shown in **Figure 3.14** and **Figure 3.15.**
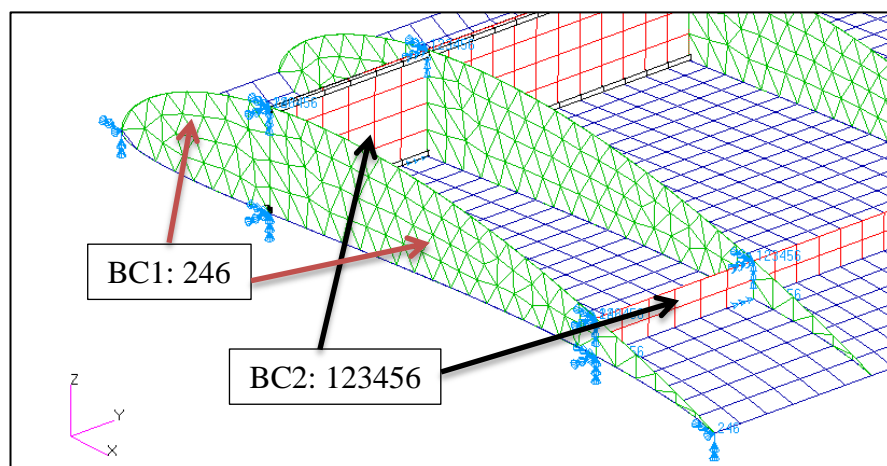
Figure 3.14. Boundary Conditions of I Spar Structure

131
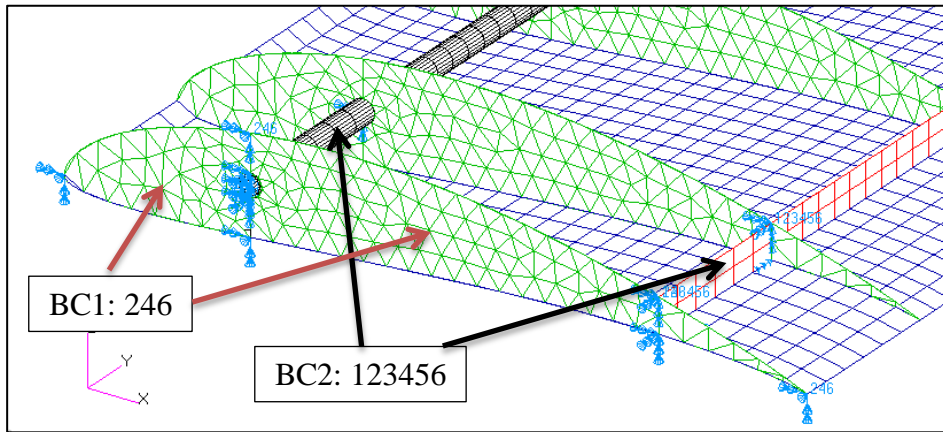
Figure 3.15. Boundary Conditions of Carbon Tube Spar Structure

Ribs of the structural configuration with carbon tube front spar have circular holes on the spar locations and tubular spars are modeled with 1D beam elements. Therefore there is no physical contact between spar holes and 1D spar elements in the finite element model and nodes on these parts do not coincide with each other. RBE2 type Multi-Point Constraint (MPC) rigid bar elements (RBE2) are defined in order to establish rib-spar connection and load transfer. Rib surfaces and 1D spar element is shown in **Figure 3.16** and defined MPC element with connection nodes are shown in **Figure 3.17.**

Figure 3.16. Rib Surfaces and Front Spar (Dot)
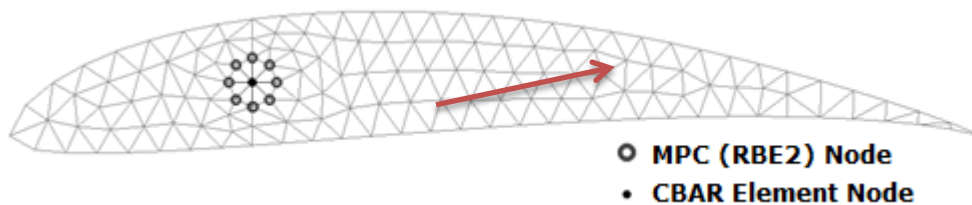
Figure 3.17. Rib Elements (CTRIA3) and MPC (RBE2) Element

3.5.2. Aerodynamic Load Interpolation

Pressure load determined from CFD analysis is applied on the finite element model. Since CFD mesh has finer mesh with small sized elements and structural elements have coarser mesh with relatively big elements, mesh and pressure data is needed to be interpolated on coarser mesh structural model. Original pressure data exported from CFD and interpolated data contours are shown in **Figure 3.18.**
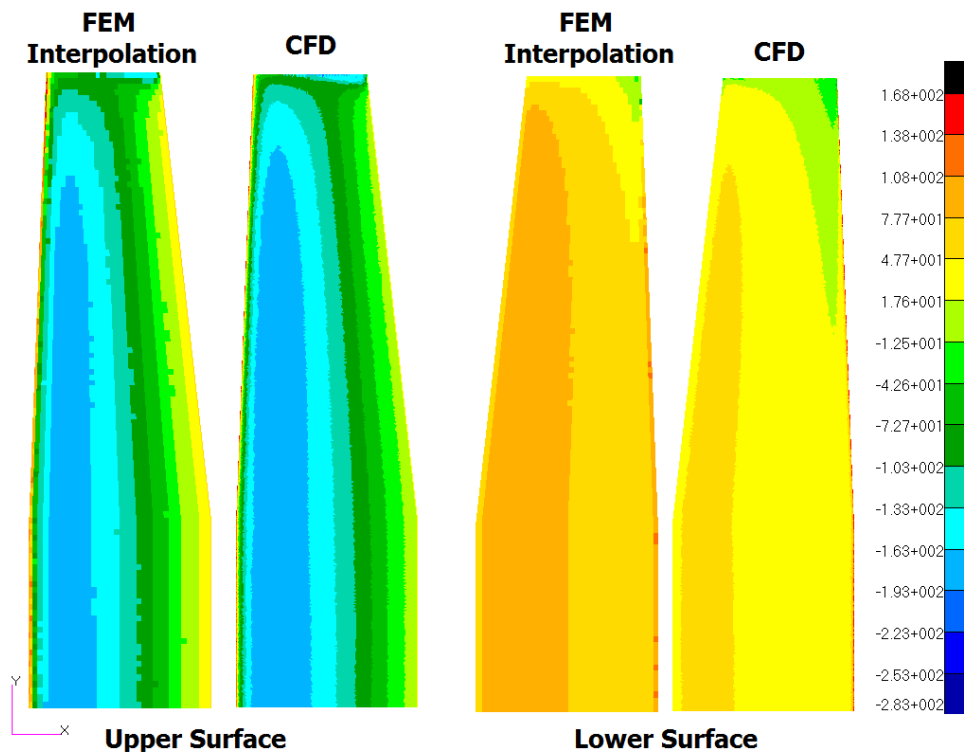
Figure 3.18. Pressure Load Interpolation

3.5.3. Structural analysis Results

Global stress is concentrated on the upside of the front spar for I spar configuration and mid panel of the upper surface for carbon tube spar configuration. As can be seen from **Figure 3.19**, stress magnitude is higher for carbon tube spar configuration which means safety factor is smaller.
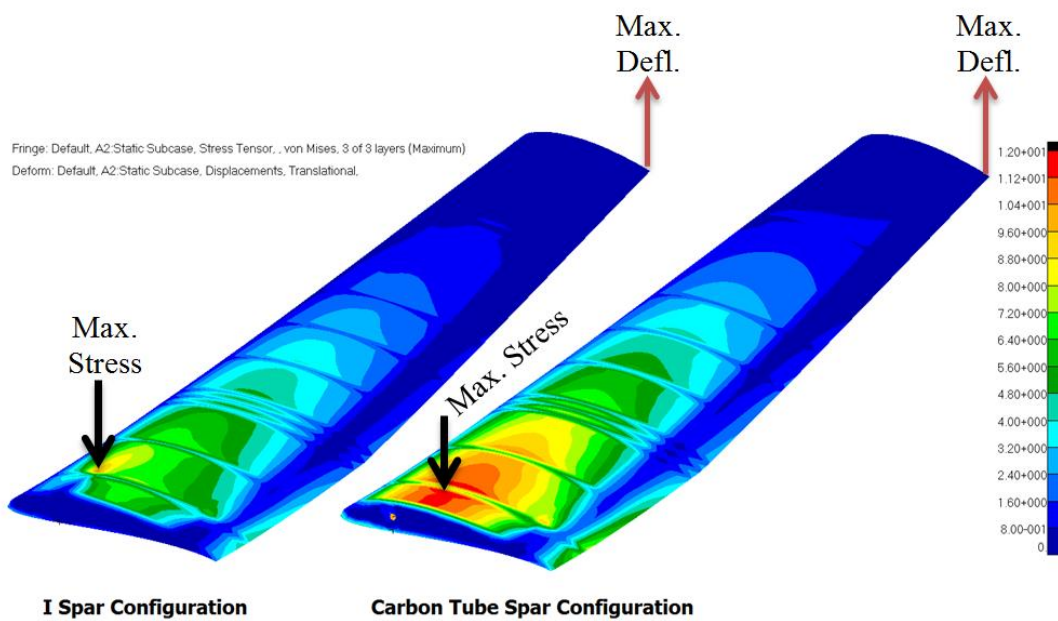
Figure 3.19. Maximum Equivalent Stresses on the Wing Structures

Maximum stress magnitudes and locations are given in **Table 3.9.**

Table 3.9. Global Maximum Stress and Deflections

	I Spar	**Location**	**Carbon Tube Spar**	**Location**
Maximum Stress	10.3 MPa	Front Spar	11.9 MPa	Skin Panel
Maximum Deflection	5.84 mm	Wing Tip TE	8.62 mm	Wing Tip TE

Stress distribution on the front spar for I spar configuration is given in **Figure 3.20**.
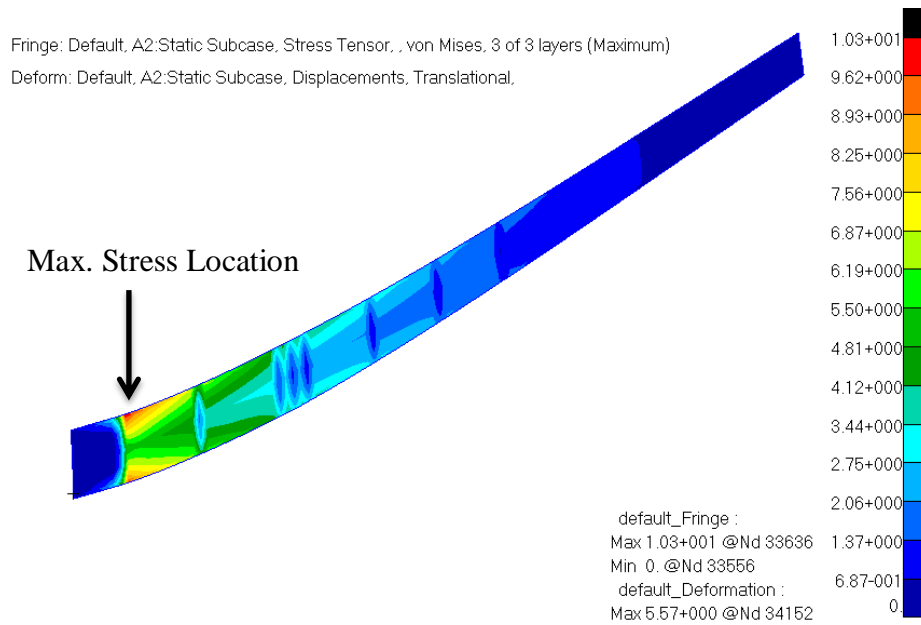
Figure 3.20. Stress Distribution on the Front Spar of I Spar Configuration

Comparison of the maximum stresses carried by rear spar surfaces is given in **Figure 3.21.** Stress magnitude and local deformations are higher for carbon tube spar configuration which are found as 6.49 Mpa – 9.74 MPa, 5.77 mm – 8.59 mm respectively
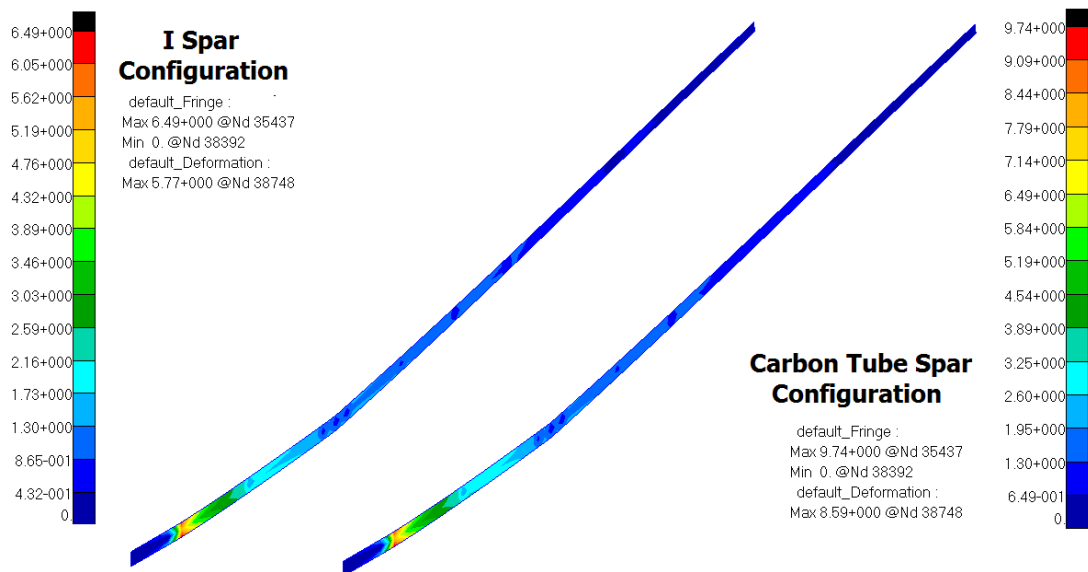
Figure 3.21. Comparison of Stress Distributions on Rear Spar

135

Stress distributions on rib surfaces are shown in **Figure 3.22** and **Figure 3.23**. Again, local maximum stress magnitude is higher for the carbon tube spar configuration and stress concentration at the spar hole on the ribs is noticeable while stress is concentrated at stiffener locations on the front spar for the I spar configuration.
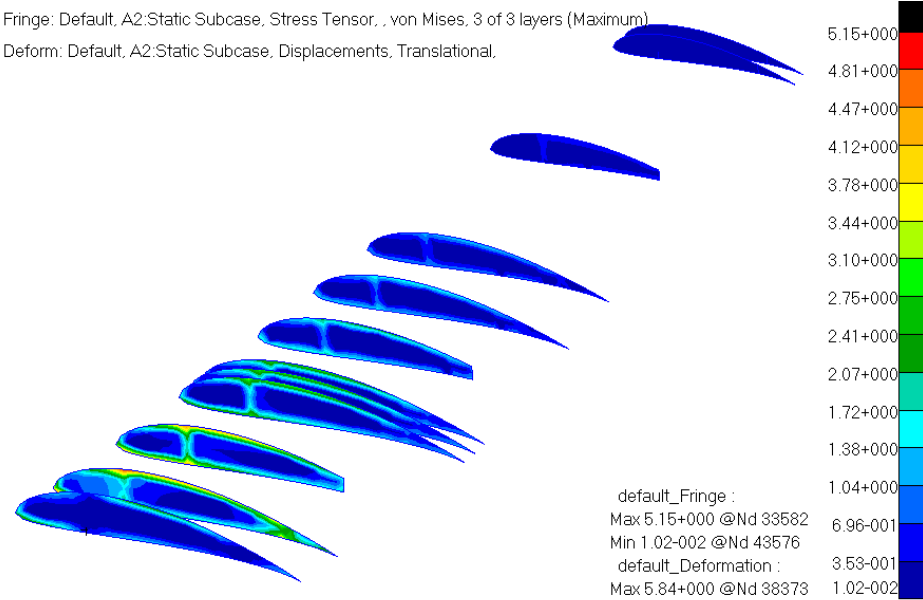
Figure 3.22. Stress Distribution on Ribs of I Spar Configuration
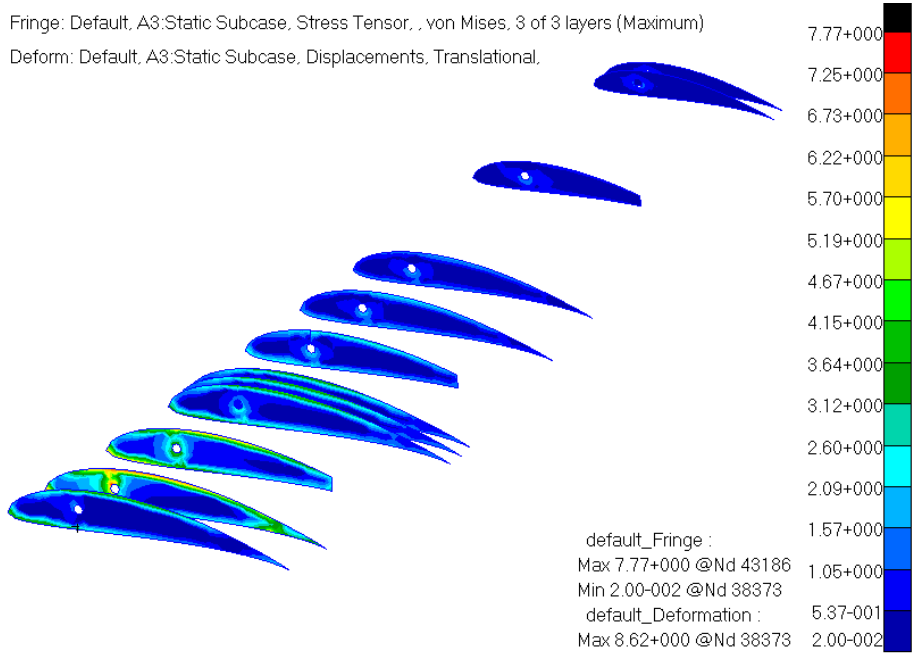
Figure 3.23. Stress Distribution on Ribs of Carbon Tube Spar Configuration

136

In order to compare stress distribution on ribs in detail, third ribs are chosen to compare which are not constrained by boundary conditions. As can be seen from **Figure 3.24**, local stress is concentrated at the stiffener location for I Spar configuration and stress concentration is maximum at upper mid panel location for carbon tube spar configuration. Similarly, magnitude of the maximum stress is higher for the carbon tube spar configuration. Low stress areas on the ribs can also be seen from stress contours clearly. Blue shaded areas are exposed to smaller stress values and they can be cut out for lightening. Openings on the rib model shown in **Figure 3.9** are perfectly fitted to the low stress locations on ribs. These openings are considered in the detail design.
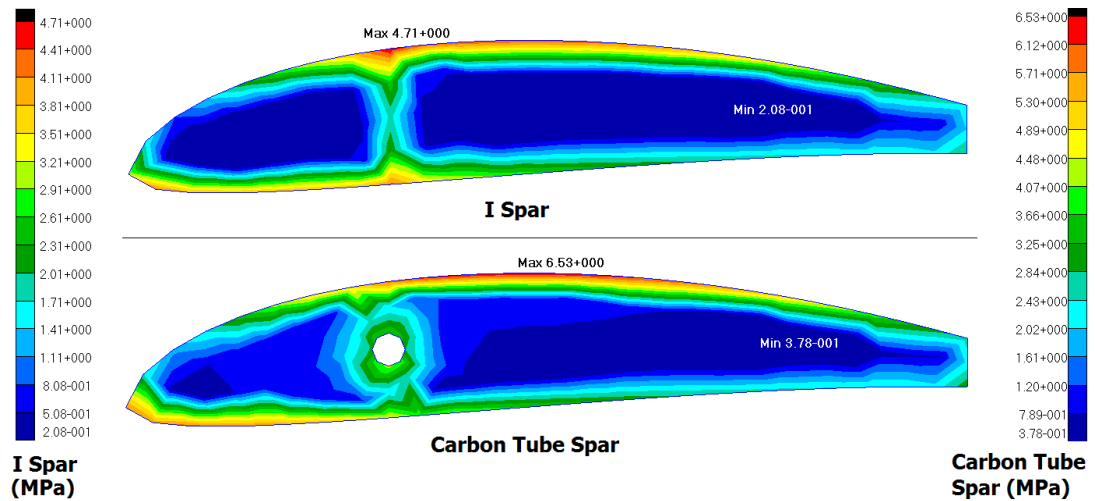
Figure 3.24. Comparison of Maximum Stress Distribution on Third Ribs
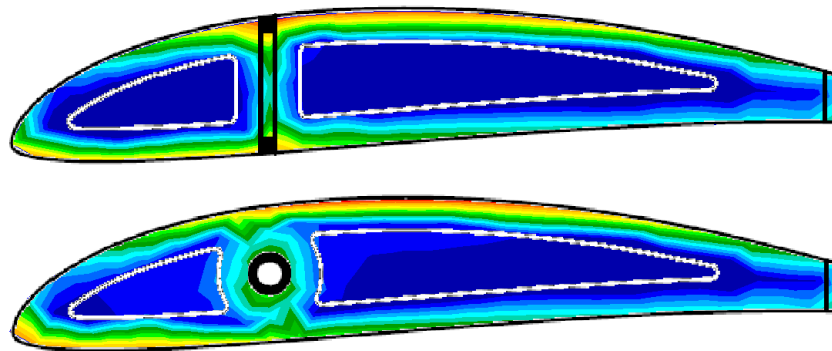
Figure 3.25. Positions of the Rib Openings

3.5.4. Structural Layout of the Wing

Structural layout of the wing is decided after examination of the structural analysis results. According to these results given in the previous section, I spar configuration is decided as the final structural layout.

Maximum stresses on the structural components of I spar configuration are lower and stresses are distributed between rib-spar and wing skin. Furthermore, maximum bending stress on the structure due to aerodynamic load is concentrated on upper surface mid panel for the tubular spar configuration while skin stresses are distributed to the front spar and ribs for I spar configuration.

Concentrated skin stresses of the tubular spar configuration may cause delamination of the skin material due to buckling problem. If an initial defect of adhesion between e-glass and balsa layers is assumed, which is highly expected in hand lay-up manufacturing methods, buckling of the defected area may cause generation and propagation of the delamination [40].

CHAPTER 4

DETAIL DESIGN

4.1. Introduction

In this chapter, detail design of the aircraft is presented. Overall design and sub-components of the aircraft are specified and weight of the design is checked to ensure MTOW of the aircraft constrained by Article (2.3) of SHT-İHA regulations [13] is not exceeded.

Detail design phase is defined as "nuts and bolts" phase of airplane design. Designing each individual rib, spar, section and skin takes place of the current design phase [15] and actual weight of the aircraft is determined by counting weights of these components. As mentioned, mainly composite materials are used in the current design, which are manufactured by hand lay-up – vacuum molding methods. However, uneven material density of balsa core material, possible composite manufacturing defects due to excess resin usage, over-impregnated or unwetted zones makes difficult to estimate material weights and reduces precision of the weight estimation. In order to make more precise weight estimation, composite material densities are referenced from the previous mini UAV design and manufacturing project ([41], [42]) studied to experience design and manufacturing methodology.

Design for manufacturing and assembly (DFMA) and portability issues are also explained in the detail design phase. Payload bay configurations are presented, system components are placed and center of gravity location is checked for the detail design. Finally, design of the aircraft is completed and it is ready to be manufactured at the end of this study.

4.2. Composite UAV Manufacturing Study

In order to experience manufacturing techniques and methodology of a composite Structure Mini UAV, "HUAVN" hand-launched Mini UAV was designed and manufactured in a particular study [41], [42]. Composite aircraft components are manufactured with wet hand lay-up method. General sizing of the HUAVN is given in **Table 4.1** and manufactured UAV is shown in **Figure 4.1.**

Table 4.1. General Sizing of HUAVN [41], [42]

Empty Weight	MTOW	Span: b (m)	Length: L (m)
2 kg	3 kg	1.8 m	1.15 m

Figure 4.1. HUAVN Composite Mini UAV [41], [42]

Figure 4.2 shows that the manufacturing process of wing and tail skin surfaces while glass fabric laid on the balsa core material is impregnating with epoxy resin by hand.
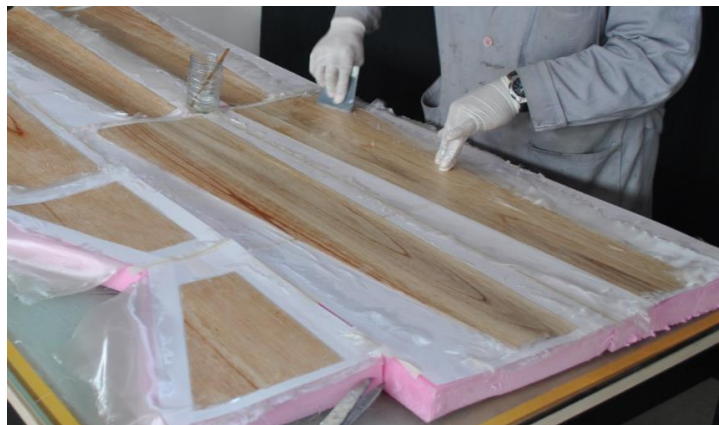
Figure 4.2. Wet Lay-up of the Wing-Tail Skin Materials

140

Vacuum bagging is a common application for hand lay-up manufacturing method. Wetted material laid on the mold is usually consolidated by a vacuum bag and entrapped air is removed by the vacuum pressure.. Vacuum bagging components are shown in **Figure 4.3.**
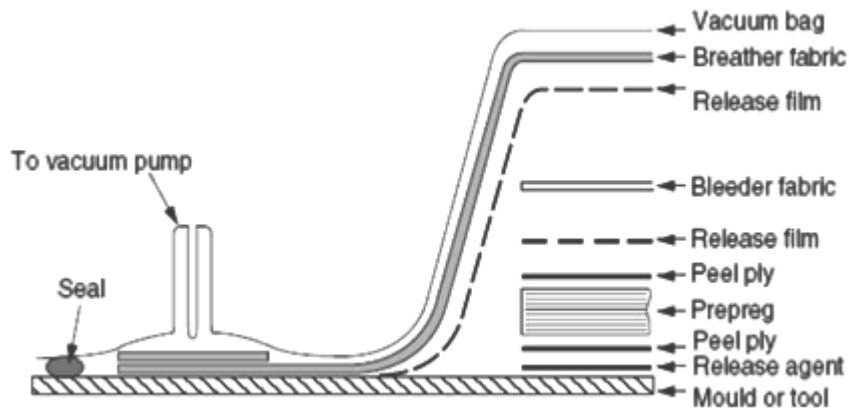
Figure 4.3. Vacuum Bagging Method [43]

After vacuum bagging and curing processes are ended, final products are ready to be assembled on the wing and tail structure. Vacuum bagging and final products are shown in **Figure 4.4.** After final product weights and dimensions are measured, average material densities, given in **Table 4.2,** are determined**.**
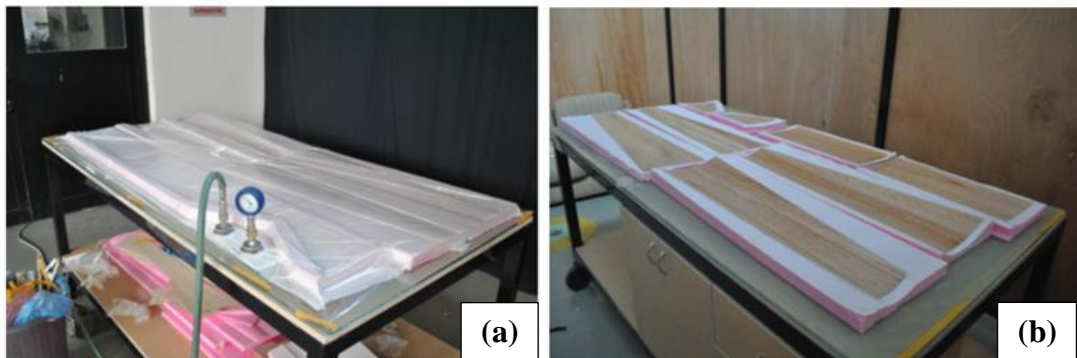
Figure 4.4. Vacuum Bagging of the Wing-Tail Surfaces (a) and Cured Products (b)

Table 4.2. E-Glass/Balsa Material Densities

Skin Material and Thickness	Density
E-Glass/Balsa – 1 mm	380 kg/m^3
E-Glass/Balsa – 2 mm	280 kg/m^3

4.3. Detail Design

Detail design of the aircraft is completed by taking design for manufacturing and assembly (DFMA) issues and portability into account. Fuselage-wing-tail joints are also shown in detail in following sections. During the detail design phase, CAD model of the design is constructed in CATIA. Overall detail design of the aircraft is shown in **Figure 4.5.a.** In order to show internal structure of main components clearly, skin on the aircraft is hidden in **Figure 4.5.b.**
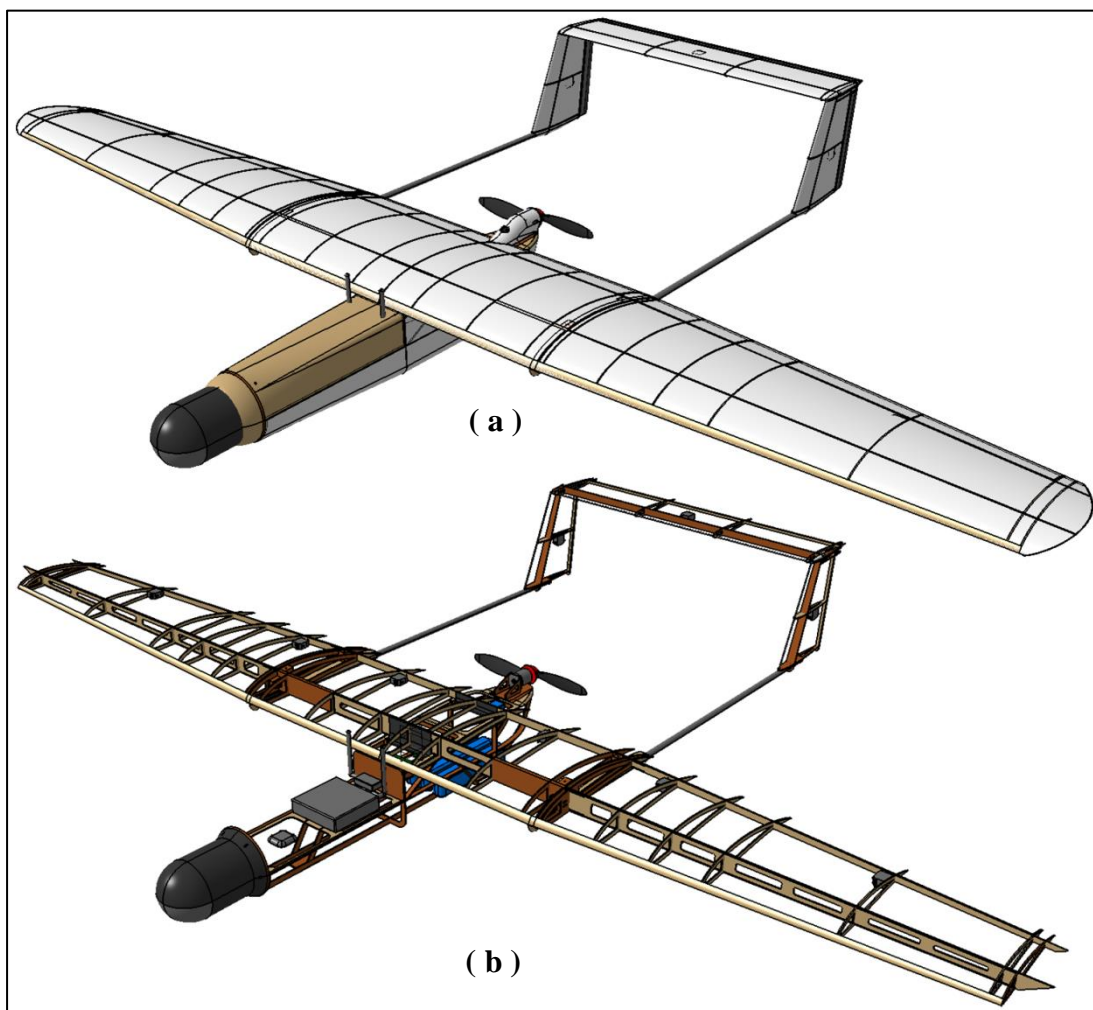
Figure 4.5. Detail Design of Demircan Mini UAV

4.3.1. Design for Manufacturing and Assembly

In order to ease manufacturing and decrease product costs, design for manufacturing and assembly (DFMA) is very important for detail design phase. Design of modular parts with self-locating and fastening features, design for a base part to locate other parts [44] features of DFMA is applied on the current design. DFMA also aims to reduce material, overhead and labor cost. Therefore, internal structures of the fuselage, wing and tail are all designed with self-locating ribs, spars, bulkheads and longitudinal frames for the ease of manufacturing. System components of the aircraft are located on floors which are connected to the respective bulkheads and longitudinal frames which are the base structures of the fuselage.

Self-locating wing rib placement is shown in **Figure 4.6**. Firstly ribs are placed from lower slots on the ribs and fixed with epoxy adhesive to the correspondent slots located on the spar. Once all ribs are placed and fixed, upper stiffener can be placed to the upper slots on ribs. Application of the self-locating slot feature is shown in **Figure 4.7**.
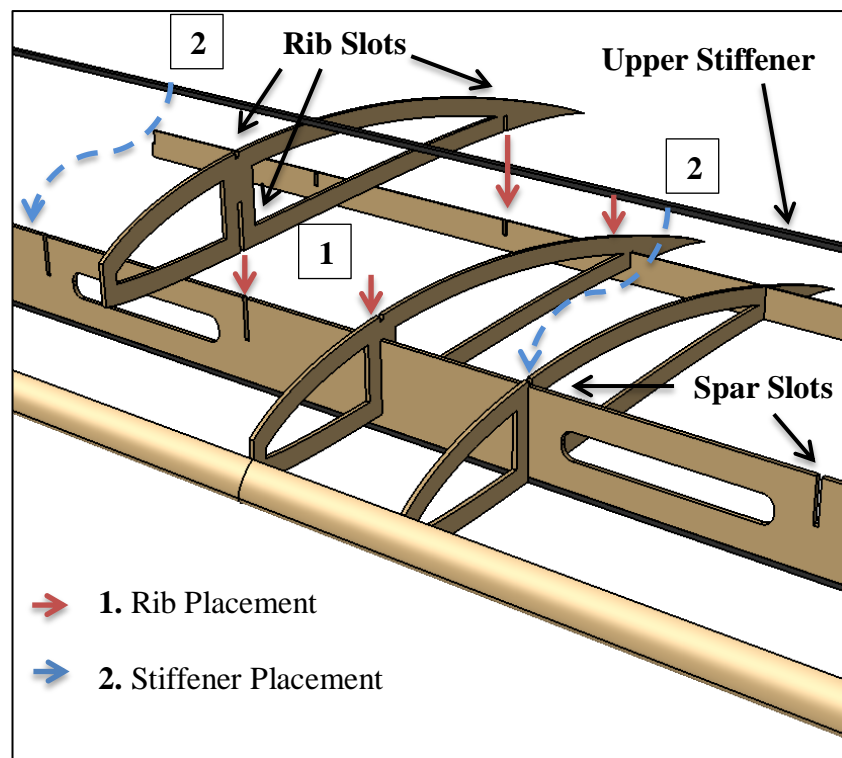
Figure 4.6. Self-Locating Slot Rib Placement

143

Figure 4.7. Rib Placement Application [42]

4.3.2. Assembly Design

Assembly design is performed to divide aircraft components in portable sizes or modules in order to satisfy portability requirement. Divided parts of the aircraft can be re-assembled in the operation field. Motor part is an individual module allows changing motor, motor mount and motor case together if needed. Components and assembly design of Demircan Mini UAV is shown in **Figure 4.8**.
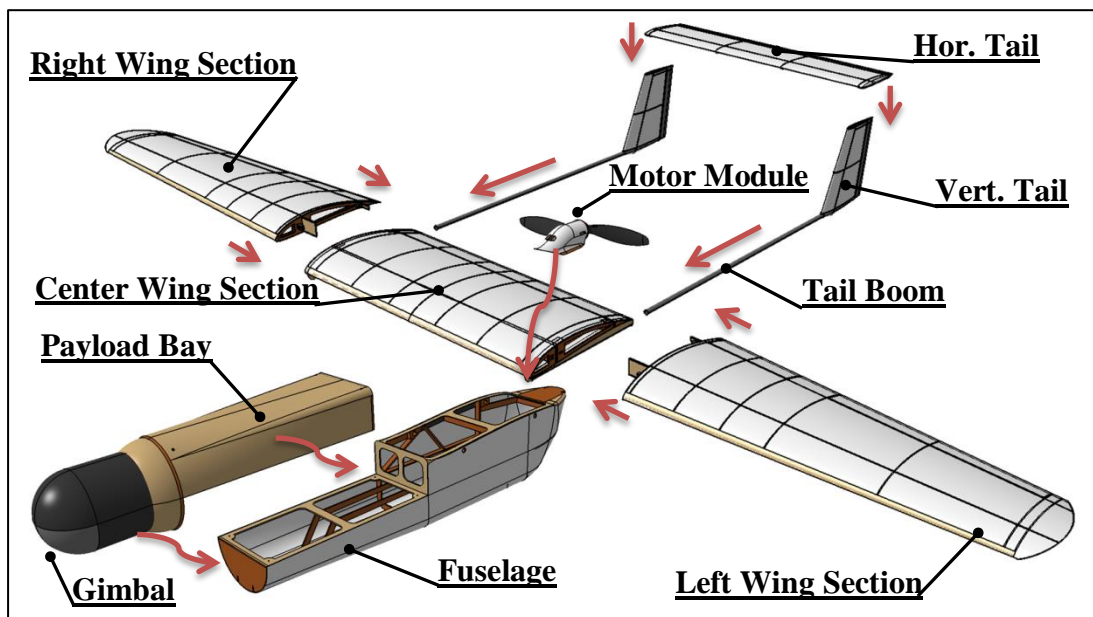
Figure 4.8. Assembly Design of Demircan Mini UAV

144

4.3.3. Portability

Portability of the Demircan Mini UAV is the design requirement. Demounted aircraft should be fitted in a case carried by one personal. Placement of the demounted aircraft in a case and dimensions of the case is shown in **Figure 4.9**. Small case dimensions allow satisfying the portability requirement which are determined as $(1m) \times (36\ cm) \times (40\ cm)$.
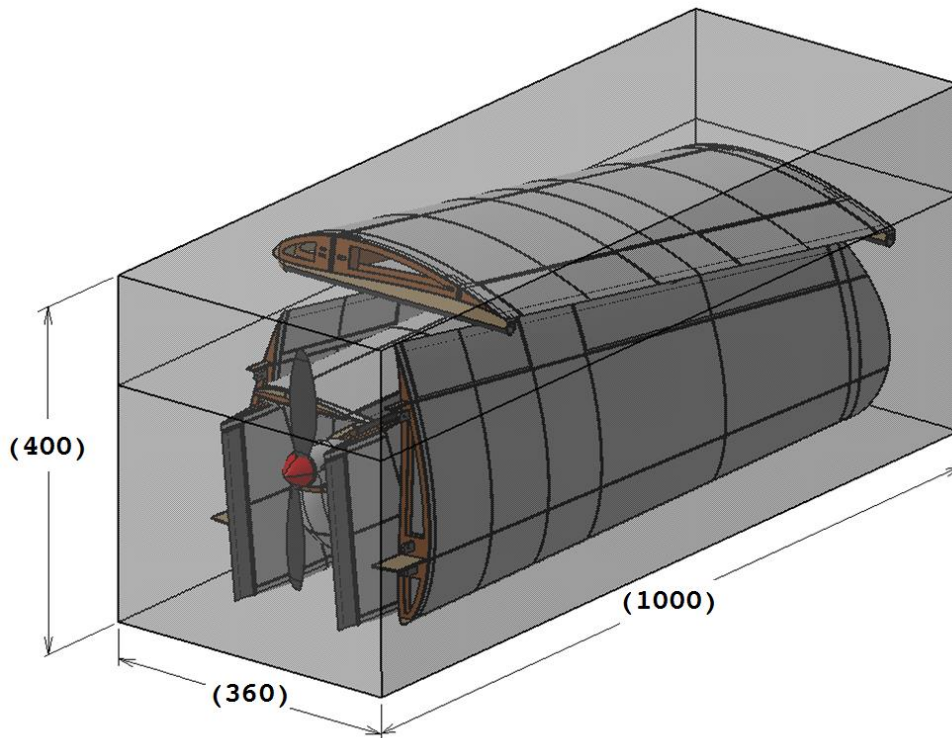
Figure 4.9. Demounted UAV in a Case

(Dimensions are in mm)

4.3.4. Fuselage – Wing – Tail Joints

Wing – body connection is one of the most problematic issues of DFMA process. Since bending moment of the wing maximized at the center (symmetry plane) of the wing, structural failure commonly occurs at the wing center. According to FEM analysis results, structural stress on the wing root can be distributed by clamping the spar. Therefore wing center is reinforced with carbon fiber – epoxy layers. In order to assemble center wing section to the body, carbon tubes are placed to the lower sides of the front and rear spars as a female joint. Spars and carbon tubes are bonded together with the carbon fiber – epoxy reinforcement. By this way, clamped like wing boundary is satisfied as mentioned in the FEM analysis.

Center wing assembly is conducted as follows; firstly wing is aligned to the wing location then fixed with connector pins from the side holes reinforced by carbon plate and plywood hard points on the fuselage structure. Finally, connector pins are secured by fixing the connector caps. Assembly procedure is shown in **Figure 4.10.** Detail of the carbon plate and plywood reinforced wing joint on the fuselage is shown in **Figure 4.11.**
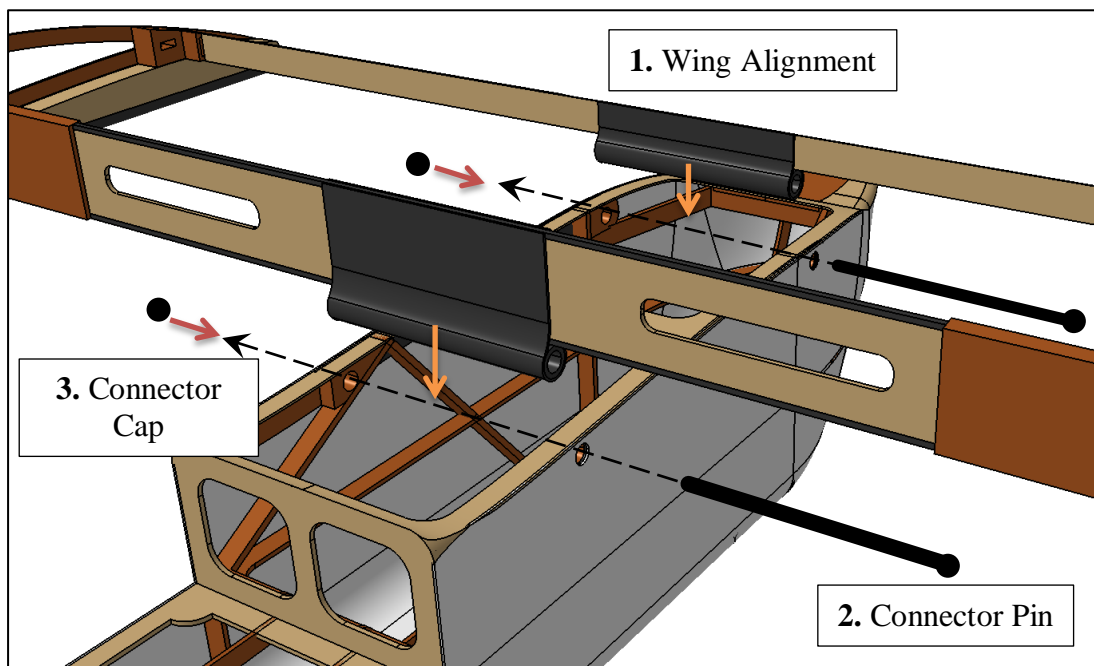
Figure 4.10. Wing and Body Joints and Assembly
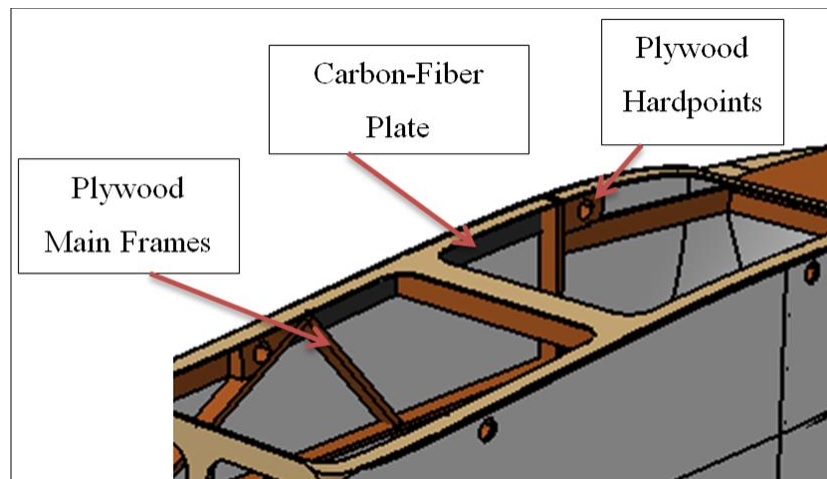
Figure 4.11. Detail of the Wing Joint on the Fuselage

Joints of the center wing section and outer wing sections are designed as a multi-joint. Both center wing and outer wing sections and tail boom are assembled at once. After all components are joined together, wing-boom connector pins are placed to secure all components at the same time. Meanwhile, flap and aileron servo connections are also established. Spar extensions on the outer wing enter to the E-Glass Fiber reinforced plywood guides located on the center wing section. Assembly procedure of the wing – tail boom is shown in **Figure 4.12.** Due to limited time, structural analysis of the wing – tail boom joints are not covered in the current study.
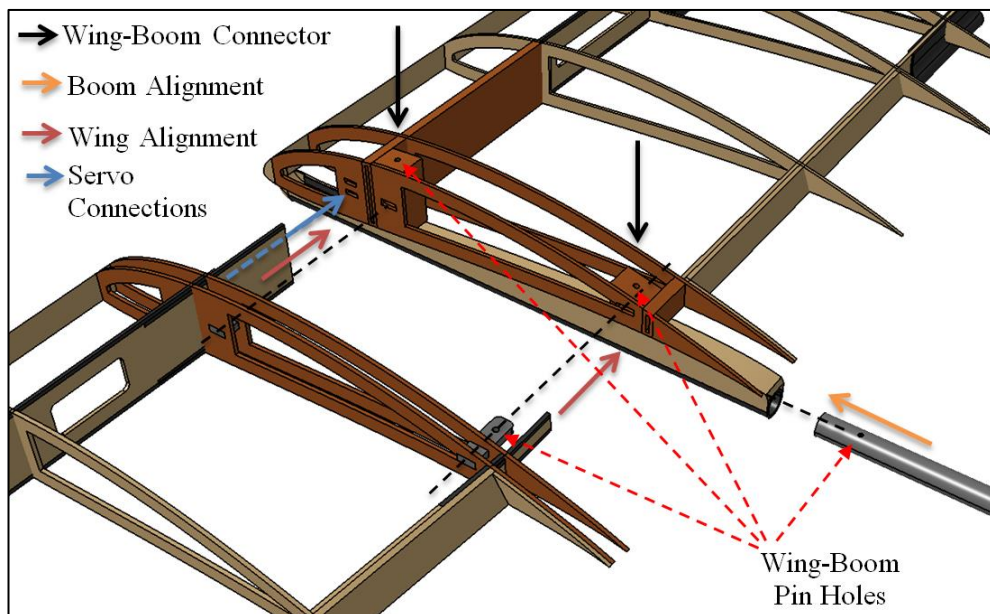
Figure 4.12. Wing and Tail Boom Joints and Assembly

147

Horizontal Tail – Vertical Tail is assembled by fitting screw. Rudder and elevator servo connections are established at the same time. Tail assembly is shown in **Figure 4.13.**
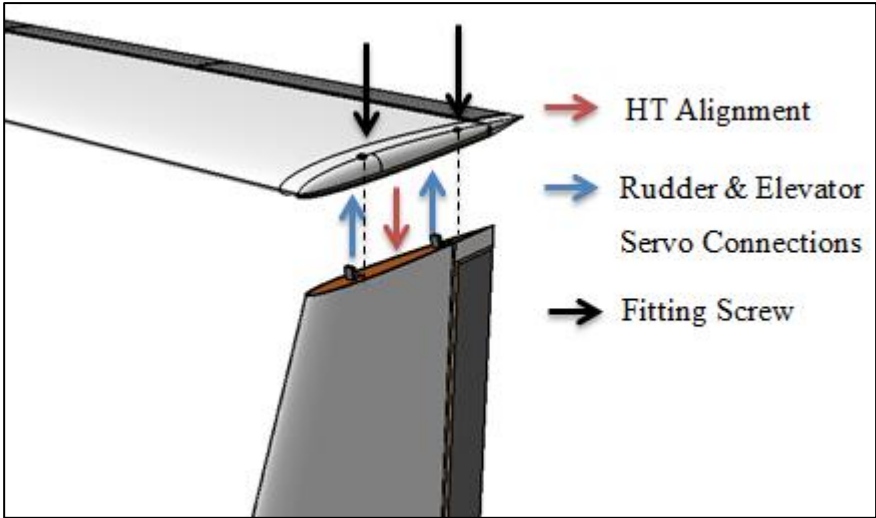
Figure 4.13. Horizontal Tail and Vertical Tail Connection

Rudder and servo cables pass through inside of the carbon booms while one boom carries rudder servo cable; the other boom carries elevator servo cable. Servo connection diagram is shown in **Figure 4.14.**
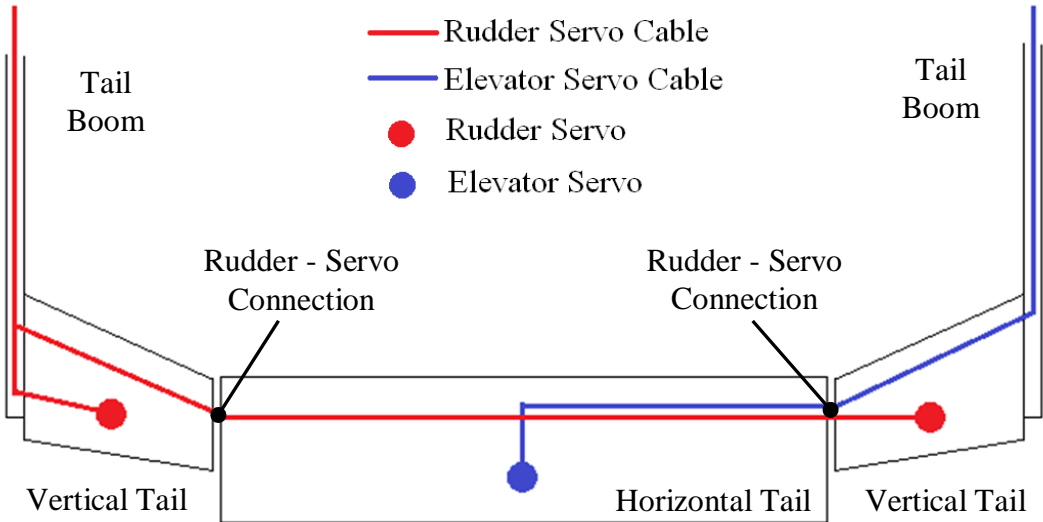
Figure 4.14. Tail Servo Connection Diagram

4.3.5. Payload Bay

Payload bay is a modular component of the design which may be designed differently for a particular mission by taking 1.5 kg of maximum payload capacity into account. For the current design payload bay consists of 3 parts. Main frame and payload bay hatch are shown in **Figure 4.15.** ISR Mission payload, the gimbal for the current design, is located on the front wall of the payload bay which is shown in **Figure 4.16.a**.
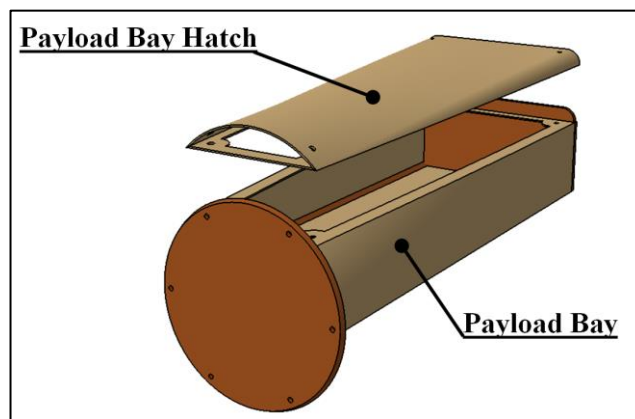
Figure 4.15. Payload Bay

In order to provide multi-mission capability to the design, different system components related to the mission can be located to the payload bay. For example, a gimbal can be attached to the nose for ISR mission (**Figure 4.16.a**), experimental data acquisition unit can be placed to the payload bay and a probe can be placed with a streamlined nose (**Figure 4.16.b**) and streamlined nose can be attached for different missions or empty weight flights (**Figure 4.16.c**).
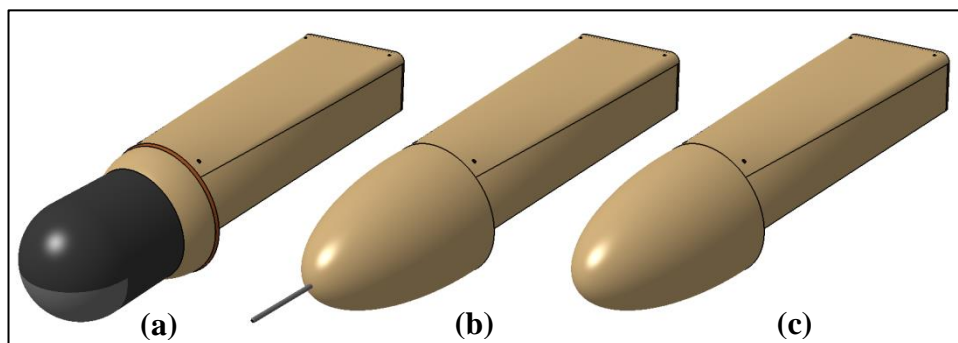
Figure 4.16. Payload Bay Configurations

149

4.3.6. Fuselage

Fuselage is mainly constructed from plywood frames. System components are also mainly attached to the longitudinal frames with individual floor panels. Landing gear ports are located on the bottom frames and main landing gear port is supported with two vertical and transverse frames which are directly connected to the carbon plate reinforcement of wing joints. Hard points of the wing joint are supported by both fuselage frames and carbon plate reinforcement. Connection point of the motor module is supported by rear of the longitudinal frames and hard point of the wing joint. Detail design of the fuselage is shown in **Figure 4.17.**
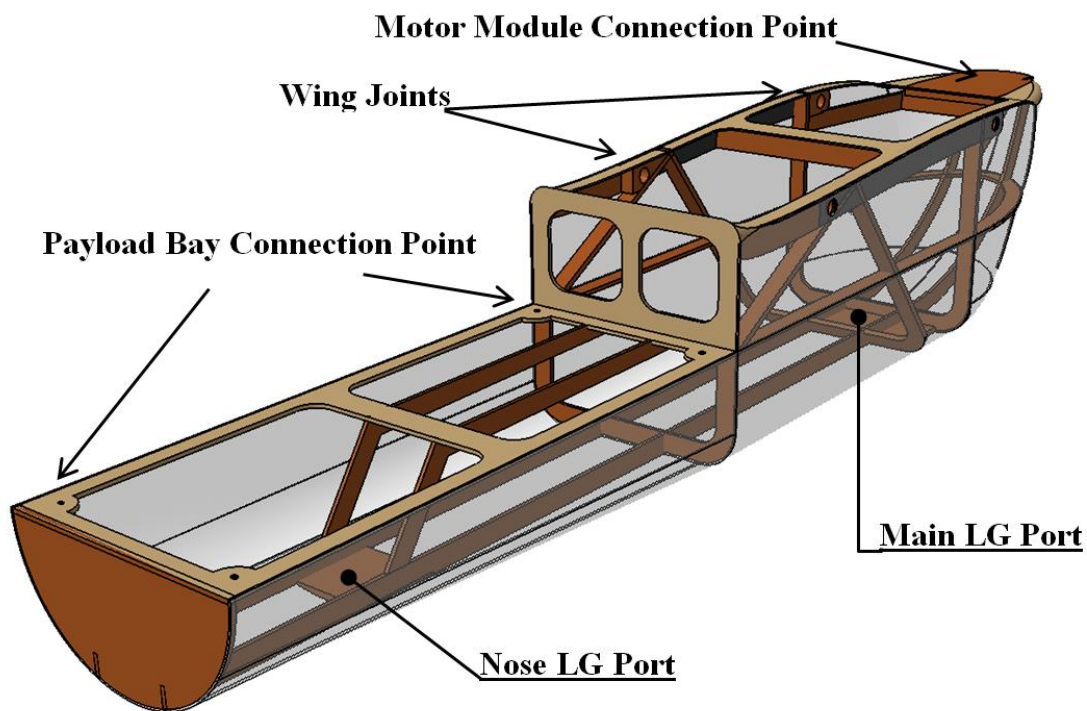
Figure 4.17. Detail Design of the Fuselage

4.4. System Components

System components of the aircraft are same as given in **Section 2.16.** During the conceptual design, system component locations were defined as point masses roughly. After detail design is completed, all component sizes, locations and weights are determined more precisely. Aircraft system components located on the fuselage are shown in **Figure 4.18**, Component weights and center of gravity locations are given in the following section.
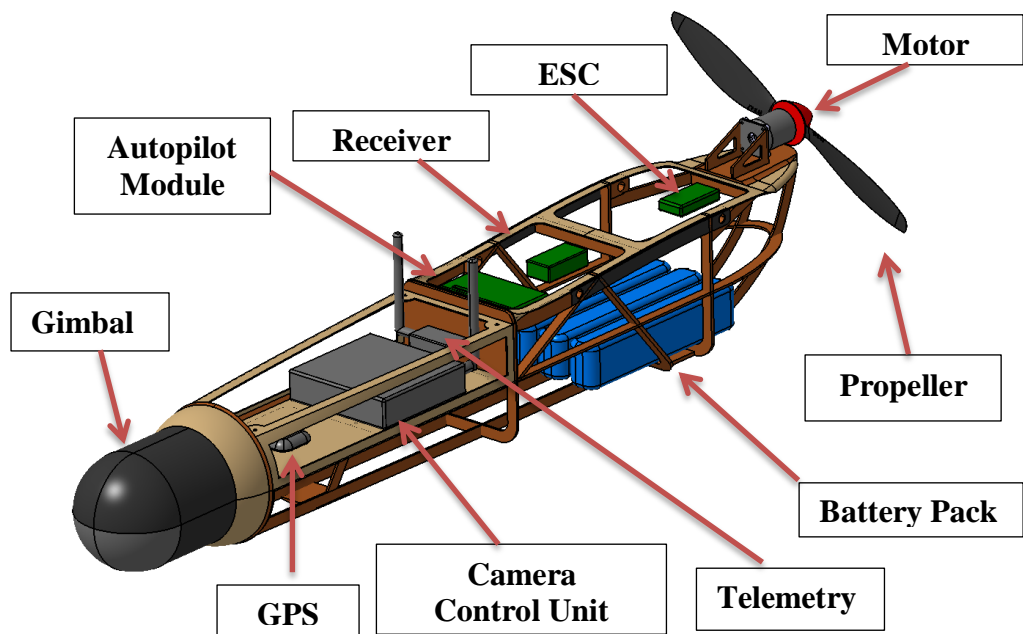
Figure 4.18. Aircraft System Components Located on the Fuselage

4.5. Weight Check and CG Location

All components of the aircraft are determined and located in the detail design phase. As mentioned before overall weight and center of gravity location are checked in this section. Comparison of conceptual design and detail design weight estimations are given in **Table 4.3**. Servo weights are included to wing and tail components.

As given in **Table 4.3**, structural weights used in the conceptual design phase and detail design results are quite close to each other. Structural weights given in the conceptual design phase has been estimated by using weight per unit wetted area values determined from the HUAVN project [41], [42]. Thus, difference between results is minimized and overall weight estimation of the conceptual design phase is verified.

Table 4.3. Comparison of Conceptual and Detail Design Weights

Component	Conceptual Design Weight Estimation Mass (g)	Detail Design Weight Estimation Mass (g)
Wing	860 gr	884.8 gr
Horizontal Tail	170 gr	133.6 gr
Vertical Tail	140 gr	191.2 gr
(Total Tail)	(310 gr)	(324.8 gr)
Fuselage	396 gr	302.7 gr
Prop System	129 gr	122.3 gr
Battery	934 gr	990 gr
Camera System	1140 gr	1130 gr
Avionics	231 gr	257.9 gr
Total Mass	**4000 gr**	**4012.5 gr**

All components of the detail design and center of gravity locations are given in **Table 4.4.** System components are located to ensure center of gravity location is preserved between **47.2% - 51.6%** of the root chord as defined in the conceptual design chapter. CG location is preserved at **47.95%** of the root chord.

Table 4.4. Aircraft System Components and CG Locations of Detail Design

Component	Mass (g)	CG,x (mm)	CG,y (mm)	CG,z (mm)
Left Wing	206.6	53.49	658.37	18.217
Center Wing	381.6	66.992	0	9.888
Right Wing	206.6	53.49	-658.37	18.217
Horizontal Tail	118.6	868.013	0	201.456
Vertical Tail 1	80.6	603.138	-333	34.464
Vertical Tail 2	80.6	603.138	333	34.464
Fuselage	302.7	-43.216	0	-53.812
Gimbal	800	-446.546	0	-60
Cam Control Unit	330.0	-179.799	-0.301	-43.002
Motor	109.3	306.175	0	19.868
Propeller	13.0	325	0	19.868
Servo - HT	15.0	870	-15	201.442
Servo - VT 1	15.0	830	-333	82.812
Servo - VT 2	15.0	830	333	82.812
Servo - RF1	15.0	145	440	14.909
Servo - LF1	15.0	145	-440	14.909
Servo - RF2	15.0	155	180	13.14
Servo - LF2	15.0	155	-180	13.14
Servo - RA	15.0	110	860	20.558
Servo - LA	15.0	110	-860	20.558
Main Battery	330.0	105	-34	-88.398
Main / Aux. Battery	330.0	105	0	-88.398
Main Battery	330.0	105	34	-88.398
Receiver	11.0	39.429	0	-30.017
Autopilot Module	40.0	-39.138	0	-30.142
GPS	17.0	-298.803	0	-54.469
Telemetry	50.0	-104.875	13.105	-24.491
ESC	40.0	216.599	0	-12.646
Wiring	100.0	220	0	0

Σm (gr)	CG,x (mm)	CG,y (mm)	CG,z (mm)
4012.5	7.300	0.082	-29.917
X_{CG} (%c_{root})	47.95%		

4.6. End of the Detail Design

Detail design phase of the aircraft has been discussed in this chapter. Design for manufacturing and assembly (DFMA) issues are considered, sub-components of the aircraft have been specified and weight and center of gravity location of the design has been checked.

Main purpose of the detail design is to present ready to be manufactured design. Overall design is constructed in CATIA in detail then weights and center of gravity location of the design is determined at once. Total weight and center of gravity location is preserved by making minor design corrections in detail and changing system component locations slightly. Assembly and portability of the design is also provided in the detail phase and finally detail design of Demircan Mini UAV is completed by the end of this phase and it is ready to be manufactured.

CHAPTER 5

CONCLUSION

In this thesis study, aerodynamic and structural design of an electric powered portable Mini UAV which has variable multi-mission capability is conducted. Conceptual design, wing analysis and detailed design is the main objective of this work. Different wing structure configurations are compared by performing finite element analysis and structural layout for the wing is decided since wing is the main structural weight contributor. At the end of this study, design is completed and it is ready for manufacturing.

In the conceptual design phase, detailed performance analysis is completed. However, drag model of the design is needed to be improved for high camber airfoil configurations. Therefore it is noticed that CFD analysis for the basic wing and aircraft configuration should be examined in the early stages of the conceptual design phase in order to check design parameters.

Dynamic thrust estimation model proposed in the conceptual design chapter is also needed to be validated experimentally at different altitudes and different motor-propeller combinations are needed to be studied in terms of propeller pitch, diameter and electric motor parameters like the KV value of the electric motor in. Detailed dynamic thrust experiments are suggested to investigate altitude effects (AF) on the propeller performance and overall propulsive performance for electric powered aircraft in terms of altitude factor (AF) and power correction factor (PcF).

CFD analysis of the wing is performed for positive low angle of attack (PLA) limit load condition. However, positive high angle of attack (PHA) limit load condition is not studied in this work. It is realized that PHA analysis is also important for

155

structural aspects since pressure center shift toward to the trailing edge and it should have been covered in the study.

Structural analysis of the wing and decision of the structural layout of the wing is presented but overall analysis of the design is not covered in this study. Especially, aeroelastic analysis of the twin boom design and impact analyses for landing loads are suggested for further structural examination.

In conclusion, structure of this thesis is based on design and analysis of an electric powered portable mini UAV with fixed pitch propeller and design phases are presented in detail until detailed design. From now on, prototype of the design will be manufactured and further developments will be completed.

5.1. Future Work

Comprehensive CFD analyses are not covered in this study, only structural load determination is examined for structural analysis purposes. Therefore, detailed CFD analysis will be completed for different configuration layouts which are focused on fundamental parameters of the whole aircraft at different angle of attacks and altitudes including PHA limit load analysis.

Structural analysis of the joints located on wing and fuselage are not covered in this study. Structural analysis of the wing is performed only to decide on the structural configuration of the wing. Including the joints, structural analysis of the aircraft structure will also be performed as a future work.

Later on, conceptual design process will be optimized by developing a computer program and aircraft performance calculation results will be validated by detailed CFD results. Furthermore aircraft performance calculations will be expanded for fixed pitch propeller propulsion. Detailed propulsion system analysis will be performed and motor-propeller selection will be optimized for different mission configurations and altitudes for the design. Finally aircraft will be manufactured from composite materials as described in the "Detailed Design" chapter and much more optimized and robust design will be presented.

REFERENCES

[1] USICO, European Civil Unmanned Air Vehicle Roadmap: Vol. 1 - Overview, USICO, 2005.

[2] *UAV Types*, Retrieved July 2015, from http://www.theuav.com .

[3] NATO, *UAS Classification Guide*, JCGUAV meeting, September 2009.

[4] Fahlstrom, P. G., Gleason, T. J., *Introduction to UAV Systems*, 1994

[5] Directory of U.S. Military Rockets and Missiles, *Sperry "Flying Bomb"*, Retrieved July 2015, from http://www.designation-systems.net/dusrm/app4/sperry-fb.html .

[6] Directory of U.S. Military Rockets and Missiles, *Kettering Bug*, Retrieved July 2015, fromhttp://www.designation-systems.net/dusrm/app4/bug.html .

[7] Directory of U.S. Military Rockets and Missiles, *Teledyne Ryan, Reconnaissance RPV's,*Retrieved July 2015, from http://www.designation-systems.net/ dusrm/m-34.html.

[8] Directory of U.S. Military Rockets and Missiles, *RQ-2 Pioneer*, Retrieved July 2015, from http://www.designation-systems.net/dusrm/app2/q-2.html.

[9] JAPCC, Strategic Concept of Employment for UAS in NATO, Jan. 2010

[10] *Skylark 1 LE Mini UAV*, Retrieved Aug. 2015, from http://dev.defense-update.com/wp-content/uploads/2011/11/skylark_1-le.jpg

[11] Skrzypietz, T., *Unmanned Aircraft Systems for Civilian Missions*, BIGS Policy Paper No. 1, Feb. 2012.

[12] Gur,O. and Rosen,A., *Optimizing Electric Propulsion Systems for Unmanned Aerial Vehicles*, Journal of Aircraft, vol. 46, no. 4, pp. 1340 - 1353, July - Aug. 2009.

[13] SHGM (DGCA),*SHT-İHA*,2015

[14] UAV Vision,*CM100*,Retrieved July 2015, from http://uavvision.com/wp-content/uploads/2015/05/UAV_VISION_CM100.pdf.

[15] Anderson, John D., *Aircraft Performance and Design*, McGraw-Hill, 1999

[16] *XFLR5*, Retrieved July 2015, from http://www.xflr5.com/xflr5.htm

[17] XFOIL, Retrieved July 2015, from http://web.mit.edu/drela/Public/web/xfoil/

[18] Raymer, Daniel P., *Aircraft Design: A conceptual Approach*, 3rd Ed., AIAA, 1999.

[19] Gudmundsson, S., *General Aviation Aircraft Design, Applied Methods and Procedures*, Butterworth-Heinemann, 2014

[20] McCormick, B. W., *Aerodynamics, Aeronautics and Flight Mechanics*, Wiley, 1979

[21] *UIUC Propeller Database – Volume 1*, Retrieved July 2015, from http://m-selig.ae.illinois.edu/props/volume-1/propDB-volume-1.html

[22] Emax, GT2218, Retrieved July 2015, from http://www.emaxmodel.com/brushless-motor/gt-series-motors/gt2218.html

[23] Ecalc, Retrieved July 2015, from http://www.ecalc.ch/motorcalc.php

[24] PropCalc, Retrieved July 2015, from http://www.drivecalc.de/PropCalc

[25] ATI F/T Sensor: Gamma, Retrieved December 2015, from http://www.ati-ia.com/products/ft/ft_models.aspx?id=Gamma

[26] National Instruments NI USB – 6211 Device Specifications, Retrieved December 2015, from http://www.ni.com/pdf/manuals/375195b.pdf

[27] Archer, R. D., Saarlas, M., *Introduction to Aerospace Propulsion*, Prentice Hall, 1996

[28] Traub, L. W., *Range and Endurance Estimates for Battery-Powered Aircraft*, Journal of Aircraft, vol. 48, no. 2, pp. 703-707, March-April 2011

[29] Iris+ Battery, 3dr Store, Retrieved February 2016, from https://store.3dr.com/products/iris-plus-battery

[30] Y+ Wall Distance Estimation, Retrieved March 2015, from http://www.cfd-online.com/Wiki/Y_plus_wall_distance_estimation

[31] Bakker. A, *Applied Computational Fluid Dynamics: Meshing*, Online CFD Class, Lecture Notes, Retrieved July 2015, from http://www.bakker.org/dartmouth06/engs150/07-mesh.pdf

[32] ANSYS Fluent, Retrieved February 2016, from http://www.ansys.com/Products/Fluids/ANSYS-Fluent

[33] ANSYS, *Fluent 12.0, User's Guide*, April 2009

[34] MSC Nastran, MSC Software, Retrieved February 2016, from
http://www.mscsoftware.com/product/msc-nastran

[35] Patran, MSC software, Retrieved February 2016, from
http://www.mscsoftware.com/product/patran

[36] Gölcük, A. İ., *Winglet Design and Analysis for Low Altitude Solar Powered UAV*, MSc Thesis, Middle East Technical University, 2016

[37] Ortiz, A. D., Quiroz, L.E., &Köck, R. A., Aerodynamic Performance Analysis of a Low-Speed Acrobatic Airplane by Numerical Simulation, Mecánica Computacional, vol. 21, pp. 378-391, October 2012

[38] Turgut, T. *Manufacturing and Structural Analysis of a Lightweight Sandwich Composite UAV Wing*, MSc Thesis, Middle East Technical University, 2007

[39] MSC Software, *MSC. Nastran 2001, Getting Started with MSC. Nastran, User's Guide*, 2004

[40] Bruno, D., Grimaldi, A., *Delamination Failure of Layered Composite Plates in Compression*, International Journal of Solids and Structures, vol. 26, issue 3, pp. 313-330, 1990

[41] Demircan, A., Kayran, A, Kurtuluş, D. F., *Kompozit Yapılı Mini İHA'lar İçin Kalıp Üretim Teknikleri ve Aerodinamik Yüzeylerin Üretimi*, 4. Ulusal Havacılık ve Uzay Konferansı, İstanbul, 2012

[42] Demircan, A., Özkanaktı, M. H., Kırdar, V., Sümer, N.N,   *Portable   Mini UAV: HUAVN,* Project Report, Middle East Technical University, 2012

[43] Miravete, A., *Processing and Manufacturing,* Composite Design Tutorial, Stanford University, 2009

[44] Boothroyd, G., Dewhurst, P., Knight, W. A., *Product Design for Manufacture and Assembly*, CRC Press, 2010

COMPETITOR MINI UAVS

Table A.1. Design Parameters of Competitor UAVs

Competitor	1	2	3	4	5	6	7	8	9	10	11	12	Average	
Wing Span	2.74	2.6	2	2.4	2.2	1.5	2.3	1.7	1.83	2.2	1.7	2.5	2.12	**m**
Length	1.83	1.8	1.2	2.2	1.35		1.32	1.2	1.22	1.2	1.4	1.3	1.46	**m**
MTOM	4.3	4.5	4.5	5.5	4.5	5	5	3.5		3.8	3.2	2.9	4.23	**kg**
Vstall		25			32.4		32.4		34			70	11.72	**m/s**
Vcruise		50	60	65	48.6		50	90					16.14	**m/s**
Vmax	80	100		111	84.6		90		129	85	80		26.57	**m/s**
Ceiling	300	3800	4000	5000	3000	2440		2000		3000			2790	**m**
Range	5	15	15	10	10	10	10	10		5	5	10	9.55	**km**
Endurance	60	210	80	90	90	90	90	72	60	60	60	60	80	**min**

Table A.2. References of Competitor UAVs

1	AeroVironment–Pointer	http://www.designation-systems.net/dusrm/m-151.html
2	AeroVironmen– Puma AE	http://www.designation-systems.net/dusrm/app4/puma.html
3	Baykar –Bayraktar	http://baykarmakina.com/sistemler/bayraktar-mini-iha/?lang=en
4	Elbit –Skylark 1	http://www.israeli-weapons.com/weapons/aircraft/uav/skylark/Skylark.html
5	Hydra Tech – E1 Gavillan	https://www.uvsr.org/docs/Hydra-Technologies_E1.pdf
6	METU – Güventürk	Turgut, T., Manufacturing and Structural Analysis of a Lightweight Sandwich Composite UAV Wing, MSc. Thesis, METU, 2007
7	MKU – Terp 2	http://www.airforce-technology.com/contractors/uav/mku-uav/
8	Nostromo – Cabure 2	http://www.nostromo-defensa.com/eng/cabure.php
9	ST Aero – Skyblade 3	https://www.staero.aero/www/keyoffering.aspx?serkeyid=ODAwMDAwMTg
10	Tasuma – Hawkeye 2	http://www.tasuma-uk.com/tasuma.php?p=32
11	Tasuma – Hawkeye 3	http://www.tasuma-uk.com/tasuma.php?p=63
12	Top I Vision – Casper 250	http://bernkastelvintners.com/files/Casper250UAV.pdf

APPENDIX B

COMPONENT DRAG BUILDUP

V	=13.9 m/s	$\rho_{,1000m}$ =1.1117	kg/m^3
M	=0.04	$\mu_{,1000m}$ =1.758×10^{-5}	kg/ms

Table B.1. Drag Coefficient Contributions of the Components

		Laminar	Turbulent	30% - Laminar 70% - Turbulent
Wing				
Re	247875			
Cf		0.002667	0.005883	
FF	0.973500			
Q	1			
$(C_{D0})_{Wing}$		0.005191	0.011448	**0.009571**

Fuselage				
Re	773510			
Cf			0.004692	
f	7.333333			
FF	1.170475			
Q	1			
$(C_{D0})_{Fslg}$		-	**0.002852**	-

Boom				
Re	10548			
Cf			0.012536	
f	82.0			
FF	1.205109			
Q	1.1			
$(C_{D0})_{Boom}$		-	**0.001001**	-

163

Table B.2. Drag Coefficient Contributions of Tail Components

Horizontal Tail				
Re	136243			
Cf		0.003598	0.006682	
FF	1.005113			
Q	1.08			
	$(C_{D0})_{HT}$	0.001310	0.002432	**0.002096**

Vertical Tail				
Re	145033			
Cf	0.003482	0.006592		
FF	1.005113			
Q	1.08			
	$(C_{D0})_{VT}$	0.000849	0.001605	**0.001378**

APPENDIX C

AERODYNAMIC RELATIONS ASSOCIATED WITH LIFT DRAG AND FLIGHT VELOCITY

$$\frac{L}{D} = \frac{C_L}{C_D} = \frac{C_L}{C_{D0} + K(C_L - C_{L,Dmin})^2} \tag{C.1}$$

$$\frac{d(C_L/C_D)}{dC_L} = \frac{C_D - C_L\left(2K(C_L - C_{L,Dmin})\right)}{(C_D)^2}$$

$$\frac{d(C_L/C_D)}{dC_L} = \frac{C_{D0} - K(C_L^2 - C_{L,Dmin}^2)}{\left(C_{D0} + K(C_L - C_{L,Dmin})^2\right)^2} \tag{C.2}$$

At $(C_L/C_D)_{max}$, numerator is zero

$$C_{D0} = K(C_L^2 - C_{L,Dmin}^2) \tag{C.3}$$

Lift coefficient at $(L/D)_{max}$ is determined as,

$$C_L = \sqrt{\frac{C_{D0}}{K} + C_{L,Dmin}^2} \tag{C.4}$$

By substituting C_L into L/D expression, $(C_L/C_D)_{max}$ can be determined as,

$$\left(\frac{L}{D}\right)_{max} = \left(\frac{C_L}{C_D}\right)_{max} = \frac{\sqrt{\frac{C_{D0}}{K} + C_{L,Dmin}^2}}{C_{D0} + K\left(\sqrt{\frac{C_{D0}}{K} + C_{L,Dmin}^2} - C_{L,Dmin}\right)^2}$$

$$\left(\frac{L}{D}\right)_{max} = \left(\frac{C_L}{C_D}\right)_{max} = \sqrt{\frac{1}{4KC_{D0}} + \left(\frac{C_{L,Dmin}}{2C_{D0}}\right)^2} + \frac{C_{L,Dmin}}{2C_{D0}} \tag{C.5}$$

$V_{(L/D)max}$ is determined bysubstituting C_L expression into the lift equation.

$$L = W = \frac{1}{2}\rho_\infty V_\infty^2 S C_L$$

$$V_\infty = \sqrt{\frac{2}{\rho_\infty}\frac{1}{C_L}\frac{W}{S}}$$

$$V_{(L/D)max} = V_{(T_R)min} = \left(\frac{2}{\rho_\infty}\sqrt{\frac{K}{C_{D0} + K C_{L,Dmin}^2}}\frac{W}{S}\right)^{1/2} \tag{C.6}$$

$$\frac{C_L^{3/2}}{C_D} = \frac{C_L^{3/2}}{C_{D0} + K(C_L - C_{L,Dmin})^2} \tag{C.7}$$

$$\frac{d(C_L^{3/2}/C_D)}{dC_L} = \frac{\frac{3}{2}C_L^{1/2}C_D - C_L^{3/2}\left(2K(C_L - C_{L,Dmin})\right)}{C_D^2}$$

$$\frac{d(C_L^{3/2}/C_D)}{dC_L}$$

$$= \frac{\frac{3}{2}C_L^{1/2}\left(C_{D0} + K(C_L - C_{L,Dmin})^2\right) - 2K C_L^{3/2}(C_L - C_{L,Dmin})}{\left(C_{D0} + K(C_L - C_{L,Dmin})^2\right)^2} \tag{C.8}$$

at $(C_L^{3/2}/C_D)_{max}$ numerator of the equation is zero.

$$\frac{3}{2}C_L^{1/2}\left(C_{D0} + K(C_L - C_{L,Dmin})^2\right) - 2K C_L^{3/2}(C_L - C_{L,Dmin}) = 0$$

$$C_{D0} = \frac{1}{3}K(C_L - C_{L,Dmin})(C_L + 3C_{L,Dmin}) \tag{C.9}$$

and lift coefficient at $(C_L^{3/2}/C_D)_{max}$ is determined

$$C_L = \sqrt{\frac{3C_{D0}}{K} + 4C_{L,Dmin}^2} - C_{L,Dmin} \tag{C.10}$$

166

By substituting **C.10** into **C.7**,$\left(C_L^{3/2}/C_D\right)_{max}$ can be determined as,

$$\left(\frac{C_L^{3/2}}{C_D}\right)_{max} = \frac{\left(\sqrt{\frac{3C_{D0}}{K} + 4C_{L,Dmin}^2} - C_{L,Dmin}\right)^{3/2}}{C_{D0} + K\left(\sqrt{\frac{3C_{D0}}{K} + 4C_{L,Dmin}^2} - 2C_{L,Dmin}\right)^2} \quad \textbf{(C.11)}$$

C.10is substituted again as $\boldsymbol{C_L^*}$in order to simplify further.

$$\left(\frac{C_L^{3/2}}{C_D}\right)_{max} = \frac{1}{4}\frac{\left(C_L^* + 3C_{L,Dmin}\right)(C_L^*)^{1/2}}{C_{D0}} \quad \textbf{(C.12)}$$

$V_{\left(C_L^{3/2}/C_D\right)_{max}}$ is determined by substituting $\boldsymbol{C_L^*}$into the lift equation.

$$V_{\left(C_L^{3/2}/C_D\right)_{max}} = \sqrt{\frac{2}{\rho_\infty}\frac{1}{C_L^*}\frac{W}{S}}$$

$$V_{\left(C_L^{3/2}/C_D\right)_{max}} = \left(\frac{2}{\rho_\infty}\frac{W}{S}\left(\sqrt{\frac{3C_{D0}}{K} + 4C_{L,Dmin}^2} - C_{L,Dmin}\right)^{-1}\right)^{1/2} \quad \textbf{(C.13)}$$

$$@ \left(L/D \right)_{max} = \left(C_L/C_D \right)_{max}$$

Table C.1. (C_L/C_D)max Relations

	Symmetrical	Cambered
C_{D0}	KC_L^2	$K\left(C_L^2 - C_{L,Dmin}^2\right)$
C_L	$\sqrt{\dfrac{C_{D0}}{K}}$	$\sqrt{\dfrac{C_{D0}}{K} + C_{L,Dmin}^2}$
$\left(L/D \right)_{max}$ $= \left(C_L/C_D \right)_{max}$	$\sqrt{\dfrac{1}{4C_{D0}K}}$	$\sqrt{\dfrac{1}{4KC_{D0}} + \left(\dfrac{C_{L,Dmin}}{2C_{D0}}\right)^2} + \dfrac{C_{L,Dmin}}{2C_{D0}}$
$V_{(L/D),max}$ $= V_{(T_R)_{min}}$	$\left(\dfrac{2}{\rho_\infty} \sqrt{\dfrac{K}{C_{D0}}} \dfrac{W}{S} \right)^{1/2}$	$\left(\dfrac{2}{\rho_\infty} \sqrt{\dfrac{K}{C_{D0} + KC_{L,Dmin}^2}} \dfrac{W}{S} \right)^{1/2}$

$$@ \left(C_L^{3/2}/C_D \right)_{max}$$

Table C.2. $(C_L^{3/2}/C_D)$max Relations

	Symmetrical	Cambered
C_{D0}	$\dfrac{1}{3}KC_L^2$	$\dfrac{1}{3}K\left(C_L - C_{L,Dmin}\right)\left(C_L + 3C_{L,Dmin}\right)$
C_L	$\sqrt{\dfrac{3C_{D0}}{K}}$	$C_L^* = \sqrt{\dfrac{3C_{D0}}{K} + 4C_{L,Dmin}^2} - C_{L,Dmin}$
$\left(C_L^{3/2}/C_D \right)_{max}$	$\dfrac{1}{4}\left(\dfrac{3}{KC_{D0}^{1/3}} \right)^{3/4}$	$\dfrac{1}{4}\dfrac{\left(C_L^* + 3C_{L,Dmin}\right)\left(C_L^*\right)^{1/2}}{C_{D0}}$
$V_{\left(C_L^{3/2}/C_D\right),max}$	$\left(\dfrac{2}{\rho_\infty} \sqrt{\dfrac{K}{3C_{D0}}} \dfrac{W}{S} \right)^{1/2}$	$\left(\dfrac{2}{\rho_\infty} \dfrac{1}{C_L^*} \dfrac{W}{S} \right)^{1/2}$

APPENDIX D

CONSTRAINT EQUATIONS

D.1. Climb Speed Constraint

$$V_{\theta_{max}} = V_{stall}$$

$$V_{\theta,max}^4 + \frac{\eta_{pr}(P/W)(W/S)}{\rho_\infty C_{D0}} V_{\theta,max} - \frac{4(W/S)^2 K}{\rho_\infty^2 C_{D0}} = 0 \qquad \textbf{(D.1)}$$

$$\frac{P_A}{W} = \frac{4K(W/S)}{\rho_\infty V_{\theta_{max}}} - \frac{\left(V_{\theta_{max}}\right)^3 \rho_\infty C_{D,0}}{(W/S)}$$

$$\frac{P_A}{W} = \frac{4K(W/S)}{\rho_\infty V_{stall}} - \frac{(V_{stall})^3 \rho_\infty C_{D,0}}{(W/S)} \qquad \textbf{(D.2)}$$

D.2. Maximum Rate of Climb Constraint

$$(R/C)_{max} = \frac{\eta_{pr}P}{W} - V_{(R/C)max} \frac{1.155}{(L/D)_{max}} \qquad \textbf{(D.3)}$$

$$\frac{\eta_{pr}P}{W} = \frac{P_A}{W}$$

$$V_{(R/C)max} \approx V_{\left(C_L^{3/2}/C_D\right)_{max}} = \left(\frac{2}{\rho_\infty} \frac{W}{S} \left(\sqrt{\frac{3C_{D0}}{K} + 4C_{L,Dmin}^2} - C_{L,Dmin} \right)^{-1} \right)^{1/2}$$

$$\left(\frac{L}{D}\right)_{max} = \sqrt{\frac{1}{4KC_{D0}} + \left(\frac{C_{L,Dmin}}{2C_{D0}}\right)^2} + \frac{C_{L,Dmin}}{2C_{D0}}$$

$$\frac{P_A}{W} = \left(\frac{R}{C}\right)_{max} + \left(\frac{2}{\rho_\infty}\frac{W}{S}\left(\sqrt{\frac{3C_{D0}}{K} + 4C_{L,Dmin}^2} - C_{L,Dmin}\right)^{-1}\right)^{1/2}$$

$$\times \frac{1.155}{\sqrt{\frac{1}{4KC_{D0}} + \left(\frac{C_{L,Dmin}}{2C_{D0}}\right)^2} + \frac{C_{L,Dmin}}{2C_{D0}}}$$

(D.4)

D.3. Maximum Speed Constraint

$$L = W = \frac{1}{2}\rho_\infty V_{max}^2 S C_L$$

(D.5)

$$V_{max} = \sqrt{\frac{2(W/S)}{\rho_\infty C_L}}, \qquad C_L = \frac{(W/S)}{\frac{1}{2}\rho_\infty V_{max}^2}$$

(D.6)

(D.7)

$$P_A = P_R = T_A V_{max} = \frac{W}{L/D}V_{max} = \frac{W}{C_L/C_D}V_{max}$$

$$\frac{P_A}{W} = \frac{V_{max}}{C_L/C_D}$$

(D.8)

$$\frac{P_A}{W} = \frac{1}{C_L/C_D}\sqrt{\frac{2(W/S)}{\rho_\infty C_L}} = \sqrt{\frac{2(W/S)C_D^2}{\rho_\infty C_L^3}} = \left(\frac{C_D}{C_L^{3/2}}\right)\sqrt{\frac{2(W/S)}{\rho_\infty}}$$

(D.9)

$$\frac{P_A}{W} = \left(\frac{C_{D0} + K\left(\frac{(W/S)}{\frac{1}{2}\rho_\infty V_{max}^2} - C_{L,Dmin}\right)^2}{\left(\frac{(W/S)}{\frac{1}{2}\rho_\infty V_{max}^2}\right)^{3/2}}\right)\sqrt{\frac{2(W/S)}{\rho_\infty}}$$

$$\frac{P_A}{W} = \sqrt{\frac{2}{\rho_\infty}}\left(C_{D0} + K\left(\frac{\left(\frac{W}{S}\right)}{\frac{1}{2}\rho_\infty V_{max}^2} - C_{L,Dmin}\right)^2\right)\left(\frac{\left(\frac{1}{2}\rho_\infty V_{max}^2\right)^{3/2}}{(W/S)}\right)$$

(D.10)

D.4. Sustained Level Turn Constraint

$$n = \left\{ \frac{\frac{1}{2}\rho_\infty V_\infty^2}{K(W/S)} \left[\left(\frac{T_A}{W}\right) - \frac{1}{2}\rho_\infty V_\infty^2 \frac{C_{D0}}{W/S} \right] \right\}^{1/2} \qquad \textbf{(D.11)}$$

$$n = \left\{ \frac{\frac{1}{2}\rho_\infty V_\infty^2}{K(W/S)} \left[\frac{1}{V_\infty} \left(\frac{P_A}{W}\right) - \frac{1}{2}\rho_\infty V_\infty^2 \frac{C_{D0}}{W/S} \right] \right\}^{1/2}$$

$$\left(\frac{P_A}{W}\right) = \frac{1}{2}\rho_\infty V_\infty^3 \frac{C_{D0}}{(W/S)} + \frac{n^2 K(W/S)}{\frac{1}{2}\rho_\infty V_\infty} \qquad \textbf{(D.12)}$$

APPENDIX E

APC – SLOW FLYER – 11X4.7 PROPELLER DATA

Table E.1. Propeller Data

J	C_T	C_P	η_{pr}
0.087	0.1151	0.0482	0.209
0.107	0.112	0.0477	0.250
0.133	0.1071	0.0468	0.305
0.155	0.1033	0.0461	0.346
0.175	0.0996	0.0454	0.385
0.197	0.096	0.0448	0.422
0.218	0.0921	0.044	0.456
0.241	0.0885	0.0434	0.492
0.264	0.0844	0.0426	0.522
0.287	0.0803	0.0417	0.553
0.31	0.0762	0.0408	0.579
0.33	0.0723	0.0399	0.598
0.347	0.0687	0.039	0.612
0.373	0.0637	0.0376	0.632
0.391	0.0597	0.0364	0.641
0.416	**0.0545**	**0.035**	**0.647**
0.436	0.0494	0.0336	0.644
0.457	0.0442	0.0322	0.628
0.479	0.0386	0.0307	0.603
0.5	0.0333	0.0293	0.568
0.528	0.0254	0.0273	0.491
0.546	0.0203	0.026	0.426
0.571	0.0131	0.0241	0.310
0.59	0.0077	0.0227	0.200
0.615	-0.0001	0.0205	-0.002
0.637	-0.0068	0.0186	-0.234